Universitat Autònoma de Barcelona

IRON-CATECHOL BASED NANOSCALE COORDINATION POLYMERS AS EFFICIENT CARRIERS IN HIV/AIDS THERAPY

Rubén Solórzano Rodríguez

Universitat Autònoma de Barcelona

IRON-CATECHOL BASED NANOSCALE COORDINATION POLYMERS AS EFFICIENT CARRIERS IN HIV/AIDS THERAPY

Rubén Solórzano Rodríguez

Ph.D Thesis

Ph.D. in Chemistry

Supervisors: Dr. Ramon Alibés Arqués

Dr. Félix Busqué Sánchez

Dr. Daniel Ruiz Molina

Departament de Química

Facultat de Ciències

Universitat Autònoma de Barcelona

Memòria presentada per aspirar el Grau de Doctor per Rubén Solórzano Rodríguez

Rubén Solórzano Rodríguez

Vist i plau

Dr. Ramon Alibés Arqués Dr. Félix Busqué Sánchez Dr. Daniel Ruiz Molina

Bellaterra, 19 de Setembre de 2019

ABSTRACT

In this thesis, synthetic methodologies for the preparation of catechol compounds conjugated to antiretroviral drugs through an enzyme-sensitive bond are presented. As a proof-of-concept, the anti-HIV drug zidovudine is used as a starting point. Iron-based nanoscale coordination polymers (NCPs) are then prepared using this zidovudine-catechol conjugate and a bis(imidazole) bridging ligand. After optimization of the synthetic methodology to achieve a suitable particle size and colloidal dispersion, the drug release profile of the NCPs in the presence or absence of esterases is determined by HPLC. Then, a biological evaluation of the nanoparticles is performed, including cytotoxicity, cellular uptake and anti-HIV activity.

As a step forward, the synthesis of additional catechol compounds attached to anti-HIV drugs is explored. Functionalization of emtricitabine and raltegravir with catechol allows the formation of analogous NCPs for each drug. After the determination of their drug release profile by methodologies developed in HPLC, NCPs containing a mixture of both drugs are prepared and their release behavior is compared to the individual NCPs.

Last, methodologies for the preparation of other catechol conjugates with lamivudine and tenofovir are explored for their application in NCPs synthesis.

ABBREVIATIONS

^{1}H NMR: ^{1}H nuclear magnetic resonance

^{13}C NMR: ^{13}C nuclear magnetic resonance

AIDS: acquired immunodeficiency syndrome

ART: antiretroviral therapy

ARV: antiretroviral

AZT: zidovudine, 3'-azido-3'-deoxythymidine

Bix: 1,4-bis(imidazol-1-ylmethyl)benzene

BSA: bovine serum albumin

cART: combinational antiretroviral therapy

CDI: 1,1'-carbonyldiimidazole

CT: computed tomography

CTAB: cetyltrimethylammonium bromide

DBU: 1,8-diazabicyclo[5.4.0]undec-7-ene

DCC: *N,N'*-dicyclohexylcarbodiimide

DIAD: diisopropyl azodicarboxylate

DIPEA: *N*,*N*-diisopropylethylamine

DMAP: 4-dimethylaminopyridine

DMF: *N,N*-dimethylformamide

DNA: deoxyribonucleic acid

dNTP: dexoynucleoside triphosphate

EDCI: 1-ethyl-3-(3-dimethylaminopropyl)carbodiimide

FDA: U.S. Food and Drug Administration

FI: fusion inhibitor

HAART: highly active antiretroviral therapy

HATU: 1-[bis(dimethylamino)methylene]-1H-1,2,3- triazolo[4,5b] pyridinium 3-oxid hexafluorophosphate

HIV: human immunodeficiency virus

HMBC: heteronuclear multiple bond correlation

HOBt: hydroxybenzotriazole

HRMS: high-resolution mass spectrometry

HSQC: heteronuclear single-quantum correlation

ICP-MS: inductively coupled plasma mass spectrometry

IPC: ion pair chromatography

MRI: magnetic resonance imaging

NCPs: nanoscale coordination polymers

NMOFs: nanoscale metal-organic frameworks

NNRTI: non-nucleoside reverse transcriptase inhibitor

NRTI: nucleoside reverse transcriptase inhibitor

PBS: phosphate buffer saline

PEG: polyethylene glycol

PET: positron emission tomography

PI: protease inhibitor

PVP: polyvinylpyrrolidone

R_f: retention factor

rt: room temperature

RT: reverse transcriptase

SEM: scanning electron microscope

SPECT: single photon emission computed-tomography

TBDPS: *tert*-butyldiphenylsilyl

*t*Bu: *tert*-butyl

TEM: transmission electron microscopy

THF: tetrahydrofuran

TLC: thin layer chromatography

Table of contents

Chapter 1

Introduction

1.1 Nanoparticles in Medicine

Nanotechnology has emerged as a promising platform for overcoming pharmacokinetic limitations of conventional drug formulations.[1,2] Drugs freely diffuse and distribute throughout blood vessels upon administration, which usually leads to unwanted side effects and a decrease in their therapeutic efficacy. By nanosizing and optimizing a drug formulation, several advantages could potentially be achieved: (i) improved drug delivery to the target tissue due to preferential accumulation of nanoparticles in tumoral tissues, thus minimizing side effects; (ii) extended blood circulation half-life because of their reduced renal clearance; (iii) enhanced solubility of poorly water-soluble drugs; (iv) sustained drug delivery which could lower the frequency of administration; and (v) simultaneous delivery of two or more drugs to generate a synergistic effect and suppress drug resistance. As a result of all these advantages, the use of nanoparticles has revealed novel and unusual phenomenologies. For instance, in 1986 Maeda and coworkers discovered the enhanced permeability and retention (EPR) effect that describes an increased accumulation of nanoparticles in tumors due to a better capillary permeability in tumor tissue and the lack of effective lymphatic drainage.[3]

Overall, nanoformulations have provided improvements in patient safety and morbidity, though their efficacy still remains moderate and only offer minimal advantages over conventional formulations. This fact can be attributed to the series of complex biological impediments that nanodrugs face upon their administration, which critically limit their bioavailability and therefore prevent their therapeutic action. These biological impediments include opsonization and sequestration by the mononuclear phagocyte system (MPS), nonspecific distribution, hemorheological/blood vessel flow limitations, pressure gradients, cellular internalization, escape from endosomal or lysosomal compartments and drug efflux pumps.[1,2] All these limitations are detailed next.

After injection, nanoparticles experience opsonization, i.e. the adsorption of plasma proteins (serum albumin, apolipoproteins and immunoglobulins, among others) onto their surface, depending on factors such as nanoparticle size, surface charge, hydrophobicity and surface chemistry. After protein adsorption, nanoparticles are recognized by phagocytes, attach to specific receptors on their surface and are internalized in organs such as the spleen, liver and bone marrow, contributing to nonspecific distribution in healthy organs. Moreover, the opsonization process has proven to be unfavorable to nanoparticle active-targeting approaches because the protein corona formed effectively masks any ligand on the particle surface.[4] Avoiding or minimizing the adsorption of plasma proteins in the first place is one of the key

points for achieving long circulation nanoformulations (figure 1.1). The most common strategy is the attachment of polyethylene glycol (PEG) moieties onto the surface of the particle, although similar effects have been described using polaxamer, polyvinyl alcohol, poly(amino acid)s or polysaccharides. PEG is an inert, FDA-approved polymer that introduces steric hindrance and prevents protein binding. In addition, its strong hydrophilic nature improves colloidal stability in biological environments. Other strategy for minimizing protein corona formation involves particle functionalization with peptides based on the membrane protein CD47, which is used to avoid recognition from macrophages and therefore prevents phagocytosis in healthy cells.[5] In addition, other surface functionalization, using biomimetic cell membranes from leukocytes[6] or red blood cells,[7] have provided an increase in circulation half-life of nanoparticles.

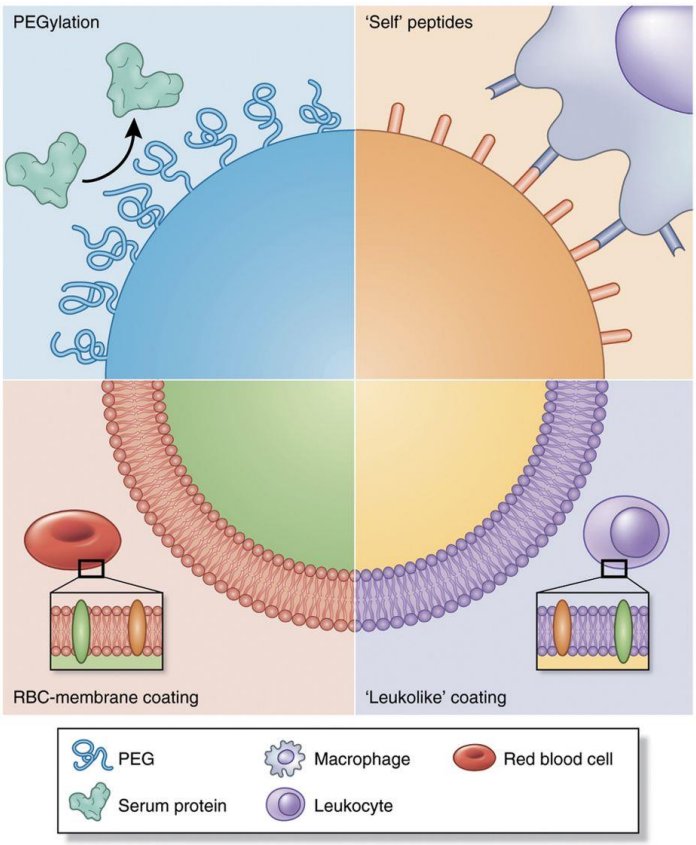

Figure 1.1. Strategies for preventing protein adsorption on nanoparticles, including the attachment of PEG, peptides that avoid recognition from macrophages and coating based on leukocytes and red blood cells. Reproduced from reference 2 with permission.

The use of a diametrically opposed approach is also of great significance, i.e. taking advantage of protein corona formation to target specific cells or disease sites. For instance, particles coated with the surfactant polysorbate 80 were observed to cross the blood-brain barrier due to adsorption of apolipoproteins onto their surface, which mimicked endogenous lipoproteins.[8] In

another example, CdSe/ZnS quantum dots were functionalized with the inflammatory metabolite cholesterol 5,6-secosterol atheronal-B which induced a misfolding in certain proteins that constitute the protein corona formed.[9] This misfolding event enhances nanoparticle uptake in macrophages, which are known to be related to inflammation and consequent diseases process, including cancer and atherosclerosis.

Once nanoparticles extravasate from blood vessels, they need to be internalized by the target organs or tissues in order to release their therapeutic cargo into the cell cytoplasm or nucleus. Unlike small molecules, which are usually internalized by diffusion through the cell lipid bilayer membrane, nano- and microparticles require active uptake mechanisms. Endocytosis mediated by the protein clathrin is the most representative pathway.[10] It involves cell membrane invagination, formation of vesicles (endosomes) and fusion with lysosomes. In addition, lysosomes provide an acidic environment (pH ~5.0) which helps to degrade small molecules, nanoparticles or genetic material. Some strategies for avoiding lysosomes or promoting endosomal rupture are based on the "proton sponge effect", in which a proton-absorbing species induces osmotic swelling and rupture of the endosome,[11,12] or on the promotion of an alternative endocytosis pathway based on caveolae formation, which eventually forms caveosomes of neutral pH.[13] The main factors that influence the behavior of nanoparticles in biological media are described next and include particle size, surface charge, particle geometry, deformability and degradability (figure 1.2).

- **Particle size:** it can affect phenomena including circulation half-life, extravasation through leaky vasculature or macrophage uptake. Particles smaller than 5 nm have been observed to endure renal clearance and thus accumulate in the kidneys.[14] Nanoparticles ranging from 100 and 200 nm have been observed to avoid filtration by liver and spleen and therefore extravasate through vascular fenestrations of tumors (EPR effect). However, as particle size increases beyond 150 nm, accumulation in the liver and spleen is preferred. Larger particles (2-5 µm) tend to accumulate within the capillaries of the lungs. Moreover, macrophages of the liver, spleen and lungs contribute considerably to particle uptake. Considering these factors, particles with sizes around 100 nm offer longer circulation half-lives which eventually leads to improved therapeutic effects.
- **Surface charge:** it influences protein adsorption, which in turn induces changes in pharmacokinetics and biodistribution of particles.[15] Cationic nanoparticles have been observed to be rapidly cleared from circulation due to their enhanced protein adsorption rates, which increases nonspecific uptake by macrophages. On the other hand, neutral or slightly negative particles show greater circulation half-lives values and less accumulation in

the organs mentioned above. Interestingly, positively-charged particles are reported to feature a greater cellular uptake than neutral or anionic particles due to interactions with the cell membrane.[16] Wang and coworkers exploited this idea by designing nanoparticles based on zwitterionic polymers.[17] At physiological pH, the particles exhibited long circulation half-lives values owing to their neutral net charge. However, once accumulated into tumor tissues, the intrinsic acidity inside caused the polymer to acquire a positive charge that incremented cellular uptake and consequently therapeutic effect.

- **Nanoparticle geometry:** it affects margination dynamics (lateral drift from the core blood vessel to endothelial walls) as well as cellular uptake and in vivo fate. Spherical particles display little lateral drift and therefore are less likely to contact endothelial walls, whereas nonspherical particles experience more complex motions like tumbling or rolling which cause an oscillation between walls in a blood vessel and favors interaction with the endothelium.[18] Particle geometry can also modify circulation half-life. Discher and coworkers reported filamentous polymer micelles (filomicelles) made by block copolymers of PEG-polyethylene or PEG-polycaprolactone which exhibited greater in vivo circulation times than their spherical analogues (up to one week for filomicelles, two or three days for spheres).[19] These results were rationalized owing to the tendency of cylindrical particles to align with blood flow and remove phagocyte as they come into contact. The role of particle geometry in phagocytosis has also been studied.[20] In this work, the internalization of ellipsoidal polystyrene particles was reported to be faster along their long axis than the shorter one, rationalized using a parameter called normalized curvature (**Ω**). These results provided the basis for the exploration of cylindrical, ellipsoidal and discoidal particles. As an example, the aforementioned filomicelles were observed to show greater accumulation and drug release in tumors than their spherical counterparts.[21]
- **Other factors:** they include deformability and degradability. Concerning deformability, it has been reported that soft particles possess longer circulation times than rigid ones.[22] The effect was examined in vivo by varying nanoparticle stiffness using different degrees of crosslinking within the reported nanogels. In short, softer particles were prone to deform, thus easily crossing through physiological barriers such as the splenic interendothelial slits, avoiding accumulation in the spleen and therefore increasing their circulation half-life. Regarding particle stability towards aggregation, it plays a major role in their cargo delivery. Yang and coworkers reported two related polymeric micelles with different kinetic stability and demonstrated that a higher kinetic stability enabled a faster accumulation in tumors than their analogues with lower kinetic stability.[23] Lastly, particle degradation represents an important feature in nanoformulations design, as drug release kinetics usually depends on

the degradation kinetics of the carrier. However, particles have to remain stable inside the body enough time to avoid accumulation in healthy organs and to maximize bioavailability in the target organ.

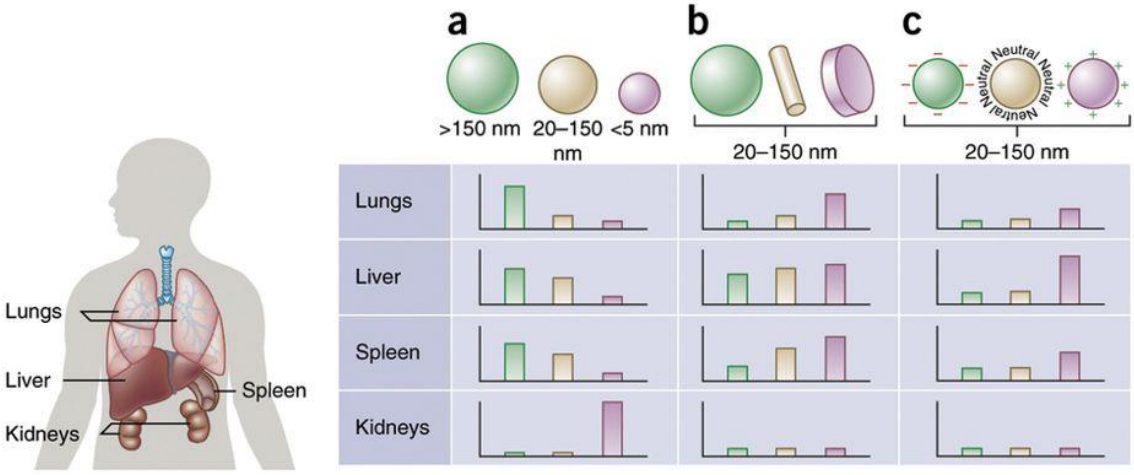

Figure 1.2. Nanoparticle size (a), shape (b) and surface charge (c) have a great impact on biodistribution among organs including the lungs, liver, spleen and kidneys. (a) Small particles (< 5 nm) are rapidly filtered through the kidneys, while larger particles accumulate in the lung, live and spleen, which becomes more relevant as particle size increases. (b) Different nanoparticle geometries display unique flow characteristic that modify their circulating lifetimes and cellular uptake, which affects biodistribution among the different organs. (c) Neutral and negatively-charged particles possess longer circulation times because of their reduced protein binding and subsequent macrophage uptake to the lung liver and spleen. On the contrary, positively charged particles experience greater protein interactions and therefore a noteworthy sequestration by macrophages in the previously mentioned organs. Reproduced from reference 2

In summary, the factors described during this section influence and should be considered for tuning the therapeutic effect of nanodrug formulations. Although nanoscaling of pharmaceuticals can enhance their bioavailability or confer them a controlled release behavior, nanoparticle-based drug delivery eventually requires a rational design involving the conception of multifunctional systems that are able to overcome the multiple biological impediments nanodrugs face upon their administration. Systems mostly used with this aim are described next.

Until 2017, 50 nanopharmaceuticals had been approved for clinical use, yet more than 60 were under clinical trials.[24,25] Currently, all FDA-approved nanodrugs fall into one of the following categories: liposomes, polymers, nanocrystals, inorganic, micelles or proteins (figure 1.3).

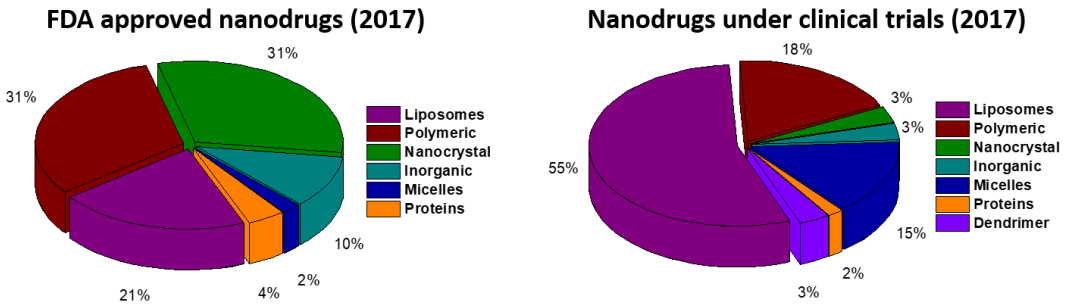

Figure 1.3. Nanodrugs approved by the FDA and under clinical trials until 2017 stratified by category. Data extracted from reference 25.

- **Liposomes**: are spherical vesicles composed by at least one lipid bilayer surrounding an aqueous core. They allow the delivery of both hydrophobic and hydrophilic compounds, ranging from small molecules to large macromolecules, while targeting ligands can also easily be integrated within the liposome structure to potentially increase therapeutic effect. In terms of pharmacokinetics, liposomes usually display short circulating half-lives; however, clearance can be minimized by PEGylation of liposome surface. Doxil®, the first liposomal nanodrug approved in 1995, consisted of the chemotherapeutic drug doxorubicin loaded into PEGylated liposomes.[26]
- **Polymeric nanopharmaceuticals:** are used either as polymer-drug conjugates for increasing drug half-lives and bioavailability and/or as degradable frameworks for controlled release. Polymers include synthetic or derived from natural compounds and span from single polymer chains to large aggregates. Copaxone®, a random copolymer composed of L-glutamic acid, L-alanine, L-lysine and L-tyrosine, is one of the most notable examples of direct use of polymers as therapeutic agents.[27] On the other hand, Eligard® can be found as an example of degradable framework.[28] This drug is composed by leuprolide, a testosterone inhibitor, inside a poly(lactic-*co*-glycolic acid) (PLGA) matrix, a well-known degradable polymer.
- **Nanocrystals:** constitute a unique class of nanodrugs in the sense that are composed by 100% of the therapeutic drug. Their increased surface area allows a faster dissolution and increases saturation solubility, which leads to improvements in diffusion-based mass transfers through biological structures such as the gastro-intestinal tract. Nanocrystal dosing can be applied to both organic and inorganic materials. Concerning organic formulations, Rapamune® was the first to be approved in 2000.[29] Based on the macrocyclic immunosuppressive agent sirolimus, also known as rapamycin, the nanocrystalline structure

provides a constant release profile to the otherwise poorly soluble free drug. On the other hand, inorganic nanocrystals approved by the FDA are limited to hydroxyapatite and calcium phosphate as bone graft substitutes.

- **Inorganic drugs**: include metallic and metal oxide materials. To date, all approved drugs within this category are based on iron, either as iron replacement therapies or as imaging agents. Other examples in clinical trials include biocompatible-coated gold nanoparticles for solid tumor treatment,[30] hafnium oxide particles to increase radiotherapy efficacy[31] or silica nanoparticles for fluorescence imaging.[32]
- **Micelles:** are based on the self-assembly of amphiphile molecules and their hydrophobic core can be used to encapsulate poorly water-soluble drugs. The use of block copolymers as the amphiphile constituents provides a lower critical micelle concentration (CMC) and therefore higher stability than conventional surfactants. To date, the only micelle-based drug approved is a formulation of estradiol (Estrasorb™), indicated as a topical treatment for vasomotor symptoms of menopause. However, several micellar formulations are in late-stage clinical trials.
- **Protein nanodrugs**: encompass different classes of medicines. One of them involves protein-drug conjugation, being Abraxane®, an albumin-bound form of the chemotherapeutic drug paclitaxel, an example.[33] This strategy for reducing drug toxicity is currently being tested in clinical trials with several types of albumin-bound nanoparticles containing, for example, docetaxel or rapamycin. Other classes of protein-based nanomedicines include engineered proteins where the protein itself is the therapeutic agent or combined nanoplatforms that depend on proteins for targeted delivery.

All the different families of nanoparticles previously described represent successful approaches for the formation of nanopharmaceuticals. From here on this dissertation, however, will focus on the family of polymeric nanoparticles, specifically in those composed by the miniaturization of coordination polymers, known as nanoscale coordination polymers (NCPs).

1.2 Nanoscale Coordination Polymers (NCPs)

Coordination polymers (CPs) are composed by metal ions or clusters linked by organic bridging ligands. CPs exhibit an interesting synthetic flexibility with directional metal-ligand bonds that can be used to systematically control and tune their chemical topology. Moreover, the limitless choice of metallic elements has allowed the formation of materials with interesting magnetic, electronic, optical, and catalytic properties. More recently, the nanoscaling of CPs became an

opportunity to merge their rich diversity with the advantages of nanomaterials, e. g., improvement of colloidal dispersion, increase of surface area and therefore catalytic, sensing or storage capabilities or the possibility of fine-tune the physical properties of the materials.[34]

Currently, CPs at the nanoscale fall into two different categories: (i) amorphous coordination polymer nanoparticles, referred from now on as nanoscale coordination polymers (NCPs),[35] also called infinite coordination polymers (ICPs)[36] or coordination polymer particles (CPPs)[37] and (ii) nanoscale crystalline and porous coordination polymer structures, referred from now on as NMOFs.[38] This last family, NMOFs, allows control over the release cargo via modification of tunable pores with an exceptionally high surface area and therefore loading capacity. The crystalline nature of MOFs also facilitates analyses of host–guest interactions and systematic drug encapsulation and release studies, as well as theoretical models. On the other hand, NCPs, their amorphous counterparts, allow more synthetic flexibility in the incorporation and release of their cargo as it can be physically entrapped or chemically attached as a part of the constitutive ligands of the polymeric structure. NCPs were first reported in 2005[39,40] and, since then, they have been examined in many applications such as gas storage and separation,[41-48] catalysis,[49-52] spin-crossover[53] sensing/biosensing,[54-59] hybrid nanoparticle-based devices,[60] precursors for inorganic particles,[61] thermochromic nanostructures,[62] biomedical imaging,[63-67] drug delivery or theranostic platforms[68-73] owing to the virtually infinite combinations between metal ions and organic ligands. Although both families of coordination polymers at the nanoscale have been used in the field of drug encapsulation, from here on this thesis will only focus on the synthetic methodology of NCPs and their application in the field of nanomedicine.

1.2.1 Synthetic Methodologies and Mechanisms of Formation

The most used methods in the synthesis of NCPs can be categorized into one of the following four approaches: nanoscale precipitation, solvothermal, surfactant-based reverse microemulsion and surfactant-templated solvothermal conditions.[69,70] Other novel, less explored approaches to obtain NCPs include AFM-assisted lithography[74] or lab-on-a-chip implementation.[75]

- **Nanoscale precipitation method:** in this method nanoparticles are usually formed due to the insolubility of the coordination polymer in a given solvent while ligands remain soluble. Thus, particles can be formed instantaneously after precursor solutions are mixed. (figure 1.4). If, in a less usual situation, particles are initially soluble in the chosen solvent, they are allowed to nucleate and grow until a poor solvent is added to induce precipitation. For example, the first common approach was used in the synthesis of photodegradable NCPs

composed by Zn^{2+} and a photocleavable organic linker containing *o*-nitrobenzyl derivatives.[76] In that way, precursor solutions in a poor solvent were mixed and a white precipitate was instantaneously observed. Moreover, in this strategy, particle size could be controlled from 160 to 1500 nm by varying the initial precursor concentration. In fact, using this strategy, particle size could also be tuned by modifying parameters like stirring rate,[77] rate of precursor addition or polarity of the poor solvent.[39]

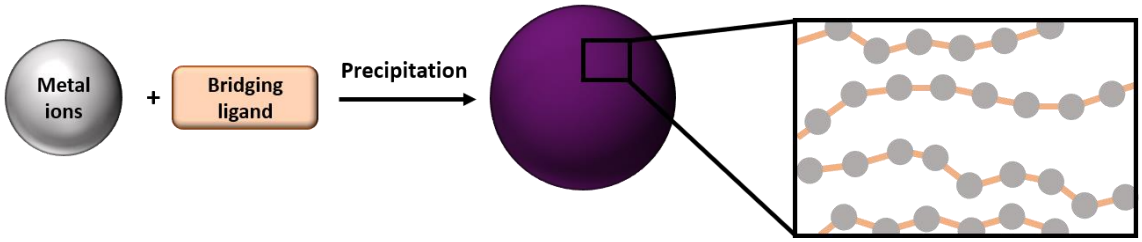

Figure 1.4. Schematic representation of a typical NCPs synthesis by the precipitation method (ref 36).

- **Solvothermal synthesis:** it relies on the control of particle nucleation and growth by heating a solution of metal ions and organic ligands. Although this approach is usually performed to obtain crystalline nanoscale frameworks, amorphous nanomaterials could be also obtained depending on the experimental conditions, for example with the used of microwave heating.[78]
- **Surfactant-based reverse microemulsions:** water in oil microemulsions are used to control nucleation and growth kinetics of particles. Like the previous strategy, the use of surfactant is related with the formation of crystalline structures, although the synthesis of NCPs using this method has also been reported. As an example, NCPs containing chemotherapeutic drugs carboplatin and gemcitabine were synthesized by mixing the precursors in two separate microemulsions,[79] as well as NCPs containing a self-assembly of Zn^{2+} and bisphosphonate prodrugs of cisplatin or oxaliplatin, made by the addition of both precursors in the form of microemulsions.[80]
- **Surfactant-templated solvothermal synthesis:** Surfactants can also be used as templates during solvothermal synthesis. This method differs from the previous approach in the sense that surfactant molecules are not incorporated in the final structure as heating destroys the microemulsions. However, their presence plays an important role in the final morphology of the particle formed. As in the microemulsion method at room temperature, this strategy is usually performed to obtain crystalline NMOFs, but synthesis of NCPs using this approach, , have also been reported.[81] As an example, NCPs containing Zn^{2+} and the drug methotrexate

were prepared by microwave-assisted heating of their respective emulsions in octanol/isooctane using CTAB as surfactant.

In order to improve size and shape control along NCPs synthesis, early studies were performed to try to understand their formation mechanisms. Mirkin and coworkers monitored the synthesis of NCPs based on the self-assembly of a Tröger's-base-derived ligand (I, figure 1.5) and Zn^{2+} cations using SEM.[82] Thus, aliquots of the reaction mixture were taken at different time intervals and analyzed by SEM, revealing the initial formation of small globular seeds which began to aggregate and form larger spherical particles with rough surface. As the reaction proceeded, particle roughness was observed to decrease to finally afford smooth spherical-shaped particles. Based on this evidence, the authors proposed a working mechanism for NCPs formation involving nucleation, oligomerization, aggregation, fusion, growth and annealing (figure 1.5).

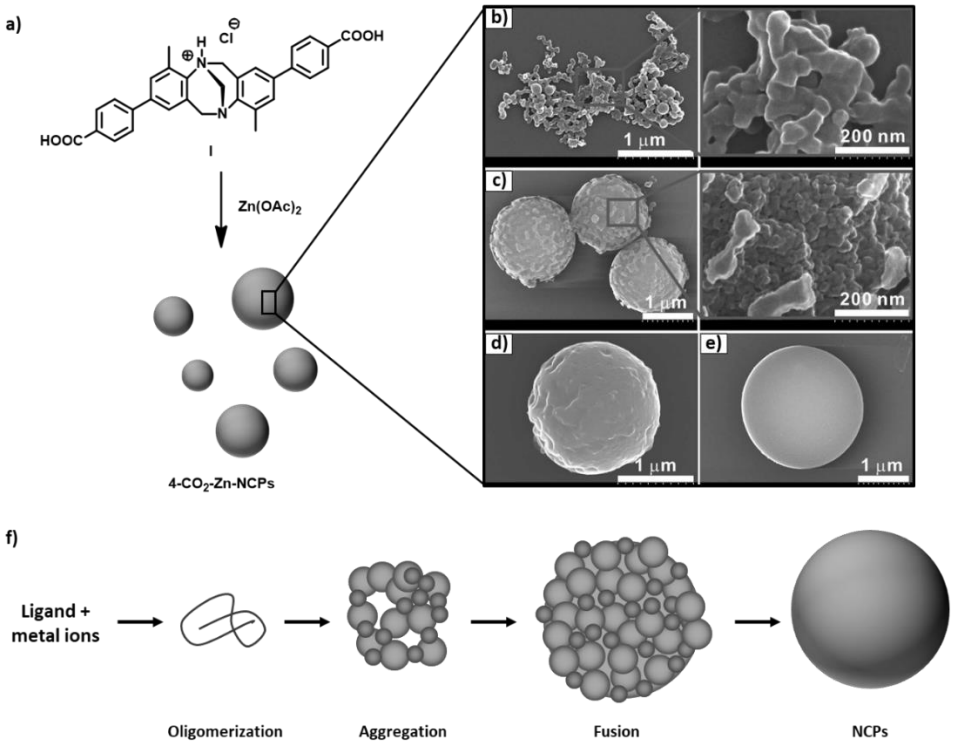

Figure 1.5. (a) Schematic synthesis of NCPs based on the self-assembly of a Tröger's-base-derived ligand and Zn^{2+}. (b – e) SEM images monitoring the formation of NCPs at different reaction times, (b) 5 min, (c) 10 min, (d) 30 min and (e) 60 min. (f) Proposed mechanism for NCPs formation. SEM micrographs reproduced from reference 82.

According to their hypothesis, the first three steps are relatively fast as both ligand and metal ion concentrations are high. However, as they decrease, particle growth and annealing prevail owing to both, the decrease of particle nucleation and the increasing importance of particle coalescence as driving force for surface tension reduction.

Similarly, Oh and coworkers studied the self-assembly of a dicarboxylic salen-based ligand (salen = *N,N'*-bis(salicylidene)ethylenediamine) and Zn^{2+} into nanocubes.[83] Interestingly, SEM images of aliquots at early stages of the reaction showed the formation of nanowires, which gradually aggregated and fused into smooth cube-shaped particles. Particle size could be then rationalized as the initial nanowires had similar dimensions regardless of the final size of the particles. Therefore, particle size could be controlled by limiting the number of nanowires in the intermediate aggregates, which could be achieved by temperature or solvent modifications.

1.2.2 Cargo Loading and Release

Among the wide range of applications for NCPs, medicine represents a technological area in which such polymers exhibit a broad impact.[68,70] As a general trend, NCPs have been shown to allow for the controlled release of active principles. For this, drugs can be trapped as constitutive building blocks of the polymeric unit (chemical entrapment) or through the physical encapsulation inside the nanoparticle, as demonstrated within our research group.[84] Both approaches are schematically represented in figure 1.6. The first one allows a high and homogeneous distribution of cargo, though nanoparticle morphology or physicochemical properties can be difficult to predict. On the other hand, physical encapsulation generally yields lower amounts of drug loaded, being strongly dependent on its physicochemical properties. As represented in figure 1.6 d, the drug release profile significantly varies between both approaches, obeying to a fast release controlled by diffusion (physical encapsulation) or by particle degradation (chemical entrapment). Physical encapsulation within micro- and nanospheres of active substances, such as organic dyes, magnetic nanoparticles, or luminescent quantum dots was already reported back in 2009.[85] One year later, our research group showed that these capsules not only can encapsulate but also can release active principles as polymeric nanoparticles do.[86] On the other side, chemical entrapment allows for a better fine-tuning of the release kinetics (up to many hours) as well as better formulation with increased encapsulation yields. The use of active metal drugs, such as Pt(IV),[87] as polymeric nodes of coordination polymers represent the most successful examples of chemical entrapment. Though also effective, less explored has been the chemical entrapment through tethering of active drugs as chelating ligands.[68,70] In this sense, the chemical flexibility of organic synthesis may allow for the design of drugs (ligands) cleaved under physiological conditions.

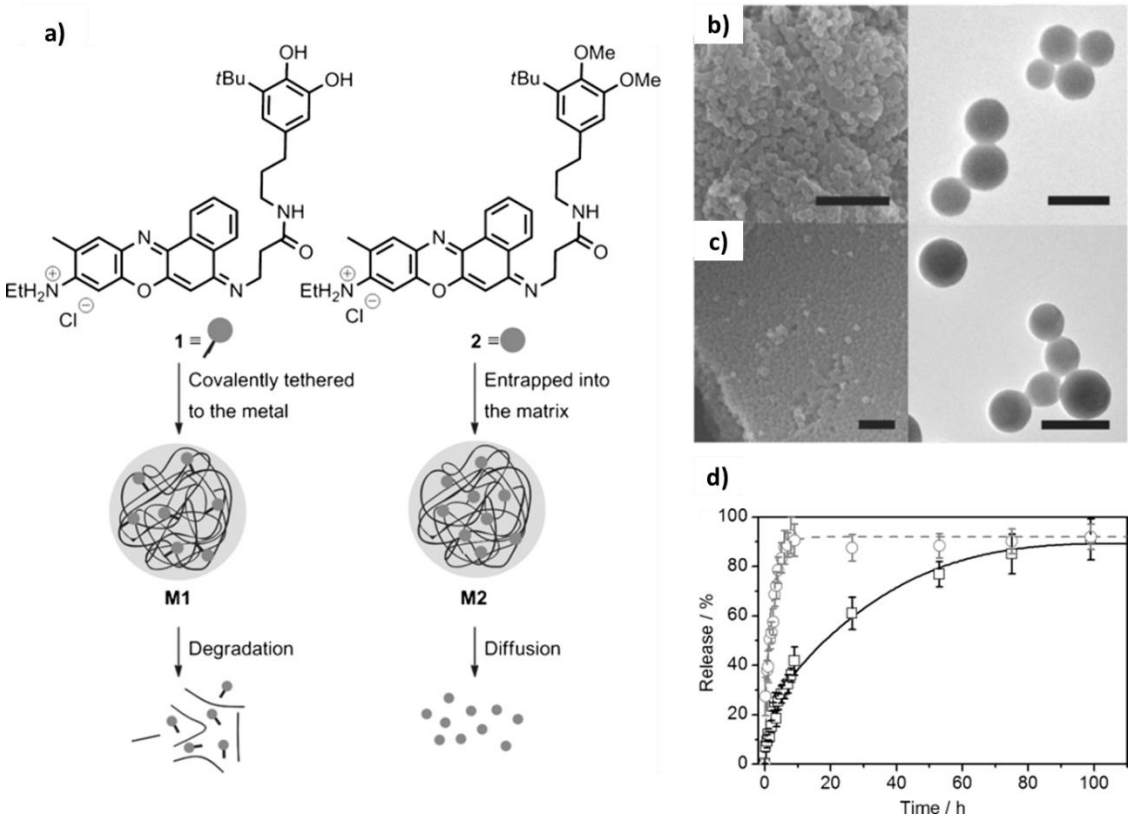

Figure 1.6. (a) Chemical structures of fluorescent guest compounds **1** and **2** used in the formation of structurally-analogous **M1** and **M2** particles, used to investigate degradation and diffusion-controlled release in NCPs. (b and c) SEM (left) and TEM (right) images of **M1** (b) and **M2** (c) particles. Scale bars for SEM are 1 µm and 200 nm for TEM. (d) Release profiles of fluorescent guest molecules from **M1** (□) and **M2** (○) at 37 °C, averaged over four independent experiments. Reproduced from reference 84 with permission of the copyright holder.

Recent examples of simple drug encapsulation into NCPs include the anticancer drug camptothecin into caffeic acid-based NCPs,[77] hydrophobic dye Nile red into nanowire coils of organometallic coordination polymers,[88] curcumin into particles made by its own self-assembly along with amino acids and Zn^{2+} ions,[89] DNA from its iron-induced self-assembly particles,[90] the chemotherapeutic drug doxorubicin into particles composed by the assembly of tryptophan-phenylalanine dipeptides to Zn^{2+} ions,[91] and different flavonoids from iron-induced microcapsules.[92]

A more interesting use of NCPs in medicine lies in the fabrication of materials with responsive properties due to the possibility of ligand fine-tuning in NCPs design. Several examples have been recently reported in which an external stimulus is able to trigger drug delivery. One of the most relevant stimulus is pH, because of both the pH-dependence nature of coordination bonds and the relevance of pH variations within intra- and extracellular environments. Their design usually falls into the same principles: particles at neutral pH are stable and ideally do not allow drug release. However, when pH is decreased around 5.0, their cargo experiences a burst or

rather sustained release. This ideal design feature obeys to the fact that nanoparticles are intended to be exposed at acidic pH only when they enter into the intracellular environment, ideally avoiding extracellular drug release.[10] Mainly, two different strategies are used to build such responsive systems. The first one relies on the nature of coordination bonds, in which often a decrease in pH implies a demetalation process, while the latter involve the design of pH-responsive ligands. Several examples of the first approach have been recently reported based on the chemistry of iron, specially using catechols as ligands,[93-100] or others.[101,102] Copper, zinc or silver are also reported as metallic nodes in the formation of pH-sensitive NCPs.[103-105] In the second strategy, the pH-responsiveness depends on the nature and design of the ligands themselves. NCPs composed by imine-based ligands have been reported to remain stable at neutral pH but experience a burst release at acidic conditions (figure 1.7).[106-108] Other examples include destabilization of the particle by a ligand-induced charge conversion of the polymer,[109] or disassemble of the coordination polymer caused by ligand protonation.[110]

Apart from pH, NCPs sensitive to other relevant stimuli have also been reported. Light-triggered release of model drugs have been described in NCPs composed by photocleavable ligands based on *o*-nitrobenzyl[76] or bis-(alkylthio) alkene units,[111] as well as particles composed by a carboxylic-functionalized diarylethene photoswitch with reversible photochromic behavior.[112] Redox-triggered release is also relevant from a biological point of view due to the reducing environment in the intracellular matrix. Thus, redox-induced disassembly of NCPs includes gallic acid-Fe(III) networks[113] or polymeric micelles including the 4-(methylthio)benzoyl unit crosslinked with [ethylenediamineplatinum(II)]$^{2+}$.[114] The virtually infinite tunability of NCPs also allows going a step forward, that is, the formation of NCPs sensitive not only to a single stimulus but two or more simultaneously. In this way, examples of pH- and redox-responsive nanoparticles have been recently reported,[115,116] as well as multi-responsive NCPs systems that act as molecular logic gates in the presence or absence of stimuli such as different metal cations, small organic molecules or pH variations.[127-120]

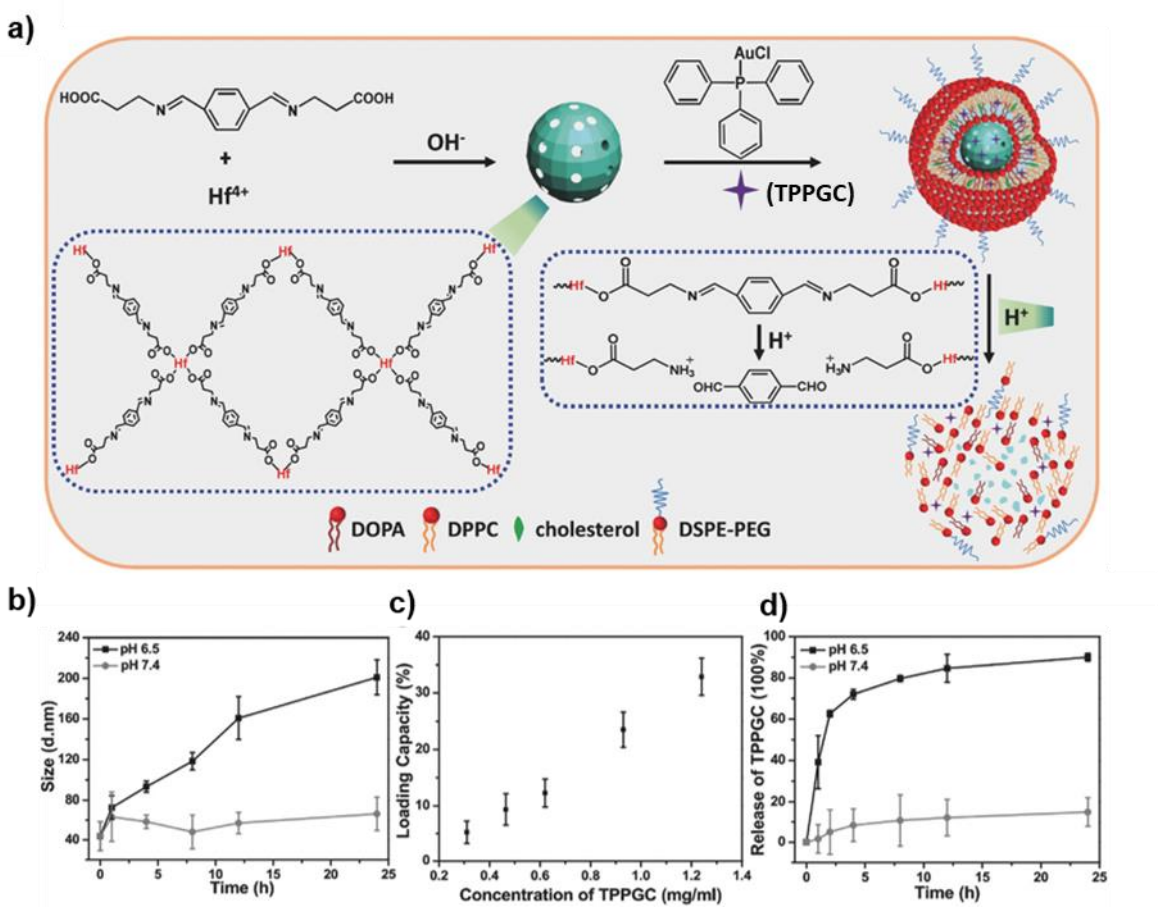

Figure 1.7. a) Synthesis of NCPs based on hafnium and a pH-responsive ligand containing an imine bond. b) Hydrodynamic size changes of the NCPs dissolved in pH 6.5 and pH 7.4 buffer solutions. c) Loading capacity of the NCPs at different feeding drug (TPPGC) concentrations. d) Cumulative release of the encapsulated drug (TPPGC) at pH 6.5 and pH 7.4. Reproduced from reference 107 with permission.

1.2.3 Nanoscale Coordination Polymers in Medicine

The potential multifunctionality of these nanosystems and the flexibility of their coordination chemistry opened new perspectives to their use as smart drug delivery systems, bioimaging probes or a combination of both (theranostics). Accordingly, as a consequence it has been a notable exponential growth in the in vitro and in vivo studies concerning the use of NCPs for diagnosis or therapy, especially to treat cancer. Most of the studies showed that different metals form coordination-driven particles with chemotherapeutic drugs such as methotrexate, daunorubicin hydrochloride, doxorubicin, mitoxantrone, pyridine-3-carboxylic acid, gossypol, and AQ4N due to the presence of carboxyl, hydroxyl, aldehyde or amino groups.[86,101,121-124] Moreover, the coordination bonds formed have adequate pH-response ability and can release drug molecules under small pH variations. Additionally, platinum-based chemotherapeutics has been often used as building blocks of NCPs,[80,125,126] which allowed the combination of platinum-based drugs and other encapsulated chemotherapeutics looking for increased synergistic

therapy.[127-130] Apart from platinum-based NCPs, other metals such as copper,[131] ruthenium,[132] cobalt,[133] arsenic,[134] bismuth,[135] lanthanum and strontium,[136] or indium[137] have been used in the formation of NCPs with anticancer activity.

NCPs have also been used in photodynamic therapy, an effective anticancer procedure involving the administration of a tumor-localizing photosensitizer followed by light activation to generate highly cytotoxic reactive oxygen species (ROS).[138] In this way, NCPs based on zinc phthalocyanine, a well-known photosensitizer, as well as DNA-based particles encapsulating the photosensitizer chlorine e6 have been reported to generate intracellular cytotoxic singlet oxygen.[139,140] The high flexibility in NCPs design also allows for combination therapy formulations, which enhance anticancer efficacy due to synergistic effects. Recent examples in the field of coordination particles include the combination of chemotherapy and photodynamic therapy for reducing drug resistance development and increasing the therapeutic effect that is achieved by using the drugs separately.[123,141,142] Other novel designs include coordination polymer hybridized Au nanocages for photothermal therapy,[143] DNA-functionalized NCPs as biocompatible gene regulation agents,[144] or direct encapsulation of individual tumor cells as whole cell vaccines.[145]

The presence of metal nodes and organic ligands in the NCPs structure allows for the design and fine-tuning of theranostic systems. These assemblies combine therapeutic and imaging agents with the idea of real-time monitoring of drug release in the target cells. Recent examples of theranostic NCPs are based on the use of magnetic resonance imaging (MRI), optical imaging and radioimaging as the diagnosis part of the theranostic assembly. The most studied ones are used in MRI. Briefly, an MRI contrast agent improves the sensitivity and image resolution of the technique by modifying the relaxation times of water protons under a magnetic field. Thus, NCPs formation aims to improve this sensitivity while reducing cell toxicity attributed to the presence of the free metals usually used such as gadolinium[146-148] and manganese[78,116,149-152] or through the formation of biocompatible iron-based NCPs with MRI properties.[153-157] NCPs exhibiting optical properties such as fluorescence include particles assembled using active ligands[158,159] or metals,[119] dye encapsulation[80,160] or particle surface functionalization with an optical active unit.[77,159] Radioimaging techniques include positron emission tomography (PET) and single photon emission computed-tomography (SPECT). Recent examples of radiolabeling include Au-[161,162] and Cu64-based NCPs.[163,164] However, the limitless combination of ligands and metals in NCPs allows for the assembly of systems with simultaneous responses in different diagnosis techniques. The most studied combination includes an MRI contrast agent coupled to optical

imaging,[165-168] although other examples include MRI + photoacoustic imaging,[155,169-171] MRI + photoacoustic imaging + PET[66] or optical + photoacoustic imaging.[172]

Despite the large number of examples of NCPs in medicine described above, the vast majority of studies reported focus on cancer, either as chemotherapeutics drug delivery systems or as more complex, multifunctional theranostic assemblies. During the early stages of this thesis, our attention was driven to the delivery of antiviral agents, specially focusing on anti-HIV drugs. To that date, the only example of coordination polymer-based nanoassemblies for the improvement of anti-HIV activity of drug zidovudine was reported in 2013 (and later updated in 2017) but described in crystalline NMOFs instead of amorphous NCPs (figure 1.8).[173,174] Thus, we decided to explore the feasibility of building nanosystems including one or more antiretroviral drugs. Before the introduction of our research plan, a brief background about HIV, antiretroviral drugs and the state of the art in antiretroviral therapy will be presented.

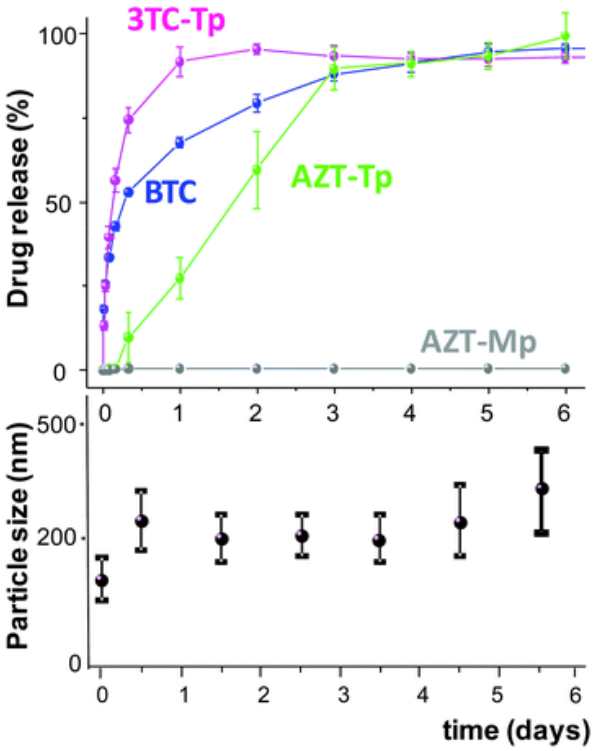

Figure 1.8. (top) Release of the anti-HIV drugs triphosphorylated lamivudine (3TC-Tp), triphosphorylated or monophosphorylated zidovudine (AZT-Tp and AZT-Mp) and the constitutive organic linker BTC from MIL-100(Fe) NMOF in simulated physiological conditions. (bottom) Monitoring of the particle size evolution during the release process. Reproduced from reference 174 with permission.

1.3 HIV

The human immunodeficiency virus (HIV) is a retrovirus that affects $CD4^+$ T-cells, macrophages and dendritic cells and eventually causes the acquired immunodeficiency syndrome (AIDS). The

main feature of AIDS is a fall in the number of circulating $CD4^+$ T-cells, which can potentially lead to life-threatening opportunistic infections.

The HIV-1 replication cycle is summarized in figure 1.9:[175] 1) the infection begins when the virus recognizes the CD4 receptor and the co-receptor CCR5 of a $CD4^+$ T-cell , leading to fusion of the viral and cellular membranes and entry into the cell; 2) partial viral capsid decomposition facilitates reverse transcription, where viral DNA is created from the original viral RNA; 3) integration of the viral DNA into the host DNA occurs within the context of nucleoprotein structures that arises from the viral core; 4) proviral transcription and nuclear export produce mRNAs that serve as a template for viral-protein production and their assembly; and 5) budding, release and maturation of a new viral particle complete the replication cycle. At this point, the new viral particles are able to infect other cells, starting the cycle all over again.

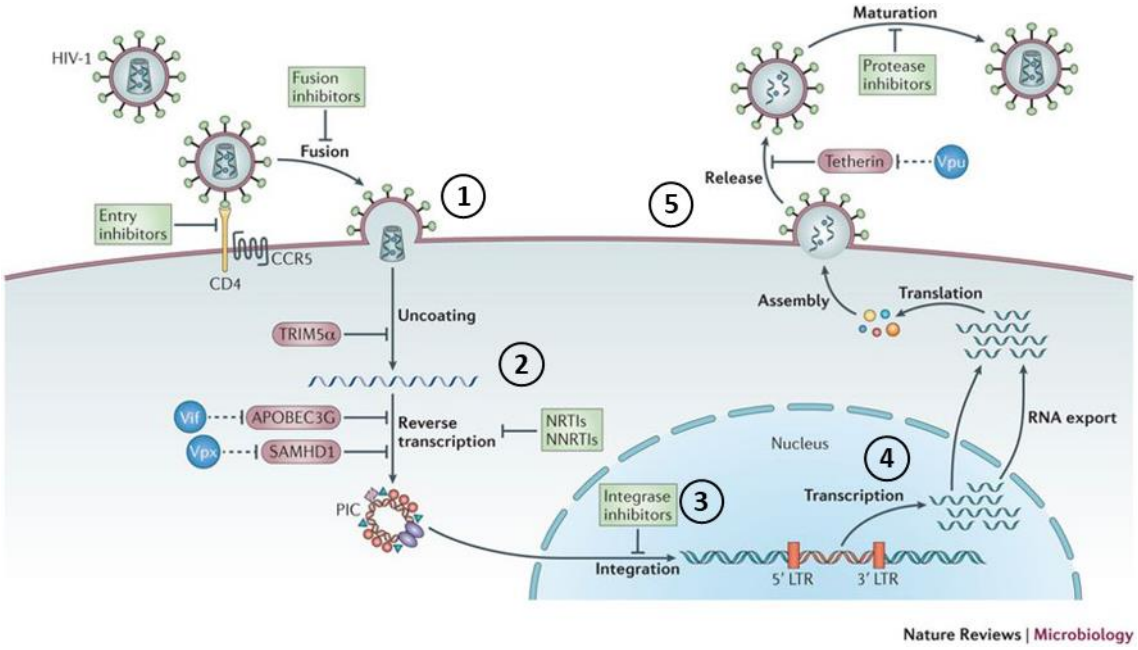

Figure 1.9. Schematic representation of the HIV-1 replication cycle. Potential targets for antiretroviral therapy are marked. Reproduced from reference 175 with permission.

In 2018, 37.9 million people were estimated to be living with HIV and around 62% (roughly 23.3 million) were receiving antiretroviral treatment, with a target of 30 million by 2020 according to the World Health Organization. In total, HIV/AIDS caused 0.8 million deaths during 2018 (figure 1.10). However, since antiretroviral therapy (ART) has been available, life expectancy of HIV-positive patients has been increased and currently nearly equals the life expectancy of HIV-negative population. Additionally, a marked decrease in HIV-related mortality has been observed while ART coverage has been increased. As an example, in 2018, data shows a decrease of 45% in deaths relative to 2000, as well as a decrease of 39% in new annual HIV diagnoses.[176]

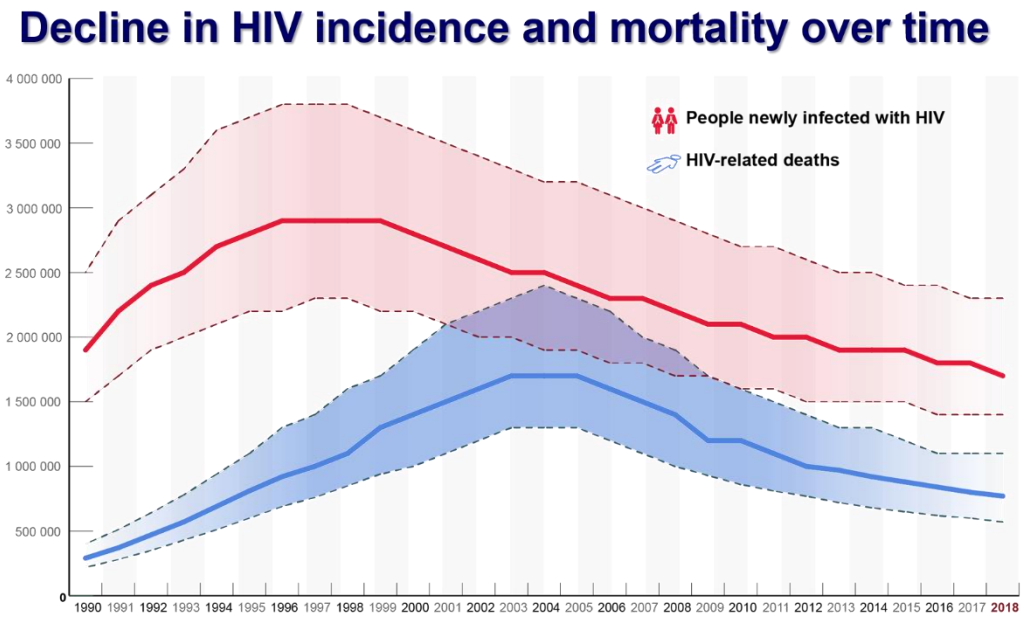

Figure 1.10. Evolution of HIV incidence and mortality since 1990. Reproduced from http://www.who.int/hiv/data/en/.

1.3.1 Historical Background of Anti-HIV Therapy

The first signs of AIDS were recognized in the United States in 1981, where cases of young men dying from infections that otherwise a healthy immune system would repel were reported.[177] In less than one year, the term AIDS was coined by the United States Centers for Disease Control and Prevention (CDC) to describe such opportunistic infections in the context of significantly low circulating $CD4^+$ T-cells count. During the following two years, the retrovirus currently known as HIV-1 was simultaneously isolated in the United States and France by Luc Montagnieri[178] (Pasteur Institute) and Robert Gallo[179] (U.S. National Cancer Institute), respectively. The astonishing achievements that arose from those early discoveries in 1985 included the development of a reliable HIV-specific test for blood screening and the identification of zidovudine (AZT) as a potential candidate for antiretroviral therapy, which culminated in its approval in 1987 by the U.S. Food and Drug Administration (FDA) as the first nucleoside reverse transcriptase inhibitor (NRTI). Other significant milestones in HIV research during the following decade comprised the adoption in 1992 of an accelerated drug approval mechanism by the FDA, the release of both the first protease inhibitor (saquinavir) and the first non-nucleoside reverse transcriptase inhibitor (NNRTI) (nevirapine) in 1995 and 1996, respectively. The introduction of the combination antiretroviral therapy (cART) as a standard of care, namely, the combination of two or more active agents allowed simplification and increased drug adherence for the patients. The first fixed-dose combination pill (zidovudine + lamivudine) was approved in 1997. Within

the 21st century, the targets of antiretroviral therapy (ART) were broadened with the inclusion of fusion inhibitors (enfuvirtide, 2003), CCR5 antagonists (maraviroc, 2007) and integrase inhibitors (raltegravir, 2007). Furthermore, in 2000, latent viral reservoirs were identified as a barrier to HIV eradication and in 2009 the first case of long-term control of HIV by CCR5-Δ32 stem-cell transplantation, known as "the Berlin patient", was reported.[180] Interestingly, a second case of long-term control of the virus via stem cell transplant was reported in 2019.[181] In the early 2010s, cART was found to effectively reduce the risk of HIV transmission in what is now known as pre-exposure prophylaxis (PrEP). All in all, Science Magazine considered it "Breakthrough of the Year 2011".[175,182]

In addition, the next improvement in fixed-dose combination pills was made in 2006 with the approval of Atripla™, the first one-pill, once-daily anti-HIV drug regimen. Atripla™ was composed by two NRTI (emtricitabine and tenofovir) and a NNRTI (efavirenz). Since its approval and until 2019, ten additional once-daily pills have been marketed, all of them containing two NRTIs and a NNRTIs or integrase inhibitor. Until now, the FDA has only approved one single-tablet regimen composed by just two antiretroviral drugs, Juluca, which combines the integrase inhibitor dolutegravir and the NNRTI rilpivirine.[183-186]

1.3.2 Antiretroviral Drugs against HIV

Nowadays, 37 antiretroviral drugs are used in the treatment of HIV infection,[187] which can be arranged into six different classes according to their target in the replication cycle: nucleoside/nucleotide reverse transcriptase inhibitor (NRTIs), non-nucleoside reverse transcriptase inhibitor (NNRTIs), protease inhibitor (PIs), entry/fusion inhibitors (FIs) and CCR5 antagonist and integrase inhibitors)(table 1.1, figure 1.11).

Table 1.1. FDA-approved drugs used in the treatment of HIV/AIDS, ordered by approval date. Drugs marked with ***** are no longer marketed.

NRTIs	Zidovudine (AZT)	**Protease Inhibitors**	Saquinavir (SQV)	**NNRTIs**	Nevirapine (NVP)
	Didanosine (ddI)		Indinavir (IDV)		Delavirdine (DLV)
	Zalcitabine* (ddC)		Ritonavir (RTV)		Efavirenz (EFV)
	Stavudine (d4T)		Nelfinavir (NFV)		Etravirine
	Lamivudine (3TC)		Amprenavir* (APV)		Rilpivirine
	Abacavir (ABC)		Lopinavir (LPV)	**Integrase Inhibitors**	Raltegravir
	Tenofovir disoproxil (TDF)		Atazanavir (ATV)		Dolutegravir
	Emtricitabine (FTC)		Fosamprenavir (FOS)		Elvitegravir
			Tipranavir (TPV)	**Fusion Inhibitors**	Enfuvirtide
			Darunavir (DRV)	**CCR5 antagonists**	Maraviroc

- **NRTIs:** they were the first antiretroviral drugs developed, based on 2',3'-dideoxynucleosides or nucleotides.[188] Once phosphorylated, they compete with endogenous deoxynucleoside triphosphates (dNTPs) in the HIV reverse transcription process, acting as chain-terminators of DNA elongation because of their lack of a 3'-hydroxyl group. Since the approval of AZT in 1987, several NRTIs haven been approved for ART (Table 1.1). The transport of NRTIs into the cell either by passive diffusion or carrier-mediated transport performs a crucial role in their bioavailability due to their intrinsic hydrophilicity and therefore limited membrane permeability. Once inside the cells, NRTIs undergo successive phosphorylation steps catalyzed by phosphotransferases and nucleoside/nucleotide kinases and become highly polar species with improved intracellular persistence. As an example, AZT half-life in plasma is estimated to range 0.5 to 3 hours,[189] while it increases to 7 hours in intracellular media.[190] Despite being the first antiretroviral drugs used, current combination therapy is based on NRTIs in synergy with either NNRTIs, PIs or integrase inhibitors.
- **NNRTIs:** they comprise a high diversity of chemical structures, unlike NRTIs, with more than 50 families of molecules described. NNRTIs inhibit the viral replication cycle by binding to the HIV retrotranscriptase enzyme in a specific hydrophobic pocket. Despite their chemical heterogeneity, all NNRTIs target at the same binding site. Additionally, unlike NRTIs, intracellular metabolization is not required to possess therapeutic effect. So far, only five NNRTIs are approved for their use in ART, although they are always used in combination with another drugs. Introduction of nevirapine and efavirenz represented, in fact, a cornerstone in combination antiretroviral therapy.[191]
- **Protease inhibitors (PIs):** they focus on the inhibition of the last step in HIV lifecycle, maturation. In short, HIV protease cleaves certain structural polyproteins to form group-specific antigen (Gag) proteins, which induces the production of new infectious virions. All PIs currently approved, with the exception of tipranavir, are competitive peptidomimetic inhibitors, mimicking the natural substrate of the viral protease. Subsequent cleavage of PIs is prohibited by the presence of a hydroxyethylene core. Tipranavir, on the other hand, contains a dihydropyrone ring as a central scaffold instead of the mentioned hydroxyethylene core.[192]
- **Entry/fusion inhibitors:** they include a complex group of drugs with multiple mechanisms of action, which block HIV entry into host cells during one of its steps: attachment to host cells and CD4 binding, coreceptor (CCR5) binding or membrane fusion. Only two entry inhibitors have been approved for ART, maraviroc and enfuvirtide.[193]

- **Integrase inhibitors:** they target the viral enzyme responsible for the insertion of viral DNA into the host genome. Currently, only three integrase inhibitors have been approved: raltegravir, dolutegravir and elvitegravir.[194]

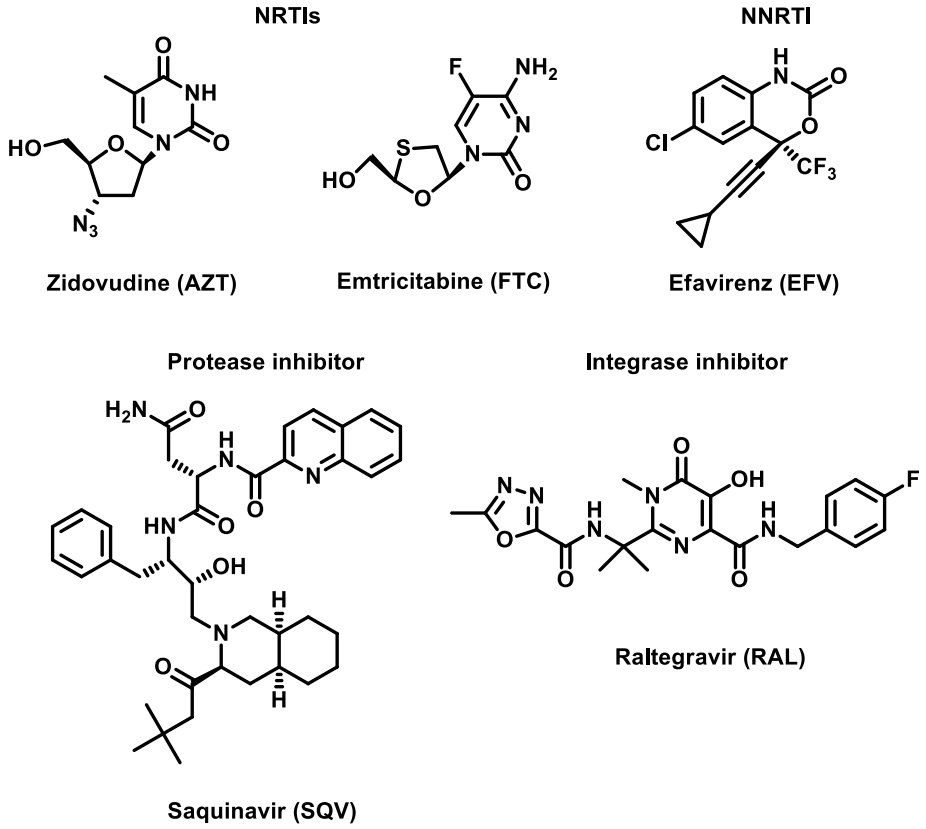

Figure 1.11. Selected examples of antiretroviral drugs of different families (NRTIs, NNRTIs, protease inhibitors and integrase inhibitors).

1.3.3 Challenges in Antiretroviral Therapy/Nanotechnology

The effectiveness of combination antiretroviral therapy (cART) still presents several challenges or drawbacks,[195] namely (i) patient adherence to the treatment, in which recent progress has been focused on the development of extended-release formulations that lower pill burden and present a more favorable short- and long-term toxicity profiles; (ii) the appearance of drug resistance due to the substantial number of replication cycles in HIV and its lack of a proof-reading mechanism; (iii) toxicity, specially long-term effects including psychiatric, metabolic, renal, bone and cardiovascular issues which indirectly contribute to discontinuation of the treatment; (iv) low solubility and poor bioavailability of antiretroviral drugs; and (v) the existence of cellular reservoirs of latent HIV viruses that escape treatment and the limited capability of ARV to reach such reservoirs.[196]

Nanotechnology has recently emerged as a powerful tool for overcoming such hurdles.[197-201] Nanosystems offer several properties that favor their use in antiretroviral therapy, including versatility, modulation of toxicity depending on used excipients, drug release modulation, high drug payloads and their ability to improve bioavailability of ARV drugs, thus protecting them from metabolism, increasing drug residence in the human body and reducing needed doses in the end. The use of nanoparticles also provides advantages for passive or active targeted delivery to cells or organs that are implicated in HIV/AIDS. Inside passive targeting, delivery to lymph nodes via normal nanoparticle uptake by macrophages is of great importance, because they are induction and HIV replication sites though T-cells. Active targeting, i. e., nanoparticle surface attachment of specific ligands that are able to recognize target cells or site, include functionalization with receptors present in HIV,[202,203] or infected macrophages/T-lymphocytes.[204-207] Additionally, nanosystems can help to overcome one important limitation of many antiretroviral drugs, that is their unavailability to circumvent efflux pumps present in the membrane of several HIV-target cells. Also, the possibility of combine different antiretroviral drugs in the same nanoformulation and modulate their release allows a simplification of drug administration. Toxicity at cellular level is also expected to decrease using the right choice of materials for building nanoconstructs, even when drug uptake is increased, probably due to their slow-release properties.[208,209]

To date, different nanostructuration approaches of ARV drugs have been reported. For example, lactoferrin-based nanoparticles have been successfully loaded with a combination of two NRTIs (zidovudine and lamivudine) and a NNRTI, efavirenz, to improve in vitro anti-HIV activity, pharmacokinetics and bioavailability (figure 1.12).[210] In this work, the nanoparticles exhibited drug loadings of approximately 5% for each anti-HIV drug and displayed an acid-induced drug release. Other approaches rely on polymeric materials, such as the use of polyhexylcyanocrylate to encapsulate either the protease inhibitor saquinavir, the NRTI zalcitabine or zidovudine,[211,212] poly(lactide-co-glycolide) (PLGA) to deliver either with efavirenz or saquinavir,[213] saquinavir-loaded poly(ethylene oxide)/poly(caprolactone) nanoparticles,[214] poly(lactic acid) particles encapsulating zidovudine,[215] cationic polymers to encapsulate nucleoside 5'-triphosphates by the formation of polyionic complexes based on nanogels[216] or hybrid nanocapsules composed by poly(*iso*-butylcyanoacrylate) and poly(ethyleneimine).[217] Nanoconstructs bearing multiple antiretroviral drugs have also been reported within polymeric materials. For instance, nanoparticles composed by poly(ethylene glycol) and poly(lactic acid) functionalized with maleimide groups were reported to encapsulate the NNRTI DAAN-14f while functionalizing its surface with the fusion inhibitor T1144.[218] Another example includes the encapsulation of the

CCR5 antagonist maraviroc, the NNRTI etravirine and the integrase inhibitor raltegravir into a PLGA matrix, improving intracellular drug uptake and anti-HIV activity.[219]

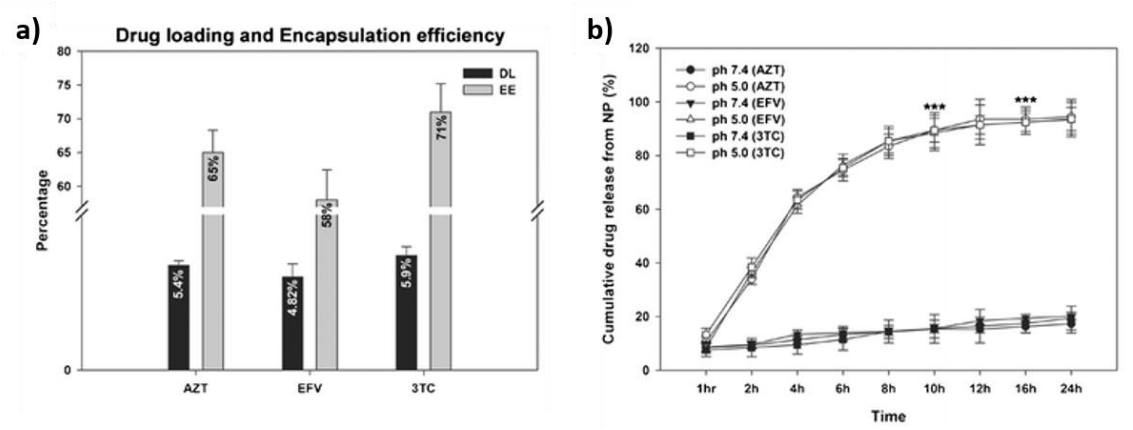

Figure 1.12. a) Drug loading (DL) and encapsulation efficiency (EE) for zidovudine (AZT) efavirenz (EFV) and lamivudine (3TC) in lactoferrin nanoparticles. b) pH-dependent cumulative release of AZT, EFV and 3TC from lactoferrin nanoparticles incubated at pH 5.0 and pH 7.4.

Nanoparticles based on lipids have also been reported, such as the encapsulation of the protease inhibitor indinavir for a sustained release,[220,221] the delivery of zidovudine using lipidic particles[222,223] or the formation of pH-responsive liposomes encapsulating the NRTI tenofovir.[224,225] Combinational drug release has also been reported for lipid nanoparticles, being able to simultaneous deliver two protease inhibitors, lopinavir and ritonavir, and a NRTI, tenofovir.[226] Interestingly, nucleoside analogues functionalized with squalene chains have been reported to self-organize in water as nanoassemblies,[227,228] as well as their cholesteryl derivatives.[229]

In general, modest to low drug loading contents (1-10%) are achieved using these approaches, although more effective encapsulation has been reported using nanoscale metal-organic frameworks (NMOFs). In 2010, Horcajada and coworkers reported a series of porous iron-based NMOFs with the ability of encapsulating different cargoes and, in particular, excellent drug loadings up to 42% were achieved for triphosphorylated zidovudine (AZT-TP).[230] Subsequent studies delved into the loading and release mechanisms of AZT-TP, the possibility of co-encapsulate two different triphosphorylated NRTIs, zidovudine and lamivudine, and the evaluation of their anti-HIV activity, which was found to be maintained through the encapsulation process.[173,174] Other examples of high drug loading can be found in solid nanoparticles obtained using emulsion-templated freeze drying. For example, encapsulation of the NNRTI efavirenz was reported to reach 70 wt%,[231] while another study reported a 50 wt% for particles loaded with the protease inhibitors ritonavir and lopinavir.[232] However,

minimization of side effects, improvement in biodistribution or the development of novel formulation allowing for metabolization into a pharmacologically active drug, mainly intracellularly, still represents a real challenge in HIV/AIDS treatment.

1.4 References

[1] Li, S.-D.; Huang, L. Pharmacokinetics and Biodistribution of Nanoparticles. *Mol. Pharm.* **2008**, *5* (4), 496–504.

[2] Blanco, E.; Shen, H.; Ferrari, M. Principles of Nanoparticle Design for Overcoming Biological Barriers to Drug Delivery. *Nat. Biotechnol.* **2015**, *33* (9), 941–951.

[3] Maeda, H.; Matsumura, Y. A New Concept for Macromolecular Therapeutics in Cancer Chemotherapy: Mechanism of Tumoritropic Accumulation of Proteins and the Antitumor Agent Smancs. *Cancer Res.* **1986**, *46*, 6387–6392.

[4] Prapainop, K.; Monopoli, M. P.; Salvati, A.; Pitek, A. S.; Dawson, K. A.; Kelly, P. M.; Åberg, C.; Bombelli, F. B.; Hristov, D. R.; Mahon, E. Transferrin-Functionalized Nanoparticles Lose Their Targeting Capabilities When a Biomolecule Corona Adsorbs on the Surface. *Nat. Nanotechnol.* **2013**, *8* (2), 137–143.

[5] Tsai, R. K.; Rodriguez, P. L.; Discher, D. E.; Pantano, D. A.; Harada, T.; Christian, D. A. Minimal "Self" Peptides That Inhibit Phagocytic Clearance and Enhance Delivery of Nanoparticles. *Science* **2013**, *339* (6122), 971–975.

[6] Parodi, A.; Quattrocchi, N.; Van De Ven, A. L.; Chiappini, C.; Evangelopoulos, M.; Martinez, J. O.; Brown, B. S.; Khaled, S. Z.; Yazdi, I. K.; Enzo, M. V.; et al. Synthetic Nanoparticles Functionalized with Biomimetic Leukocyte Membranes Possess Cell-like Functions. *Nat. Nanotechnol.* **2013**, *8* (1), 61–68.

[7] Hu, C.-M. J.; Fang, R. H.; Aryal, S.; Cheung, C.; Zhang, L. Erythrocyte Membrane-Camouflaged Polymeric Nanoparticles as a Biomimetic Delivery Platform. *Proc. Natl. Acad. Sci.* **2011**, *108* (27), 10980–10985.

[8] Shamenkov, D.; Ramge, P.; Cychutek, K.; Kreuter, J.; Petrov, V.; Koch-Brandt, C.; Alyautdin, R. Apolipoprotein-Mediated Transport of Nanoparticle-Bound Drugs Across the Blood-Brain Barrier. *J. Drug Target.* **2002**, *10* (4), 317–325.

[9] Prapainop, K.; Witter, D. P.; Wentworth, P. A Chemical Approach for Cell-Specific Targeting of Nanomaterials: Small-Molecule-Initiated Misfolding of Nanoparticle Corona Proteins. *J. Am. Chem. Soc.* **2012**, *134* (9), 4100–4103.

[10] Le Roy, C.; Wrana, J. L. Clathrin- and Non-Clathrin-Mediated Endocytic Regulation of Cell Signalling. *Nat. Rev. Mol. Cell Biol.* **2005**, *6* (2), 112–126.

[11] Chou, L. Y. T.; Ming, K.; Chan, W. C. W. Strategies for the Intracellular Delivery of Nanoparticles. *Chem. Soc. Rev.* **2011**, *40* (1), 233–245.

[12] Martens, T. F.; Remaut, K.; Demeester, J.; De Smedt, S. C.; Braeckmans, K. Intracellular Delivery of Nanomaterials: How to Catch Endosomal Escape in the Act. *Nano Today* **2014**, *9* (3), 344–364.

[13] Mulcahy, L. A.; Pink, R. C.; Carter, D. R. F. Routes and Mechanisms of Extracellular Vesicle Uptake. *J. Extracell. Vesicles* **2014**, *3* (1).

[14] Soo Choi, H.; Misra, P.; Bawendi, M. G.; Frangioni, J. V; Itty Ipe, B.; Liu, W.; Zimmer, J. P.; Tanaka, E. Renal Clearance of Quantum Dots. *Nat. Biotechnol.* **2007**, *25* (10), 1165–1170.

[15] Arvizo, R. R.; Miranda, O. R.; Moyano, D. F.; Walden, C. A.; Giri, K.; Bhattacharya, R.; Robertson, J. D.; Rotello, V. M.; Reid, J. M.; Mukherjee, P. Modulating Pharmacokinetics, Tumor Uptake and Biodistribution by Engineered Nanoparticles. *PLoS One* **2011**, *6* (9), 3–8.

[16] Arvizo, R. R.; Miranda, O. R.; Thompson, M. A.; Pabelick, C. M.; Bhattacharya, R.; David Robertson, J.; Rotello, V. M.; Prakash, Y. S.; Mukherjee, P. Effect of Nanoparticle Surface Charge at the Plasma Membrane and Beyond. *Nano Lett.* **2010**, *10* (7), 2543–2548.

[17] Yuan, Y. Y.; Mao, C. Q.; Du, X. J.; Du, J. Z.; Wang, F.; Wang, J. Surface Charge Switchable Nanoparticles Based on Zwitterionic Polymer for Enhanced Drug Delivery to Tumor. *Adv. Mater.* **2012**, *24* (40), 5476–5480.

[18] Decuzzi, P.; Pasqualini, R.; Arap, W.; Ferrari, M. Intravascular Delivery of Particulate Systems: Does Geometry Really Matter? *Pharm. Res.* **2009**, *26* (1), 235–243.

[19] Dalhaimer, P.; Tewari, M.; Minko, T.; Discher, D. E.; Cai, S.; Geng, Y.; Tsai, R. Shape Effects of Filaments versus Spherical Particles in Flow and Drug Delivery. *Nat. Nanotechnol.* **2007**, *2* (4), 249–255.

[20] Champion, J. A.; Mitragotri, S. Role of Target Geometry in Phagocytosis. *Proc. Natl. Acad. Sci.* **2006**, *103* (13), 4930–4934.

[21] Minko, T.; Harada, T.; Zajac, A. L.; Cai, S.; Garbuzenko, O. B.; Christian, D. A.; Discher, D. E. Flexible Filaments for in Vivo Imaging and Delivery: Persistent Circulation of Filomicelles Opens the Dosage Window for Sustained Tumor Shrinkage. *Mol. Pharm.* **2009**, *6* (5), 1343–1352.

[22] Zhang, L.; Cao, Z.; Li, Y.; Ella-Menye, J. R.; Bai, T.; Jiang, S. Softer Zwitterionic Nanogels for Longer Circulation and Lower Splenic Accumulation. *ACS Nano* **2012**, *6* (8), 6681–6686.

[23] Ebrahim Attia, A. B.; Yang, C.; Tan, J. P. K.; Gao, S.; Williams, D. F.; Hedrick, J. L.; Yang, Y.-Y. The Effect of Kinetic Stability on Biodistribution and Anti-Tumor Efficacy of Drug-Loaded Biodegradable Polymeric Micelles. *Biomaterials* **2013**, *34* (12), 3132–3140.

[24] Bobo, D.; Robinson, K. J.; Islam, J.; Thurecht, K. J.; Corrie, S. R. Nanoparticle-Based Medicines: A Review of FDA-Approved Materials and Clinical Trials to Date. *Pharm. Res.* **2016**, *33* (10), 2373–2387.

[25] Ventola, C. Progress in Nanomedicine: Approved and Investigational Nanodrugs. *Pharm. Ther.* **2017**, *42* (12), 742–755.

[26] James, N. D.; Coker, R. J.; Tomlinson, D.; Harris, J. R.; Gompels, M.; Pinching, A. J.; Stewart, J. S. Liposomal doxorubicin (Doxil): An effective new treatment for Kaposi's sarcoma in AIDS. *Clin. Oncol.* **1994**, *6* (5), 294-296.

[27] Myers, L. W.; Panitch, H. S.; Goldstein, J.; Schiffer, R. B.; Lisak, R. P.; Ford, C. C.; Brooks, B. R.; Wolinsky, J. S.; Johnson, K. P.; Vollmer, T.; et al. Extended Use of Glatiramer Acetate (Copaxone) Is Well Tolerated and Maintains Its Clinical Effect on Multiple Sclerosis Relapse Rate and Degree of Disability. *Neurology* **1998**, *50* (3), 701–708.

[28] Berges, R. Eligard®: Pharmacokinetics, Effect on Testosterone and PSA Levels and Tolerability. *Eur. Urol. Suppl.* **2005**, *4* (5), 20–25.

[29] Sirolimus: AY 22989, NSC 226080, NSC 606698, Rapamycin, Rapamune. *Drugs in R & D.* **1999**, *1* (1), 100–107.

[30] Libutti, S. K.; Paciotti, G. F.; Byrnes, A. A.; Alexander, H. R.; Gannon, W. E.; Walker, M.; Seidel, G. D.; Yuldasheva, N.; Tamarkin, L. Phase I and Pharmacokinetic Studies of CYT-6091, a Novel PEGylated Colloidal Gold-RhTNF Nanomedicine. *Clin. Cancer Res.* **2010**, *16* (24), 6139–6149.

[31] Marill, J.; Anesary, N. M.; Zhang, P.; Vivet, S.; Borghi, E.; Levy, L.; Pottier, A. Hafnium Oxide Nanoparticles: Toward an in Vitro Predictive Biological Effect? *Radiat. Oncol.* **2014**, *9*, 150–161.

[32] Phillips, E.; Humm, J.; Wiesner, U.; Mohan, P.; Strauss, H. W.; Larson, S. M.; Ye, Y.; Carvajal, R. D.; Kalaigian, H.; Schoder, H.; et al. Clinical Translation of an Ultrasmall Inorganic Optical-PET Imaging Nanoparticle Probe. *Sci. Transl. Med.* **2014**, *6* (260), 260ra149-260ra149.

[33] Green, M. R.; Manikhas, G. M.; Orlov, S.; Afanasyev, B.; Makhson, A. M.; Bhar, P.; Hawkins, M. J. Abraxane®, a Novel Cremophor®-Free, Albumin-Bound Particle Form of Paclitaxel for the Treatment of Advanced Non-Small-Cell Lung Cancer. *Ann. Oncol.* **2006**, *17* (8), 1263–1268.

[34] Chen, L. J.; Yang, H. B. Construction of Stimuli-Responsive Functional Materials via Hierarchical Self-Assembly Involving Coordination Interactions. *Acc. Chem. Res.* **2018**, *51* (11), 2699–2710.

[35] Lin, W.; Rieter, W. J.; Taylor, K. M. L. Modular Synthesis of Functional Nanoscale Coordination Polymers. *Angew. Chem. Int. Ed.* **2009**, *48* (4), 650–658.

[36] Spokoyny, A. M.; Kim, D.; Sumrein, A.; Mirkin, C. A. Infinite Coordination Polymer Nano- and Microparticle Structures. *Chem. Soc. Rev.* **2009**, *38* (5), 1218–1227.

[37] Lee, H. J.; Cho, Y. J.; Cho, W.; Oh, M. Controlled Isotropic or Anisotropic Nanoscale Growth of Coordination Polymers: Formation of Hybrid Coordination Polymer Particles. *ACS Nano* **2013**, *7* (1), 491–499.

[38] Dang, S.; Zhu, Q. L.; Xu, Q. Nanomaterials Derived from Metal-Organic Frameworks. *Nat. Rev. Mater.* **2017**, *3*.

[39] Oh, M.; Mirkin, C. a. Chemically Tailorable Colloidal Particles from Infinite Coordination Polymers. *Nature* **2005**, *438* (7068), 651–654.

[40] Sun, X.; Dong, S.; Wang, E. Coordination-Induced Formation of Submicrometer-Scale, Monodisperse, Spherical Colloids of Organic-Inorganic Hybrid Materials at Room Temperature. *J. Am. Chem. Soc.* **2005**, *127* (38), 13102–13103.

[41] Suh, M. P.; Park, H. J.; Prasad, T. K.; Lim, D.-W. Hydrogen Storage in Metal−Organic Frameworks. *Chem. Rev.* **2012**, *112*, 782− 835.

[42] Gassensmith, J. J.; Furukawa, H.; Smaldone, R. A.; Forgan, R. S.; Botros, Y. Y.; Yaghi, O. M.; Stoddart, J. F. Strong and Reversible Binding of Carbon Dioxide in a Green Metal−Organic Framework. *J. Am. Chem. Soc.* **2011**, *133*, 15312−15315.

[43] Li, J.-R.; Kuppler, R. J.; Zhou, H.-C. Selective gas adsorption and separation in metal-organic frameworks. *Chem. Soc. Rev.* **2009**, *38*, 1477−1504

[44] Li, J.-R.; Sculley, J.; Zhou, H.-C. Metal−Organic Frameworks for Separations. *Chem. Rev.* **2012**, *112*, 869−932.

[45] Zhang, Y.; Feng, X.; Yuan, S.; Zhou, J.; Wang, B. Challenges and Recent Advances in MOF-Polymer Composite Membranes for Gas Separation. *Inorg. Chem. Front.* **2016**, *3* (7), 896–909.

[46] Qiu, S.; Xue, M.; Zhu, G. Metal-Organic Framework Membranes: From Synthesis to Separation Application. *Chem. Soc. Rev.* **2014**, *43* (16), 6116–6140.

[47] Denny Jr, M. S.; Moreton, J. C.; Benz, L.; Cohen, S. M. Metal-Organic Frameworks for Membrane-Based Separation. *Nat. Rev. Mater.* **2016**, *1* (12), 16078.

[48] Novio, F.; Ruiz-Molina, D. Hydrophobic Coordination Polymer Nanoparticles and Application for Oil-Water Separation. *RSC Adv.* **2014**, *4* (29), 15293–15296.

[49] Lee, J.; Farha, O. K.; Roberts, J.; Scheidt, K. A.; Nguyen, S. T.; Hupp, J. T. Metal-Organic Framework Materials as Catalysts. *Chem. Soc. Rev.* **2009**, *38* (5), 1450–1459.

[50] Liu, J.; Chen, L.; Cui, H.; Zhang, J.; Zhang, L.; Su, C. Y. Applications of Metal-Organic Frameworks in Heterogeneous Supramolecular Catalysis. *Chem. Soc. Rev.* **2014**, *43* (16), 6011–6061.

[51] Wu, C. De; Zhao, M. Incorporation of Molecular Catalysts in Metal–Organic Frameworks for Highly Efficient Heterogeneous Catalysis. *Adv. Mater.* **2017**, *29* (14).

[52] Gkaniatsou, E.; Sicard, C.; Ricoux, R.; Mahy, J. P.; Steunou, N.; Serre, C. Metal-Organic Frameworks: A Novel Host Platform for Enzymatic Catalysis and Detection. *Mater. Horizons* **2017**, *4* (1), 55–63.

[53] a) Forestier, T.; Mornet, S.; Daro, N.; Nishihara, T.; Mouri, S.; Tanaka, K.; Fouché, O.; Freysz, E.; Létard, J.-F. Nanoparticles of Iron(II) Spin-Crossover. *Chem. Commun.* **2008**, No. 36, 4327. b) Volatron, F.; Catala, L.; Rivière, E.; Gloter, A.; Stéphan, O.; Mallah, T. Spin-Crossover Coordination Nanoparticles. *Inorg. Chem.* **2008**, *47* (15), 6584–6586. c) Boldog, I.; Gaspar, A. B.; Martínez, V.; Pardo-Ibañez, P.; Ksenofontov, V.; Bhattacharjee, A.; Gütlich, P.; Real, J. A. Spin-Crossover Nanocrystals with Magnetic, Optical, and Structural Bistability Near Room Temperature. *Angew. Chem. Int. Ed.* **2008**, *47* (34), 6433–6437. d) Coronado, E.; Galán-Mascarós, J. R.; Monrabal-Capilla, M.; García-Martínez, J.; Pardo-Ibáñez, P. Bistable Spin-Crossover Nanoparticles Showing Magnetic Thermal Hysteresis near Room Temperature. *Adv. Mater.* **2007**, *19* (10), 1359–1361. e) Galán-Mascarós, J. R.; Coronado, E.; Forment-Aliaga, A.; Monrabal-Capilla, M.; Pinilla-Cienfuegos, E.; Ceolin, M. Tuning Size and Thermal Hysteresis in Bistable Spin Crossover Nanoparticles. *Inorg. Chem.* **2010**, *49* (12), 5706–5714.

[54] Kreno, L. E.; Leong, K.; Farha, O. K.; Allendorf, M.; Van Duyne, R. P.; Hupp, J. T. Metal–Organic Framework Materials as Chemical Sensors. *Chem. Rev.* **2012**, *112*, 1105−1125.

[55] Song, Y.; Hao, J.; Hu, D.; Zeng, M.; Li, P.; Li, H.; Chen, L.; Tan, H.; Wang, L. Ratiometric Fluorescent Detection of Superoxide Anion with Polystyrene@nanoscale Coordination Polymers. *Sensors Actuators, B Chem.* **2017**, *238*, 938–944.

[56] Asha, K. S.; Vaisakhan, G. S.; Mandal, S. Picogram Sensing of Trinitrophenol in Aqueous Medium through a Water Stable Nanoscale Coordination Polymer. *Nanoscale* **2016**, *8* (23), 11782–11786.

[57] Lu, Y.; Yan, B. A Ratiometric Fluorescent pH Sensor Based on Nanoscale Metal-Organic Frameworks (MOFs) Modified by Europium(Iii) Complexes. *Chem. Commun.* **2014**, *50* (87), 13323–13326.

[58] Pu, F.; Ran, X.; Ren, J.; Qu, X. Artificial Tongue Based on Metal-Biomolecule Coordination Polymer Nanoparticles. *Chem. Commun.* **2016**, *52* (16), 3410–3413.

[59] Lin, N.; Li, J.; Lu, Z.; Bian, L.; Zheng, L.; Cao, Q.; Ding, Z. A Turn-on Coordination Nanoparticle-Based Fluorescent Probe for Phosphate in Human Serum. *Nanoscale* **2015**, *7* (11), 4971–4977.

[60] González-Monje, P.; Novio, F.; Ruiz-Molina, D. Covalent Grafting of Coordination Polymers on Surfaces: The Case of Hybrid Valence Tautomeric Interphases. *Chem. Eur. J.* **2015**, *21* (28), 10094–10099.

[61] a) Hu, M.; Belik, A. A.; Imura, M.; Mibu, K.; Tsujimoto, Y.; Yamauchi, Y. Synthesis of Superparamagnetic Nanoporous Iron Oxide Particles with Hollow Interiors by Using Prussian Blue Coordination Polymers. *Chem. Mater.* **2012**, *24* (14), 2698–2707. b) Wang, K.; Geng, Z.; Zheng, M.; Ma, L.; Ma, X.; Wang, Z. Controllable Fabrication of Coordination Polymer Particles (CPPs): A Bridge between Versatile Organic Building Blocks and Porous Copper-Based Inorganic Materials. *Cryst. Growth Des.* **2012**, *12* (11), 5606–5614. c) Shahverdizadeh, G. H.; Masoudian, S.; Soudi, A. A.; Bigdeli, F.; Monfared, H. H.; Morsali, A.; Khavasi, H. R. Direct Synthesis of Cd3OSO4 Nano-Particles from a New Three-Dimensional Cadmium(II) Coordination Polymer Precursor. *J. Inorg. Organomet. Polym.* **2011**, *21*, 171–174.

[62] Guardingo, M.; Busqué, F.; Novio, F.; Ruiz-Molina, D. Design and Synthesis of a Noninnocent Multitopic Catechol and Pyridine Mixed Ligand: Nanoscale Polymers and Valence Tautomerism. *Inorg. Chem.* **2015**, *54* (14), 6776–6781.

[63] Wang, H. S. Metal–organic Frameworks for Biosensing and Bioimaging Applications. *Coord. Chem. Rev.* **2017**, *349*, 139–155.

[64] Miller, S. E.; Teplensky, M. H.; Moghadam, P. Z.; Fairen-Jimenez, D. Metal-Organic Frameworks as Biosensors for Luminescence-Based Detection and Imaging. *Interface Focus* **2016**, *6* (4).

[65] Peller, M.; Böll, K.; Zimpel, A.; Wuttke, S. Metal-Organic Framework Nanoparticles for Magnetic Resonance Imaging. *Inorg. Chem. Front.* **2018**, *5* (8), 1760–1779.

[66] Jin, Q.; Zhu, W.; Jiang, D.; Zhang, R.; Kutyreff, C. J.; Engle, J. W.; Huang, P.; Cai, W.; Liu, Z.; Cheng, L. Ultra-Small Iron-Gallic Acid Coordination Polymer Nanoparticles for Chelator-Free Labeling Of64Cu and Multimodal Imaging-Guided Photothermal Therapy. *Nanoscale* **2017**, *9* (34), 12609–12617.

[67] Pan, Y.; Chen, W.; Yang, J.; Zheng, J.; Yang, M.; Yi, C. Facile Synthesis of Gadolinium Chelate-Conjugated Polymer Nanoparticles for Fluorescence/Magnetic Resonance Dual-Modal Imaging. *Anal. Chem.* **2018**, *90* (3), 1992–2000.

[68] Novio, F.; Simmchen, J.; Vázquez-Mera, N.; Amorín-Ferré, L.; Ruiz-Molina, D. Coordination Polymer Nanoparticles in Medicine. *Coord. Chem. Rev.* **2013**, *257* (19–20), 2839–2847.

[69] He, C.; Lu, J.; Lin, W. Hybrid Nanoparticles for Combination Therapy of Cancer. *J. Control. Release* **2015**, *219*, 224–236.

[70] He, C.; Liu, D.; Lin, W. Nanomedicine Applications of Hybrid Nanomaterials Built from Metal-Ligand Coordination Bonds: Nanoscale Metal-Organic Frameworks and Nanoscale Coordination Polymers. *Chem. Rev.* **2015**, *115* (19), 11079–11108.

[71] Shen, S.; Wu, Y.; Liu, Y.; Wu, D. High Drug-Loading Nanomedicines: Progress, Current Status, and Prospects. *Int. J. Nanomedicine* **2017**, *12*, 4085–4109.

[72] Lu, K.; Aung, T.; Guo, N.; Weichselbaum, R.; Lin, W. Nanoscale Metal–Organic Frameworks for Therapeutic, Imaging, and Sensing Applications. *Adv. Mater.* **2018**, *30* (37), 1–20.

[73] Lan, G.; Ni, K.; Lin, W. Nanoscale Metal–organic Frameworks for Phototherapy of Cancer. *Coord. Chem. Rev.* **2019**, *379*, 65–81.

[74] a) Guardingo, M.; González-Monje, P.; Novio, F.; Bellido, E.; Busqué, F.; Molnár, G.; Bousseksou, A.; Ruiz-Molina, D. Synthesis of Nanoscale Coordination Polymers in Femtoliter Reactors on Surfaces. *ACS Nano* **2016**, *10* (3), 3206–3213. b) Bellido, E.; González-Monje, P.; Guardingo, M.; Novio, F.; Sánchez, A.; Montero, M.; Molnar, G.; Bousseksou, A.; Ruiz-Molina, D. Nanoscale Coordination Polymers Obtained in Ultrasmall Liquid Droplets on Solid Surfaces and Its Comparison to Different Synthetic Volume Scales. *RSC Adv.* **2016**, *6* (80), 76666–76672. c) Guardingo, M.; Busqué, F.; Ruiz-Molina, D. Reactions in Ultra-Small Droplets by Tip-Assisted Chemistry. *Chem. Commun.* **2016**, *52* (78), 11617–11626.

[75] Puigmartí-Luis, J. Microfluidic Platforms: A Mainstream Technology for the Preparation of Crystals. *Chem. Soc. Rev.* **2014**, *43* (7), 2253–2271.

[76] Zhang, Y.; Guo, Y.; Wu, S.; Liang, H.; Xu, H. Photodegradable Coordination Polymer Particles for Light-Controlled Cargo Release. *ACS Omega* **2017**, *2* (6), 2536–2543.

[77] Novio, F.; Lorenzo, J.; Nador, F.; Wnuk, K.; Ruiz-Molina, D. Carboxyl Group (-CO2H) Functionalized Coordination Polymer Nanoparticles as Efficient Platforms for Drug Delivery. *Chem. Eur. J.* **2014**, *20* (47), 15443–15450.

[78] Liu, D. M.; He, C. B.; Poon, C.; Lin, W. B. Theranostic nanoscale coordination polymers for magnetic resonance imaging and bisphosphonate delivery. *J. Mater. Chem. B* **2014**, *2*, 8249−8255.

[79] Poon, C.; Duan, X.; Chan, C.; Han, W.; Lin, W. Nanoscale Coordination Polymers Codeliver Carboplatin and Gemcitabine for Highly Effective Treatment of Platinum-Resistant Ovarian Cancer. *Mol. Pharm.* **2016**, *13* (11), 3665–3675.

[80] Liu, D.; Poon, C.; Lu, K.; He, C.; Lin, W. Self-Assembled Nanoscale Coordination Polymers with Trigger Release Properties for Effective Anticancer Therapy. *Nat. Commun.* **2014**, *5*, 1–11.

[81] Huxford, R. C.; Dekrafft, K. E.; Boyle, W. S.; Liu, D.; Lin, W. Lipid-Coated Nanoscale Coordination Polymers for Targeted Delivery of Antifolates to Cancer Cells. *Chem. Sci.* **2012**, *3* (1), 198–204.

[82] Jeon, Y.-M.; Armatas, G. S.; Kim, D.; Kanatzidis, M. G.; Mirkin, C. a. Tröger's-Base-Derived Infinite Co-Ordination Polymer Microparticles. *Small* **2009**, *5* (1), 46–50.

[83] Jung, S.; Oh, M. Monitoring Shape Transformation from Nanowires to Nanocubes and Size-Controlled Formation of Coordination Polymer Particles. *Angew. Chem. Int. Ed.* **2008**, *47* (11), 2049–2051.

[84] Amorín-Ferré, L.; Busqué, F.; Bourdelande, J. L.; Ruiz-Molina, D.; Hernando, J.; Novio, F. Encapsulation and Release Mechanisms in Coordination Polymer Nanoparticles. *Chem. Eur. J.* **2013**, *19* (51), 17508–17516.

[85] Imaz, I.; Hernando, J.; Ruiz-Molina, D.; Maspoch, D. Metal-Organic Spheres as Functional Systems for Guest Encapsulation. *Angew. Chem. Int. Ed.* **2009**, *48* (13), 2325–2329.

[86] Imaz, I.; Rubio-Martínez, M.; García-Fernández, L.; García, F.; Ruiz-Molina, D.; Hernando, J.; Puntes, V.; Maspoch, D. Coordination Polymer Particles as Potential Drug Delivery Systems. *Chem. Commun.* **2010**, *46* (26), 4737–4739.

[87] Rieter, W. J.; Pott, K. M.; Taylor, K. M. L.; Lin, W. Nanoscale Coordination Polymers for Platinum-Based Anticancer Drug Delivery. *J. Am. Chem. Soc.* **2008**, *130* (35), 11584–11585.

[88] Liang, G.; Ni, H.; Bao, S.; Zhu, F.; Gao, H.; Wu, Q. Synthesis and Characterization of Nanowire Coils of Organometallic Coordination Polymers for Controlled Cargo Release. *J. Phys. Chem. B* **2014**, *118* (23), 6339–6345.

[89] Yan, X.; Li, Y.; Zou, Q.; Yuan, C.; Li, S.; Xing, R. Amino Acid Coordination-Driven Self-Assembly for Enhancing Both Biological Stability and Tumor Accumulation of Curcumin. *Angew. Chem. Int. Ed.* **2018**, 17084–17088.

[90] Li, M.; Wang, C.; Di, Z.; Li, H.; Zhang, J.; Xue, W.; Zhao, M.; Zhang, K.; Zhao, Y.; Li, L. Engineering Multifunctional DNA Hybrid Nanospheres through Coordination-Driven Self-Assembly. *Angew. Chem. Int. Ed.* **2019**, *58* (5), 1350–1354.

[91] Fan, Z.; Sun, L.; Huang, Y.; Wang, Y.; Zhang, M. Bioinspired Fluorescent Dipeptide Nanoparticles for Targeted Cancer Cell Imaging and Real-Time Monitoring of Drug Release. *Nat. Nanotechnol.* **2016**, *11* (4), 388–394.

[92] Bertleff-Zieschang, N.; Rahim, M. A.; Ju, Y.; Braunger, J. A.; Suma, T.; Dai, Y.; Pan, S.; Cavalieri, F.; Caruso, F. Biofunctional Metal-Phenolic Films from Dietary Flavonoids. *Chem. Commun.* **2017**, *53* (6), 1068–1071.

[93] Han, K.; Zhang, W. Y.; Zhang, J.; Ma, Z. Y.; Han, H. Y. pH-Responsive Nanoscale Coordination Polymer for Efficient Drug Delivery and Real-Time Release Monitoring. *Adv. Healthc. Mater.* **2017**, *6* (19), 1–9.

[94] Ejima, H.; Richardson, J. J.; Liang, K.; Best, J. P.; Van Koeverden, M. P.; Such, G. K.; Cui, J.; Caruso, F. One-Step Assembly of Coordination Complexes for Versatile Film and Particle Engineering. *Science* **2013**, *341* (6142), 154–157.

[95] Rahim, M. A.; Ejima, H.; Cho, K. L.; Kempe, K.; Müllner, M.; Best, J. P.; Caruso, F. Coordination-Driven Multistep Assembly of Metal-Polyphenol Films and Capsules. *Chem. Mater.* **2014**, *26* (4), 1645–1653.

[96] Ping, Y.; Guo, J.; Ejima, H.; Chen, X.; Richardson, J. J.; Sun, H.; Caruso, F. pH-Responsive Capsules Engineered from Metal-Phenolic Networks for Anticancer Drug Delivery. *Small* **2015**, *11* (17), 2032–2036.

[97] Ju, Y.; Cui, J.; Sun, H.; Müllner, M.; Dai, Y.; Guo, J.; Bertleff-Zieschang, N.; Suma, T.; Richardson, J. J.; Caruso, F. Engineered Metal-Phenolic Capsules Show Tunable Targeted Delivery to Cancer Cells. *Biomacromolecules* **2016**, *17* (6), 2268–2276.

[98] Ju, Y.; Dai, Q.; Cui, J.; Dai, Y.; Suma, T.; Richardson, J. J.; Caruso, F. Improving Targeting of Metal-Phenolic Capsules by the Presence of Protein Coronas. *ACS Appl. Mater. Interfaces* **2016**, *8* (35), 22914–22922.

[99] Park, J. H.; Kim, K.; Lee, J.; Choi, J. Y.; Hong, D.; Yang, S. H.; Caruso, F.; Lee, Y.; Choi, I. S. A Cytoprotective and Degradable Metal-Polyphenol Nanoshell for Single-Cell Encapsulation. *Angew. Chem. Int. Ed.* **2014**, *53* (46), 12420–12425.

[100] Besford, Q. A.; Ju, Y.; Wang, T. Y.; Yun, G.; Cherepanov, P. V.; Hagemeyer, C. E.; Cavalieri, F.; Caruso, F. Self-Assembled Metal–Phenolic Networks on Emulsions as Low-Fouling and pH-Responsive Particles. *Small* **2018**, *14* (39), 1–9.

[101] Gao, P. F.; Zheng, L. L.; Liang, L. J.; Yang, X. X.; Li, Y. F.; Huang, C. Z. A New Type of pH-Responsive Coordination Polymer Sphere as a Vehicle for Targeted Anticancer Drug Delivery and Sustained Release. *J. Mater. Chem. B* **2013**, *1* (25), 3202–3208.

[102] Xu, S.; Liu, J.; Li, D.; Wang, L.; Guo, J.; Wang, C.; Chen, C. Fe-Salphen Complexes from Intracellular pH-Triggered Degradation of Fe_3O_4@Salphen-InIIICPPs for Selectively Killing Cancer Cells. *Biomaterials* **2014**, *35* (5), 1676–1685.

[103] Bai, L.; Song, F.; Wang, X. H.; Cao, J. Y. Q.; Han, X.; Wang, X. L.; Wang, Y. Z. Ligand-Metal-Drug Coordination Based Micelles for Efficient Intracellular Doxorubicin Delivery. *RSC Adv.* **2015**, *5* (59), 47629–47639.

[104] Wang, T.; Liu, X.; Zhu, Y.; Cui, Z. D.; Yang, X. J.; Pan, H.; Yeung, K. W. K.; Wu, S. Metal Ion Coordination Polymer-Capped pH-Triggered Drug Release System on Titania Nanotubes for Enhancing Self-Antibacterial Capability of Ti Implants. *ACS Biomater. Sci. Eng.* **2017**, *3* (5), 816–825.

[105] Huang, W.; Hao, P.; Qin, J.; Luo, S.; Zhang, T.; Peng, B.; Chen, H.; Zan, X. Hexahistidine-Metal Assemblies: A Promising Drug Delivery System. *Acta Biomater.* **2019**, *90*, 441–452.

[106] Nador, F.; Novio, F.; Ruiz-Molina, D. Coordination Polymer Particles with Ligand-Centred PH-Responses and Spin Transition. *Chem. Commun.* **2014**, *50* (93), 14570–14572.

[107] Liu, J.; Wang, H.; Yi, X.; Chao, Y.; Geng, Y.; Xu, L.; Yang, K.; Liu, Z. pH-Sensitive Dissociable Nanoscale Coordination Polymers with Drug Loading for Synergistically Enhanced Chemoradiotherapy. *Adv. Funct. Mater.* **2017**, *27* (44), 1–10.

[108] Liu, J.; Tian, L.; Zhang, R.; Dong, Z.; Wang, H.; Liu, Z. Collagenase-Encapsulated pH-Responsive Nanoscale Coordination Polymers for Tumor Microenvironment Modulation and Enhanced Photodynamic Nanomedicine. *ACS Appl. Mater. Interfaces* **2018**, *10* (50), 43493–43502.

[109] Yang, Y.; Xu, L.; Zhu, W.; Feng, L.; Liu, J.; Chen, Q.; Dong, Z.; Zhao, J.; Liu, Z.; Chen, M. One-Pot Synthesis of pH-Responsive Charge-Switchable PEGylated Nanoscale Coordination Polymers for Improved Cancer Therapy. *Biomaterials* **2018**, *156*, 121–133.

[110] Wang, B.; Jacquet, M.; Wang, K.; Xiong, K.; Yan, M.; Courtois, J.; Royal, G. pH-Induced Fragmentation of Colloids Based on Responsive Self-Assembled Copper(Ii) Metallopolymers. *New J. Chem.* **2018**, *42* (10), 7823–7829.

[111] Liu, J.; Yang, G.; Zhu, W.; Dong, Z.; Yang, Y.; Chao, Y.; Liu, Z. Light-Controlled Drug Release from Singlet-Oxygen Sensitive Nanoscale Coordination Polymers Enabling Cancer Combination Therapy. *Biomaterials* **2017**, *146*, 40–48.

[112] Hu, X. G.; Li, X.; Yang, S. I. Novel Photochromic Infinite Coordination Polymer Particles Derived from a Diarylethene Photoswitch. *Chem. Commun.* **2015**, *51* (53), 10636–10639.

[113] Cherepanov, P. V.; Rahim, M. A.; Bertleff-Zieschang, N.; Sayeed, M. A.; O'Mullane, A. P.; Moulton, S. E.; Caruso, F. Electrochemical Behavior and Redox-Dependent Disassembly of Gallic Acid/FeIIIMetal-Phenolic Networks. *ACS Appl. Mater. Interfaces* **2018**, *10* (6), 5828–5834.

[114] Buwalda, S.; Nottelet, B.; Bethry, A.; Kok, R. J.; Sijbrandi, N.; Coudane, J. Reversibly Core-Crosslinked PEG-P(HPMA) Micelles: Platinum Coordination Chemistry for Competitive-Ligand-Regulated Drug Delivery. *J. Colloid Interface Sci.* **2019**, *535*, 505–515.

[115] Li, S.; Zou, Q.; Li, Y.; Yuan, C.; Xing, R.; Yan, X. Smart Peptide-Based Supramolecular Photodynamic Metallo-Nanodrugs Designed by Multicomponent Coordination Self-Assembly. *J. Am. Chem. Soc.* **2018**, *140* (34), 10794–10802.

[116] Liu, J.; Chen, Q.; Zhu, W.; Yi, X.; Yang, Y.; Dong, Z.; Liu, Z. Nanoscale-Coordination-Polymer-Shelled Manganese Dioxide Composite Nanoparticles: A Multistage Redox/pH/H_2O_2-Responsive Cancer Theranostic Nanoplatform. *Adv. Funct. Mater.* **2017**, *27* (10).

[117] Pu, F.; Ju, E.; Ren, J.; Qu, X. Multiconfigurable Logic Gates Based on Fluorescence Switching in Adaptive Coordination Polymer Nanoparticles. *Adv. Mater.* **2014**, *26* (7), 1111–1117.

[118] Pu, F.; Ren, J.; Qu, X. "Plug and Play" Logic Gates Based on Fluorescence Switching Regulated by Self-Assembly of Nucleotide and Lanthanide Ions. *ACS Appl. Mater. Interfaces* **2014**, *6* (12), 9557–9562.

[119] Gao, R.-R.; Shi, S.; Li, Y.-J.; Wumaier, M.; Hu, X.-C.; Yao, T.-M. Coordination Polymer Nanoparticles from Nucleotide and Lanthanide Ions as a Versatile Platform for Color-Tunable Luminescence and Integrating Boolean Logic Operations. *Nanoscale* **2017**, *9* (27), 9589–9597.

[120] Bai, L.; Wang, X. H.; Song, F.; Wang, X. L.; Wang, Y. Z. "aND" Logic Gate Regulated pH and Reduction Dual-Responsive Prodrug Nanoparticles for Efficient Intracellular Anticancer Drug Delivery. *Chem. Commun.* **2015**, *51* (1), 93–96.

[121] Xing, L.; Cao, Y.; Che, S. Synthesis of Core-Shell Coordination Polymer Nanoparticles (CPNs) for pH-Responsive Controlled Drug Release. *Chem. Commun.* **2012**, *48* (48), 5995–5997.

[122] Fan, C.; Wang, D. A. Novel Gelatin-Based Nano-Gels with Coordination-Induced Drug Loading for Intracellular Delivery. *J. Mater. Sci. Technol.* **2016**, *32* (9), 840–844.

[123] Zhang, D.; Wu, M.; Cai, Z.; Liao, N.; Ke, K.; Liu, H.; Li, M.; Liu, G.; Yang, H.; Liu, X.; et al. Chemotherapeutic Drug Based Metal–Organic Particles for Microvesicle-Mediated Deep Penetration and Programmable pH/NIR/Hypoxia Activated Cancer Photochemotherapy. *Adv. Sci.* **2018**, *5* (2).

[124] Shen, S.; Wu, Y.; Li, K.; Wang, Y.; Wu, J.; Zeng, Y.; Wu, D. Versatile Hyaluronic Acid Modified AQ4N-Cu(II)-Gossypol Infinite Coordination Polymer Nanoparticles: Multiple Tumor Targeting, Highly Efficient Synergistic Chemotherapy, and Real-Time Self-Monitoring. *Biomaterials* **2018**, *154*, 197–212.

[125] Huxford-Phillips, R. C.; Russell, S. R.; Liu, D.; Lin, W. Lipid-Coated Nanoscale Coordination Polymers for Targeted Cisplatin Delivery. *RSC Adv.* **2013**, *3* (34), 14438–14443.

[126] Adarsh, N. N.; Frias, C.; Ponnoth Lohidakshan, T. M.; Lorenzo, J.; Novio, F.; Garcia-Pardo, J.; Ruiz-Molina, D. Pt(IV)-Based Nanoscale Coordination Polymers: Antitumor Activity, Cellular Uptake and Interactions with Nuclear DNA. *Chem. Eng. J.* **2018**, *340* (January), 94–102.

[127] Poon, C.; He, C.; Liu, D.; Lu, K.; Lin, W. Self-Assembled Nanoscale Coordination Polymers Carrying Oxaliplatin and Gemcitabine for Synergistic Combination Therapy of Pancreatic Cancer. *J. Control. Release* **2015**, *201*, 90–99.

[128] Poon, C.; Duan, X.; Chan, C.; Han, W.; Lin, W. Nanoscale Coordination Polymers Codeliver Carboplatin and Gemcitabine for Highly Effective Treatment of Platinum-Resistant Ovarian Cancer. *Mol. Pharm.* **2016**, *13* (11), 3665–3675.

[129] He, C.; Liu, D.; Lin, W. Self-Assembled Nanoscale Coordination Polymers Carrying SiRNAs and Cisplatin for Effective Treatment of Resistant Ovarian Cancer. *Biomaterials* **2015**, *36*, 124–133.

[130] He, C.; Poon, C.; Chan, C.; Yamada, S. D.; Lin, W. Nanoscale Coordination Polymers Codeliver Chemotherapeutics and Sirnas to Eradicate Tumors of Cisplatin-Resistant Ovarian Cancer. *J. Am. Chem. Soc.* **2016**, *138* (18), 6010–6019.

[131] Wang, K.; Ma, X.; Shao, D.; Geng, Z.; Zhang, Z.; Wang, Z. Coordination-Induced Assembly of Coordination Polymer Submicrospheres: Promising Antibacterial and in Vitro Anticancer Activities. *Cryst. Growth Des.* **2012**, *12* (7), 3786–3791.

[132] Li, J.; Murakami, T.; Higuchi, M. Metallo-Supramolecular Polymers: Versatile DNA Binding and Their Cytotoxicity. *J. Inorg. Organomet. Polym. Mater.* **2013**, *23* (1), 119–125.

[133] Raja, D. S.; Bhuvanesh, N. S. P.; Natarajan, K. A Novel Water Soluble Ligand Bridged Cobalt(II) Coordination Polymer of 2-Oxo-1,2-Dihydroquinoline-3-Carbaldehyde (Isonicotinic) Hydrazone: Evaluation of the DNA Binding, Protein Interaction, Radical Scavenging and Anticancer Activity. *Dalt. Trans.* **2012**, *41* (15), 4365–4377.

[134] Zhang, Q.; Vakili, M. R.; Li, X. F.; Lavasanifar, A.; Le, X. C. Polymeric Micelles for GSH-Triggered Delivery of Arsenic Species to Cancer Cells. *Biomaterials* **2014**, *35* (25), 7088–7100.

[135] Carraher, C. E.; Roner, M. R.; Pham, N.; Moric-Johnson, A. Group VA Polyesters Containing Thiodiglycolic Acid-Synthesis and Preliminary Cancer Activity. *J. Macromol. Sci. Part A Pure Appl. Chem.* **2014**, *51* (7), 547–556.

[136] Wang, Y.; Duan, L.; Luo, X.; Deng, Q.; Xie, J.; Jin, J.; Zhang, K. Two New Metal Coordination Polymers: Anticancer Activity in Endometrial Carcinoma. *Inorg. Nano-Metal Chem.* **2018**, *48* (4–5), 257–261.

[137] Shu, D.; Chen, W. Synthesis, Structure, and in Vitro Anti-Lung Cancer Activity on an In-Based Nanoscale Coordination Polymer. *Main Group Met. Chem.* **2018**, *41* (3–4), 129–133.

[138] Agostinis, P.; Berg, K.; Cengel, K. A.; Foster, T. H.; Girotti, A. W.; Gollnick, S. O.; Hahn, S. M.; Hamblin, M. R.; Juzeniene, A.; Kessel, D.; et al. Photodynamic Therapy of Cancer: An Update. *CA. Cancer J. Clin.* **2017**, *61*, 250–281.

[139] Huang, Z.; Huang, L.; Huang, Y.; He, Y.; Sun, X.; Fu, X.; Xu, X.; Wei, G.; Chen, D.; Zhao, C. Phthalocyanine-Based Coordination Polymer Nanoparticles for Enhanced Photodynamic Therapy. *Nanoscale* **2017**, *9* (41), 15883–15894.

[140] Yang, Y.; Zhu, W.; Feng, L.; Chao, Y.; Yi, X.; Dong, Z.; Yang, K.; Tan, W.; Liu, Z.; Chen, M. G-Quadruplex-Based Nanoscale Coordination Polymers to Modulate Tumor Hypoxia and Achieve Nuclear-Targeted Drug Delivery for Enhanced Photodynamic Therapy. *Nano Lett.* **2018**, *18* (11), 6867–6875.

[141] He, C.; Liu, D.; Lin, W. Self-Assembled Core-Shell Nanoparticles for Combined Chemotherapy and Photodynamic Therapy of Resistant Head and Neck Cancers. *ACS Nano* **2015**, *9* (1), 991–1003.

[142] He, C.; Duan, X.; Guo, N.; Chan, C.; Poon, C.; Weichselbaum, R. R.; Lin, W. Core-Shell Nanoscale Coordination Polymers Combine Chemotherapy and Photodynamic Therapy to Potentiate Checkpoint Blockade Cancer Immunotherapy. *Nat. Commun.* **2016**, *7*, 1–12.

[143] Yang, Q.; Zhou, Z.; Cui, L.; Yang, H.; Yan, C.; Zhou, X.; Yang, S.; Pan, L.; Zhang, X. Coordination Polymer Hybridized Au Nanocages: A Nanoplatform for Dual-Modality Imaging Guided near-Infrared Driven Photothermal Therapy in Vivo. *J. Mater. Chem. B* **2017**, *5* (44), 8761–8769.

[144] Calabrese, C. M.; Merkel, T. J.; Briley, W. E.; Randeria, P. S.; Narayan, S. P.; Rouge, J. L.; Walker, D. A.; Scott, A. W.; Mirkin, C. A. Biocompatible Infinite-Coordination-Polymer Nanoparticle-Nucleic-Acid Conjugates for Antisense Gene Regulation. *Angew. Chem. Int. Ed.* **2015**, *54* (2), 476–480.

[145] Wang, X.; Liang, J.; Zhang, C.; Ma, G.; Wang, C.; Kong, D. Coordination Microparticle Vaccines Engineered from Tumor Cell Templates. *Chem. Commun.* **2019**, *55* (11), 1568–1571.

[146] He, Z.; Zhang, P.; Xiao, Y.; Li, J.; Yang, F.; Liu, Y.; Zhang, J. R.; Zhu, J. J. Acid-Degradable Gadolinium-Based Nanoscale Coordination Polymer: A Potential Platform for Targeted Drug Delivery and Potential Magnetic Resonance Imaging. *Nano Res.* **2018**, *11* (2), 929–939.

[147] Perrier, M.; Gallud, A.; Ayadi, A.; Kennouche, S.; Porredon, C.; Gary-Bobo, M.; Larionova, J.; Goze-Bac, C.; Zanca, M.; Garcia, M.; et al. Investigation of Cyano-Bridged Coordination Nanoparticles $Gd^{3+}/[Fe(CN)_6]^{3-}$/D-Mannitol as T_1-Weighted MRI Contrast Agents. *Nanoscale* **2015**, *7* (28), 11899–11903.

[148] Ma, J.; Dong, H.; Zhu, H.; Li, C. W.; Li, Y.; Shi, D. Deposition of Gadolinium onto the Shell Structure of Micelles for Integrated Magnetic Resonance Imaging and Robust Drug Delivery Systems. *J. Mater. Chem. B* **2016**, *4* (36), 6094–6102.

[149] Yang, Y.; Liu, J.; Liang, C.; Feng, L.; Fu, T.; Dong, Z.; Chao, Y.; Li, Y.; Lu, G.; Chen, M.; et al. Nanoscale Metal-Organic Particles with Rapid Clearance for Magnetic Resonance Imaging-Guided Photothermal Therapy. *ACS Nano* **2016**, *10* (2), 2774–2781.

[150] Zhao, J.; Yang, Y.; Han, X.; Liang, C.; Liu, J.; Song, X.; Ge, Z.; Liu, Z. Redox-Sensitive Nanoscale Coordination Polymers for Drug Delivery and Cancer Theranostics. *ACS Appl. Mater. Interfaces* **2017**, *9* (28), 23555–23563.

[151] Zhang, H.; Liu, K.; Li, S.; Xin, X.; Yuan, S.; Ma, G.; Yan, X. Self-Assembled Minimalist Multifunctional Theranostic Nanoplatform for Magnetic Resonance Imaging-Guided Tumor Photodynamic Therapy. *ACS Nano* **2018**, *12* (8), 8266–8276.

[152] Shin, H.-W.; Sohn, H.; Jeong, Y.-H.; Lee, S.-M. Construction of Paramagnetic Manganese-Chelated Polymeric Nanoparticles Using Pyrene-End-Modified Double-Hydrophilic Block copolymers for Enhanced magnetic Resonance Relaxivity: A Comparative Study with Cisplatin Pharmacophore. *Langmuir* **2019**, *35*, 6421–6428.

[153] Mu, X.; Yan, C.; Tian, Q.; Lin, J.; Yang, S. BSA-Assisted Synthesis of Ultrasmall Gallic Acid-Fe(III) Coordination Polymer Nanoparticles for Cancer Theranostics. *Int. J. Nanomedicine* **2017**, *12*, 7207–7223.

[154] Xin, K.; Li, M.; Lu, D.; Meng, X.; Deng, J.; Kong, D.; Ding, D.; Wang, Z.; Zhao, Y. Bioinspired Coordination Micelles Integrating High Stability, Triggered Cargo Release, and Magnetic Resonance Imaging. *ACS Appl. Mater. Interfaces* **2017**, *9* (1), 80–91.

[155] Chen, Y.; Ai, K.; Liu, J.; Ren, X.; Jiang, C.; Lu, L. Polydopamine-Based Coordination Nanocomplex for T_1/T_2 Dual Mode Magnetic Resonance Imaging-Guided Chemo-Photothermal Synergistic Therapy. *Biomaterials* **2016**, *77*, 198–206.

[156] Borges, M.; Yu, S.; Laromaine, A.; Roig, A.; Suárez-García, S.; Lorenzo, J.; Ruiz-Molina, D.; Novio, F. Dual T_1/T_2MRI Contrast Agent Based on Hybrid SPION@coordination Polymer Nanoparticles. *RSC Adv.* **2015**, *5* (105), 86779–86783.

[157] Suárez-García, S.; Arias-Ramos, N.; Frias, C.; Candiota, A. P.; Arús, C.; Lorenzo, J.; Ruiz-Molina, D.; Novio, F. Dual T_1/T_2 Nanoscale Coordination Polymers as Novel Contrast Agents for MRI: A Preclinical Study for Brain Tumor. *ACS Appl. Mater. Interfaces* **2018**, *10* (45), 38819–38832.

[158] Ban, Q.; Du, J.; Sun, W.; Chen, J.; Wu, S.; Kong, J. Intramolecular Copper-Containing Hyperbranched Polytriazole Assemblies for Label-free Cellular Bioimaging and Redox-Triggered Copper Complex Delivery. *Macromol. Rapid Commun.* **2018**, *39*, 1800171.

[159] Nador, F.; Wnuk, K.; García-Pardo, J.; Lorenzo, J.; Solorzano, R.; Ruiz-Molina, D.; Novio, F. Dual-Fluorescent Nanoscale Coordination Polymers via a Mixed-Ligand Synthetic Strategy and Their Use for Multichannel Imaging. *ChemNanoMat* **2018**, *4* (2), 183–193.

[160] Sahub, C.; Tumcharern, G.; Chirawatkul, P.; Ruangpornvisuti, V.; Ekgasit, S.; Wanichweacharungruang, S.; Tuntulani, T.; Palaga, T.; Tomapatanaget, B. Self-Assembly of Gd^{3+} /SDS/HEPES Complex and Curcumin Entrapment for Enhanced Stability, Fluorescence Image in Cellular System. *Colloids Surfaces B Biointerfaces* **2017**, *156*, 254–261.

[161] Oh, M. S.; Jung, S. H.; Choi, S. H. Synthesis and Characterization of Coordination Polymer Nanoparticles as Radioisotope Tracers. *Appl. Radiat. Isot.* **2014**, *85*, 19–22. https://doi.org/10.1016/j.apradiso.2013.11.026.

[162] Oh, M. S.; Jung, S. H.; Choi, S. H. Preparation of Radioisotope Nanoparticles Constructed with Au-Ligand Framework by Self-Assembly Process for Radiotracer. *J. Radioanal. Nucl. Chem.* **2014**, *302* (3), 1151–1158.

[163] Shen, S.; Jiang, D.; Cheng, L.; Chao, Y.; Nie, K.; Dong, Z.; Kutyreff, C. J.; Engle, J. W.; Huang, P.; Cai, W.; et al. Renal-Clearable Ultrasmall Coordination Polymer Nanodots for Chelator-Free 64Cu-Labeling and Imaging-Guided Enhanced Radiotherapy of Cancer. *ACS Nano* **2017**, *11* (9), 9103–9111.

[164] Lu, H. D.; Wang, L. Z.; Wilson, B. K.; McManus, S. A.; Jumai'An, J.; Padakanti, P. K.; Alavi, A.; Mach, R. H.; Prud'Homme, R. K. Copper Loading of Preformed Nanoparticles for PET-Imaging Applications. *ACS Appl. Mater. Interfaces* **2018**, *10* (4), 3191–3199.

[165] Lu, Y.; Xue, F.; Yang, H.; Shi, M.; Yan, Y.; Qin, L.; Zhou, Z.; Yang, S. Phosphorescent Coordination Polymer Nanoparticles as a Three-in-One Platform for Optical Imaging, T_1-Weighted Magnetic Resonance Imaging, and Photodynamic Therapy. *J. Phys. Chem. C* **2015**, *119* (1), 573–579.

[166] Wang, Y. M.; Liu, W.; Yin, X. B. Multifunctional Mixed-Metal Nanoscale Coordination Polymers for Triple-Modality Imaging-Guided Photodynamic Therapy. *Chem. Sci.* **2017**, *8* (5), 3891–3897.

[167] Cui, J.; Zhang, G.; Xin, L.; Yun, P.; Yan, Y.; Su, F. Functional Nanoscale Metal–organic Particles Synthesized from a New Vinylimidazole-Based Polymeric Ligand and Dysprosium Ions. *J. Mater. Chem. C* **2017**, *6*, 280–289.

[168] Wang, Y. M.; Liu, W.; Yin, X. B. Self-Limiting Growth Nanoscale Coordination Polymers for Fluorescence and Magnetic Resonance Dual-Modality Imaging. *Adv. Funct. Mater.* **2016**, *26* (46), 8463–8470.

[169] An, Q.; Liu, J.; Yu, M.; Wan, J.; Li, D.; Wang, C.; Chen, C.; Guo, J. Multifunctional Magnetic Gd^{3+}-Based Coordination Polymer Nanoparticles: Combination of Magnetic Resonance and Multispectral Optoacoustic Detections for Tumor-Targeted Imaging in Vivo. *Small* **2015**, *11* (42), 5675–5686.

[170] Hu, D.; Liu, C.; Song, L.; Cui, H.; Gao, G.; Liu, P.; Sheng, Z.; Cai, L. Indocyanine Green-Loaded Polydopamine-Iron Ions Coordination Nanoparticles for Photoacoustic/Magnetic Resonance Dual-Modal Imaging-Guided Cancer Photothermal Therapy. *Nanoscale* **2016**, *8* (39), 17150–17158.

[171] Yang, Y.; Chao, Y.; Liu, J.; Dong, Z.; He, W.; Zhang, R.; Yang, K.; Chen, M.; Liu, Z. Core-Shell and Co-Doped Nanoscale Metal-Organic Particles (NMOPs) Obtained via Post-Synthesis Cation Exchange for Multimodal Imaging and Synergistic Thermo-Radiotherapy. *NPG Asia Mater.* **2017**, *9* (1), e344-11.

[172] Chu, C.; Ren, E.; Zhang, Y.; Yu, J.; Lin, H.; Pang, X.; Zhang, Y.; Liu, H.; Qin, Z.; Cheng, Y.; Wang, X.; Li, W.; Kong, X.; Chen, X.; Liu, G. Zinc(II)-Dipicolylamine Coordination Nanotheranostics: Toward Synergistic Nanomedicine by Combined Photo/Gene Therapy. *Angew. Chem. Int. Ed.* **2019**, *58*, 269 –272.

[173] Agostoni, V.; Chalati, T.; Horcajada, P.; Willaime, H.; Anand, R.; Semiramoth, N.; Baati, T.; Hall, S.; Maurin, G.; Chacun, H.; et al. Towards an Improved Anti-HIV Activity of NRTI via Metal-Organic Frameworks Nanoparticles. *Adv. Healthc. Mater.* **2013**, *2* (12), 1630–1637.

[174] Marcos-Almaraz, M. T.; Gref, R.; Agostoni, V.; Kreuz, C.; Clayette, P.; Serre, C.; Couvreur, P.; Horcajada, P. Towards Improved HIV-Microbicide Activity through the Co-Encapsulation of NRTI Drugs in Biocompatible Metal Organic Framework Nanocarriers. *J. Mater. Chem. B* **2017**, *5* (43), 8563–8569..

[175] Barré-Sinoussi, F.; Ross, A. L.; Delfraissy, J. F. Past, Present and Future: 30 Years of HIV Research. *Nat. Rev. Microbiol.* **2013**, *11* (12), 877–883.

[176] World Health Organization. Global summary of the AIDS epidemic, 2018. Web. Consulted on September 1st **2019**

[177] Rowland-Jones, S. AIDS Pathogenesis: What Have Two Decades of Research Taught Us? *Bull. Mem. Acad. R. Med. Belg.* **2004**, *159* (Pt 2), 171–175.

[178] Barré-Sinoussi, F.; Chermann, J. C.; Rey, F.; Nugeyre, M. T.; Chamaret, S.; Gruest, J.; Dauguet, C.; Axler-Blin, C.; Vézinet-Brun, F.; Rouzioux, C.; et al. Isolation of a T-Lymphotropic Retrovirus from a Patient at Risk for Acquired Immune Deficiency Syndrome (AIDS). 1983. *Rev. Invest. Clin.* **1983**, *56* (2), 126–129.

[179] Popovic, M.; Sarngadharan, M. G.; Read, E.; Gallo, R. C. Detection, Isolation, and Continuous Production of Cytopathic Retroviruses (HTLV-III) from Patients with AIDS and Pre-AIDS. *Science* **1984**, *224* (4648), 497–500.

[180] Hütter, G.; Nowak, D.; Mossner, M.; Ganepola, S.; Müßig, A.; Allers, K.; Schneider, T.; Hofmann, J.; Kücherer, C.; Blau, O.; et al. Long-Term Control of HIV by CCR5 Delta32/Delta32 Stem-Cell Transplantation. *N. Engl. J. Med.* **2009**, *360* (7), 692–698.

[181] Gupta, R. K.; Abdul-Jawad, S.; McCoy, L. E.; Mok, H. P.; Peppa, D.; Salgado, M.; Martinez-Picado, J.; Nijhuis, M.; Wensing, A. M. J.; Lee, H.; et al. HIV-1 Remission Following CCR5Δ32/Δ32 Haematopoietic Stem-Cell Transplantation. *Nature* **2019**, *4* (March).

[182] Cohen, J. HIV Treatment as Prevention. *Science* **2011**, *334* (6063), 1628.

[183] Broder, S. The Development of Antiretroviral Therapy and Its Impact on the HIV-1/AIDS Pandemic. *Antiviral Res.* **2010**, *85* (1), 1–18.

[184] Esté, J. a; Cihlar, T. Current Status and Challenges of Antiretroviral Research and Therapy. *Antiviral Res.* **2010**, *85* (1), 25–33.

[185] AIDSinfo. FDA-approved HIV medicines. Web. Consulted on March 1st, 2019. https://aidsinfo.nih.gov/understanding-hiv-aids/fact-sheets/21/58/fda-approved-hiv-medicines

[186] Emamzadeh-Fard, S.; E. Fard, S.; SeyedAlinaghi, S.; Paydary, K. Adherence to Anti-Retroviral Therapy and Its Determinants in HIV/AIDS Patients: A Review. *Infect. Disord. - Drug Targets* **2012**, *12* (5), 346–356.

[187] U.S. Food and Drug Administration. Antiretroviral Drugs Used in the Treatment of HIV Infection. Web. 1st March **2019**.

[188] Cihlar, T.; Ray, A. S. Nucleoside and Nucleotide HIV Reverse Transcriptase Inhibitors: 25 Years after Zidovudine. *Antiviral Res.* **2010**, *85* (1), 39–58.

[189] U.S. Food and Drug Administration. FDA Approved Drug Products. Retrovir. Web. 2nd March **2019**. http://www.accessdata.fda.gov/drugsatfda_docs/label/2012/019655s053,019910s040,020518s023lbl.pdf

[190] Anderson, P. L.; Kakuda, T. N.; Kawle, S.; Fletcher, C. V. Antiviral Dynamics and Sex Differences of Zidovudine and Lamivudine Triphosphate Concentrations in HIV-Infected Individuals. *AIDS* **2003**, *17* (15), 2159–2168.

[191] de Béthune, M. P. Non-Nucleoside Reverse Transcriptase Inhibitors (NNRTIs), Their Discovery, Development, and Use in the Treatment of HIV-1 Infection: A Review of the Last 20 Years (1989-2009). *Antiviral Res.* **2010**, *85* (1), 75–90.

[192] Wensing, A. M. J.; van Maarseveen, N. M.; Nijhuis, M. Fifteen Years of HIV Protease Inhibitors: Raising the Barrier to Resistance. *Antiviral Res.* **2010**, *85* (1), 59–74.

[193] Tilton, J. C.; Doms, R. W. Entry Inhibitors in the Treatment of HIV-1 Infection. *Antiviral Res.* **2010**, *85* (1), 91–100.

[194] McColl, D. J.; Chen, X. Strand Transfer Inhibitors of HIV-1 Integrase: Bringing IN a New Era of Antiretroviral Therapy. *Antiviral Res.* **2010**, *85* (1), 101–118.

[195] Tseng, A.; Seet, J.; Phillips, E. J. The Evolution of Three Decades of Antiretroviral Therapy: Challenges, Triumphs and the Promise of the Future. *Br. J. Clin. Pharmacol.* **2015**, *79* (2), 182–194.

[196] Titanji, B. K.; Pillay, D.; Jolly, C. Combination Antiretroviral Therapy and Cell–cell Spread of Wild-Type and Drug-Resistant Human Immunodeficiency Virus-1. *J. Gen. Virol.* **2017**, *98* (4), 821–834.

[197] das Neves, J.; Amiji, M. M.; Bahia, M. F.; Sarmento, B. Nanotechnology-Based Systems for the Treatment and Prevention of HIV/AIDS. *Adv. Drug Deliv. Rev.* **2010**, *62* (4–5), 458–477.

[198] Mahajan, S. D.; Aalinkeel, R.; Law, W. C.; Reynolds, J. L.; Nair, B. B.; Sykes, D. E.; Yong, K. T.; Roy, I.; Prasad, P. N.; Schwartz, S. A. Anti-HIV-1 Nanotherapeutics: Promises and Challenges for the Future. *Int. J. Nanomedicine* **2012**, *7*, 5301–5314.

[199] Lisziewicz, J.; Toke, E. R. Nanomedicine Applications towards the Cure of HIV. *Nanomedicine* **2013**, *9* (1), 28–38.

[200] Adhikary, R. R.; More, P.; Banerjee, R. Smart Nanoparticles as Targeting Platforms for HIV Infections. *Nanoscale* **2015**, *7* (17), 7520–7534.

[201] das Neves, J.; Nunes, R.; Rodrigues, F.; Sarmento, B. Nanomedicine in the Development of Anti-HIV Microbicides. *Adv. Drug Deliv. Rev.* **2016**, *103*, 57–75.

[202] Martínez-Ávila, O.; Bedoya, L. M.; Marradi, M.; Clavel, C.; Alcamí, J.; Penadés, S. Multivalent Manno-Glyconanoparticles Inhibit DC-SIGN-Mediated HIV-1 Trans-Infection of Human T Cells. *ChemBioChem* **2009**, *10* (11), 1806–1809.

[203] Di Gianvincenzo, P.; Marradi, M.; Martínez-Ávila, O. M.; Bedoya, L. M.; Alcamí, J.; Penadés, S. Gold Nanoparticles Capped with Sulfate-Ended Ligands as Anti-HIV Agents. *Bioorganic Med. Chem. Lett.* **2010**, *20* (9), 2718–2721.

[204] Martínez-Ávila, O.; Bedoya, L. M.; Marradi, M.; Clavel, C.; Alcamí, J.; Penadés, S. Multivalent Manno-Glyconanoparticles Inhibit DC-SIGN-Mediated HIV-1 Trans-Infection of Human T Cells. *ChemBioChem* **2009**, *10* (11), 1806–1809.

[205] Dou, H.; Rabinow, B. E.; Poluektova, L.; Destache, C. J.; Nelson, J.; Gorantla, S.; Mosley, R. L.; Boska, M.; Gendelman, H. E. Quantitative Magnetic Resonance and SPECT Imaging for Macrophage Tissue Migration and Nanoformulated Drug Delivery. *J. Leukoc. Biol.* **2006**, *80* (5), 1165–1174.

[206] Werling, J.; Nelson, J. A.; Kingsley, J.; Poluektova, L.; Destache, C. J.; Gendelman, H. E.; Kipp, J.; Mosley, R. L.; Boska, M. D.; Chaubal, M.; et al. Development of a Macrophage-Based Nanoparticle Platform for Antiretroviral Drug Delivery. *Blood* **2006**, *108* (8), 2827–2835.

[207] Gagneé, J. F.; Deésormeaux, A.; Perron, S.; Tremblay, M. J.; Bergeron, M. G. Targeted Delivery of Indinavir to HIV-1 Primary Reservoirs with Immunoliposomes. *Biochim. Biophys. Acta - Biomembr.* **2002**, *1558* (2), 198–210.

[208] Kohli, E.; Han, H. Y.; Zeman, A. D.; Vinogradov, S. V. Formulations of Biodegradable Nanogel Carriers with 5'-Triphosphates of Nucleoside Analogs That Display a Reduced Cytotoxicity and Enhanced Drug Activity. *J. Control. Release* **2007**, *121* (1–2), 19–27.

[209] Phillips, N. C.; Tsoukas, C. Liposomal Encapsulation of Azt Results in Decreased Bone Marrow Toxicity and Activity against Murine Acquired Immunodeficiency Syndrome (MAIDS)-Induced Immunosuppression. *Blood* **1992**, *79* (5), 1137–1143.

[210] Kumar, P.; Lakshmi, Y. S.; Kondapi, A. K. Triple Drug Combination of Zidovudine, Efavirenz and Lamivudine Loaded Lactoferrin Nanoparticles: An Effective Nano First-Line Regimen for HIV Therapy. *Pharm. Res.* **2017**, *34* (2), 257–268.

[211] Bender, A. R.; Von Briesen, H.; Kreuter, J.; Duncan, I. B.; Rubsamen-Waigmann, H. Efficiency of Nanoparticles as a Carrier System for Antiviral Agents in Human Immunodeficiency Virus-Infected Human Monocytes/Macrophages in Vitro. *Antimicrob. Agents Chemother.* **1996**, *40* (6), 1467–1471.

[212] a) Löbenberg, R.; Araujo, L.; Kreuter, J. Body Distribution of Azidothymidine Bound to Nanoparticles after Oral Administration. *Eur. J. Pharm. Biopharm.* **1997**, *44* (2), 127–132. b) Löbenberg, R.; Maas, J.; Kreuter, J. Improved Body Distribution Of14C-Labelled AZT Bound to Nanoparticles in Rats Determined by Radioluminography. *J. Drug Target.* **1998**, *5* (3), 171–179. c) Löbenberg, R.; Araujo, L.; Von Briesen, H.; Rodgers, E.; Kreuter, J. Body Distribution of Azidothymidine Bound to Hexyl-Cyanoacrylate Nanoparticles after i.v. Injection to Rats. *J. Control. Release* **1998**, *50* (1–3), 21–30. d) Dembri, A.; Montisci, M.; Gantier, J. C.; Chacun, H.; Ponchel, G. Targeting of 3'-Azido Nanospheres to the Gastrointestinal Mucosa and Associated Lymphoid Tissues. *Pharm. Res.* **2001**, *18* (4), 467–473.

[213] Chaowanachan, T.; Krogstad, E.; Ball, C.; Woodrow, K. A. Drug Synergy of Tenofovir and Nanoparticle-Based Antiretrovirals for HIV Prophylaxis. *PLoS One* **2013**, *8* (4).

[214] Shah, L. K.; Amiji, M. M. Intracellular Delivery of Saquinavir in Biodegradable Polymeric Nanoparticles for HIV/AIDS. *Pharm. Res.* **2006**, *23* (11), 2638–2645.

[215] Mainardes, R. M.; Gremiao, M. P. D.; Brunetti, I. L.; Fonseca, L. M. da; Khalil, N. M. Zidovudine-Loaded PLA and PLA–PEG Blend Nanoparticles: Influence of Polymer Type on Phagocytic Uptake by Polymorphonuclear Cells. *J. Pharm. Sci.* **2009**, *98* (1), 257–267.

[216] Vinogradov, S. V.; Kohli, E.; Zeman, A. D. Cross-Linked Polymeric Nanogel Formulations of 5'-Triphosphates of Nucleoside Analogues: Role of the Cellular Membrane in Drug Release. *Mol. Pharm.* **2005**, *2* (6), 449–461.

[217] Hillaireau, H.; Le Doan, T.; Appel, M.; Couvreur, P. Hybrid Polymer Nanocapsules Enhance in Vitro Delivery of Azidothymidine-Triphosphate to Macrophages. *J. Control. Release* **2006**, *116* (3), 346–352.

[218] Li, W.; Yu, F.; Wang, Q.; Qi, Q.; Su, S.; Xie, L.; Lu, L.; Jiang, S. Co-Delivery of HIV-1 Entry Inhibitor and Nonnucleoside Reverse Transcriptase Inhibitor Shuttled by Nanoparticles: Cocktail Therapeutic Strategy for Antiviral Therapy. *AIDS* **2016**, *30* (6), 827–837.

[219] Jiang, Y.; Cao, S.; Bright, D. K.; Bever, A. M.; Blakney, A. K.; Suydam, I. T.; Woodrow, K. A. Nanoparticle-Based ARV Drug Combinations for Synergistic Inhibition of Cell-Free and Cell-Cell HIV Transmission. *Mol. Pharm.* **2015**, *12* (12), 4363–4374.

[220] Dou, H.; Morehead, J.; Destache, C. J.; Kingsley, J. D.; Shlyakhtenko, L.; Zhou, Y.; Chaubal, M.; Werling, J.; Kipp, J.; Rabinow, B. E.; et al. Laboratory Investigations for the Morphologic, Pharmacokinetic, and Anti-Retroviral Properties of Indinavir Nanoparticles in Human Monocyte-Derived Macrophages. *Virology* **2006**, *358* (1), 148–158.

[221] a) Kinman, L.; Bui, T.; Larsen, K.; Tsai, C. C.; Anderson, D.; Morton, W. R.; Hu, S. L.; Ho, R. J. Y. Optimization of Lipid-Indinavir Complexes for Localization in Lymphoid Tissues of HIV-Infected Macaques. *J. Acquir. Immune Defic. Syndr.* **2006**, *42* (2), 155–161. b) Snedecor, S. J.; Sullivan, S. M.; Ho, R. J. Y. Feasibility of Weekly HIV Drug Delivery to

Enhance Drug Localization in Lymphoid Tissues Based on Pharmacokinetic Models of Lipid-Associated Indinavir. *Pharm. Res.* **2006**, *23* (8), 1750–1755.

[222] Dalpiaz, A.; Ferraro, L.; Perrone, D.; Leo, E.; Iannuccelli, V.; Pavan, B.; Paganetto, G.; Beggiato, S.; Scalia, S. Brain Uptake of a Zidovudine Prodrug after Nasal Administration of Solid Lipid Microparticles. *Mol. Pharm.* **2014**, *11* (5), 1550–1561.

[223] a) Jain, S.; Tiwary, A.; Jain, N. Sustained and Targeted Delivery of an Anti-HIV Agent Using Elastic Liposomal Formulation: Mechanism of Action. *Curr. Drug Deliv.* **2006**, *3* (2), 157–166. b) Jain, S.; Tiwary, A.; Jain, N. PEGylated Elastic Liposomal Formulation for Lymphatic Targeting of Zidovudine. *Curr. Drug Deliv.* **2008**, *5* (4), 275–281.

[224] Düzgünes, N.; Simoes, S.; Slepushkin, V.; Pretzer, E.; Rossi, J. J.; Clercq, E. De; Antao, V. P.; Collins, M. L.; Lima, M. C. P. de. Enhanced Inhibition of HIV-1 Replication in Macrophages by Antisense Oligonucleotides, Ribozymes and Acyclic Nucleoside Phosphonate Analogs Delivered in PH-Sensitive Liposomes. *Nucleosides, Nucleotides and Nucleic Acids* **2001**, *20* (4–7), 515–523.

[225] Choi, S.; Bui, T.; Ho, R. J. y. pH-Dependent Interactions of Indinavir and Lipids in Nanoparticles and Their Ability to Entrap a Solute. *J. Pharm. Sci.* **2008**, *97*, 931–947.

[226] Freeling, J. P.; Koehn, J.; Shu, C.; Sun, J.; Ho, R. J. Y. Long-Acting Three-Drug Combination Anti-HIV Nanoparticles Enhance Drug Exposure in Primate Plasma and Cells within Lymph Nodes and Blood. *AIDS* **2014**, *28* (17), 2625–2627.

[227] Couvreur, P.; Stella, B.; Harivardhan Reddy, L.; Hillaireau, H.; Dubernet, C.; Desmaëie, D.; Lepêtre-Mouelhi, S.; Rocco, F.; Dereuddre-Bosquet, N.; Clayette, P.; et al. Squalenoyl Nanomedicines as Potential Therapeutics. *Nano Lett.* **2006**, *6* (11), 2544–2548.

[228] Bekkara-Aounallah, F.; Gref, R.; Othman, M.; Reddy, L. H.; Pili, B.; Allain, V.; Bourgaux, C.; Hillaireau, H.; Lepêtre-Mouelhi, S.; Desmaële, D.; et al. Novel PEGylated Nanoassemblies Made of Self-Assembled Squalenoyl Nucleoside Analogues. *Adv. Funct. Mater.* **2008**, *18* (22), 3715–3725.

[229] a) Jin, Y.; Ai, P.; Xin, R.; Chen, D. Morphological Transformation of Self-Assembled Nanostructures Prepared from Cholesteryl Acyl Didanosine and the Optimal Formulation of Nanoparticulate Systems: Effects of Solvents, Acyl Chain Length and Poloxamer 188. *J. Colloid Interface Sci.* **2008**, *326* (1), 275–282. b) Jin, Y.; Xin, R.; Ai, P.; Chen, D. Self-Assembled Drug Delivery Systems. 2. Cholesteryl Derivatives of Antiviral Nucleoside Analogues: Synthesis, Properties and the Vesicle Formation. *Int. J. Pharm.* **2008**, *350* (1–2), 330–337. c) Jin, Y.; Ai, P.; Xin, R.; Tian, Y.; Dong, J.; Chen, D.; Wang, W. Self-Assembled Drug Delivery Systems. Part 3. In Vitro/in Vivo Studies of the Self-Assembled Nanoparticulates of Cholesteryl Acyl Didanosine. *Int. J. Pharm.* **2009**, *368* (1–2), 207–214.

[230] Horcajada, P.; Chalati, T.; Serre, C.; Gillet, B.; Sebrie, C.; Baati, T.; Eubank, J. F.; Heurtaux, D.; Clayette, P.; Kreuz, C.; et al. Porous Metal-Organic-Framework Nanoscale Carriers as a Potential Platform for Drug Deliveryand Imaging. *Nat. Mater.* **2010**, *9* (2), 172–178.

[231] Mcdonald, T. O.; Giardiello, M.; Martin, P.; Siccardi, M.; Liptrott, N. J.; Smith, D.; Roberts, P.; Curley, P.; Schipani, A.; Khoo, S. H.; et al. Antiretroviral Solid Drug Nanoparticles with Enhanced Oral Bioavailability: Production, Characterization, and In Vitro-In Vivo Correlation. *Adv. Healthc. Mater.* **2014**, *3* (3), 400–411.

[232] Giardiello, M.; Liptrott, N. J.; McDonald, T. O.; Moss, D.; Siccardi, M.; Martin, P.; Smith, D.; Gurjar, R.; Rannard, S. P.; Owen, A. Accelerated Oral Nanomedicine Discovery from Miniaturized Screening to Clinical Production Exemplified by Paediatric HIV Nanotherapies. *Nat. Commun.* **2016**, *7*, 1–10.

Chapter 2

Objectives

Within this context and due to the ongoing challenges in HIV therapy, our proposal was to investigate the unexplored field of NCPs for the delivery of antiretroviral drugs and it can be found summarized in figure 2.1. To start, owing to our previous knowledge in catechol synthesis, we planned on designing a synthetic route for a conjugated compound between the anti-HIV drug zidovudine and a catechol moiety, namely **catAZT**. Moreover, we envisioned the conjugation between the catechol part and the drug through an enzyme-responsive linker such as an ester bond. The presence of catechol also obeyed, ultimately, to the formation of NCPs composed by the polymerization of iron-catechol complexes aided by a bis(imidazole) bridging ligand, as it had been already described within our research group and outlined in the introduction. Thus, we expected to form particles following similar procedures using **catAZT**. In the end, the active drug zidovudine would be chemically tethered to the building blocks of the NCPs, namely **catAZT-NCPs**, effectively increasing the expected drug loading capacity and moderating their drug release when compared to a physical entrapment.

As we have also seen in the introduction, our group showed that these families of NCPs gradually degrade in aqueous media into their constituents. With this in mind, we conceived the release of zidovudine in physiological media as a two-step process, outlined in figure 2.1 b. Therefore, we expected **catAZT-NCPs** to degrade in aqueous media and release their constitutive ligands, constituting the rate-limiting step of the process. The ligand bearing the anti-HIV drug, **catAZT**, would be then susceptible to enzymatic hydrolysis by endogenous esterases, finally releasing the drug zidovudine. From an experimental point of view, this release process would be performed in vitro in a simulated physiological media and chromatographic methodologies would be developed in order to unequivocally quantify the amount of zidovudine released at different time intervals. Moreover, and firstly, the hydrolysis of non-nanostructured **catAZT** should be evaluated under the same experimental conditions and analysis techniques for comparison purposes. Then, different parameters of the interaction of **catAZT-NCPs** with biological media would be evaluated in different cell lines, namely cytotoxicity and cellular uptake, and compared to the free drug zidovudine. As a blank for the biological tests, a similar catechol-nucleoside conjugate using non-active thymidine, namely **catTHY**, would also be prepared to form structurally analogous NCPs, **catTHY-NCPs**, without expected anti-HIV activity. Finally, their anti-HIV activity would be evaluated in infected lymphocytes.

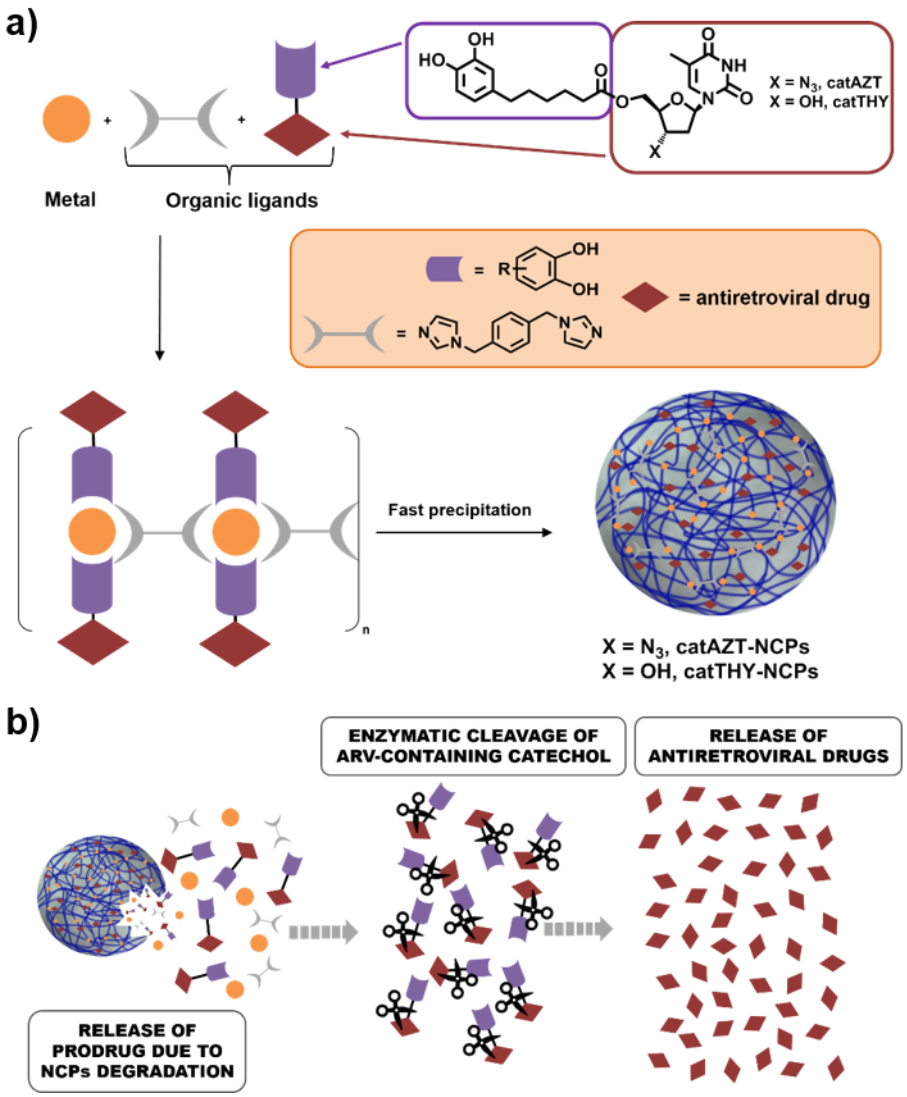

Figure 2.1. (a) Scheme of the synthesis of **catAZT-NCPs** and **catTHY-NCPs**. (b) Schematic representation of the drug release process involving NCPs degradation and subsequent enzymatic cleavage of the antiretroviral drug.

Once established, the scope of the previous proof-of-concept **catAZT-NCPs** would be expanded with the preparation of NCPs bearing multiple antiretroviral drugs. In particular, we expected to emulate the fixed-dose commercial formulation Dutrebis™, consisting of 150 mg of the NRTI lamivudine and 300 mg of integrase inhibitor raltegravir. As this dosage equates roughly to a 1:1 molar ratio between both antiretroviral drugs, our ultimate goal in this chapter would be the formation of NCPs bearing both drugs in an equimolar ratio. To achieve this, catechol-drug conjugates using raltegravir (RAL) and emtricitabine (FTC) would be prepared taking advantage of the methodologies developed during the previous chapter, namely **catRAL** and **catFTC** respectively (scheme 2.1).

Then, in the first place, these new conjugates would be used separately to form NCPs and they would be characterized in a similar way to that previously described, including drug release kinetics of the free conjugates and NCPs. Once each particle system is fully characterized, our research would move on the formation of NCPs using mixtures of antiretroviral drugs with the aim of achieving the aforementioned equimolar ratio and their characterization, specially their drug release profile. To fully characterize this multi-drug systems, chromatographic methodologies should be developed in order to unequivocally quantify each species resulting of NCPs degradation.

Lastly, synthetic methodologies will be explored for the obtention of additional conjugates between catechol and ARV drugs. Specifically, the synthesis will be focus on lamivudine (3TC) and tenofovir (TFV) conjugates, **cat3TC** and **catTFV**, respectively (scheme 2.1). The novelty in this step resides in the presence of two free hydroxyl groups within the phosphonate unit of tenofovir. Thus, we envisioned the attachment of two different catechol moieties to it, to form the conjugate **catTFV**, with the idea of enabling its polymerization with iron ions without the addition of the bis(imidazole) bridging ligand, therefore increasing drug loading capacity and simplifying its chemical structure. Despite not presenting an ester bond like the previous conjugates, **catTFV** contains carbonyloxymethyl phosphonates moieties, which are known to be affected by esterases in a similar way to alkyl esters.

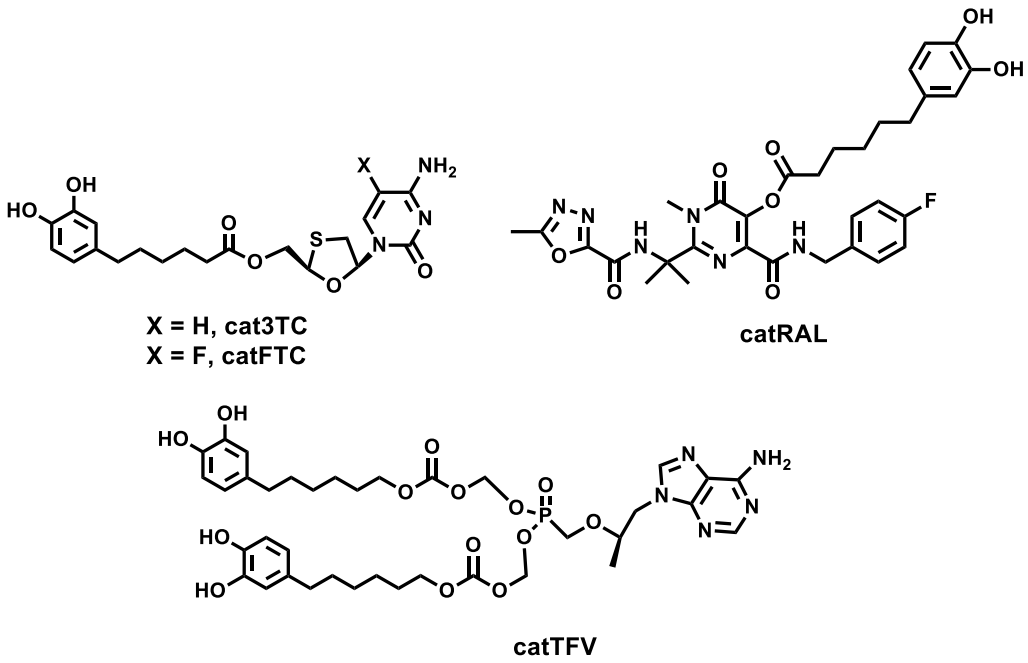

Scheme 2.1. Proposed structures for catechol-ARV conjugation using lamivudine (3TC), emtricitabine (FTC), raltegravir (RAL) or tenofovir (TFV); **cat3TC**, **catFTC**, **catRAL** and **catTFV** respectively.

To achieve this, the following specific objectives of this PhD thesis were set:

1. To develop a synthetic methodology for the obtention of a catechol-zidovudine conjugate, **catAZT**, and its non-active counterpart catechol-thymidine conjugate, **catTHY**.
2. To form iron-based nanoscale coordination particles (NCPs) using **catAZT** or **catTHY** and a bis-imidazole bridging ligand, **bix**.
3. To characterize the aforementioned NCPs, **catAZT-NCPs** and **catTHY-NCPs**, and prove their feasibility as drug delivery systems.
4. To expand the scope of antiretroviral-containing NCPs formation by first synthesizing catechol-ARV conjugates using the clinically-relevant combination of emtricitabine (FTC), **catFTC**, and raltegravir (RAL), **catRAL**, and their subsequent use for the formation of dual-ARV drug NCPs in order to emulate single pill dosage.
5. To develop additional synthetic approaches for the functionalization of the antiretroviral drugs lamivudine (3TC) and tenofovir (TFV), **cat3TC** and **catTFV**, respectively.

Chapter 3

Synthesis of NCPs based on zidovudine-catechol conjugates

This chapter will focus on the synthesis and characterization of NCPs containing the antiretroviral drug zidovudine (AZT) as part of the building blocks of the particles themselves. Thus, an organic synthetic pathway for the formation of zidovudine-catechol (**catAZT**) conjugates will be initially presented, followed by the description of the synthesis of NCPs using **catAZT**, their subsequent characterization, including physicochemical, in vitro drug release profile, cytotoxicity, cellular uptake and anti-HIV activity evaluation. The synthesis and characterization of NCPs formed by the self-assembly of thymidine-catechol conjugates (**catTHY**) will also be presented for comparison purposes.

3.1 Development of synthetic methodologies for the obtention of catAZT

3.1.1 Synthetic route for the obtention of catAZT and catTHY

Target molecules **catAZT** and **catTHY**, were conceived as the sum of three basic units: a catechol moiety, an alkyl chain containing a carboxylic acid and an antiretroviral (ARV) drug attached to it (scheme 3.1). The proposed synthesis would consist on a common pathway to obtain pivotal intermediate **4** in a multi-gram scale and its posterior use to attach the ARV drug using suitable methodologies. The first choice for the ARV drug was zidovudine (AZT) owing to the fact that (i) it was the first ARV drug approved by the FDA in HIV/AIDS therapy;[1] (ii) it is a representative model for nucleoside reverse transcriptase inhibitors (NRTIs), which are still used in current therapy in combination with other classes of ARV drugs; and (iii) it is commercially available through common suppliers. A Wittig reaction between 3,4-dibenzyloxybenzaldehyde, **1**, and the phosphonium ylide **2**, followed by a catalytic hydrogenation was chosen as the starting point for their synthesis. The election of benzyl protecting groups would allow the direct synthesis, after the reduction step, of unprotected catechol bearing a carboxylic group, **3**, and its further protection as a *tert*-butyldiphenylsilyl (TBDPS) ether, **4**. This second protection step would provide a protection for catechol that would allow a final deprotection step using mild experimental conditions compatible with ester and azide moieties. Commercially-available AZT and thymidine would be then incorporated to intermediate **4** by an esterification reaction. Lastly, removal of TBDPS protecting groups would allow the isolation of the catechol conjugates containing AZT and thymidine, **catAZT** and **catTHY** respectively.

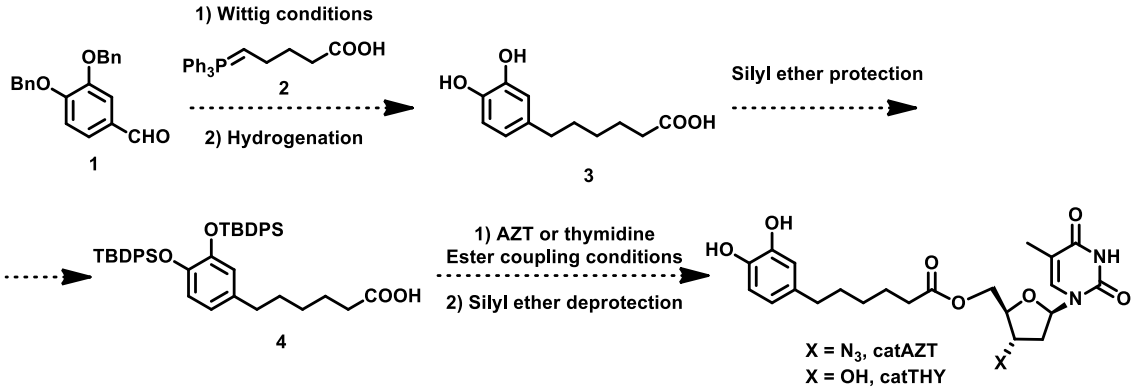

Scheme 3.1. Proposed synthetic route for the obtention of target molecules **catAZT** and **catTHY**.

3.1.2 Synthesis of catAZT

3.1.2.1 Synthesis of 6-(3,4-bis(benzyloxy)phenyl)hex-5-enoic acid, 5.

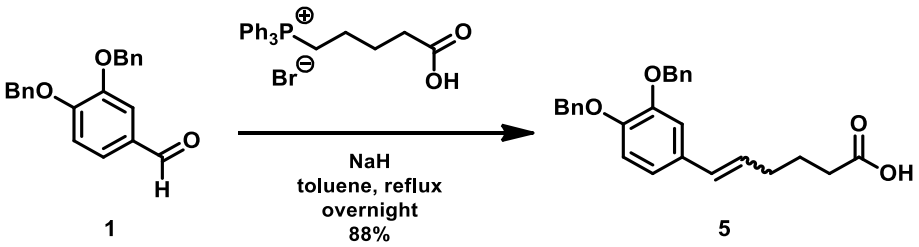

The synthetic sequence started form commercially-available 3,4-dibenzyloxybenzaldehyde, **1**, which was converted into carboxylic acid **5** through a Wittig reaction using the nonstabilized phosphonium ylide prepared *in situ* by treatment of (4-carboxybutyl)triphenylphosphonium bromide with base. The reaction was performed in dry toluene and NaH, because the use of other solvents and bases, such as dry THF or potassium *tert*-butoxide, proved to be less efficient for this process. It is worth noticing that, although a high reactivity between an aldehyde and a nonstabilized ylide is expected, the reaction did not take place until it was heated to reflux temperature. After purification by liquid-liquid extraction and flash column chromatography, carboxylic acid **5** was obtained in 88% yield as a 5:1 mixture of the *E* and *Z* isomers, identified by the olefinic ^{1}H NMR coupling constants ($^3J_{trans}$ = 15.8 Hz, $^3J_{cis}$ = 11.8 Hz). However, these isomers were not further separated as the next synthetic step involved a catalytic hydrogenation of the double bond.

3.1.2.2 Synthesis of 6-(3,4-dihydroxyphenyl)hexanoic acid, 3.

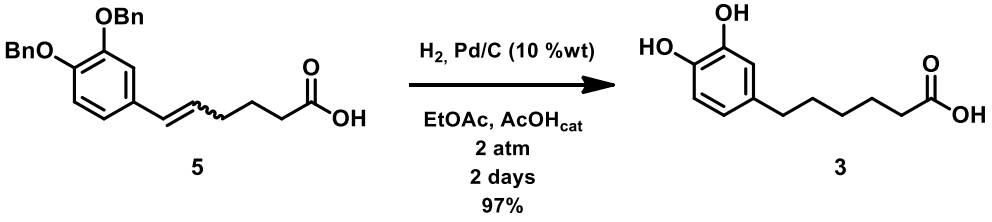

Next, a simultaneous hydrogenation of the alkene moiety and removal of the benzyl protecting group was performed to the previous mixture of *E* and *Z* isomers using high pressure of H_2 under Pd/C as catalyst to furnish catechol **3**. Nevertheless, this transformation was more problematic than it appeared. At first, the olefin was observed to be hydrogenated easily when **5** was dissolved in an aprotic solvent such ethyl acetate, but the benzyl moieties remained unmodified under these conditions. The introduction of traces of acetic acid, combined with frequently H_2 refilling in the reaction vessel, facilitated the removal of the benzyl protecting groups, easily

monitored by ^{1}H NMR. Catechol **3** was obtained almost quantitatively by simple filtration of the catalyst and evaporation of the solvent under reduced pressure.

3.1.2.3 Synthesis of 6-(3,4-bis((tert-butyldiphenylsilyl)oxy)phenyl)hexanoic acid, 4.

Preliminary tests were initially performed to explore the possibility of the straightforward esterification between AZT and catechol **3** without further protection, thus simplifying the synthetic pathway and therefore increasing its overall yield (scheme 3.2). In this way, different coupling agents that enhance the reactivity of carboxylic acids were employed (table 3.1). Starting with a Steglich esterification (table 3.1, entry 1)) and moving to more complex coupling agents such as HATU and EDCI,[2] the reaction did not take place. Next, to test the feasibility of the esterification, a proof-of-concept using protected catechol **5** and HATU as coupling agent (table 3.1, entry 4) was performed and a new compound, less polar than both **5** and AZT was detected, purified and later identified as **6** in 32% yield. Although target molecule **catAZT** would be derived from the deprotection of benzyl groups in **6** by simple hydrogenation, this synthetic step could not be accomplished because the azide group of the nucleoside would be reduced to amine.

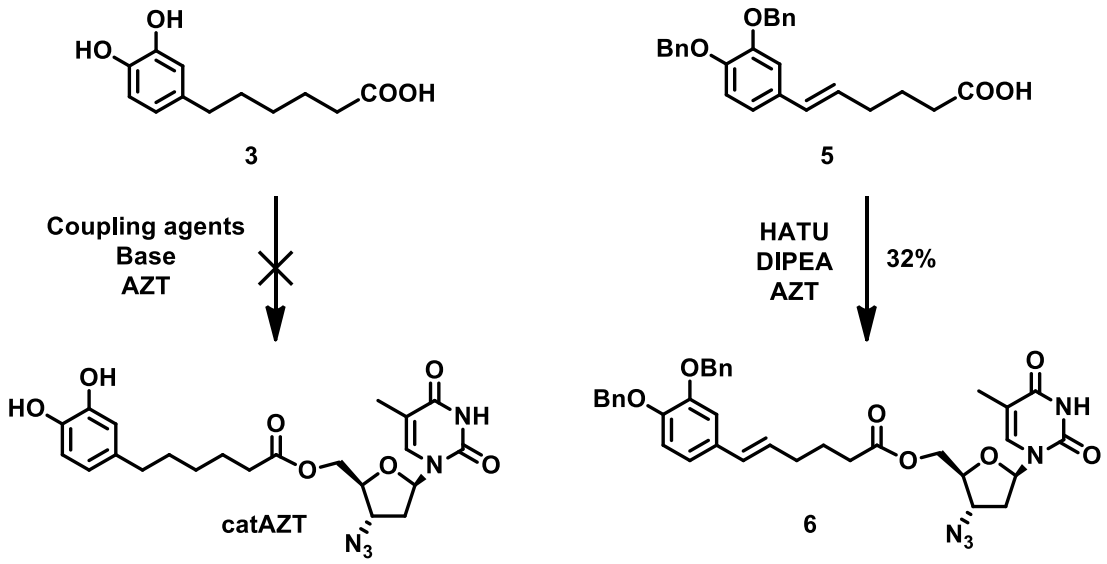

Scheme 3.2. Schematic representation of the two different approaches to conjugate the antiretroviral drug zidovudine to the selected catechol moiety, direct coupling (left) was unsuccessful while conjugation to a catechol-protected carboxylic acid (right) was proven to be feasible.

Table 3.1. Synthesis tests for the direct formation of **catAZT**.

Entry	Substrate	Coupling Agent	Base	Solvent	Reaction conditions	Yield
1	**3**	DCC	DMAP	THF	0 °C, overnight	No conversion
2	**3**	HATU	DIPEA	THF	rt, 2 days	No conversion
3	**3**	EDCI	DIPEA	THF	rt, 4 days	No conversion
4	**5**	HATU	DIPEA	THF	rt, overnight	32%

After the successful test coupling of AZT to **5**, the challenge was now to protect the hydroxyl moieties in catechol **3** in a manner that could be eliminated chemoselectively under mild conditions but, at the same time, would not affect the nucleoside or the ester linkage at all. The use of a silyl ether protecting group was then envisioned as it had been successfully used in our research group for catechol compounds. Specifically, the silylation of 3-bromo-4,5-dihydroxybenzaldehyde, **7**, was reported by our research group in 2008 using *tert*-butyldiphenylsilyl, 1,8-diazabicyclo[5.4.0]undec-7-ene (DBU) as base and a THF/DMF mixture as solvent (scheme 3).[3]

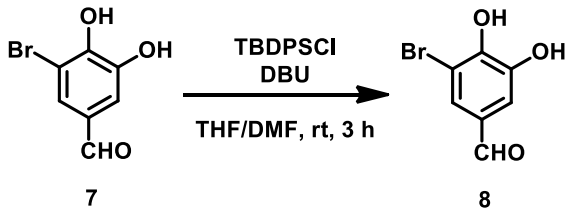

7 8

Scheme 3.3. Silylation of **7** using TBDPS reported by our research group (ref 3).

After failed attempts to introduce the TBDPS protecting group using this methodology, the reaction was attempted using dry acetonitrile at 40 °C while maintaining the initial reagents, i.e. *tert*-butyldiphenylsilyl chloride and DBU as base. In these reaction conditions, compound **4** was obtained in 64% yield (scheme 3.4).

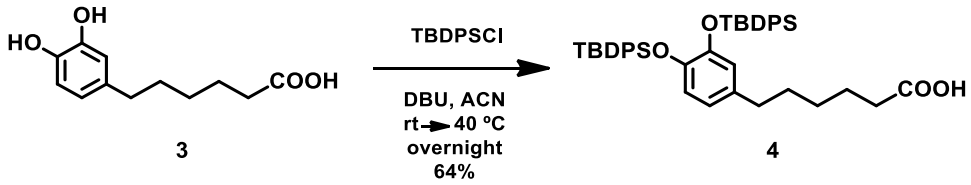

3 4

Scheme 3.4. Protection of catechol moieties in compound **3** as *tert*-butyldiphenylsilyl (TBDPS) ethers.

Interestingly, when the reaction was scaled-up, a highly-nonpolar fraction was also isolated during purification with flash column chromatography. This fraction was identified as the pure compound bearing three TBDPS groups **9**, which was easily hydrolyzed to recover intermediate

4 (scheme 3.5) using basic conditions and a mixture of solvents (EtOH/THF/H_2O) in order to increase its solubility.

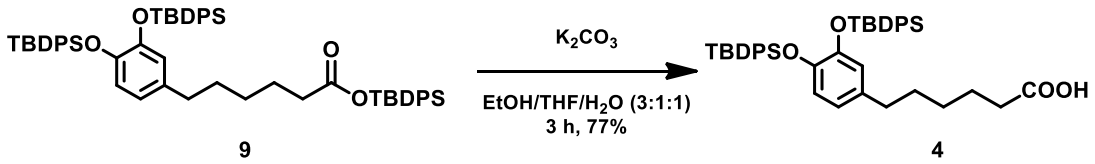

Scheme 3.5. Basic hydrolysis of side product **9** to recover **4**.

3.1.2.4 Synthesis of ((2*S*,3*S*,5*R*)-3-azido-5-(5-methyl-2,4-dioxo-3,4-dihydropyrimidin-1(2*H*)-yl)tetrahydrofuran-2-yl)methyl 6-(3,4-bis((tert-butyldiphenylsilyl)oxy)phenyl)hexanoate, 14.

The next step in the synthetic sequence involved the tethering of AZT to the carboxylic acid **4**. In a previous research project, the conjugation of unsaturated carboxylic acids to AZT had been explored (scheme 3.6). Specifically, 4-pentenoic acid, **10**, was successfully attached to AZT in mild experimental conditions, using *N*,*N*'-dicyclohexylcarbodiimide (DCC) as a coupling agent in the presence of catalytic 4-dimethylaminopyridine (DMAP).

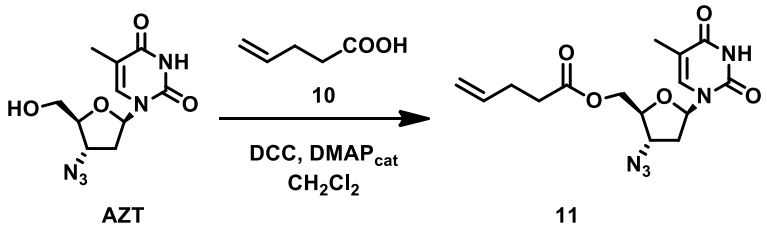

Scheme 3.6. Coupling of 4-pentenoic acid, **10**, to AZT to yield conjugate **11** performed in previous research.

At this point, as the amount of available compound **4** was limited, these coupling conditions were tested in a protected catechol used in previous research, compound **12**. As **12** only differed from **4** in their protecting groups, their reactivity towards an esterification reaction was expected to be similar. However, when using DCC, the reaction did not take place. Additional tests with the available coupling agent HATU revealed the formation of a new product, later identified as the expected ester **13** (scheme 3.7).

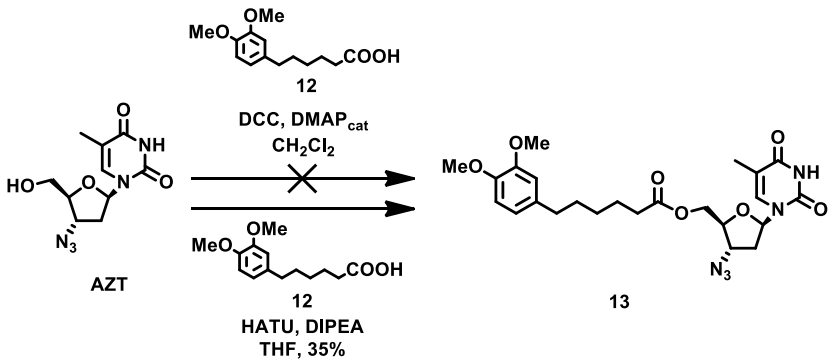

Scheme 3.7. Attempts to synthesize **13** as a model reaction for the subsequent esterification of **4** and AZT. Esterification of AZT and **12** was finally achieved using HATU as coupling agent.

The conditions found for the obtention of **13** were then successfully applied in the esterification of AZT and compound **4**. Thus, using HATU as coupling agent and *N*,*N*-diisopropylethylamine as base in THF, compound **14** was isolated in 86% yield (scheme 3.8). The ^{1}H-^{13}C HMBC spectrum of **14** displayed a cross peak attributed to the coupling of H-5' and C-1', indicating the correct formation of the ester bond (figure 3.1).

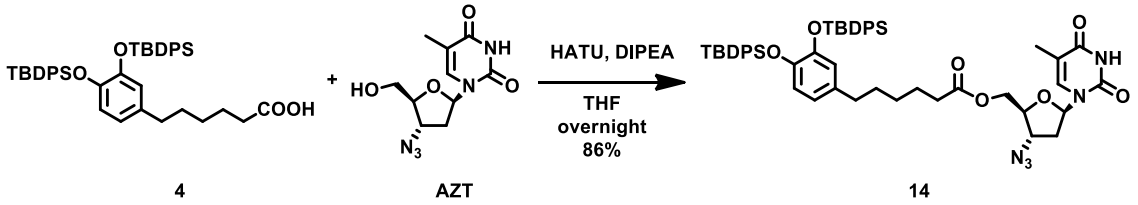

Scheme 3.8. Esterification reaction of AZT and carboxylic acid **4**.

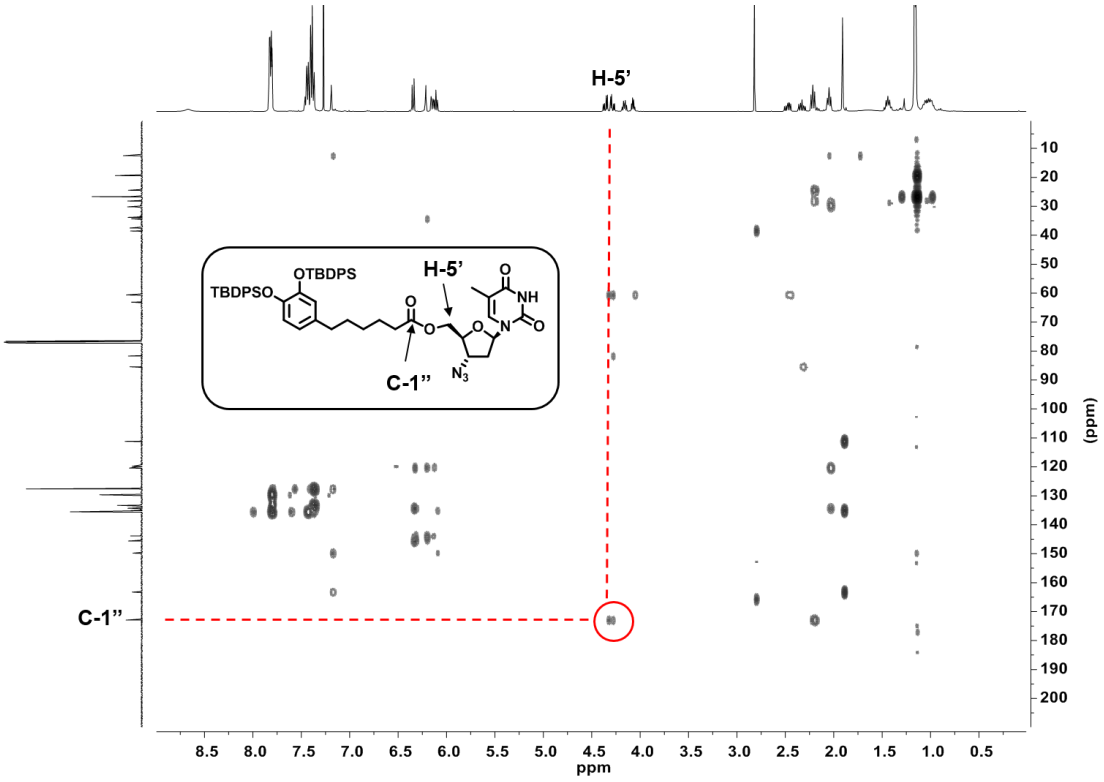

Figure 3.1. ^{1}H-^{13}C HMBC spectrum of **14** indicating the coupling between H-5' and C-1'.

3.1.2.5 Synthesis of ((2*S*,3*S*,5*R*)-3-azido-5-(5-methyl-2,4-dioxo-3,4-dihydropyrimidin-1(2*H*)-yl)tetrahydrofuran-2-yl)methyl 6-(3,4-dihydroxyphenyl)hexanoate, catAZT.

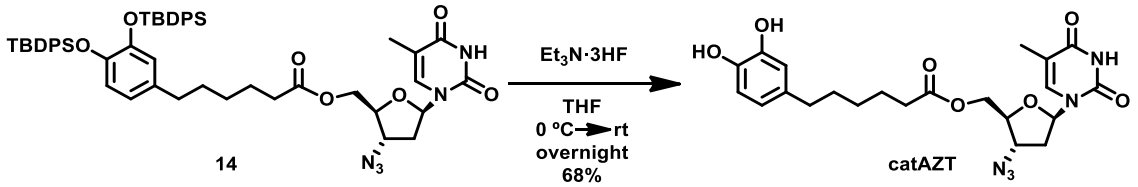

The final step in the synthesis of **catAZT** involved removal of the TBDPS protecting groups using a standard methodology previously used in our research group.[3] Thus, the simple addition of trimethylamine trihydrofluoride to **14** in dry THF furnished a more polar compound, which after quenching of the excess of $Et_3N{\cdot}3HF$ and purification by flash column chromatography was identified as the target molecule, **catAZT**, in 68% yield. In summary, the synthesis of **catAZT** was achieved through a 5-step sequence with 32% overall yield.

3.2 Synthesis of catAZT-NCPs

Ligand **catAZT** was used to prepare the corresponding antiretroviral nanoparticles **catAZT-NCPs** based on a well-stablished methodology developed in our research group for the self-assembly of caffeic acid, a bis-imidazole ligand (1,4-bis((1*H*-imidazol-1-yl)methyl)benzene, **bix**,) and metal ions (Co, Fe) to yield NCPs (scheme 3.9).[4]

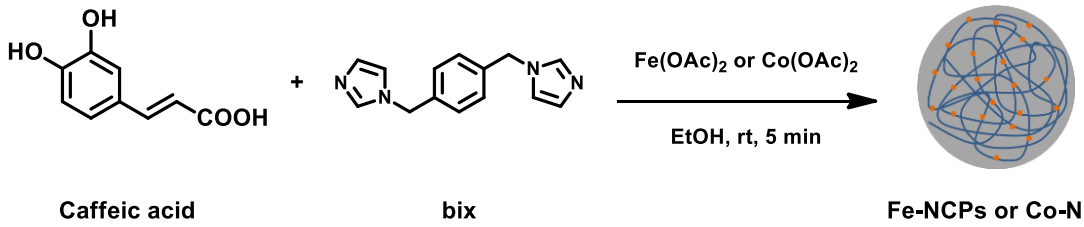

Scheme 3.9. Synthesis of NCPs based on caffeic acid, **bix** and Fe or Co ions developed in our research group.

Thus, for the formation of **catAZT-NCPs**, the bridging ligand **bix**, was prepared in a single synthetic step according to a previously reported methodology (scheme 3.10).[5] Iron, in the form of iron (II) acetate, was selected as the metallic nodes due to its high biocompatibility compared with other metals used within our research group for NCPs formation (Co, Mn, Zn).

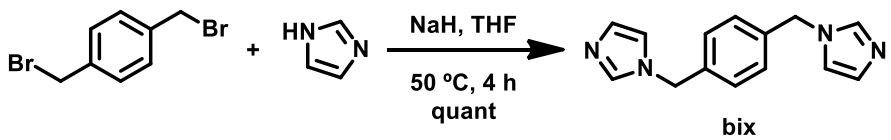

Scheme 3.10. Synthesis of the bridging ligand 1,4-bis((1*H*-imidazol-1-yl)methyl)benzene, **bix**, used in **catAZT-NCPs** formation.

In an initial approximation, **catAZT**, **bix** and $Fe(CH_3COO)_2$ were mixed in a molar ratio of 2:1:1 respectively, as it was the molar ratio between ligands and metal ions in the expected composition of the NCPs (scheme 3.11). Thus, a solution of iron (II) acetate in absolute ethanol was added dropwise to a stirred ethanolic solution of **catAZT** and **bix** and, instantaneously, a dark-purple precipitate appeared. After stirring at room temperature, the precipitate was collected by centrifugation, washed several times with ethanol and dried over vacuum.

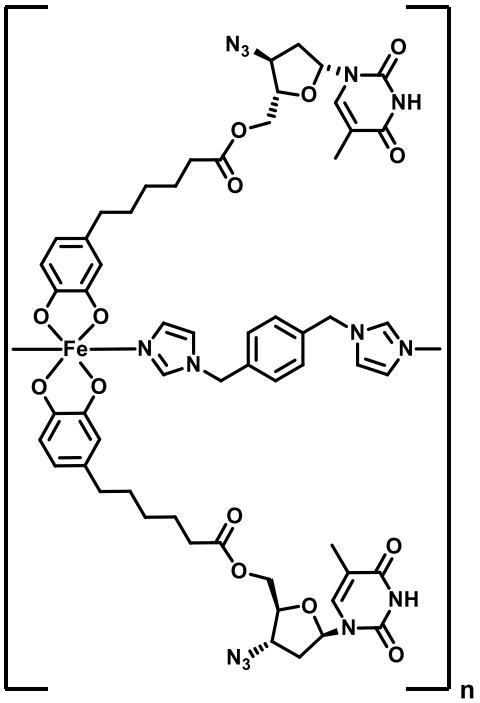

Scheme 3.11. Expected composition for **catAZT-NCPs**, consisting in the ligands **catAZT**, **bix** and Fe ions in a 2:1:1 ratio.

As a first screening, Fourier-transform infrared spectroscopy (FTIR), dynamic light scattering (DLS) and scanning electron microscopy (SEM) were used as characterization techniques for determining chemical composition and morphology of the obtained material. Once the experimental conditions of the synthetic process would be optimized, additional and more time-consuming techniques would be then used to fully characterize **catAZT-NCPs**. As mentioned in Chapter 1, particles ranging from 100 to 200 nm offer larger circulation half-lives which enhances their therapeutic effect. Therefore, the synthesis of NCPs with sizes around 150 nm was the aim at this point. Interestingly, the dark-purple precipitate obtained was formed by rather spherical particles in the range of 120 to 200 nm when observed by SEM (figure 3.2, a). Additionally, the FTIR spectrum of the material showed a characteristic band for the asymmetric azido stretching (2106 cm^{-1}), as also observed in **catAZT** (2108 cm^{-1}), in addition to bands attributed to **bix** ligand (1519, 1263, 1097 cm^{-1}) (figure 3.2, b). Unfortunately, DLS showed a discrepancy with SEM

results, as measurements in ethanol displayed an average hydrodynamic diameter of 782 ± 64 nm (PDI = 0.32) (figure 3.2, c), which suggested particle aggregation in solution. In fact, transmission electron microscopy (TEM) images (figure 3.2, d) revealed that, although sphere-shaped particles were formed due to their tendency to minimize the interfacial free energy between their surface and the solvent, the NCPs formed clusters of few particles bonded together.

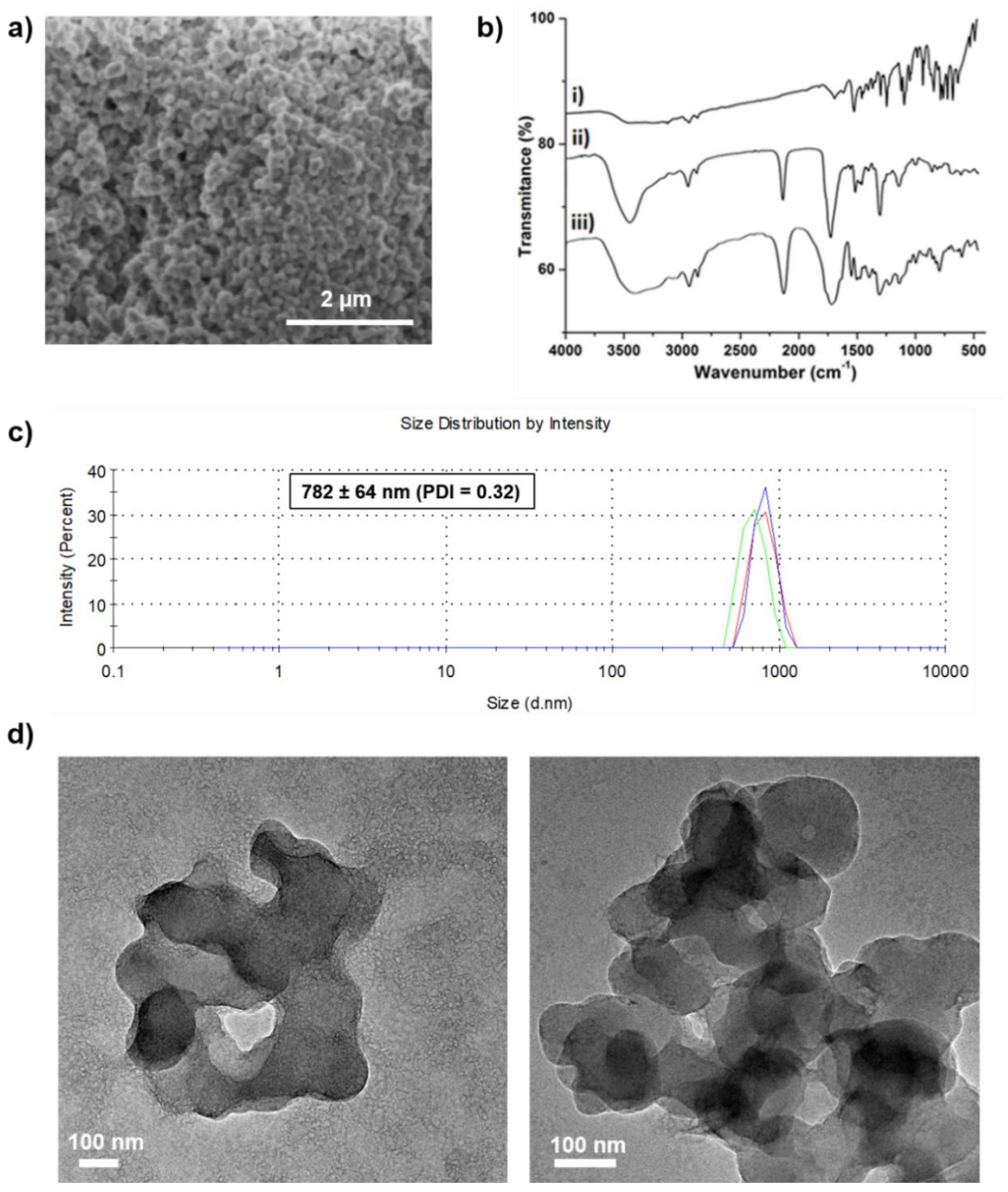

Figure 3.2. a) Representative SEM image of the firsts attempts in **catAZT-NCPs** synthesis. b) FTIR spectra of (i) **bix**, (ii) **catAZT** and (iii) **catAZT-NCPs**. c) Dynamic light scattering (DLS) measurements of **catAZT-NCPs** dispersed in ethanol. d) Representative TEM images of the firsts attempts in **catAZT-NCPs** synthesis.

This observation was reinforced when all attempts to disaggregate the material by means of ultrasonication or heating failed. Attempts to improve colloidal stability using solutions of a series of biocompatible stabilizers, namely, polyvinylpyrrolidone (PVP), polyethylene glycol (PEG) or the polysorbates Tween™ 80 and Span™ 80 or decreasing ligand/metal concentration during the synthetic process were also unsuccessful. Moreover, colloidal suspensions of the material presented sedimentation in few minutes. However, in order to perform further characterization tests, including release kinetics and especially in vitro assays, particles in colloidal dispersion should exhibit a hydrodynamic diameter around 150 nm and also stability against sedimentation in the range of hours.

To achieve a particle size comparable to SEM images in dispersion, two approaches were followed. The first one involved the inclusion of small quantities of caffeic acid in addition to **catAZT** during the synthetic process, while the latter relied on the use of stabilizers during the synthetic process to control particle size. The hypothesis within the first approach was to introduce certain number of moieties (-COOH) bearing a negative charge at physiological pH so that those located on the particle surface could apply an electrostatic repulsion to other particles, therefore preventing aggregation. Moreover, particles composed entirely by caffeic acid had been already prepared in our research group with excellent colloidal stability.[4] Thus, particles were formed according to scheme 3.12. A mixture of **catAZT** and caffeic acid (catAZT/caffeic acid molar ratio = 9) and **bix** was dissolved in ethanol, iron (II) acetate was added dropwise and a dark-purple precipitate appeared instantaneously. Taking advantage of the disassemble of the NCPs in acidic media, the ^{1}H NMR spectra of the material was recorded in a mixture of deuterated methanol and hydrochloric acid. **catAZT**:caffeic acid molar ratio was then determined using peak integrals from both ligands. Although initially this molar ratio was set to 9, the ^{1}H NMR spectra data revealed a value of approximately 1, which could be attributed due to differences in ligand affinity and steric hindrance between **catAZT** and caffeic acid. DLS measurements of the material in both ethanol and phosphate buffer saline/bovine serum albumin 0.5 mM (PBS/BSA) showed a hydrodynamic diameter around 900 nm, which could be reduced to 450 nm using ultrasonication. Unfortunately, it reverted to 900 nm within 30 minutes.

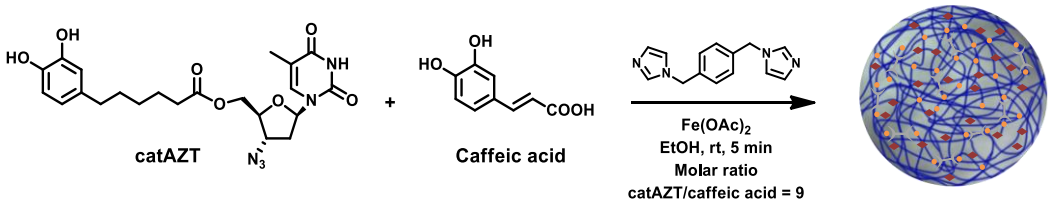

Scheme 3.12. Attempts to increase colloidal stability of **catAZT-NCPs** by the addition of caffeic acid.

The second strategy for increasing colloidal stability was more successful. Polyvinylpyrrolidone (PVP) was selected as potential stabilizer due to its wide use in colloidal nanoparticle synthesis, especially for metallic ones.[6] PVP is a non-toxic, neutral polymer that contains a strongly hydrophilic moiety (pyrrolidone) and a substantial hydrophobic part (alkyl chain) (figure 3.3). It prevents the aggregation of nanoparticles due to steric hindrance, that is, as a result of the repulsive forces between their hydrophobic moieties.[6]

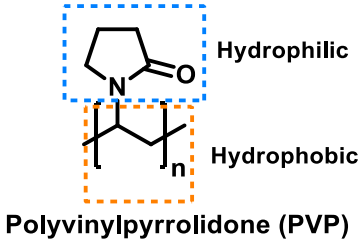

Figure 3.3. Chemical structure of polyvinylpyrrolidone (PVP), containing a hydrophilic moiety (pyrrolidone) and a hydrophobic part (alkyl chain).

Thus, **catAZT-NCPs** synthesis was attempted using the previously described methodology but instead of pure ethanol, ligands were dissolved in an ethanolic solution of PVP. First tests showed a reduction of hydrodynamic particle size to the 150-200 nm range using 1 wt% PVP, which was further reduced to 0.1 wt% with the same outcome. As a result, with this approach, summarized in scheme 3.13, the dark-purple precipitate obtained showed similar size values when observed by SEM or DLS.

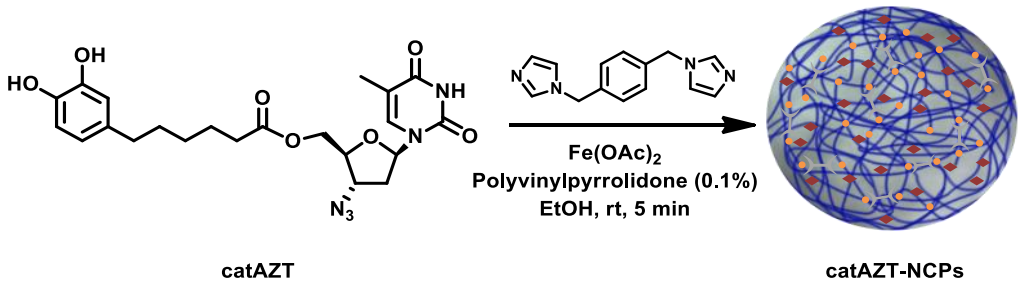

Scheme 3.13. Schematic synthesis of **catAZT-NCPs** using polyvinylpyrrolidone as stabilizing agent.

Before further characterization, two blank experiments were performed in order to shed more light on NCPs formation. The first test was to check if Fe cations and ligand **bix** formed nanostructures based on their coordination, as previously reported for Zn in our research group.[7] In this research, NCPs based on the assembly of Zn^{2+} ions and **bix** were prepared as capsules for encapsulation of guest molecules (figure 3.4). In our case, no nanostructuration was found in Fe-**bix** mixtures as determined by DLS and SEM.

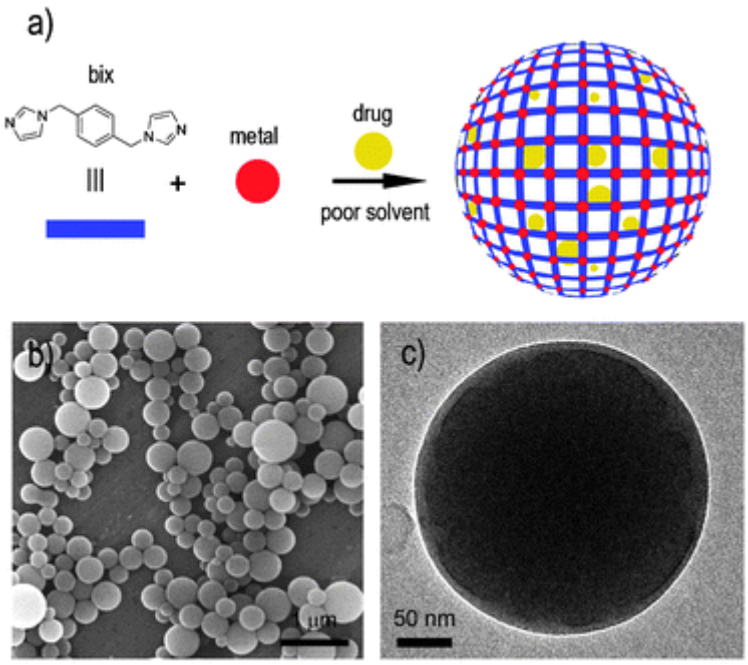

Figure 3.4. NCPs prepared previously in our research group by the assembly of Zn^{2+} ions and the bis(imidazole) ligand **bix**. Reproduced with permission from reference 7.

The second test presented more interesting results. The addition of $Fe(OAc)_2$ to a solution of **catAZT** in presence of PVP caused the appearance of a dark-purple precipitate composed by particles in the 600-700 nm range, as determined by SEM and DLS measurements (figure 3.5). Because no bridging ligands were incorporated into the reaction mixture, the resulting particles were hypothesized to be formed by the supramolecular interactions between nucleosides in Fe-**catAZT** coordination complexes. Although the formation of such particles would be advantageous for biomedical applications because drug loading would be increased with respect to **catAZT-NCPs**, their size and colloidal stability were not suitable for it. Modifications in the reaction conditions, i. e., a decrease in **catAZT** or $Fe(AOc)_2$ concentration or the addition of other stabilizers did not improve this aspect and therefore a comprehensive characterization was performed for **catAZT-NCPs** as a potential drug delivery system.

Thus, NCPs composed by ligands **catAZT** and **bix** were prepared using the experimental conditions represented in scheme 3.13. SEM images showed spherical particles with an average diameter of 147 ± 33 nm (figure 3.6), which were in agreement with DLS measurements, showing a hydrodynamic diameter of 202 ± 10 nm in ethanol and 257 ± 6 nm in PBS/BSA 0.5 mM buffer. Similar FTIR peaks to those explained in the initial screening confirmed the presence of **catAZT** and **bix**. The X-ray powder diffraction (XRD) pattern of the particles was characteristic of an amorphous material.

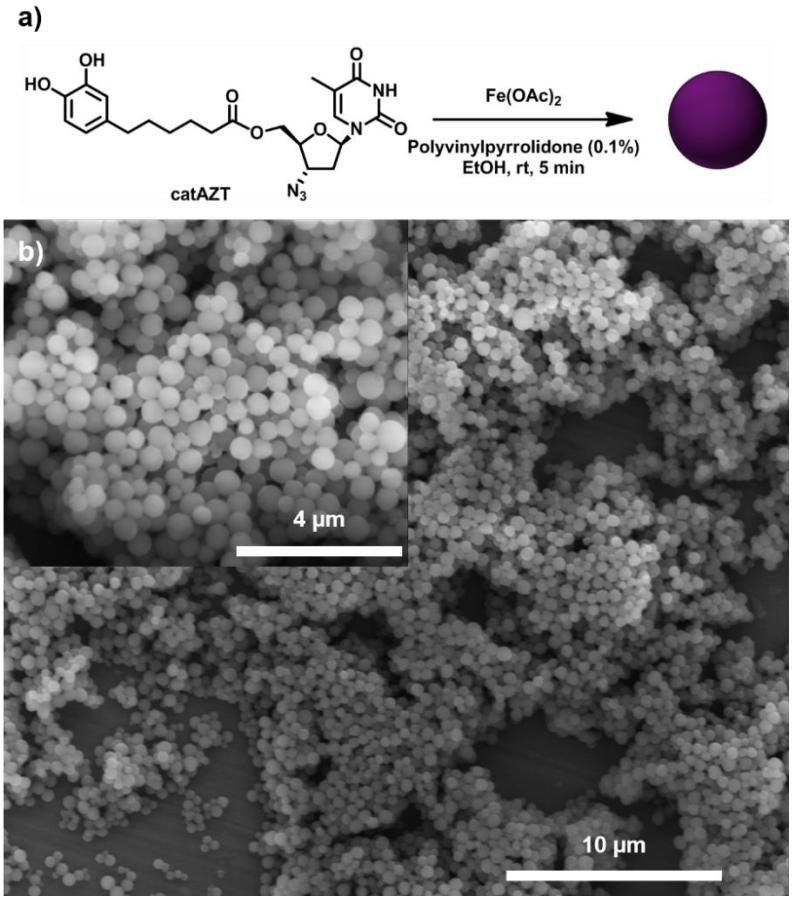

Figure 3.5. a) Schematic representation of particle formation using **catAZT** and Fe ions including b) representative SEM images.

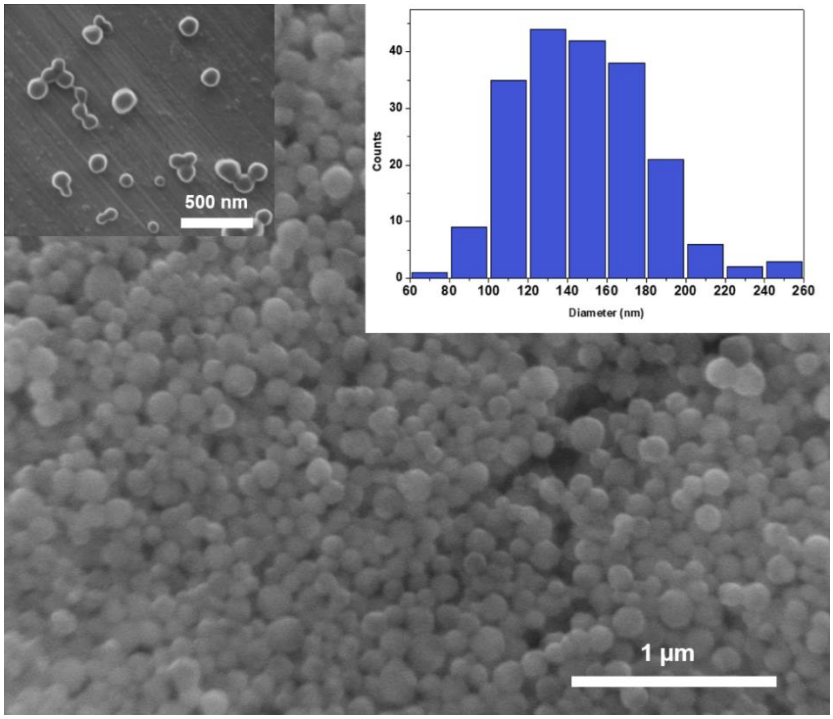

Figure 3.6. Representative SEM images of catAZT-NCPs obtained using polyvinylpyrrolidone as stabilizer. (inset) Histogram of **catAZT-NCPs** particle size extracted from SEM micrographs (200 particles, mean size 147 ± 33 nm).

To determine the chemical composition of **catAZT-NCPs**, a combination of characterization techniques was used: ^{1}H NMR, inductively coupled plasma mass spectrometry (ICP-MS), elemental analysis and high-performance liquid chromatography (HPLC). Then, an empirical formula was proposed in agreement with the resulting data. Additionally, all characterization analyses were performed to three independent batches of **catAZT-NCPs**, displaying comparable results between batches and therefore proving the robustness of the synthetic procedure. In the first place, ^{1}H NMR was used to determine the ratio between **catAZT** and **bix**. We knew from previous studies on different NCPs that these materials experience a disassemble process induced by an acidic media. Thus, ^{1}H NMR spectra of **catAZT-NCPs** were recorded in a solution of deuterated hydrochloric acid and methanol, as well as the spectra of **catAZT**, AZT and **bix** (figure 3.7). The **catAZT-NCPs** ^{1}H NMR spectrum revealed the presence of **catAZT** and **bix**, as well as acetate ions coming from the iron (II) acetate salt used in the synthetic process. Thus, integration of their characteristic signals shown in figure 3.7 allowed the determination of the **catAZT**/**bix** ratio, which averaged 2.5.

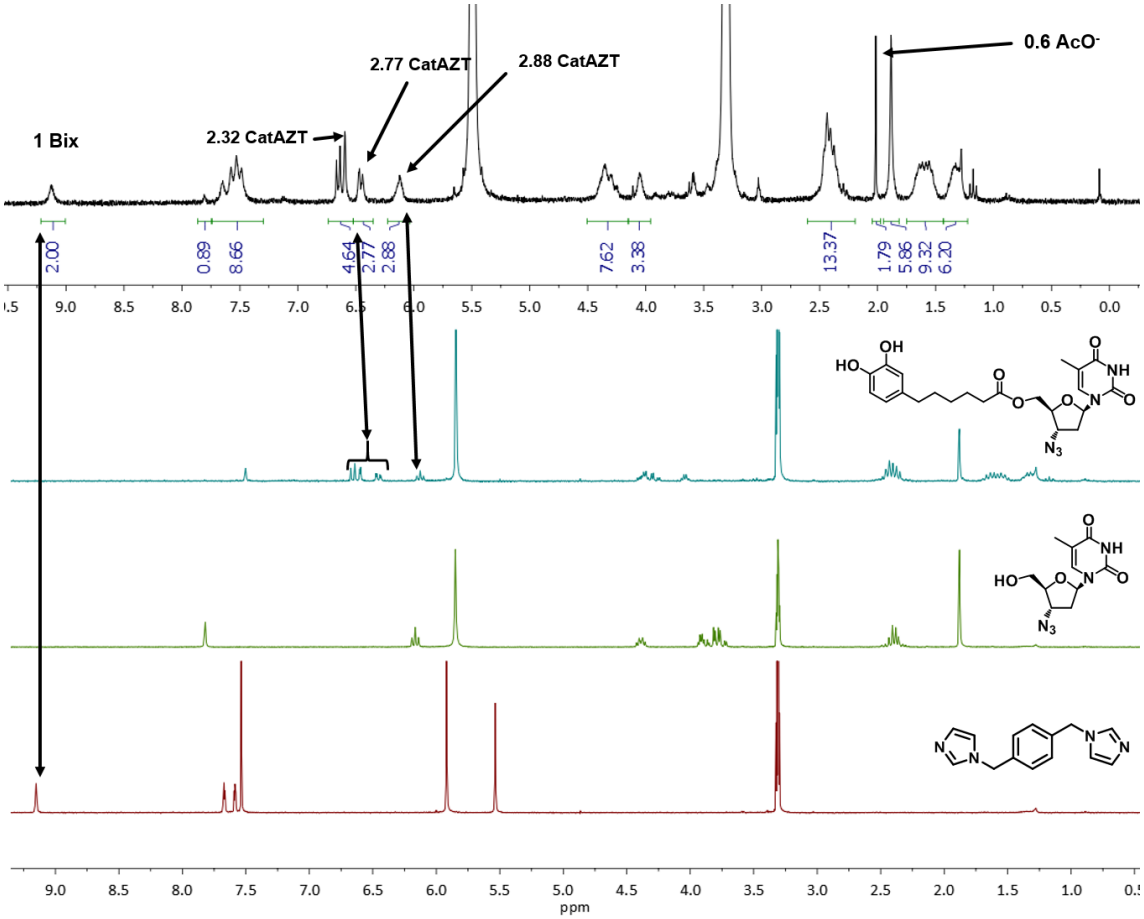

Figure 3.7. ^{1}H NMR spectra of (top to bottom) disassembled **catAZT-NCPs**, **catAZT**, AZT and **bix** recorded in a DCl/CD_3OD acidic solution (50 µL DCl/mL CD_3OD). Peaks corresponding to **catAZT**, **bix** and acetate are observed in the ^{1}H NMR spectrum of **catAZT-NCPs**.

ICP-MS measurements allowed the determination of Fe content in NCPs, which was found to be 5.5%. Elemental analysis displayed also reproducible %CHNS values among different **catAZT-NCPs** batches, although values differed from the expected composition for the NCPs, consisting on **catAZT**:**bix**:Fe in a molar ratio of 2:1:1.

HPLC quantification of **catAZT** and **bix** was done using ion pair chromatography (IPC) coupled to a UV detector. IPC relies on the use of mobile phase additives, usually alkylsulfonates, to increase the retention times of ionic analytes that otherwise would not be retained and therefore separated using a standard reverse-phase column (figure 3.8).[8] In this case, as mobile phase was set acidic to avoid catechol deprotonation,[9] **bix** was expected to be present in its protonated form. In fact, initial screening injections of **bix** standards using a conventional reversed-phase column displayed a poor separation due to its fast elution through the column. However, when sodium 1-octanesulfonate was added to the mobile phase, **bix** retention time increased and therefore facilitated its separation and posterior quantification.

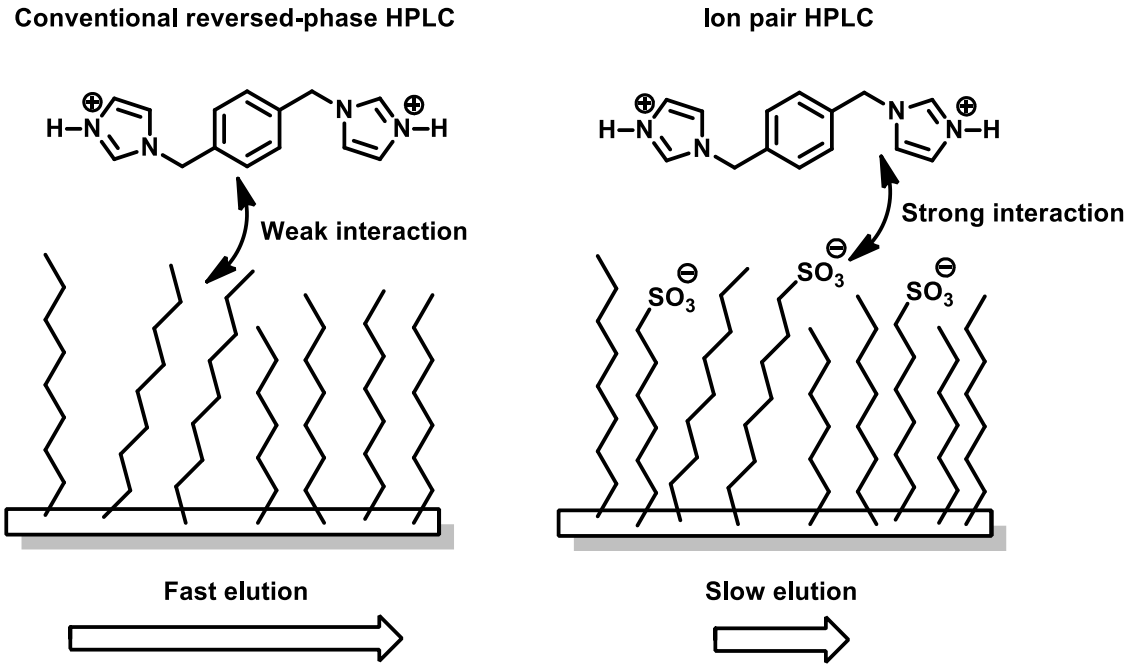

Figure 3.8. Comparison between conventional reversed-phase HPLC (left) and ion pair HPLC (right) applied to the elution of protonated **bix**. In conventional reversed-phase HPLC (left), protonated **bix** interacts weakly with the hydrophobic stationary phase consisting in silica coated with C18 alkyl chains. When an alkylsulfonate is added as additive (right), it is adsorbed onto the stationary phase surface, allowing a stronger interaction with protonated **bix** due to its anionic sulfonyl moieties, and therefore enhancing the separation process.

Thus, a calibration curve was prepared using standards of **catAZT** and **bix** at concentrations ranging from 20 to 450 µM and 40 to 890 µM, respectively ($R^2 > 0.999$). The wavelength of the UV detector was set simultaneously at 214 and 280 nm to match the maximum absorptivity of

bix and **catAZT** respectively. Then, known amounts of **catAZT-NCPs** were dissolved in an acidic HCl/CH_3OH solution and injected into the HPLC system. Peaks corresponding to **catAZT** were then integrated and its concentration determined by interpolation with the previous calibration curve. Finally, a loading content of 25 wt% of AZT (44 wt% **catAZT**) was calculated using this data. Representative chromatograms for both standards and NCPs samples can be found in figure 3.9.

Considering all data about **catAZT-NCPs** showed above, an empirical formula was adjusted by iterative fit of the ligand stoichiometry using a software developed in our research group. This software determined the optimal empirical formula that minimized the error with experimental CHNS % values while being simultaneously in agreement with all the experimental data showed above. Thus, $FeC_{43.9}H_{54.3}N_{10.0}O_{15.0}$., adjusted to $[Fe(catAZT)_{1.5}(bix)_{0.6}(AcO)(H_2O)_{2.4}]$ was proposed as a plausible fit, with an error lower than 0.3% in elemental analysis data and 0.02% in Fe content.

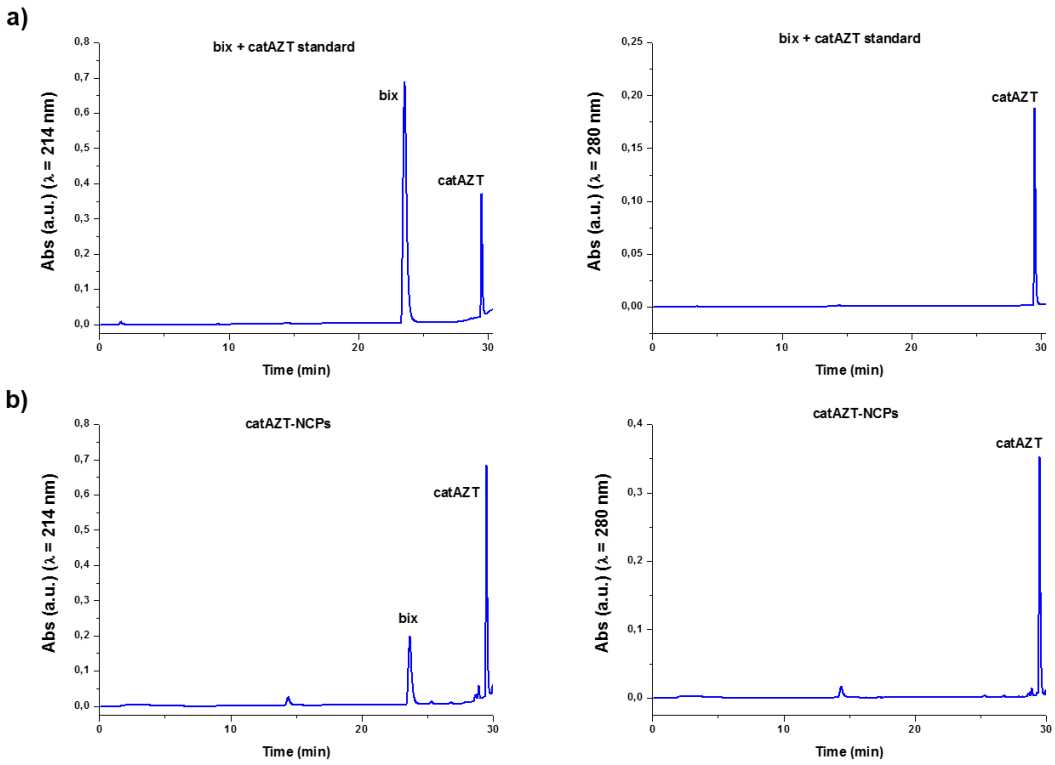

Figure 3.9. Representative chromatograms of a) standards containing bix (675 µM) and **catAZT** (346 µM) and b) **catAZT-NCPs** (311 µg/mL) dissolved in a mixture of HCl/CH_3OH (50 µL concentrated HCl/mL CH_3OH). Detection was made by UV detector at 214 and 280 nm.

Mössbauer spectroscopy, which relies in the absorption and emission of gamma rays in solid phase and it is especially useful for the analysis of iron complexes, was used to determine the electronic state of iron inside the NCPs coordination network. Although the original source of iron was an Fe^{2+} salt, the complex was shown to be stabilized as high-spin Fe^{3+}. This electronic modification results from a redox interplay between the metal ion and electroactive catechol ligands in air, as previously reported.[10] The presence of iron within the NCPs structure allowed, at first, the possibility of a multifunctional character as magnetic resonance imaging (MRI) contrast agent.[11,12] Although this technique possesses low sensitivity and specificity, contrast agents are able to improve image resolution by modifying the relaxation times of water protons under a magnetic field and their selective accumulation in certain regions. Contrasts agents are classified into two groups, positive ones, which are usually based on paramagnetic metal ions such as Gd^{3+} or Mn^{2+} and reduce longitudinal (T_1) relaxation times and negative ones, which mainly involve super-paramagnetic iron oxide compounds and reduce transversal (T_2) relaxivity. To confirm this character for the **catAZT-NCPs** system, magnetic resonance relaxometry experiments were performed at different concentrations under an external magnetic field of 7 Teslas and in two phantom sequences. The particles were dispersed in PBS/agarose 1% pH 7.4 solution and the obtained relaxation rate values were plotted against iron concentration (figure 3.10).

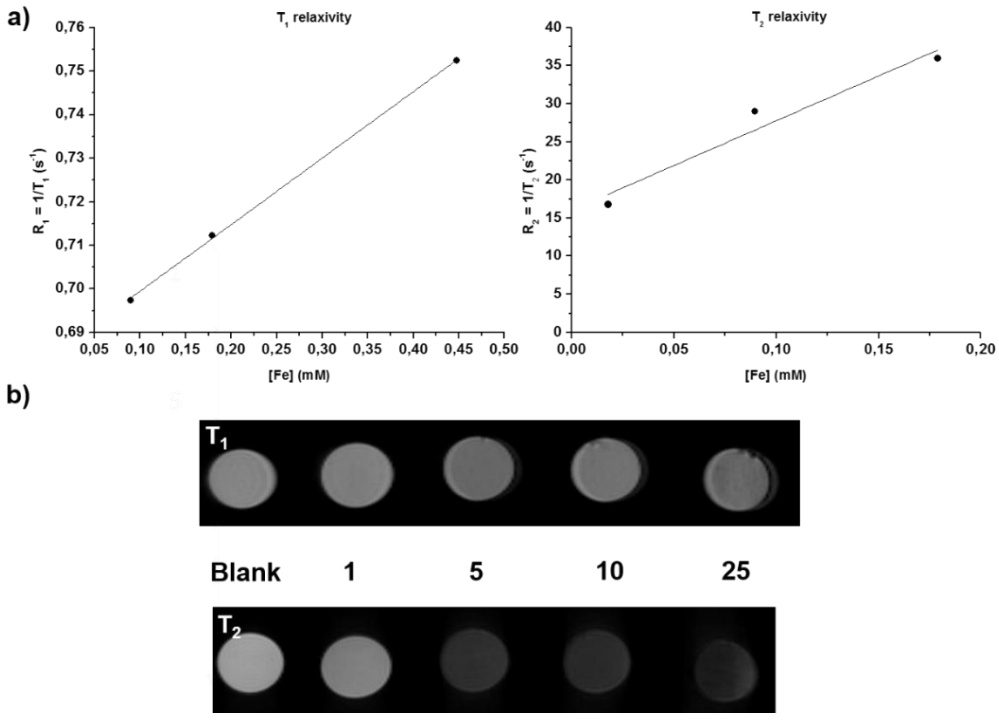

Figure 3.10. a) Results of the magnetic resonance relaxivity experiments with **catAZT-NCPs**. The relaxation rates were measured related to [Fe]. Plot of R_1 ($1/T_1$) and R_2 ($1/T_2$) in front of total [Fe]. b) ^{1}H MRI T_1 and T_2 phantom maps of **catAZT-NCPs** in a PBS/agarose 1% solution at pH 7.4 at different concentrations (0, 1, 5, 10 and 25 mM, referred to Fe concentration).

The NCPs displayed signal enhancement depending on concentration with a T_1 positive contrast of r_1 = 0.15 $mM^{-1}s^{-1}$ and T_2 negative contrast of r_2 = 117.5 $mM^{-1}s^{-1}$. Interestingly, they exhibited low r_1 in comparison to the commonly used gadolinium contrast agents (i. e. Gd-DTPA; r_1 = 3.3 $mM^{-1}s^{-1}$) or other related iron-based NCPs synthesized in our research group (r_1 = 4.4 $mM^{-1}s^{-1}$).[13,14] Similar low r_1 values were recently reported for Gd-based NCPs and attributed to a low water accessibility to metal ion.[15] On the other hand, **catAZT-NCPs** presented a high T_2 negative contrast, related to the interaction with water molecules out of the first coordination sphere. These values make **catAZT-NCPs** very promising as a T_2 contrast agent with r_2 relaxivities nearly 25 times higher than those of commercial Gd-DTPA.

3.3 Synthesis of catTHY and catTHY-NCPs

3.3.1 Synthesis of catTHY

3.3.1.1 Synthesis of ((2*R*,3*S*,5*R*)-3-hydroxy-5-(5-methyl-2,4-dioxo-3,4-dihydropyrimidin-1(2*H*)-yl)tetrahydrofuran-2-yl)methyl 6-(3,4-bis((tert-butyldiphenylsilyl)oxy)phenyl)hexanoate, 15.

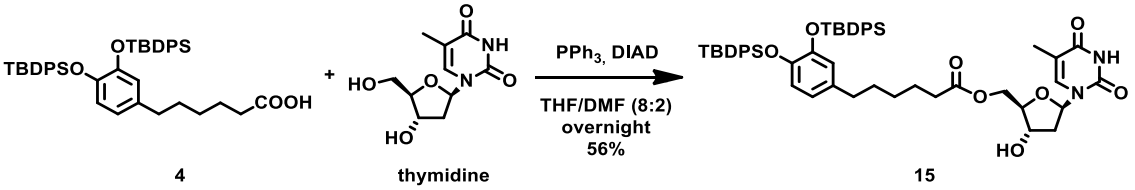

The synthesis of **catTHY** was envisioned for comparison purposes. Thymidine was selected because it is the endogenous analogue of AZT and, therefore, NCPs comparable in morphology, chemical composition, colloidal stability or release kinetics were expected to be formed using either **catAZT** or **catTHY**. At the end, the fact that thymidine is not active against HIV would make **catTHY-NCPs** an excellent blank for the in vitro testing of anti-HIV activity.

Synthesis of **catTHY**, was also envisioned from the common intermediate **4**, following the sequence described in the section above. However, initial attempts to perform the coupling of **4** and thymidine using a similar approach to the one described above for **catAZT** were unsuccessful. Additional tests using stablished coupling methodologies (HATU, EDCI, HOBt or CDI) also met with failure, as only starting material or activated carboxylic acid species were obtained. Then, it was found that similar reactions, that is, coupling of thymidine to different carboxylic acids, were completed under Mitsunobu conditions (scheme 3.14).[16-19] Therefore, the use of PPh_3 and diisopropyl azodicarboxylate (DIAD) under a mixture of dry THF and DMF to solubilize all the reagents afforded compound **15** in 56% yield.

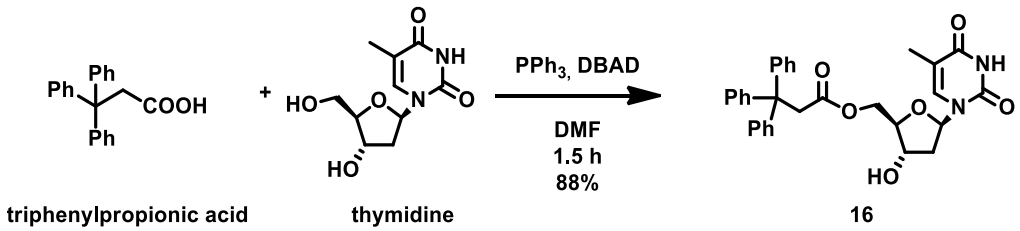

Scheme 3.14. Representative example of the esterification of thymidine and a carboxylic acid using Mitsunobu methodology, extracted from reference 16.

3.3.1.2 Synthesis of ((2*R*,3*S*,5*R*)-3-hydroxy-5-(5-methyl-2,4-dioxo-3,4-dihydropyrimidin-1(2*H*)-yl)tetrahydrofuran-2-yl)methyl 6-(3,4-dihydroxyphenyl)hexanoate, catTHY.

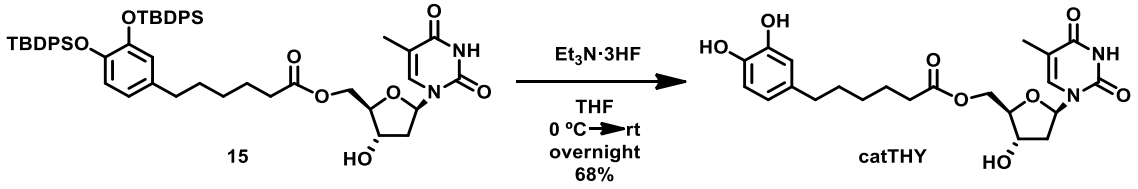

With conjugate **15** in hands, the removal of its silyl protecting groups was performed using the same well-stablished methodology as in **catAZT**.[3] Thus, the addition of triethylamine trihydrofluoride to **15** in dry THF afforded a more polar compounds, which was identified as target molecule **catTHY** after purification by column chromatography. In summary, the synthesis of catTHY was achieved through a 5-step sequence with 19% overall yield.

3.3.2 Synthesis and characterization of catTHY-NCPs

At this point, NCPs using the ligand **catTHY** were prepared following the optimized methodology for **catAZT-NCPs**. Thus, when **catTHY**, **bix** and iron ions were allowed to self-assemble in an ethanolic solution in the presence of polyvinylpyrrolidone as stabilizing agent, a dark-purple precipitate was obtained and identified as **catTHY-NCPs** (scheme 3.15).

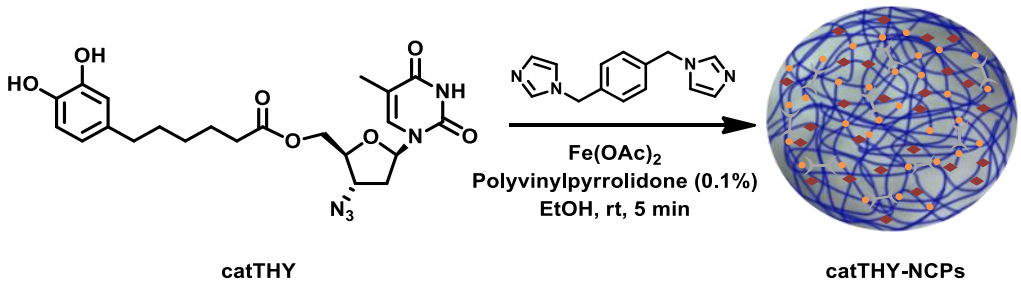

Scheme 3.15. Schematic synthesis of **catTHY-NCPs** using polyvinylpyrrolidone as stabilizing agent.

These nanoparticles showed comparable physicochemical features to those of **catAZT-NCPs**; for example, an average diameter of 87 ± 26 nm was measured by SEM micrographs, while DLS

measurements displayed a hydrodynamic diameter of 172 ± 2 nm in ethanol and 192 ± 10 nm in PBS/BSA 0.5 mM buffer (figure 3.11, a, b and c). FTIR spectra confirmed the coordination of **bix** and **catTHY** to the metal ions, as characteristic bands for **bix** (1512, 1239 and 1101 cm^{-1}) as well as a strong carbonyl band at 1658 cm^{-1} attributed to **catTHY** were observed. ^{1}H NMR spectra of dissassembled **catTHY-NCPs**, measured in an acidic solution of deuterated methanol, showed the presence of the characteristic peaks of **catTHY**, **bix** and acetate ions and allowed the determination of the **catTHY**/**bix** ratio by the integration of their characteristic signals, which averaged 2.2 among different batches of **catTHY-NCPs** (figure 3.11, d). Elemental analysis of **catTHY-NCPs** displayed a good reproducibility in chemical composition among different independent batches of nanoparticles. Considering this data, an empirical formula was adjusted by iterative fit of the ligand stoichiometry using a software developed in our research group. Thus, the empirical formula $FeC_{63.4}H_{113.2}N_{8.4}O_{39.0}$ minimized the error with experimental CHNS % values while in agreement with the rest of the data obtained for **catTHY-NCPs**. Lastly, this formula was adjusted to Fe(**catTHY**)$_{2.18}$**bix**$(AcO)_{0.7}H_2O)_{20.2}$; which also presented deviation from the expected stoichiometry of two **catTHY** and one **bix** bridging ligand per metal ion.

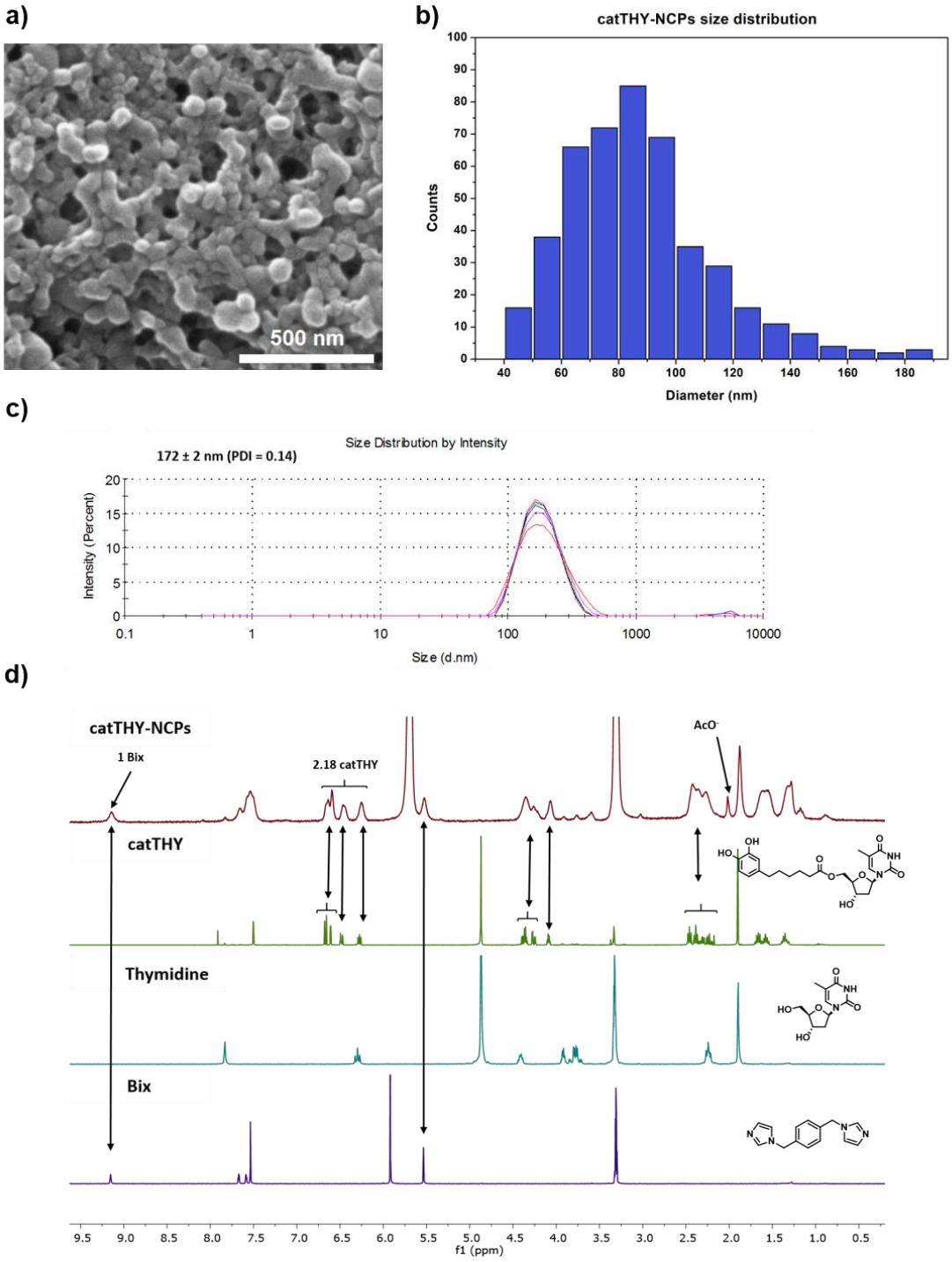

Figure 3.11. a) Representative SEM images of **catTHY-NCPs**. b) Histogram of particle sizes extracted from SEM micrographs (457 particles, mean size 87 ± 26 nm). c) DLS measurements of **catTHY-NCPs** particle size in ethanol. d) ^{1}H NMR spectra of (top to bottom) disassembled **catTHY-NCPs**, **catTHY**, thymidine and **bix**. All spectra were recorder in DCl/CD_3OD (50 µL DCl/mL CD_3OD). Peaks corresponding to **catTHY**, **bix** and acetate are observed in the ^{1}H NMR spectrum of **catTHY-NCPs**.

3.4 Quantification of drug release in catAZT-NCPs and biological evaluation

3.4.1 Drug release profile determination in catAZT-NCPs

The release of AZT from the NCPs was envisioned as a two-step process (figure 3.12). The first one would involve the release of **catAZT** from the nanoparticles as a result of their gradual degradation in aqueous media, while subsequent transformation of **catAZT** into the drug AZT would be promoted by enzymatic cleavage due to endogenous esterases.[20]

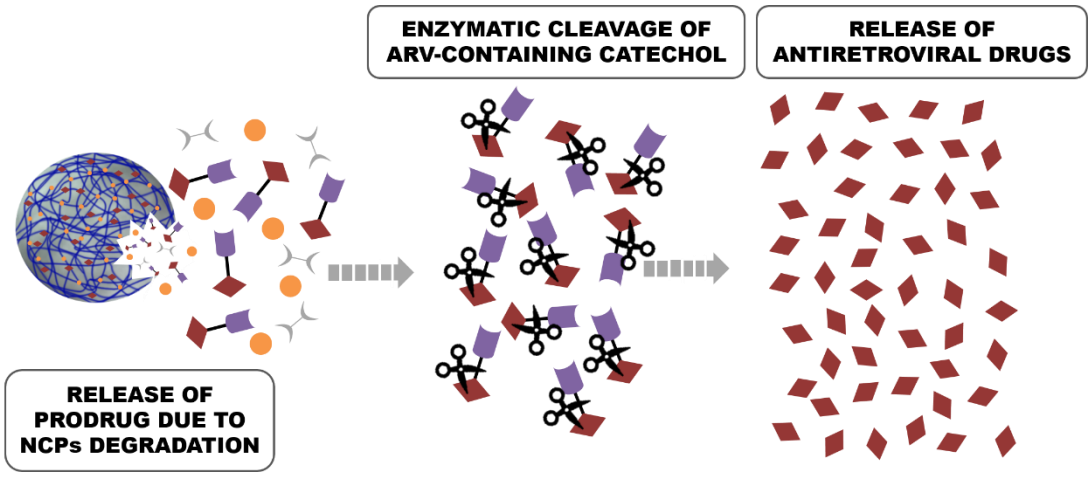

Figure 3.12. Scheme of the AZT release process, involving a first step of NCPs degradation followed by enzymatic cleavage of released **catAZT** into the active drug.

One of the first challenges in AZT release profile quantification arose from the fact that, unlike previous NCPs drug release modelling done in our research group, AZT does not present fluorescence. For example, NCPs containing a red-fluorescent benzophenoxazine dye as model drug were previously prepared in our research group for the study of the different release mechanisms in NCPs.[21] During these studies, the concentration of the drug released in the different aliquots was easily determined by fluorescence measurements in an unequivocally manner, as the only fluorescent species was the model dye. These approach, however, could not be applied to AZT, and it urged to create an analytical methodology in which AZT signal could be unequivocally quantified among degradation by-products. Therefore, high-performance liquid chromatography (HPLC) coupled to a UV detector was chosen. Previous to the determination of the kinetics according to the whole process (figure 3.12), the enzymatic hydrolysis of pure **catAZT** was studied. Thus, **catAZT** was incubated in a simulated physiological media, consisting of a PBS/BSA 0.5 mM buffer at 37 °C at neutral pH (7.4) or acidic pH (5.1), in

the presence or absence of model esterases (pig liver esterase, PLE) at a concentration comparable to that found inside the body (180 U/L).[20] Aliquots were taken after different periods of time and filtered through a 10 kDa membrane before injection into the HPLC system. Using a phase-reversed C18 column, an HPLC methodology was developed in order to separate AZT from **catAZT** and also from other products of **catAZT-NCPs** degradation, namely **bix** and catechol-containing carboxylic acid **3** . Detector wavelength was set to 275 nm because the maximum UV absorbance of the species lay on that region, except **bix,** which does not absorb at all at that wavelength. Therefore, external standards containing **catAZT**, **AZT** and **3** were prepared and HPLC parameters, involving mobile phase composition and flow rate were modified in a systematic approach until an acceptable chromatographic resolution was accomplished for all three species. Initially, separation was achieved using an isocratic elution, i.e., maintaining the composition of the mobile phase constant throughout the analysis. Nevertheless, the method was fine-tuned using solvent gradients to reduce analysis runtime, which was especially important due to the large number of samples analyzed (figure 3.14, top). Using these chromatographic conditions, calibration curves using standards containing AZT, **3** and **catAZT** at concentrations ranging from 1 to 1800 µM were successfully prepared integrating the corresponding peak area for each analyte ($R^2 \geq 0.99$) (figure 3.13).

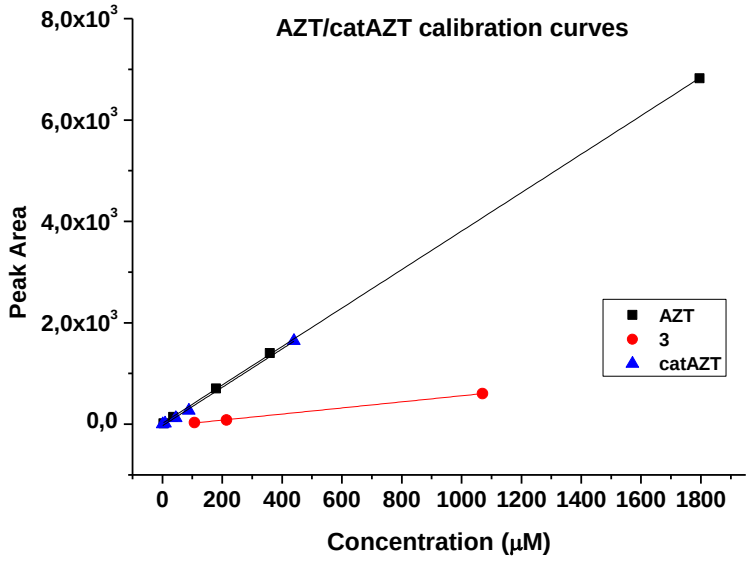

Figure 3.13. Calibration curves prepared using standards containing AZT, **3** and **catAZT** (n = 5, $R^2 \geq 0.99$).

Next, aliquots resulting from **catAZT** incubation at different conditions were then analyzed using this optimized HPLC methodology (figure 3.14, bottom). Chromatographic peaks were integrated, and concentration was determined by interpolation with the corresponding

calibration curves. A representation of the amount of AZT released at different time intervals, in the presence or absence of esterases can be found in figure 3.15. The data is presented as % of antiretroviral drug released versus time. This % of release drug was calculated as follows: for each point, a concentration of AZT, determined by interpolation with its corresponding calibration curve, was divided by the AZT concentration at the completion of the hydrolysis. These values were extracted by triplicate from incubation aliquots acidified with HCl.

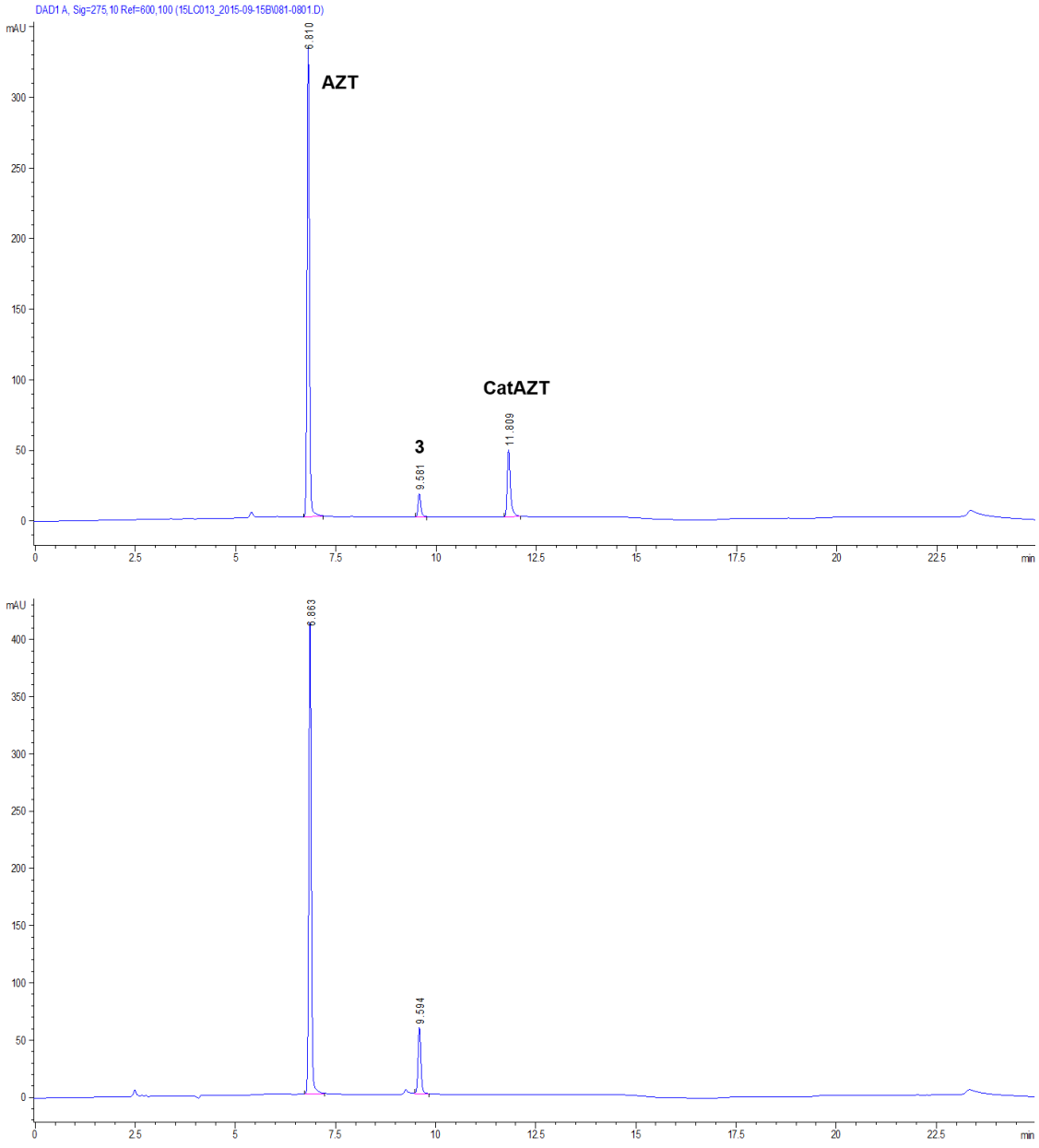

Figure 3.14. (top) Representative chromatogram of a standard containing AZT, **XX3** and **catAZT** at 360, 214 and 89 µM, respectively. (bottom) Representative chromatogram of **catAZT** incubation at 37 °C in the presence of esterases, t = 211 min. $\lambda_{detector}$ = 275 nm.

As shown in figure 3.15, in the absence of pig liver esterase and independently of the pH used, there was almost no hydrolysis of the ligand (~35% in 72 h, pH 7.4). On the other hand, addition

of PLE under the same experimental conditions resulted in a fast release of the antiviral drug (~90% in 1 h). The release profiles for both pH 5.1 and 7.4 offered similar results, indicating weak dependence of the enzymatic activity on pH.

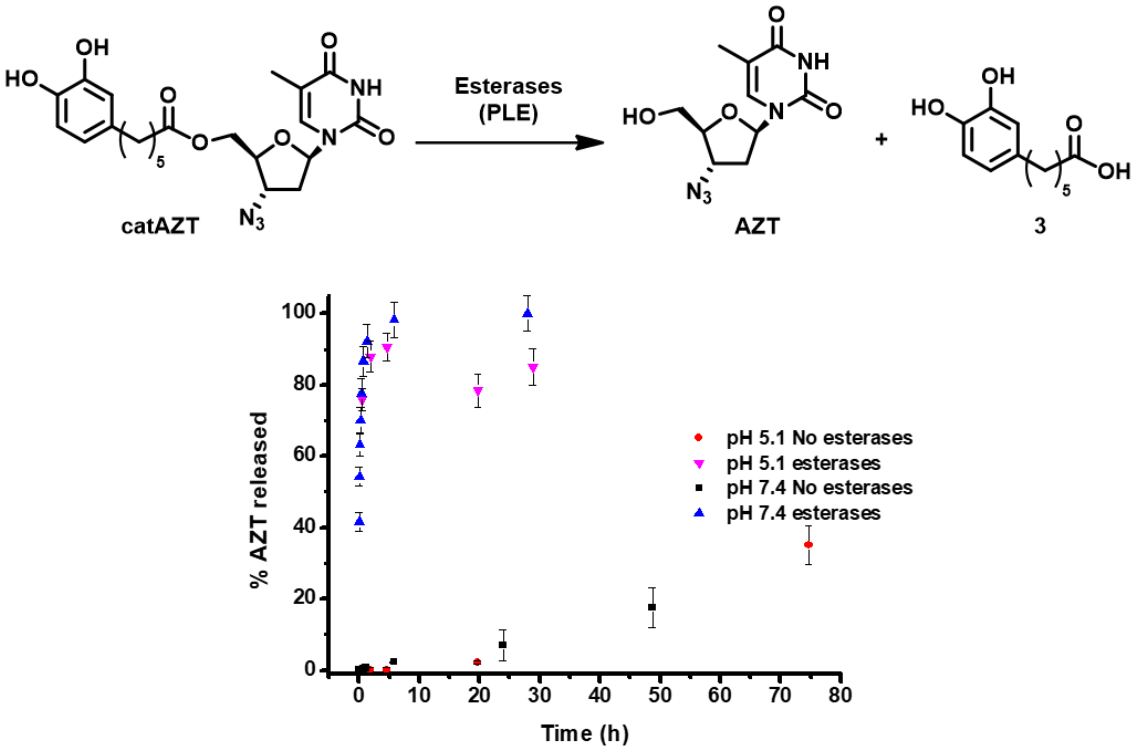

Figure 3.15. Hydrolysis kinetics of **catAZT** in the absence (no esterases) or presence (esterases) of pig liver esterases (PLE) at the indicated pH values. In all cases, experiments were performed by duplicate in PBS/BSA 0.5 mM buffer at 37 °C. (top) Schematic representation of the enzymatic cleavage of **catAZT** by PLE.

Once the behavior of **catAZT** under incubation conditions was understood, the study moved on the determination of AZT release from the NCPs, summarized on figure 3.16. First experiments were conducted to determine the kinetics of **catAZT** release (step 1) using the same previous HPLC methodology for the study of **catAZT** hydrolysis. In this way, NCPs were incubated at 37 °C in PBS/BSA 0.5 mM buffer solution at pH 5.1 and 7.4. Aliquots were taken at different time periods, filtered through a 10 kDa membrane to eliminate BSA and undegraded NCPs and injected into the HPLC system. Additionally, final aliquots were taken by triplicate and treated with HCl in methanol to completely disintegrate the NCPs, which set the 100% release reference value. First experiments in the absence of esterases at pH 7.4 showed no detectable presence of **catAZT**, indicating high stability of the coordination polymer at this pH. However, significant amounts were found at the lowest pH of 5.1, even at early stages of the release, due to the lower stability of coordinative bond between iron and catechol al low pH values. This pH-triggered release of the **catAZT** ligand could favor the release inside the cells (that is, acidic pH present in

lysosomes),[22] decreasing toxicity-associated side effects. Independent of pH and in absence of esterases, the presence of free AZT was low (~15% at 72 h). Overall, the release rates are sufficient for NCPs to circulate throughout the body at physiological pH, enhancing their biodistribution. Completely different results were obtained in the presence of the model esterase PLE (180 U/L). In this case, AZT release appeared to be faster, reaching almost 100% after 50 hours, with estimated half-lives of ~4.5 h (pH 5.1) and ~10 h (pH 7.4). These results confirmed that the enzymatic hydrolysis was faster, as previously described for the free **catAZT** ligand. Moreover, it was confirmed that nanostructuring protects the **catAZT** ligand from rapid hydrolysis. Meanwhile, for the free **catAZT**, complete AZT release was achieved at 10 h in the presence of esterases; 100% hydrolysis of **catAZT** loaded into NCPs required much longer time (*ca.* 50 h). This experimental observation corroborates the protective ability of NCPs, as the release of **catAZT** was proposed as limiting step for the antiretroviral release process.

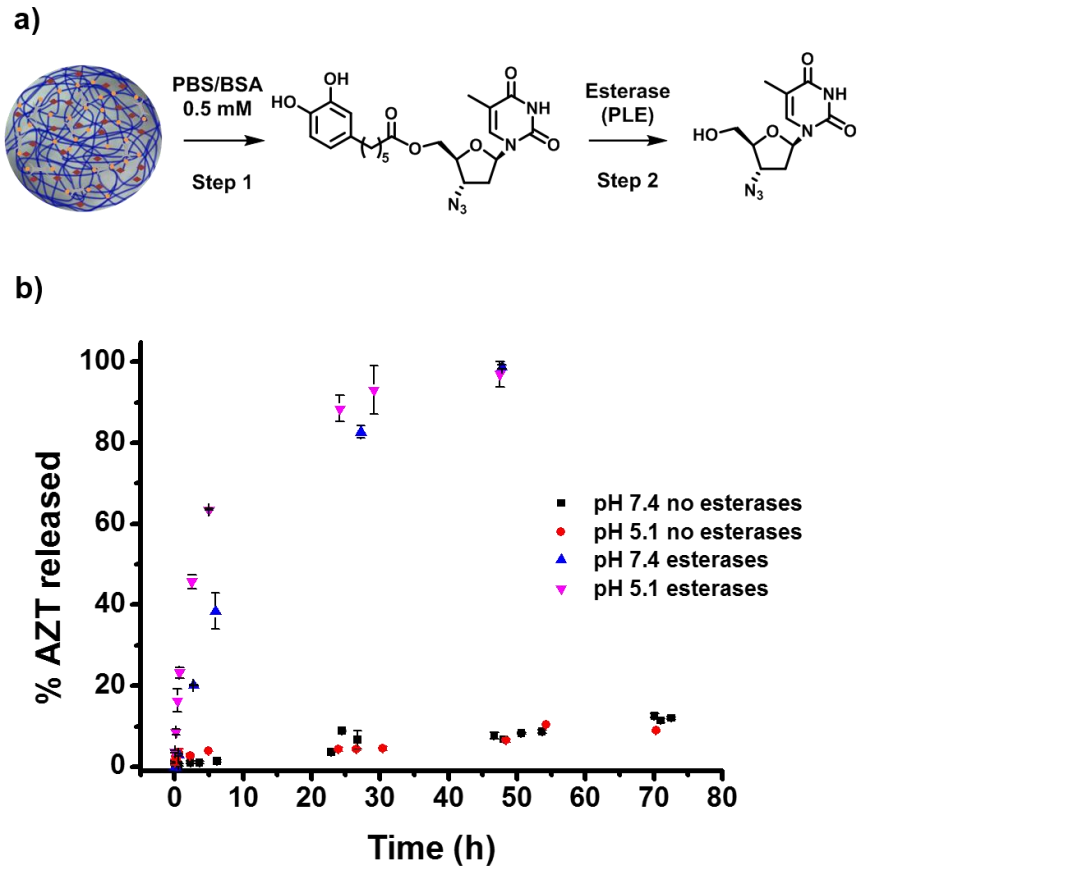

Figure 3.16. a) AZT release process involving NCPs degradation (step 1) and subsequent enzymatic hydrolysis of **catAZT** (step 2). b) AZT release kinetics from **catAZT-NCPs** in the absence (no esterases) or in the presence (esterases) of pig liver esterase (PLE) at pH 5.1 or 7.4. In all the cases, the experiments were performed in PBS/BSA 0.5 mM buffer at 37 °C.

3.4.2 Cytotoxicity, cellular uptake and anti-HIV activity evaluation

As a final step in the characterization of the NCPs, their cytotoxicity, cellular uptake and anti-HIV activity was evaluated in cellular models. It is worth mentioning that, for the following in vitro characterization, the methodology of **catAZT-NCPs** synthesis was slightly adapted to perform it inside a biosafety cabinet so that all reagents and material were sterilized. As mentioned earlier, colloidal stability is a crucial parameter to control, especially in biological media where it is a common phenomenon.[23] Particle aggregation includes irreversible inter-particular adherence leading to the formation of large clusters and can lead to unreproducible experiments by modifying the cellular uptake and toxicity profile of the studied material.[24]

Although particle size during the synthetic process was controlled by the presence of stabilizers and allowed the particles to be easily dispersed in ethanol, zeta-potential values close to -8.0 mV were obtained for **catAZT-NCPs** dispersed in PBS buffer at pH 7.4. In agreement with such low values, a time-dependent aggregation process was observed that eventually resulted in the sedimentation of the sample even at low-moderate concentrations. The addition of bovine serum albumin (BSA) has been extensively used for dispersing inorganic and polymeric nanoparticles.[25,26] In our case, fluorescence quenching studies of BSA in the presence of NCPs suggested an interaction of particles with the surface of this model protein (figure 3.17). Accordingly, in the presence of such protein, nanoparticles were stable except at very high concentrations (i.e., concentrations >2 mg/mL), where the addition of sucrose is needed.

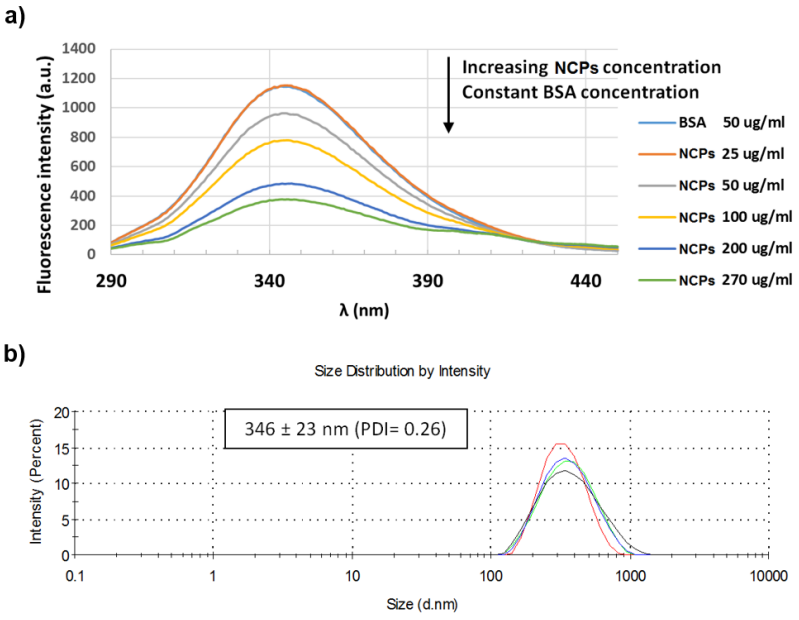

Figure 3.17. a) Study of **catAZT-NCPs** interaction with bovine serum albumin (BSA) by the measurement of the fluorescence quenching of BSA after the addition of different amounts of **catAZT-NCPs**. b) DLS measured of **catAZT-NCPs** particle size in a water/sucrose solution (1:1 ratio).

Toxicity towards lymphocytic function is one of the major considerations in the clinical applicability of novel antiviral compounds. Moreover, it has been extensively demonstrated that AZT is highly toxic to human lymphocytes.[27] Therefore, the cytotoxic effect of **catAZT-NCPs** particles against endogenous human $CD4^+$ T lymphocytes was examined (figure 3.18). Primary $CD4^+$ T cells, isolated from human peripheral blood mononuclear cells (PBMCs) of healthy human donors, were treated for 24 h with **catAZT-NCPs** and free AZT; the latter was used as the reference compound. When the $CD4^+$ T cells were treated with free AZT, a clear cytotoxic effect was observed at concentration of 10 µM (or higher), with an IC_{50} value of 64 µM; whereas the same cells treated with **catAZT-NCPs** displayed irrelevant cytotoxic effects even at the highest concentration tested (500 µM). At this concentration, the nanoparticles maintained a cell viability of 70%, while for free AZT, it was lower than 10% (IC_{50} > 500 µM). These results confirmed that nanostructuration reduced the toxicity of AZT remarkably on primary $CD4^+$ T lymphocytes.

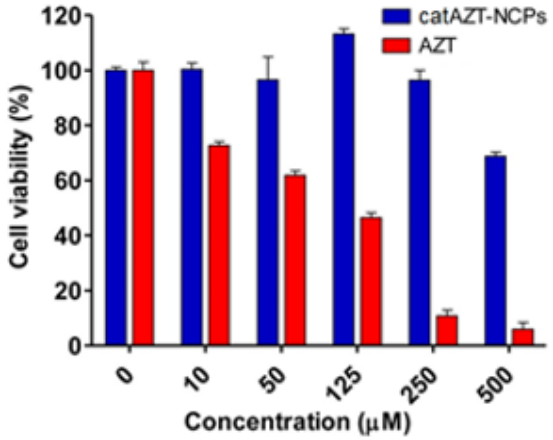

Figure 3.18. Effect of **catAZT-NCPs** and free AZT on the cell viability of human primary $CD4^+$ T lymphocytes. $CD4^+$ T cells were incubated during 24 h in the presence of the indicated concentrations of **catAZT-NCPs** or AZT. Cell viability is expressed as percentage compared to an untreated control. Values are mean ± standard error of the mean (SEM) (n = 3).

Cellular uptake and antiviral activity of all synthesized nanoparticles and control molecules were tested on a model MT-2 human lymphocytic cell line (purchased from NIH AIDS Reagent Program) by means of an MTT assay in a biohazard P3 laboratory specially prepared for it. MT-2 cells is an established cell line of $CD4^+$ T cells, which is easier to manipulate and obtain than primary human cells; thus, it is suitable for first line studies of anti-HIV effect and therefore broadly used to test the efficacy of experimental antiviral agents due to its high reproducibility.[28-30] HIV-1 exerts a profound cytopathic effect (CPE) against $CD4^+$ T lymphocytes. Once infected, the lymphocytes accumulate viral DNA and actively produce HIV proteins, which

results in the concomitant lysis of such infected cells apoptosis. MT-2 cells are profoundly sensitive to the CPE of HIV-1.

The therapeutic efficacy of an anti-HIV drug depends on its intracellular concentration, which in turn is directly related to its uptake kinetics (in addition to other factors such as its metabolism and/or cellular efflux).[31,32] To assess this parameter, MT-2 cells were incubated for 4 hours in the presence of different concentrations of **catAZT-NCPs** (AZT and **catAZT** were also used as model compounds). After this time, cells were lysed, and the amount of intracellular AZT was determined by HPLC-UV as follows. As before, the HPLC analytical methodology was optimized in a systematic approach. In this way, standards containing **catAZT** and AZT were analyzed using a reversed-phase HPLC column and UV-Vis detection. Mobile phase composition, solvent gradients and flow rate were fine-tuned in order to achieve acceptable resolution between the analytes. Then, calibration curves for **catAZT** and AZT were prepared using a series of standards at concentration ranging from 10 to 100 μM for AZT and from 40 to 250 μM for **catAZT** (R^2 > 0.999). After, the samples containing lysed cells were analyzed following the same methodology, and intracellular concentration of AZT was determined by interpolation of its corresponding peak area with the calibration curve (figure 3.19, a). This data was then divided by the total number of cells in each incubation sample to express it as nmol AZT per 10^6 cells.

The results showed that the intracellular levels of AZT up to concentrations of 500 μM (<0.070 nmol per 10^6 cells) were undetectable after AZT or **catAZT** incubation. Only at an extremely high concentration of such compounds of 1000 μM, detectable intracellular levels of AZT (0.81 ± 0.15 and 0.62 ± 0.11 nmol per 10^6 for AZT and **catAZT**, respectively) were measured. Interestingly, concentrations of **catAZT-NCPs** as low as 100 μM (normalized versus the AZT concentration) resulted in detectable intracellular levels of AZT with a significant concentration-dependent increase up to 500 μM (3.48 ± 0.33 nmol of AZT per 10^6 cells) (figure 3.19, b).

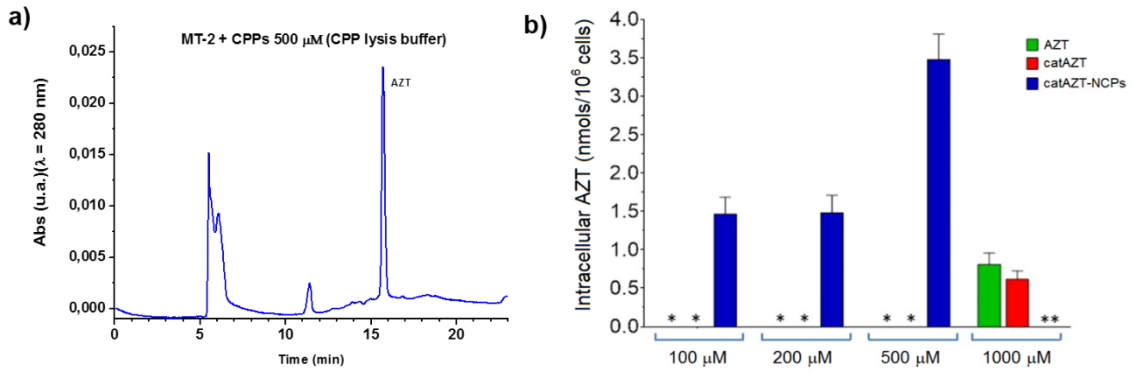

Figure 3.19. a) Representative chromatograms of MT-2 cell lysates incubated with **catAZT-NCPs** 500 µM for 4 hours at 37 °C. b) Intracellular levels of AZT in MT-2 cells after 4 hours of incubation in the presence of different concentration (100 µM, 200 µM, 500 µM, referred to AZT equivalent concentrations) of AZT, **catAZT** or **catAZT-NCPs**. The asterisk (*) indicates those conditions with levels of AZT in the samples under the limit of detection of the method (<0.070 nmol per 10^6 cells). For AZT and catAZT, an additional concentration of 1000 µM was assayed. Please note that this concentration was not assayed for **catAZT-NCPs** (**) because nanoparticles were not stable at concentrations higher than 10 mg/mL.

Considering the detection limit of the HPLC method used for quantification as a reference (<0.070 nmol per 10^6 cells), it can be easily estimated that treatment with the nanostructured material resulted in >50-fold increase at 500 µM in comparison with free AZT. This could potentially be due to the mechanism of uptake. Nanoparticles are generally taken up by endocytosis mechanisms as opposed to small molecules, which are taken up by other pathways.[33-36] In the case of AZT, it has been reported to enter the cells through membranes via passive diffusion and/or by uptake transporters.[37,38] Similar results were observed in a recent report, in which a nanoformulation of the antiviral drug dolutegravir resulted in higher uptake by human monocyte-derived macrophages in comparison with the free molecule.[39] It is worth mentioning that cellular dolutegravir reached maximum at 4 h after treatment with 100 µM of the nanoformulated drug.

Regarding the anti-HIV activity determination of **catAZT-NCPs** and control molecules, cytotoxicity on non-infected human MT-2 lymphocytes was determined first (figure 3.20). No appreciable cytotoxicity was observed for any of the antiretroviral agents at concentrations of 20 µM (normalized versus AZT concentration) or lower after 3- or 7-day incubation except for the highest concentration tested (100 µM), which showed reduced cell viability for all compounds except for the saccharose blank.

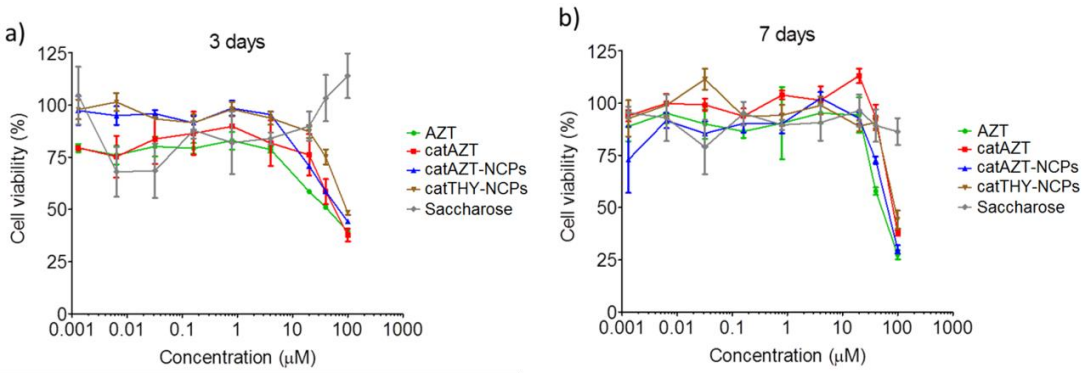

Figure 3.20. Cytotoxic effects of **catAZT-NCPs** against MT-2 lymphocytes. Cytotoxicity of **catAZT-NCPs** and equivalent concentrations of AZT, **catAZT**, **catTHY-NCPs** and saccharose (vehicle) on MT-2 cell viability assessed by the MTT assay. Cell viability is expressed as percentage compared to an untreated control at a) 3 days or b) 7 days after applying the compounds. Values are shown as mean ± standard error of the mean (SEM) of two independent experiments performed in triplicate.

When the same experiments were repeated using MT-2 cells infected with the virus, decrease in the cytopathic effect of HIV on human MT-2 cells was observed in the cultures treated with AZT, **catAZT** and **catAZT-NCPs** for 3- and 7-day treatments (figure 3.21). In particular, a substantial increase in cell viability was observed after three days following the order AZT > **catAZT-NCPs** > **catAZT**. The most efficient antiviral response was obtained for free AZT (followed closely by that with **catAZT-NCPs**), which recovered cell viability within the 0.16-40 μM concentration range and with a maximum antiviral activity centered at 4 μM. At this concentration, the efficiency of **catAZT-NCPs** was slightly but non-significantly inferior to that of AZT, whereas the ligand **catAZT** showed the lowest activity. Control systems, **catTHY-NCPs** and saccharose, did not show any significant effect. Interestingly, when the same experiment was evaluated after seven days of incubation, the relative activities of AZT and **catAZT-NCPs** were very similar due to the accumulated long-lasting release effect of the nanoparticles, whereas the difference in activity with **catAZT** ligand became more evident. As observed, the mechanisms for extended half-life of the present nanosystems lie beyond its structural properties. Nanostructuring provides longer release rates for AZT with reduced peak concentrations, reflecting controlled release of the drug from the nanoparticles while the inhibition efficiency of nanostructured AZT is very similar to free drug. This study shows a methodology to achieve long-acting ARVs that can offer effective drug concentrations and prevention of viral resistance patterns. Additionally, NCPs exhibit enhanced cellular entry, forming intracellular drug depots that provide sustained and effective drug release and long-term protection against HIV, as observed in a recent publication that reported similar conclusions using a nanoformulation based on an injectable drug currently in clinical trials.[40]

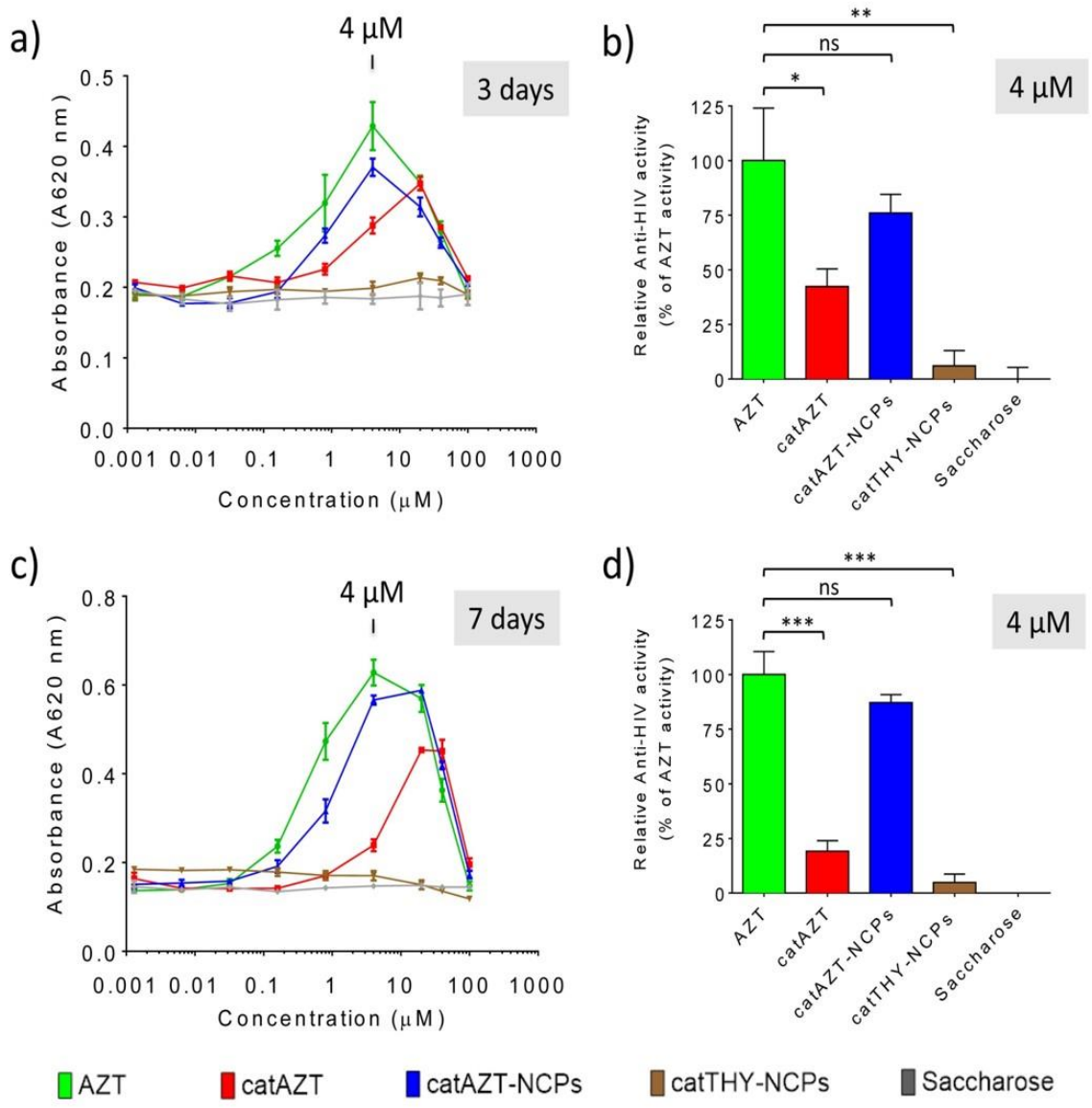

Figure 3.21. HIV-antiviral activity. Cell viability of different concentrations of AZT, **catAZT**, **catAZT-NCPs** and **catTHY-NCPs** on HIV-infected MT-2 cell culture after 3-day (a, b) and 7-day (c, d,) incubation. The cytopathic effect of HIV (decrease in cell viability) is observed after incubating HIV-infected MT-2 cells with the compounds with no antiviral effect (**catTHY-NCPs** and saccharose). The antiviral effect of the compounds was indirectly measured as an increase in cell viability (increase in absorbance ay 620 nm), as shown when incubating HIV-infected MT-2 cells in the presence of AZT, **catAZT-NCPs** or **catAZT** (a, c). (b, d) Relative anti-HIV activity expressed as percentage compared to the absence of activity (saccharose); maximal anti-viral activity in the assay was determined for the most effective concentration of AZT (4 µM) after (b) 3-day or (d) 7-day incubation. An unpaired *t*-test was performed to compare anti-HIV efficacies of the compounds at 4 µM compared to the reference compound AZT. Please note that the anti-HIV efficacy of **catAZT-NCPs** was similar to that of AZT, whereas the effects of the prodrug **catAZT** and the control **catTHY-NCPs** were significantly lower. ns, non-significant; * $p < 0.05$; ** $p < 0.01$; *** $p < 0.0001$.

3.5 Summary and conclusions

To sum up, novel iron-catechol-based nanoscale coordination polymers that incorporate a prodrug molecule tethered to a catechol ligand were designed and successfully synthesized. As

a proof-of-concept, AZT, a well-known antiretroviral drug, was linked through an enzymatically cleavable ester bond to a catechol moiety (**catAZT**) in a 5-step synthetic sequence with an overall yield of 32%. The presence of a chelating catechol group allowed reproducible incorporation of **catAZT** with high payloads within the coordination polymer nanoparticles of 147 ± 33 nm average size. Following this approach, the effective antiretroviral activity of free AZT was successfully reproduced, while, at the same time, nanostructuration allowed the following significant advantages: i) stabilization of the drug in physiological media as a colloidal suspension; ii) control over the release properties of the drug by pH and the presence of enzymes; iii) inherent multifunctionality of particles due to the presence of iron ions with MRI responses; iv) significant reduction in AZT toxicity and v) enhancement of cellular uptake (up to 50-fold increase.

According to these results, the tethering of active drugs as coordinating ligands represents a novel but promising family of carriers to optimize pharmacological characteristics of known antiretroviral drugs with controlled release while substantially minimizing side effects derived from systemic toxicity effects. It is expected that these new class of nanocarriers will have the capacity to address challenges associated with delivering drug combinations, increasing bioavailability in tissue sanctuaries and latently infected cells, and improving cellular uptake contributing to the development of the next generation of pharmacological strategies for HIV treatment. Specifically, the extension of this approach to the delivery of drug combinations will be explored in the next chapter.

3.6 Experimental section

Characterization Methods. 250 MHz ^{1}H NMR spectra were recorded on a Bruker DPX 250 MHz spectrometer; 360 MHz ^{1}H NMR, ^{1}H-^{1}H COSY, ^{1}H-^{13}C HSQC, ^{1}H-^{13}C HMBC, DEPT135 and 100 MHz ^{13}C NMR were recorder on a Bruker DPX 360 MHz spectrometer; 400 MHz ^{1}H NMR, ^{1}H-^{1}H COSY, ^{1}H-^{13}C HSQC, ^{1}H-^{13}C HMBC, DEPT135 and 100 MHz ^{13}C NMR spectra were recorded on a Bruker DPX 400 MHz spectrometer. Chemical shifts (δ) are given in ppm, using the residual non-deuterated solvent as internal reference. Signal multiplicities are described using the following abbreviations: singlet (s), doublet (d), triplet (t), quartet (q), quintet (quint), doublet of doublets (dd), doublet of triplets (dt), doublet of doublet of doublets (ddd), multiplet (m) and *J* to indicate the coupling constant (Hz). High-resolution mass spectra were obtained by direct injection of the sample with electrospray techniques in a Bruker microTOF-Q instrument. SEM images were performed on a scanning electron microscope (FEI Quanta 650 FEG) at acceleration voltages of 5–20 kV. The samples were prepared by drop casting of the corresponding dispersion on aluminum tape followed by evaporation of the solvent under room conditions. Before analysis, the samples were metalized with a thin layer of platinum by using a sputter coater (Emitech K550). IR spectra were recorded by using a Tensor 27 (Bruker) spectrophotometer equipped with a single-reflection diamond window ATR accessory (MKII Golden Gate, Specac). Size distribution and surface charge of the nanoparticles were measured by DLS, using a ZetasizerNano 3600 instrument (Malvern Instruments, UK), the size range limit of which is 0.6 nm to 6 mm. Note: the diameter measured by DLS is the hydrodynamic diameter. The samples were comprised of aqueous dispersions of the nanoparticles in distilled water or in buffer. All samples were diluted to obtain an adequate nanoparticle concentration. Powder XRD spectra were recorded at room temperature on a high-resolution texture diffractometer (PANalyticalX'Pert PRO MRD) equipped with a CoKα radiation source (λ = 1.7903 Å) and operating in reflection mode. The solid samples were placed in an amorphous silicon oxide flat plate and measured directly. The longitudinal r1 and transverse r2 relaxation rates for different concentrations of catAZT-NCPs were measured in solution under an external magnetic field of 7 Teslas (Bruker Biospec7T) in two phantom sequences. The nanoprobes were dispersed in PBS/agarose 1% solutions to ensure a good colloidal stability, resulting in a series with different metal concentrations ranging from 1 mg/mL to 25 mg/mL. The obtained relaxation rate values were plotted versus the concentrations of iron.

Synthesis of 6-(3,4-bis(benzyloxy)phenyl)hex-5-enoic acid, **5**.

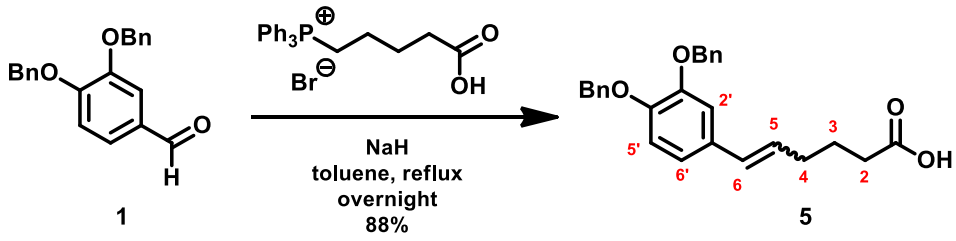

To a 2 h stirred suspension of (4-carboxybutyl)triphenylphosphonium bromide (9.08 g, 20.5 mmol) and NaH (suspension 60% wt) (3.27 g, 81.7 mmol) in dry toluene (50 mL) under N_2 atmosphere, a solution of 3,4-bis(benzyloxy)benzaldehyde, **1**,(6.50 g, 20.4 mmol) in dry toluene (70 mL) was added dropwise. The mixture was then heated to reflux and stirred overnight. TLC analysis (EtOAc 100%) revealed the entire consumption of 3,4-bis(benzyloxy)benzaldehyde. The reaction crude was washed with water (70 mL and 2x30 mL), acidified with HCl (5%) to pH 3 and then extracted with EtOAc (4x60 mL). The combined organic phases were dried over anhydrous Na_2SO_4 and concentrated under vacuum. The resulting brownish wax was purified by column chromatography (CH_2Cl_2/EtOAc, 90:10 → 80:20 → 50:50) to afford a yellow solid identified as a mixture of isomers (5:1 *E*/*Z*) of carboxylic acids **5** (7.21 g, 17.93 mmol, 88% yield); R_f (EtOAc 100%) = 0.40. HRMS (EI) calcd for $[C_{26}H_{26}O_4]^+$ 402.1831, found 402.1829. mp. 70 – 72 °C (CH_2Cl_2/EtOAc).

^{1}H NMR of the major isomer E (400 MHz, $CDCl_3$) δ 7.49 – 7.41 (m, 4H, Ph), 7.39 – 7.29 (m, 6H, Ph), 6.98 (d, $^4J_{2',6'}$ = 1.7 Hz, 1H, H-2'), 6.86 – 6.84 (m, 2H, H-5', H-6'), 6.29 (d, $^3J_{6,5}$ = 15.8 Hz, 1H, H-6), 5.98 (dt, $^3J_{5,6}$ = 15.7 Hz, $^3J_{5,4}$ = 7.0 Hz, 1H, H-5), 5.16 (s, 2H, OCH_2-Ph), 5.14 (s, 2H, OCH_2-Ph), 2.40 (t, $^3J_{2,3}$ = 7.4 Hz, 2H, H-2), 2.24 (qd, $^3J_{4,3}$ = 6.7 Hz, $^3J_{4,5}$ = 6.7 Hz, 2H, H-4), 1.81 (quint, $^3J_{3,2}$ = 7.5 Hz, $^3J_{3,4}$ = 7.5 Hz, 2H, H-3). **^{13}C NMR** of the major isomer *E* (100 MHz, $CDCl_3$) δ 178.20 (C-1), 148.47 (C-3'/C-4'), 147.71 (C-4'/C-3'), 136.70 (C-1'), 130.85 (Ph), 129.79 (C-6), 127.82 (C-5), 127.80 (Ph), 127.77 (Ph), 127.14 (Ph), 127.10 (Ph), 127.07 (Ph), 126.73 (Ph), 126.64 (Ph), 118.99 (C-5'/C-6'), 114.59 (C-6'/C-5'), 112.02 (C-2'), 70.78 (Ph-CH2-O), 32.51 (C-2), 31.49 (C-4), 23.68 (C-3).

Synthesis of 6-(3,4-dihydroxyphenyl)hexanoic acid, 3.

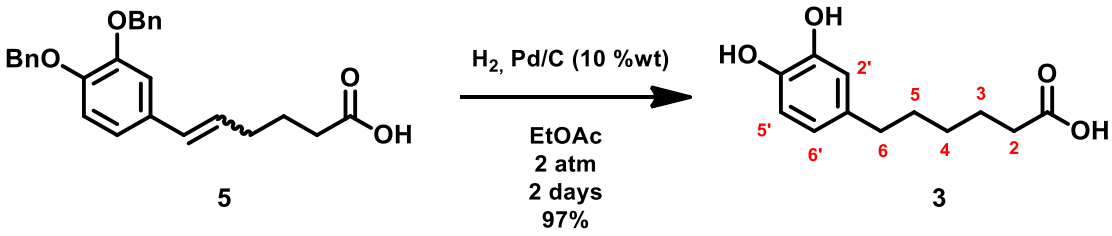

Pd/C (10% wt.) (0.03 g) was added to a solution of the (5:1 *E/Z*) mixture of olefins **5** (0.31 g, 0.76 mmol) in 15 mL EtOAc. H_2 (2 atm) was then introduced into the reaction vessel and the mixture was stirred at rt for 2 days, refilling H_2 pressure every day. After no presence of the benzyl signal was observed at ^{1}H NMR spectrum, the mixture was filtered through Celite® and the resulting brownish solid was purified by column chromatography (EtOAc 100%) to afford a yellow solid identified as the saturated carboxylic acid **3** (0.17 g, 0.74 mmol, 97% yield). R_f (EtOAc) = 0.41. HRMS (EI) calcd for $[C_{12}H_{16}O_4]^+$ 224.1049, found 224.1046. IR (ATR) v 3424, 3180 (broad), 2923, 1707, 1290, 1245, 1196, 1171 cm^{-1} mp. 86 – 88 °C (EtOAc).

^{1}H NMR (400 MHz, acetone-d6) δ 5.45 (d, $^3J_{5',6'}$ = 8.0 Hz, 1H, H-5'), 5.39 (s, 1H, H-2'), 5.25 (dd, $^3J_{6',5'}$ = 8.0 Hz, $^4J_{6',2'}$ = 2.2 Hz, 1H, H-6'), 1.21 (t, $^3J_{6,5}$ = 7.6 Hz, 2H, H-6), 1.03 (t, $^3J_{2,3}$ = 7.5 Hz, 2H, H-2), 0.43 – 0.25 (m, 4H, 2H-3, 2H-5), 0.15 – 0.00 (m, 2H, H-4). **^{13}C NMR** (100 MHz, acetone-d6) δ 175.3 (C-1) 143.20 (C-3'), 141.28 (C-4'), 132.86 (C-1'), 118.04 (C-6'), 113.85 (C-2'), 113.56 (C-5'), 33.36 (C-6), 32.10 (C-2), 29.82 (C-3/C-5), 27.04 (C-4), 23.26 (C-5/C-3).

Synthesis of ((2S,3S,5R)-3-azido-5-(5-methyl-2,4-dioxo-3,4-dihydropyrimidin-1(2*H*)-yl)tetrahydrofuran-2-yl)methyl 6-(3,4-bis(benzyloxy)-phenyl)hex-5-enoate, 6

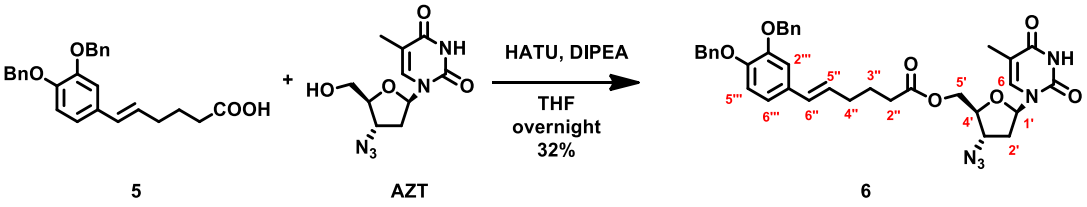

The mixture of carboxylic acids **5** (5:1 *E/Z* mixture), (25 mg, 0.06 mmol), HATU (26 mg, 0.07 mmol) and DIPEA (40 µL, 0.23 mmol) were dissolved in dry THF (0.8 mL) under N_2 atmosphere and stirred at rt. After 35 min, a solution of AZT (15 mg, 0.06 mmol) in dry THF (0.8 mL) was added dropwise. The mixture was stirred overnight at rt. Then, the solvent was removed under vacuum and the crude was purified by column chromatography (hexane/EtOAc 50:50 to 20:80) to furnish **6**, (12 mg, 0.02 mmol, 32% yield) as an oil. **R_f** (Hexane/EtOAc 40:60) = 0.34; **^{1}H NMR**

(250 MHz, $CDCl_3$) δ 8.79 (s, 1H, NH), 7.50 – 7.29 (m, 10H, Ph), 7.19 (d, $^4J_{6,CH3\text{-}C\text{-}5}$ = 1.2 Hz, 1H, H-6), 6.97 (d, $^4J_{2''',6'''}$ = 1.6 Hz, 1H, H-2'''), 6.87 – 6.83 (m, 2H, H-5'''+H-6'''), 6.27 (d, $^3J_{6'',5''}$ = 15.8 Hz, 1H, H-6''), 6.08 (t, $^3J_{1',2'}$ = 6.4 Hz, 1H, H-1'), 5.96 (dt, $^3J_{5'',6''}$ = 15.7 Hz, $^3J_{5'',4''}$ = 7.0 Hz, 1H, H-5''), 5.16 (s, 2H, OCH_2-Ph), 5.15 (s, 2H, OCH_2-Ph), 4.36 (dd, J_{gem} = 12.2 Hz, $^3J_{5',4'}$ = 4.5 Hz, 1H, H-5'), 4.27 (dd, J_{gem} = 12.2 Hz, $^3J_{5',4'}$ 3.9 Hz, 1H, H-5'), 4.13 (dt, $^3J_{3',4'}$ = 7.4 Hz, $^3J_{3',2'}$ = 5.3 Hz, 1H, H-3'), 4.08 – 4.00 (m, 1H, H-4'), 2.51 – 2.17 (m, 6H, H-2' + H-2'' + H-4''), 1.91 (d, $^4J_{CH3\text{-}C\text{-}5,6}$ = 1.2 Hz, 3H, C**H₃**-C-5), 1.82 (quin, $^3J_{3'',2''}$ = 7.27 Hz, $^3J_{3'',4''}$ = 7.27 Hz, 2H, H-3'').

Synthesis of 6-(3,4-bis((*tert*-butyldiphenylsilyl)oxy)phenyl)hexanoic acid, 4.

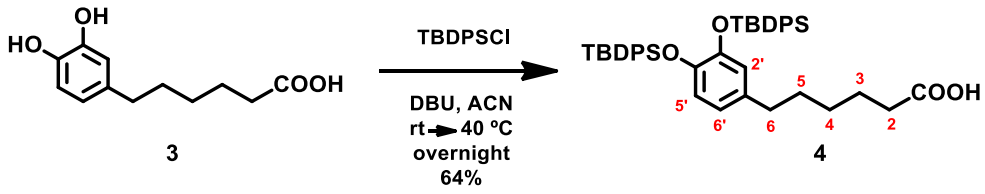

DBU (0.11 mL, 0.74 mmol) was added dropwise to a stirred solution of catechol **3** (0.039 g, 0.17 mmol) and TBDPSCl (0.13 mL, 0.52 mmol) in dry ACN (1 mL) under N_2 atmosphere at rt. After 1 h, the reaction was heated to 40 °C and stirred overnight. Then, the solvent was evaporated, the crude was dissolved in CH_2Cl_2 and washed with NH_4Cl (~ 0.1 M) (3x5mL). The organic layers were combined and dried over anhydrous Na_2SO_4. Evaporation of the solvent furnished a brown waxy crude, which was purified by column chromatography (hexane/EtOAc 90:10 → 60:40) to afford **4** (0.079 g, 0.11 mmol, 64% yield) as a white solid. R_f (Hexane/EtOAc 60:40) = 0.31. HRMS (EI) calcd for $[C_{44}H_{52}O_4Si_2]^+$ 700.3404, found 700.3401. IR (ATR) ν 3071, 2930, 1705, 1513, 1129 cm^{-1}. mp. 50 – 53 °C (hexane/EtOAc).

^{1}H NMR (400 MHz, $CDCl_3$) δ 7.85 – 7.78 (m, 8H, Ph), 7.48 – 7.35 (m, 12H, Ph), 6.34 (d, $^3J_{5',6'}$ = 8.2 Hz, 1H, H-5'), 6.21 (d, $^4J_{2',6'}$ = 2.2 Hz, 1H, H-2'), 6.15 (dd, $^3J_{6',5'}$ = 8.2 Hz, $^4J_{6',2'}$ = 2.2 Hz, 1H, H-6'), 2.17 (t, $^3J_{2,3}$ = 7.6 Hz, 2H, H-2), 2.04 (t, $^3J_{6,5}$ = 7.2 Hz, 2H, H-6), 1.41 (quint, $^3J_{4,3}$ = 7.4 Hz, $^3J_{4,5}$ = 7.4 Hz, 2H, H-4), 1.16 (s, 9H, *t*Bu), 1.15 (s, 9H, *t*Bu), 1.07 – 0.93 (m, 4H, 2H-3, 2H-5). **^{13}C NMR** (100 MHz, $CDCl_3$) δ 179.56 (C-1), 146.01 (C-3'), 144.22 (C-4'), 135.99 (Ph), 135.97 (Ph), 134.88 (C-1'), 133.78 (Ph), 133.70 (Ph), 130.11 (Ph), 130.08 (Ph), 128.07 (Ph), 128.05 (Ph), 120.84 (C-2'), 120.73 (C-6'), 120.23 (C-5'), 34.76 (C-6), 34.06 (C-2), 30.58 (C-3), 28.48 (C-5), 27.13 (TBDPS), 27.09 (TBDPS), 24.71 (C-4), 19.86 (TBDPS).

Synthesis of 6-(3,4-bis((*tert*-butyldiphenylsilyl)oxy)phenyl)hexanoic acid, 4. Basic hydrolysis of 9.

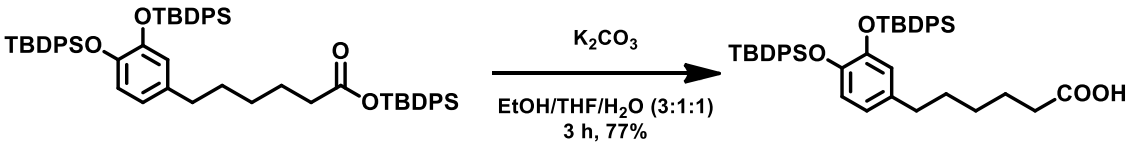

9 4

9 (2.24 g, 2.39 mmol) was dissolved in an EtOH/THF/H_2O mixture (60 mL/20 mL/20 mL) and K_2CO_3 (8.1 g, 58.6 mmol) was added and stirred for 3 h. The crude was acidified to pH 2-3 using HCl 1M and extracted with CH_2Cl_2 (3x100 mL). The organic layers were combined and dried over anhydrous Na_2SO_4. Purification by flash column chromatography (hexane/EtOAc 90:10 → EtOAc 100%) afforded **4** (1.32 g, 1.84 mmol, 77% yield) as a white solid. Physicochemical data of **4** is described above.

Synthesis of ((2*S*,3*S*,5*R*)-3-azido-5-(5-methyl-2,4-dioxo-3,4-dihydropyrimidin-1(2*H*)-yl)tetrahydrofuran-2-yl)methyl 6-(3,4-dimethoxyphenyl)hexanoate, 13.

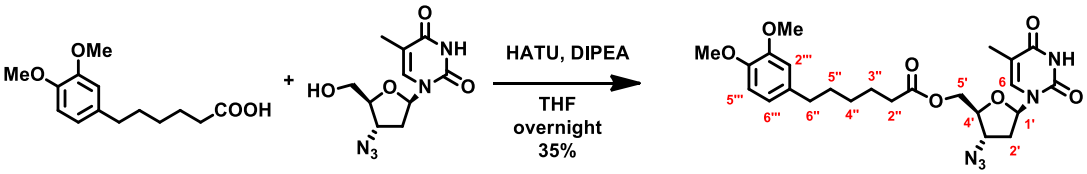

12 AZT 13

Compound **12**, (47 mg, 0.19 mmol), HATU (70 mg, 0.18 mmol) and DIPEA (90 µL, 0.52 mmol) were dissolved in dry THF (1.5 mL) under N_2 atmosphere and stirred at rt. After 35 min, a solution of AZT (41 mg, 0.15 mmol) in dry THF (2 mL) was added dropwise. The mixture was stirred overnight at rt. Then, the solvent was removed under vacuum and the crude was purified by column chromatography (hexane/EtOAc 40:60 to EtOAc 100%) to furnish compound **13**, (27 mg, 0.05 mmol, 35%) as a brownish wax. $\mathbf{R_f}$ (EtOAc) = 0.55. **HRMS** (ESI)$^+$: calculated for $[C_{24}H_{31}N_5O_7+Na]^+$ 524.2116; found 524.2113. **IR** (ATR) ν 2925, 2854, 2104, 1686, 1259, 1234 cm^{-1}. **^{1}H NMR** (400 MHz, $CDCl_3$) δ 7.21 (d, $^4J_{6,CH3\text{-}C\text{-}5}$ = 1.4 Hz, 1H, H-6), 6.78 (d, $^3J_{5',6'}$ = 8.6 Hz, 1H, H-5'''), 6.72 – 6.67 (m, 2H, H-2''' + H-6'''), 6.09 (t, $^3J_{1',2'}$ = 6.3 Hz, 1H, H-1'), 4.37 (dd, J_{gem} = 12.2 Hz, $^3J_{5',4'}$ = 4.6 Hz, 1H, H-5'), 4.30 (dd, J_{gem} = 12.1 Hz, $^3J_{5',4'}$ = 3.9 Hz, 1H, H-5'), 4.16 (dt, $^3J_{3',4'}$ = 7.6 Hz, $^3J_{3',2'}$ = 5.4 Hz, 1H, H-3'), 4.09 – 4.04 (m, 1H, H-4'), 3.87 (s, 3H, OMe), 3.85 (s, 3H, OMe), 2.56 (td, $^3J_{6'',5''}$ = 7.6 Hz, $^4J_{6'',6'''}$ = 1.7 Hz, 2H, H-6''), 2.40 – 2.33 (m, 2H, H-2''), 1.92 (d, $^4J_{CH3\text{-}C\text{-}5,\,6}$ = 1.2 Hz, 3H, C**H**$_3$-C-5), 1.73 – 1.56 (m, 6H, H-2' + H-3'' + H-5''), 1.41 – 1.31 (m, 2H, H-4''). **^{13}C NMR** (100 MHz, $CDCl_3$) δ 173.15 (C-1''), 163.96 (C-4), 150.17 (C-2), 148.91 (C-3'''/C-4'''), 147.25 (C-4'''/C-3'''), 135.50 (C-6), 135.29 (C-5/C-1'''), 135.06 (C-1'''/C-5), 120.24 (C-5'''/C-6'''), 111.86 (C-6'''/C-5'''),

111.84 (C-2'''), 85.75 (C-1'), 81.95 (C-4'), 63.33 (C-5'), 60.78 (C-3'), 56.05 (OMe), 55.96 (OMe), 35.43 (C-6''), 35.38 (C-2''), 33.97 (C-2'/C-3''/C-5''), 31.35 (C-5''/C-2'/C-3''), 28.82 (C-4''), 24.82 (C-3''/C-5''/C-2'), 12.75 (**C**H_3-C-5). ^{1}H-^{1}H COSY, ^{1}H-^{13}C HSQC, ^{1}H-^{13}C HMBC and DEPT 135 spectra were also recorded.

Synthesis of ((2*S*,3*S*,5*R*)-3-azido-5-(5-methyl-2,4-dioxo-3,4-dihydropyrimidin-1(2*H*)-yl)tetrahydrofuran-2-yl)methyl 6-(3,4-bis((*tert*-butyldiphenylsilyl)oxy)phenyl)hexanoate, 14.

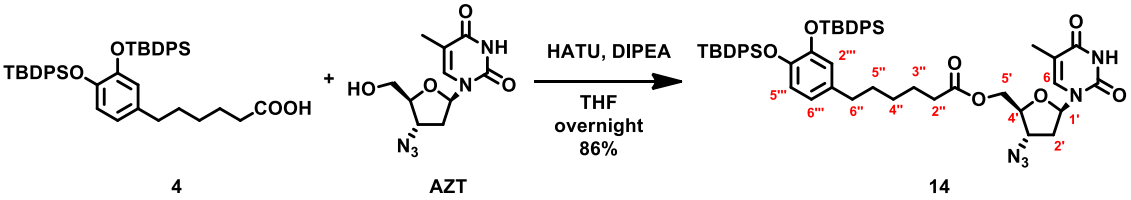

Carboxylic acid **4** (5.77 g, 8.23 mmol), HATU (4.27 g, 11.23 mmol) and DIPEA (5.2 mL, 29.94 mmol) were dissolved in dry THF (70 mL) under N_2 atmosphere and stirred at rt. After 45 min, a solution of AZT (2.00 g, 7.48 mmol) in dry THF (45 mL) was added dropwise. The mixture was stirred overnight at rt. Then, the mixture was filtered, the solvent was removed under vacuum and the crude was purified by column chromatography (CH_2Cl_2/EtOAc 80:20 to EtOAc 100%) to furnish the title compound **14** (6.09 g, 6.4 mmol, 86%) as a white solid. R_f (EtOAc) = 0.67. HRMS (EI) calcd for $[C_{54}H_{63}N_5O_7Si_2]^+$ 949.4266, found 949.4262. IR (ATR) ν 3049, 2932, 2859, 2101, 1703, 1512, 1128 cm^{-1}. $[\alpha]_D^{20}$ = + 11.6 (*c* 1, $CHCl_3$). mp. 55 – 58 °C (CH_2Cl_2/EtOAc).

^{1}H NMR (400 MHz, $CDCl_3$) δ 8.66 (s, 1H, H-3), 7.84 – 7.77 (m, 8H, Ph (TBDPS)), 7.47 – 7.34 (m, 12H, Ph(TBDPS)), 7.18 (q, $^4J_{6,CH3-C5}$ = 1.2 Hz, 1H, H-6), 6.33 (d, $^3J_{5''',6'''}$ = 8.1 Hz, 1H, H-5'''), 6.20 (d, $^3J_{2''',6'''}$ = 2.1 Hz, 1H, H-2'''), 6.14 (dd, $^3J_{6''',5'''}$ = 8.2 Hz, $^3J_{6''',2'''}$ = 2.2 Hz, 1H, H-6'''), 6.10 (t, $^3J_{1',2'}$ = 6.4 Hz, 1H, H-1'), 4.35 (dd, J_{gem} = 12.2 Hz, $^3J_{5',4'}$ = 4.7 Hz, 1H, H-5'), 4.27 (dd, J_{gem} = 12.2 Hz, $^3J_{5',4'}$ = 4.0 Hz, 1H, H-5'), 4.15 (dt, $^3J_{3',2'}$ = 7.6 Hz, $^3J_{3',4'}$ = 5.2 Hz, 1H, H-3'), 4.08 – 4.04 (m, 1H, H-4'), 2.47 (ddd, J_{gem} = 13.9 Hz, $^3J_{2',1'}$ = 6.4 Hz, $^3J_{2',3'}$ = 5.2 Hz, 1H, H-2'), 2.32 (ddd, J_{gem} = 13.9 Hz, $^3J_{2',3'}$ = 7.6 Hz, $^3J_{2',1'}$ = 6.4 Hz, 1H, H-2'), 2.21 (t, $^3J_{6'',5''}$ = 7.7 Hz, 2H, H-6''), 2.04 (t, $^3J_{2'',3''}$= 7.2 Hz, 2H, H-2''), 1.90 (d, $^4J_{CH3-C5,6}$ = 1.2 Hz, 3H), 1.48 – 1.38 (m, 2H, H-3''), 1.15 (s, 9H, *t*Bu), 1.14 (s, 9H, *t*Bu), 1.09 – 0.94 (m, 4H, 2H-4'', 2H-5''). **^{13}C NMR** (100 MHz, $CDCl_3$) δ 173.34 (C-1''), 163.67 (C-4), 150.20 (C-2), 146.02 (C-3'''), 144.27 (C-4'''), 135.97 (Ph (TBDPS)), 135.96 (Ph (TBDPS)), 135.51 (C-6), 134.72 (Ph (TBDPS)), 133.74 (C-1'''), 133.71(Ph (TBDPS)), 130.08 (Ph (TBDPS)), 130.06 (Ph (TBDPS)), 128.07 (Ph

(TBDPS)), 128.06 (Ph (TBDPS)), 120.83 (C-2'''), 120.66 (C-6'''), 120.23 (C-5'''), 111.60 (C-5), 85.86 (C-1'), 82.13 (C-4'), 63.53 (C-5'), 61.04 (C-3'), 37.91 (C-2'), 34.75 (C-2''), 34.25 (C-6''), 30.60 (C-5''), 28.60 (C-4''), 27.11($(CH_3)_3C$ (TBDPS), 24.88 (C-3''), 19.84 ($(CH_3)_3C$ (TBDPS)), 12.96 (CH_3-C5).

Synthesis of ((2*S*,3*S*,5*R*)-3-azido-5-(5-methyl-2,4-dioxo-3,4-dihydropyrimidin-1(2*H*)-yl)tetrahydrofuran-2-yl)methyl 6-(3,4-dihydroxyphenyl)hexanoate, catAZT.

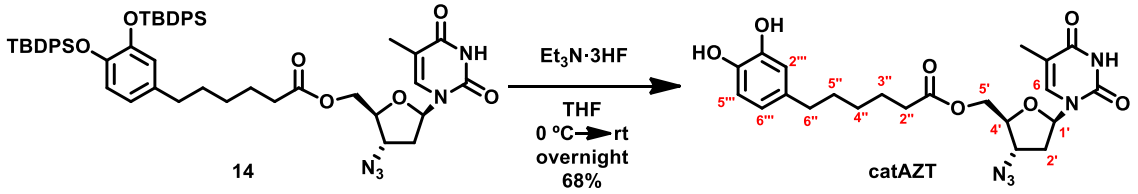

Triethylamine trihydrofluoride (2.1 mL, 12.9 mmol) was added to a stirred ice-cooled solution of **14** (1.97 g, 2.07 mmol) in dry THF (40 mL). The mixture was allowed to warm to rt and stirred overnight. The reaction was quenched with 0.3 mL of brine, diluted with 20 mL diethyl ether and filtered. The resulting crude was purified by column chromatography ($CHCl_3$/MeOH 97:3 → 94:6) to furnish **catAZT** as a white solid (0.669 g, 1.41 mmol, 68%). R_f (EtOAc) = 0.55. HRMS (EI) calcd for $[C_{22}H_{27}N_5O_7]^+$ 473.1910, found 473.1915. $[\alpha]_D^{20}$ = + 28.8 (*c* 1, $CHCl_3$). mp. 50 – 51 °C ($CHCl_3$/MeOH).

^{1}H NMR (400 MHz, $CDCl_3$) δ 7.29 (d, $^4J_{6,CH3\text{-}C5}$ = 1.2 Hz, 1H, H-6), 6.76 (d, $^3J_{5''',6'''}$ = 8.1 Hz, 1H, H-5'''), 6.63 (d, $^4J_{2''',6'''}$ = 2.0 Hz, 1H, H-2'''), 6.55 (dd, $^3J_{6''',5'''}$ = 8.1 Hz, $^3J_{6''',2'''}$ = 2.0 Hz, 1H, H-6'''), 6.06 (t, $^3J_{1',2'}$ = 6.2 Hz, 1H, H-1'), 4.40 (dd, J_{gem} = 12.4 Hz, $^3J_{5',4'}$ = 3.6 Hz, 1H, H-5'), 4.31 (dd, J_{gem} = 12.4 Hz, $^3J_{5',4'}$ = 3.6 Hz, 1H, H-5'), 4.13 (dt, $^3J_{3',2'}$ = 7.4 Hz, $^3J_{3',4'}$ = 5.4 Hz, 1H, H-3'), 4.07 (dt, $^3J_{4',3'}$ = 5.4 Hz, $^3J_{4',5'}$ = 3.6 Hz, 1H, H-4'), 2.51 – 2.44 (m, 3H, 2H-6'', H-2'), 2.38 – 2.30 (m, 3H, 2H-2'', H-2'), 1.89 (d, $^4J_{CH3\text{-}C5,6}$ = 1.3 Hz, 3H, CH3-C5), 1.70 – 1.61 (m, 2H, H-3''), 1.59 – 1.51 (m, 2H, H-5''), 1.35 – 1.27 (m, 2H, H-4''). **^{13}C NMR** (100 MHz, $CDCl_3$) δ 172.39 (C-1''), 163.31 (C-4), 149.25 (C-2), 142.97 (C-3'''), 141.20 (C-4'''), 135.12 (C-6), 134.35 (C-1'''), 119.99 (C-6'''), 114.68 (C-5'''), 114.66 (C-2'''), 110.26 (C-5), 85.25 (C-1'), 81.49 (C-4'), 62.18 (C-5'), 59.66 (C-3'), 37.18 (C-2'), 34.08 (C-6''), 33.38 (C-2''), 30.17 (C-5''), 27.54 (C-4''), 24.04 (C-3''), 11.96 (CH_3-C5).

Synthesis of 1,4-bis((1*H*-imidazol-1-yl)methyl)benzene, bix

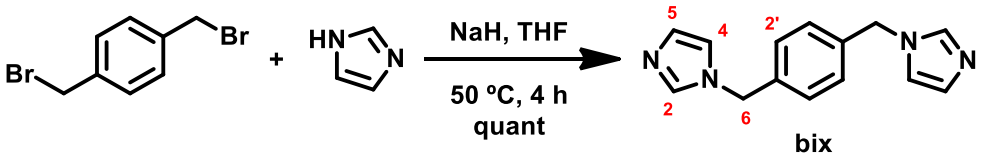

To a stirred suspension of NaH (suspension 60% wt) (1.455 g, 36.37 mmol) in dry toluene (10 mL) under Ar atmosphere, a solution of imidazole (2.27 g, 33.34 mmol) in dry toluene (12 mL) was added dropwise. The reaction mixture was allowed to stir for 30 min at room temperature and then 1,4-bis(bromomethyl)benzene (4.00 g, 15.15 mmol) was added dissolved in 20 mL of dry THF. The temperature of the reaction was then raised to 50 °C for 4 h. After cooling, the reaction was treated with 20 mL of ice-cooled water and stirred for 20 min. The organic phase was extracted with chloroform (3 x 30 mL), and the combined organic phase was dried over anhydrous sodium sulfate. The solvent was removed under reduced pressure to furnish **bix** as a yellow solid (3.61 g, 15.15 mmol, quantitative yield). **HRMS** (ESI)+: calculated for $[C_{14}H_{14}N_4+Na]^+$ 261.1118; found 261.1110.

^{1}H NMR (400 MHz, CDCl3) δ 7.72 (s, 2H, H-2), 7.23 (s, 4H, H-2'), 7.07 (s, 2H, H-5), 6.97 (s, 2H, H-4), 5.18 (s, 4H, H-6). **^{13}C NMR** (101 MHz, CDCl3) δ 138.64 (C-1), 138.31 (C-2), 129.40 (C-4), 129.17 (C-2'), 120.93 (C-5), 51.13 (C-6).

Synthesis of catAZT-NCPs

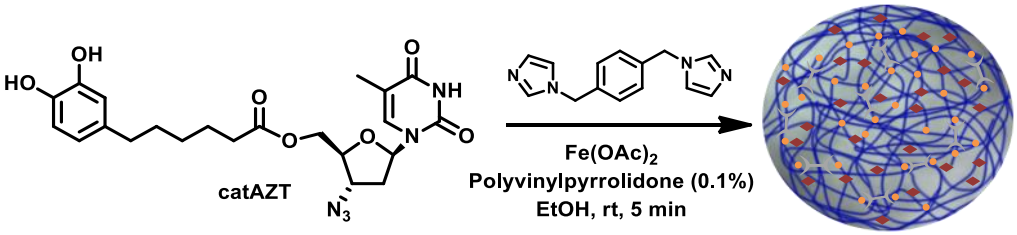

catAZT-NCPs

To prepare a material suitable for biological experiments, synthesis of the nanoparticles was performed inside a biosafety cabinet (Telstar BioVanguard B Green) and all the material and solvents used were sterilized. 1,4-Bis(imidazole-1-ylmethyl)-benzene (**bix**) (7.8 mg, 0.032 mmol), **catAZT** (30.5 mg, 0.064 mmol) and polyvinylpyrrolidone (PVP) (average MW 40000) (19.5 mg) were dissolved in ethanol (17.2 mL). Under stirring (700 rpm), a solution of $Fe(CH_3COO)_2$ (5.45 mg, 0.032 mmol in 2.3 mL ethanol) was added dropwise. Instantaneously, a dark-purple precipitate appeared. After the reaction

mixture was stirred at rt for 5 min, the precipitate was collected by centrifugation and then washed with ethanol four times. Finally, the solid was irradiated with a UV lamp for 15 min, and the nanoparticles stored as a solid or in the fridge at a concentration of 44 mg/ml in ethanol. SEM images of the resulting material showed spherical nanoparticles with a size distribution of 147 ± 33 nm. Elemental analysis: found (%) C 51.76, H 5.38, N 13.79. Calculated empirical formula: $FeC_{43.9}H_{54.3}N_{10.0}O_{15.0}$., adjusted to $[Fe(catAZT)_{1.5}(bix)_{0.6}(AcO)(H_2O)_{2.4}]$. MS: 5.46% Fe.

Synthesis of ((2*R*,3*S*,5*R*)-3-hydroxy-5-(5-methyl-2,4-dioxo-3,4-dihydropyrimidin-1(2*H*)-yl)tetrahydrofuran-2-yl)methyl 6-(3,4-bis((tert-butyldiphenylsilyl)oxy)phenyl)hexanoate, 15.

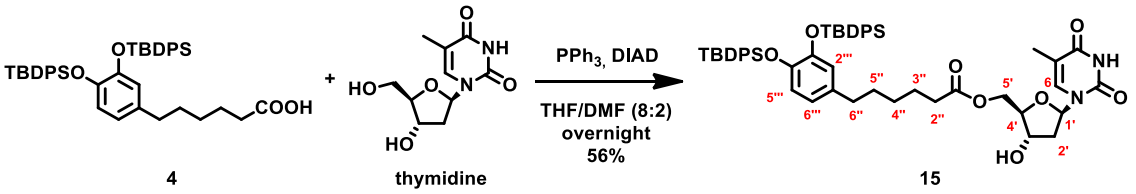

Diisopropyl azodicarboxylate (DIAD) (0.15 mL, 0.57 mmol) was added dropwise to an ice-cooled solution of carboxylic acid **4** (0.200 g, 0.29 mmol), triphenylphosphine (0.112 g, 0.43 mmol) and thymidine (0.090 g, 0.37 mmol) in a mixture of anhydrous THF/DMF (3 and 0.8 mL, respectively). The mixture was allowed to warm to rt and stirred overnight. The solvent was evaporated under vacuum and the crude was purified by column chromatography (EtOAc 100%) to afford **15** as a white solid (0.193 g, 0.21 mmol, 56%). R_f (EtOAc) = 0.39. HRMS (ESI+) calcd for $[C_{54}H_{65}N_2O_8Si_2]^+$ 925.4274, found 925.4263.

^{1}H NMR (400 MHz, $CDCl_3$) δ 8.41 (s, 1H, H-3), 7.84 – 7.77 (m, 8H, Ph (TBDPS)), 7.47 – 7.34 (m, 12H, Ph(TBDPS)), 7.23 (q, $^4J_{6,CH3\text{-}C5}$ = 0.9 Hz, 1H, H-6), 6.33 (d, $^3J_{5''',6'''}$ = 8.2 Hz, 1H, H-5'''), 6.27 (t, $^3J_{1',2'}$ = 6.7 Hz, 1H, H-1'), 6.20 (d, $^3J_{2''',6'''}$ = 2.1 Hz, 1H, H-2'''), 6.13 (dd, $^3J_{6''',5'''}$ = 8.2 Hz, $^3J_{6''',2'''}$ = 2.2 Hz, 1H, H-6'''), 4.36 (dd, J_{gem} = 12.2 Hz, $^3J_{5',4'}$ = 4.5 Hz, 1H, H-5'), 4.31 (dt, $^3J_{3',2'}$ = 6.8 Hz, $^3J_{3',4'}$ = 3.8 Hz, 1H, H-3'), 4.23 (dd, J_{gem} = 12.2 Hz, $^3J_{5',4'}$ = 3.8 Hz, 1H, H-5'), 4.11 (dt, $^3J_{4',5'}$ = 4.5 Hz, $^3J_{4',3'}$ = 3.8 Hz, 1H, H-4'), 2.38 (ddd, J_{gem} = 13.8 Hz, $^3J_{2',1'}$ = 6.7 Hz, $^3J_{2',3'}$ = 3.8 Hz, 1H, H-2'), 2.21 (t, $^3J_{6'',5''}$ = 7.5 Hz, 2H, H-6''), 2.09 (ddd, J_{gem} = 13.8 Hz, $^3J_{2',1'}$ = $^3J_{2',3'}$ = 6.8 Hz, 1H, H-2'), 2.03 (t, $^3J_{2'',3''}$= 7.5 Hz, 2H, H-2''), 1.89 (d, $^4J_{CH3\text{-}C5,6}$ = 1.2 Hz, 3H), 1.43 (quint, $^3J_{3'',2''}$ = $^3J_{3'',4''}$ = 7.5 Hz, 2H, H-3''), 1.15 (s, 9H, *t*Bu), 1.14 (s, 9H, *t*Bu), 1.05 – 0.93 (m, 4H, 2H-4'', 2H-5''). **^{13}C NMR** (100 MHz, $CDCl_3$) δ 173.52 (C-1''), 163.40 (C-4), 150.11 (C-2), 145.81 (C-3'''), 144.06 (C-4'''), 135.77 (Ph (TBDPS)), 135.66 (Ph (TBDPS)),

135.51 (C-6), 135.02 (Ph (TBDPS)), 133.48 (C-1'''), 129.90 (Ph (TBDPS)), 129.71 (Ph (TBDPS)), 129.51 (Ph (TBDPS)), 127.86 (Ph (TBDPS)), 127.76 (Ph (TBDPS)), 120.64 (C-2'''), 120.50 (C-6'''), 120.02 (C-5'''), 111.26 (C-5), 85.22 (C-1'), 84.34 (C-4'), 71.76 (C-5'), 63.69 (C-3'), 40.52 (C-2'), 34.54 (C-2''), 34.13 (C-6''), 30.37 (C-5''), 28.36 (C-4''), 26.88($(CH_3)_3C$ (TBDPS), 24.72 (C-3''), 19.65 ($(CH_3)_3C$ (TBDPS)), 12.80 (CH_3-C5).

Synthesis of ((2*S*,3*S*,5*R*)-3-hydroxy-5-(5-methyl-2,4-dioxo-3,4-dihydropyrimidin-1(2*H*)-yl)tetrahydrofuran-2-yl)methyl 6-(3,4-dihydroxyphenyl)hexanoate, catTHY.

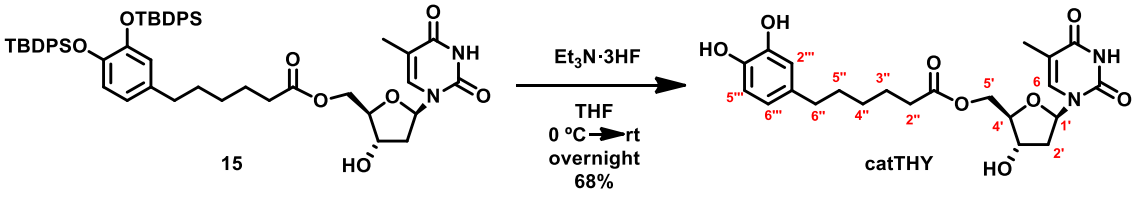

Triethylamine trihydrofluoride (0.45 mL, 2.75 mmol) was added to a stirred ice-cooled solution of **15** (0.490 g, 0.53 mmol) in dry THF (15 mL). The mixture was allowed to warm to rt and stirred overnight. The reaction was quenched with 0.15 mL of brine, diluted with 10 mL diethyl ether and filtered. The resulting crude was purified by column chromatography ($CHCl_3$/MeOH 95:5) to furnish **catTHY** as a white solid (0.162 g, 0.36 mmol, 68%). R_f (EtOAc) = 0.09. HRMS (EI) calcd for $[C_{22}H_{29}N_2O_8]^+$ 449.1919; found 449.1918. $[\alpha]_D^{20}$ = + 5.1 (*c* 1, DMSO). mp. 72 – 75 °C ($CHCl_3$/MeOH).

^{1}H NMR (400 MHz, CD_3OD) δ 7.48 (d, $^4J_{6,CH3\text{-}C5}$ = 1.3 Hz, 1H, H-6), 6.64 (d, $^3J_{5''',6'''}$ = 8.0 Hz, 1H, H-5'''), 6.59 (d, $^4J_{2''',6'''}$ = 2.1 Hz, 1H, H-2'''), 6.46 (dd, $^3J_{6''',5'''}$ = 8.0 Hz, $^3J_{6''',2'''}$ = 2.1 Hz, 1H, H-6'''), 6.25 (t, $^3J_{1',2'}$ = 7.0 Hz, 1H, H-1'), 4.35 (dd, J_{gem} = 12.1 Hz, $^3J_{5',4'}$ = 4.4 Hz, 1H, H-5'), 4.33 (m, 1H, H-4'), 4.24 (dd, J_{gem} = 12.1 Hz, $^3J_{5',4'}$ = 3.5 Hz, 1H, H-5'), 4.06 (dt, $^3J_{3',2'}$ = 5.4 Hz, $^3J_{3',4'}$ = $^3J_{3',2'}$ = 3.5 Hz, 1H, H-3'), 2.44 (t, $^3J_{2'',3''}$ = 7.5 Hz, 2H, H-2''), 2.36 (td, $^3J_{6'',3''}$ = 7.3 Hz, $^3J_{6'',6'''}$ = 1.2 Hz, 2H, H-6''), 2.30 (ddd, J_{gem}= 13.8 Hz, $^3J_{2',1'}$ = 7.0 Hz, $^3J_{2',3'}$ = 3.5 Hz, 1H, H-2'), 2.21 (ddd, J_{gem}= 13.8 Hz, $^3J_{2',1'}$ = 7.0 Hz, $^3J_{2',3'}$ = 5.4 Hz, 1H, H-2') 1.88 (d, $^4J_{CH3\text{-}C5,6}$ = 1.2 Hz, 3H, CH_3-C5), 1.64 (quint, $^3J_{3'',2''}$ = $^3J_{3'',4''}$ = 7.2 Hz, 2H, H-3''), 1.56 (quint, $^3J_{5'',4''}$ = $^3J_{5'',6''}$ = 7.2 Hz, 2H, H-5''), 1.38 – 1.28 (m, 2H, H-4''). **^{13}C NMR** (100 MHz, CD_3OD) δ 174.92 (C-1''), 166.24 (C-4), 152.15 (C-2), 145.91 (C-3'''), 144.00 (C-4'''), 137.49 (C-6), 135.33 (C-1'''), 120.59 (C-6'''), 116.45 (C-5'''), 114.18 (C-2'''), 111.66 (C-5), 86.52 (C-1'), 85.72 (C-4'), 72.26 (C-5'), 64.89 (C-3'), 40.61 (C-2'), 35.96 (C-6''), 34.90 (C-2''), 32.38 (C-5''), 29.58 (C-4''), 25.81 (C-3''), 12.62 (CH_3-C5).

Synthesis of catTHY-NCPs

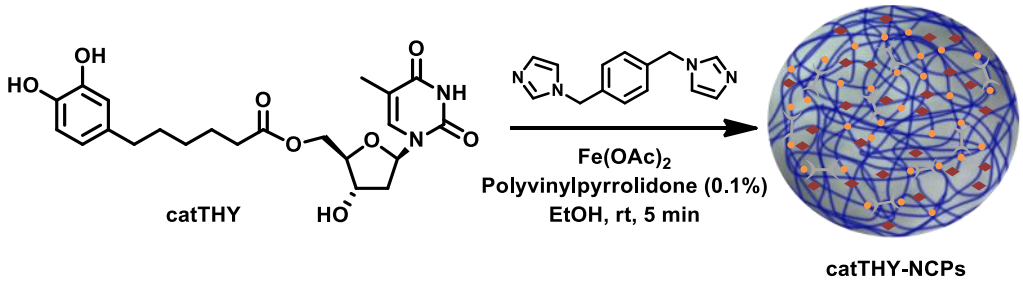

1,4-Bis(imidazole-1-ylmethyl)-benzene (**bix**) (8.7 mg, 0.037 mmol), **catTHY** (30.0 mg, 0.067 mmol) and polyvinylpyrrolidone (PVP) (average MW 40000) (19.6 mg) were dissolved in ethanol (17 mL). Under stirring (700 rpm), a solution of $Fe(CH_3COO)_2$ (6.4 mg, 0.037 mmol in 2.6 mL ethanol) was added dropwise. Instantaneously, a dark-purple precipitate appeared. After the reaction mixture was stirred at rt for 5 min, the precipitate was collected by centrifugation and then washed with ethanol four times. Finally, the solid was irradiated with a UV lamp for 15 min, and the nanoparticles stored as a solid. SEM images of the resulting material showed spherical nanoparticles with a size distribution of 87 ± 26 nm. Elemental analysis: found (%) C 45.33, H 4.91, N 6.80. Calculated empirical formula: $FeC_{63.4}H_{113.2}N_{8.4}O_{39.0}$, adjusted to $Fe(catTHY)_{2.18}(bix)(AcO)_{0.7}(H_2O)_{20.2}$

HPLC methodology for ARV-NCPs analysis

Chromatographic conditions: Analyses were performed using a HPLC Waters 2695 separation module coupled to a Waters 2487 UV-Vis detector (suitable for dual detection). The column used was a Chromolith® Performance RP-18e (100 mm x 4.6 mm). Eluent A was a 0.1% (v/v) H_3PO_4 aqueous solution containing 262 mg/L sodium 1-octanesulfonate and eluent B was methanol absolute (HPLC grade). Before the analysis, the RP column was pre-equilibrated using the starting conditions of the method (99 % A (v/v)) for 6 min. The elution began with an isocratic elution of 99% A (v/v) for 5 min, followed by a gradual increase of A from 1% to 40% (v/v) until 25 min. Then, the mobile phase was raised to 98% B (v/v) (between minutes 25 and 30) to elute tight bound compounds and kept at 98% B (v/v) for additional 5 min. Finally, mobile phase was reset to the initial conditions (A:B) 99:1 (v/v) and stayed for 6 min to equilibrate for the next injection. The flow rate was set at 1.0 mL/min and the column temperature was kept at 25 °C. The detection wavelengths were 214 and 280 nm. Sample preparation: NCPs

samples were prepared dissolving 1.5 mg **catAZT-NCPs**/mL in 0.15 mL of a methanol/HCl mixture (50 µL concentrated HCl/mL methanol). The initial samples were diluted with 1.35 mL of deionized water to have a final water/methanol ratio of 90:10 and sonicated for 5 min. Then, samples were further diluted 3 and 5 times in buffer A before their injection into the HPLC system. All samples were prepared in duplicate. Calibration curves: A calibration curve using **bix** and **catAZT** as external standards was prepared. Standards were prepared by duplicate, diluting a stock solution containing **bix** and **catAZT** (960 and 980 µg/mL, respectively) dissolved in a methanol/HCl mixture (50 µL concentrated HCl/mL methanol) and diluted with distilled water to a final water/methanol ratio of 90:10. In both cases, results were adjusted to linear regression models with $R^2 > 0.999$ between the ranges of 9-261, 8-220 µg/mL for **bix** and **catAZT**, respectively.

In vitro drug release studies at different pH and in presence/absence of esterases

catAZT (5 mg) **or catAZT-NCPs** (6 mg) were added to a PBS/BSA 0.5 mM buffer solution at pH 5.1 or 7.4 (20 mL) with and without pig liver esterases (PLE) (180 U/L). All the samples were maintained at 37 ˚C under constant stirring. Aliquots (400 µL) were taken after different periods of time, and the volume extracted was replaced with additional 400 µL of the PBS/BSA 0.5 mM solution. Then, all the aliquots were filtered through a 10 kDa membrane (Amicon® Ultra 0.5 mL) (15 min x 14.5k RFC) before their injection in the HPLC system. When the last aliquot was taken, three additional aliquots (390 µL) were extracted and treated with HCl 2 M in methanol (10 µL) to measure the remaining amount of non-released drug.

HPLC method for release kinetics quantification

Chromatographic conditions: Analyses were performed using a HPLC Waters 2695 separation module coupled to a Waters 2487 UV-Vis detector (suitable for dual detection). The column used was a Restek Ultra C18 (250 mm x 4.6 mm). Eluent A was a 0.1% (v/v) H_3PO_4 aqueous solution and eluent B was acetonitrile (HPLC grade). Injection volume was 20 µL. Before the analysis, the RP column was pre-equilibrated using the starting conditions of the method (80 % A (v/v)) for 30 min. Initial flow rate was set at 0.8 mL/min. The elution began with a gradual increase of B from 20% to 60% (v/v) until 8 min. Then, an isocratic elution was maintained for 5.5 min. A second gradient was then

performed, raising eluent B from 60% to 80% in 1 min and flow rate to 1.2 mL/min and maintained for an additional 5.5 min. Finally, mobile phase composition and flow rate was reset to the initial conditions (A:B) 80:20 (v/v) and 0.8 mL/min and stayed for 4.5 min to equilibrate for the next injection. Column temperature was kept at 25˚C and the detection wavelengths were 214 and 280 nm. Calibration curves: A calibration curve using zidovudine (AZT) and **catAZT** as external standards was prepared. Standards were prepared by duplicate, diluting a stock solution containing AZT and **catAZT** (3 mg/mL) dissolved in methanol and diluted with distilled water to a final water/methanol ratio of 80:20. In both cases, results were adjusted to linear regression models with $R^2 > 0.99$ between the ranges of 1-480 and 4-208 μg/mL for AZT and **catAZT**, respectively.

Cell culture

$CD4^+$ T cells were isolated from the PBMCs of healthy human donors by FACS-sorting using the rapid expansion method (REM). IL-2 was added at day 1 and cells remained untouched during the first 5 days of culture, and then cells were split every 3–4 days. Human T cell leukemia virus carrier MT-2 cell line was obtained from the American Type Culture Collection (ATCC, Manassas, VA, USA). Cells were routinely cultured in cultured in RPMI 1640 medium with L-Glutamine (Lonza, Verviers, Belgium, #12-702 F), further supplemented with 10% heat-inactivated fetal bovine serum (FBS, Gibco, #10270-106), 100 U/ml penicillin, 100 mg/ml streptomycin (Penicillin-Streptomycin, S/P; Lonza, Verviers, Belgium). Cells were routinely maintained in a humidified atmosphere at 37 ºC with 5% CO2 in the biohazard P3 laboratory. Cells were maintained at $0.3x10^6$ cells/ml.

Generation of virus stock

NL4-3 HIV-1 virus was produced by transient transfection in HEK293-T cells. Briefly, the previous day $1.5x10^6$ HEK293-T cells were seeded in 75 cm^2 tissue culture flasks in DMEM medium with L-Glutamine, supplemented with 10% heat-inactivated fetal bovine serum, 100 U/ml penicillin, and 100 mg/ml streptomycin (DMEM-10). Cells were replaced with fresh DMEM-10 medium three hours before transfection by the calcium-phosphate method (ProFectionH Mammalian Transfection System; Promega, Madison, WI) according to the manufacturer's instructions, using 5 mg of pNL4-3 DNA previously purified (Qiagen, Valencia, CA).[41] Growth medium was replaced with fresh DMEM-10 medium 16–18 h post-transfection. The supernatants were harvested approximately two

days after transfection, clarified by centrifugation at 800 g/4C for 10 minutes, aliquoted and stored at -80ºC. Viruses were quantified by determining the concentration of p24 in the supernatant with an antigen capture assay (ELISA; INNOTEST® HIV Antigen mAb test, Fugirebio, Gent, Belgium). P24 ELISA should be sufficient to determine the level of viral production (at a protein level). Viral DNA would be a step further but notice that the viral HIV genome gets integrated into the cells genome and our delivery system does not avoid infection. The level of replication-competent infectious viruses was evaluated through the tissue culture infective dose (TCID50) in TZM-bl indicator cells. The viruses were titred in vitro for their cytopathic effect on MT-2 cells with the MTT assay.

Cytotoxicity assays

Cytotoxicity of **catAZT-NCPs** was tested against primary human CD4+ T lymphocytes by using the PrestoBlue cell viability assay (Invitrogen). Primary CD4+T cells previously isolated by the rapid expansion method (REM) were seeded in a 96-well plate at 1×10^5 cells/well, then 100 µL medium per well containing various concentrations of **catAZT-NCPs** and AZT were added (500, 250, 125, 50 and 10 µg/mL) and incubated for 24h. Cytotoxicity was evaluated adding 20 µL of prestoBlue reagent per well. After incubation at 37°C for 4 h, fluorescence intensities were measured at a 532-nm excitation wavelength and a 571-nm emission wavelength in a microplate reader (Multilabel Processor Victor™X3 Perkin Elmer, USA). Cell cytotoxicity of the antiviral effect of the free compounds (AZT and **catAZT**) and **catAZT-NCPs** against MT-2 cells was evaluated by the MTT (3-(4,5-dimethylthiazol-2-yl)-2,5-diphenyltetrazolium bromide) assay. To perform the experiments, exponentially growing MT-2 cell were plated in 96-well plates at a density of $0.4x10^5$ cells per well. The cells were treated with the vehicle (saccharose), a range of concentrations of each compound (10 different concentrations from 0 to 100 µg/mL), or with the nanoparticles at equivalent concentrations to those assayed for AZT/**catAZT**. After incubation at the indicated time points at 37 ºC under a humidified atmosphere with 5% CO_2, 100 µl of the cell media were carefully discarded and 10 µl of MTT solution were added to each well and incubated for 4h at 37 °C. Then, 100 µl of solubilization solution was added to each well containing the MTT, and then plates were incubated at 37 °C under 5% CO_2 for ON. After incubation, the colour formed on each well was measured using a spectrophotometric plate reader (BioTek, Synergy HT) at 620 nm wavelength. All the cytotoxicity experiments were performed in triplicate, and at

least two independent assays. Cell cytotoxicity was evaluated in terms of cell grown inhibition in treated cultures and expressed as % of the control condition.

Uptake experiments

MT-2 cells were seeded at a concentration of $1.0x10^6$ cells/ml. The cells were incubated with AZT, **catAZT** or **catAZT-NCPs** at the indicated concentrations (referred to the AZT concentration) for 4 h at 37 ºC under a humidified atmosphere with 5% CO_2. Saccharose was used as vehicle control. Immediately after incubation, cells were washed with PBS and lysed in 1000 µl of a water/methanol (80%/20%) solution containing 0.1% phosphoric acid (pH=2.5) to determined intracellular free AZT. In the case of **catAZT-NCPs**, the samples were lysed in 100 µl of water/methanol solution containing 1.85 % (v/v) HCl. The concentration of AZT in all the samples was determined by HPLC-UV as following described. The intracellular concentration of AZT present in the cells (expressed as nmols/10^6 cells) was calculated dividing the concentration of AZT by the number of cells present in each sample. The experiment was performed per duplicate and at least two independent assays.

HPLC methodology for AZT uptake quantification.

Chromatographic conditions: Analyses were performed using a HPLC Waters 2695 separation module coupled to a Waters 2487 UV-Vis detector (suitable for dual detection). The column used was a Restek® C-18 (250 mm x 4.6 mm). Eluent A was a 0.1% (v/v) H_3PO_4 aqueous solution and eluent B was methanol absolute (HPLC grade). Injection volume was 20 µL. Before the analysis, the RP column was pre-equilibrated using the starting conditions of the method (80 % A (v/v)) for 30 min. The elution began with a gradual increase of B from 20% to 60% (v/v) for 8 min, followed by isocratic elution (60% B) for 7 min. Then, the mobile phase was raised to 80% B (v/v) for 1 min to elute tight bound compounds. Finally, mobile phase was reset to the initial conditions (A:B) 80:20 (v/v) for 4 min and stayed for 5 min to equilibrate for the next injection. The flow rate was set at 0.4 mL/min and the column temperature was kept at 25 °C. The detection wavelengths were 214 and 280 nm. Calibration curves: A calibration curve using AZT and **catAZT** as external standards was prepared. Standards were prepared diluting a stock solution containing AZT and **catAZT** (2 mM) dissolved in methanol and diluted with distilled water to a final water/methanol ratio of 50:50. In both cases, results were

adjusted to linear regression models with R2 > 0.999 between the ranges of 10-100 and 40-250 μM for AZT and **catAZT**, respectively.

HIV-1 in vitro antiviral assay

The antiviral effects of AZT, **catAZT** and **catAZT-NCPs** nanoparticles on MT-2 cells infected with HIV-1 were evaluated by the soluble-formazan method in order to follow the cytopathic effect of the infection, similarly as previously described.[42,43] Briefly, MT-2 cells were plated at a concentration of $0.4x10^5$ cells/ml in 96-well plates. Cells were then treated with different concentrations of vehicle (saccharose), AZT, **catAZT** or **catAZT-NCPs** and control nanoparticles containing thymidine (**catTHY-NCPs**). Following the addition of these compounds, cells were infected with CXCR4 tropic NL4.3 HIV-1 viruses (TCID50/ml=129000; p24=1.2 ug/ml). For the 7-day incubation experiments the infection was performed at MOI=0.002. For the 3-day assay, the pure stock of virus was used (100 ul) and diluted 1:2 in the well. Infected cells were incubated for 3 and 7 days in a humidified atmosphere at 37ºC with 5% CO2 in the biohazard P3 laboratory. After incubation, the HIV-1 cytopathic effect in the cells was determined by the MTT method under identical conditions as described above for the cytotoxicity experiments.

References

[1] Cihlar, T.; Ray, A. S. Nucleoside and Nucleotide HIV Reverse Transcriptase Inhibitors: 25 Years after Zidovudine. *Antiviral Res.* **2010**, *85* (1), 39–58.

[2] Montalbetti, C. A. G. N.; Falque, V. Amide Bond Formation and Peptide Coupling. *Tetrahedron* **2005**, *61* (46), 10827–10852.

[3] Evangelio, E.; Hernando, J.; Imaz, I.; Bardají, G. G.; Alibés, R.; Busqué, F.; Ruiz-Molina, D. Catechol Derivatives as Fluorescent Chemosensors for Wide-Range PH Detection. *Chem. Eur. J.* **2008**, *14* (31), 9754–9763.

[4] Novio, F.; Lorenzo, J.; Nador, F.; Wnuk, K.; Ruiz-Molina, D. Carboxyl Group (-CO_2H) Functionalized Coordination Polymer Nanoparticles as Efficient Platforms for Drug Delivery. *Chem. - A Eur. J.* **2014**, *20* (47), 15443–15450.

[5] Dhal, P. K.; Arnold, F. H. Metal-Coordination Interactions in the Template-Mediated Synthesis of Substrate-Selective Polymers: Recognition of Bis(Imidazole) Substrates by Copper(II) Iminodiacetate Containing Polymers. *Macromolecules* **1992**, *25* (25), 7051–7059.

[6] Koczkur, K. M.; Mourdikoudis, S.; Polavarapu, L.; Skrabalak, S. E. Polyvinylpyrrolidone (PVP) in Nanoparticle Synthesis. *Dalt. Trans.* **2015**, *44* (41), 17883–17905.

[7] a) Imaz, I.; Hernando, J.; Ruiz-Molina, D.; Maspoch, D. Metal-Organic Spheres as Functional Systems for Guest Encapsulation. *Angew. Chem. Int. Ed.* **2009**, *48* (13), 2325–2329. b) Imaz, I.; Rubio-Martínez, M.; García-Fernández, L.; García, F.; Ruiz-Molina, D.; Hernando, J.; Puntes, V.; Maspoch, D. Coordination Polymer Particles as Potential Drug Delivery Systems. *Chem. Commun.* **2010**, *46* (26), 4737–4739.

[8] Stahlberg, J. *Ion Chromatography : Mechanisms*; **2000**, 676-684.

[9] Neue, U. D.; Mndez, A.; Tran, K.; Diehl, D. M.; McBrien, M.; Kuss, H.-J.; Schmer, S. Fundamentals of Optimization: Sections 1.3–1.6. *HPLC Made to Measure: A Practical Handbook for Optimization*. **2006**, 71–147.

[10] Jo, D. H.; Chiou, Y. M.; Que, J. Models for Extradiol Cleaving Catechol Dioxygenases: Syntheses, Structures, and Reactivities of Iron(II)-Monoanionic Catecholate Complexes. *Inorg. Chem.* **2001**, *40* (13), 3181–3190.

[11] Hasebroock, K. M.; Serkova, N. J. Toxicity of MRI and CT Contrast Agents. *Expert Opin. Drug Metab. Toxicol.* **2009**, *5* (4), 403–416.

[12] Cabrera-García, A.; Checa-Chavarria, E.; Pacheco-Torres, J.; Bernabeu-Sanz, Á.; Vidal-Moya, A.; Rivero-Buceta, E.; Sastre, G.; Fernández, E.; Botella, P. Engineered Contrast Agents in a Single Structure for: T 1- T 2 Dual Magnetic Resonance Imaging. *Nanoscale* **2018**, *10* (14), 6349–6360.

[13] Borges, M.; Yu, S.; Laromaine, A.; Roig, A.; Suárez-García, S.; Lorenzo, J.; Ruiz-Molina, D.; Novio, F. Dual T1/T2MRI Contrast Agent Based on Hybrid SPION@coordination Polymer Nanoparticles. *RSC Adv.* **2015**, *5* (105), 86779–86783.

[14] Suárez-García, S.; Arias-Ramos, N.; Frias, C.; Candiota, A. P.; Arús, C.; Lorenzo, J.; Ruiz-Molina, D.; Novio, F. Dual T1/ T2 Nanoscale Coordination Polymers as Novel Contrast Agents for MRI: A Preclinical Study for Brain Tumor. *ACS Appl. Mater. Interfaces* **2018**, *10* (45), 38819–38832.

[15] He, Z.; Zhang, P.; Xiao, Y.; Li, J.; Yang, F.; Liu, Y.; Zhang, J. R.; Zhu, J. J. Acid-Degradable Gadolinium-Based Nanoscale Coordination Polymer: A Potential Platform for Targeted Drug Delivery and Potential Magnetic Resonance Imaging. *Nano Res.* **2018**, *11* (2), 929–939.

[16] Yamada, K.; Taguchi, H.; Ohkubo, A.; Seio, K.; Sekine, M. Synthesis and Properties of Nucleoside Derivatives Acylated by Chemically Stable 2-(Trimethylsilyl)Benzoyl Group. *Bioorganic Med. Chem.* **2009**, *17*, 5928–5932.

[17] Diez-Torrubia, A.; Balzarini, J.; Andrei, G.; Snoeck, R.; De Meester, I.; Camarasa, M. J.; Velázquez, S. Dipeptidyl Peptidase IV Dependent Water-Soluble Prodrugs of Highly Lipophilic Bicyclic Nucleoside Analogues. *J. Med. Chem.* **2011**, *54* (6), 1927–1942.

[18] Casanova, E.; Moreno, D.; Gigante, A.; Rico, E.; Genes, C. M.; Oliva, C.; Camarasa, M.-J.; Gago, F.; Jiménez-Ruiz, A.; Pérez-Pérez, M.-J. 5′-Trityl-Substituted Thymidine Derivatives as a Novel Class of Antileisshmanial Agents: Leishmania Infantum EndoG as a Potential Target. *ChemMedChem* **2013**, *8*, 1161–1174.

[19] Swamy, K. C. K.; Kumar, N. N. B.; Balaraman, E.; Kumar, K. V. P. P. Mitsunobu and Related Reactions: Advances and Applications. *Chem. Rev.* **2009**, *109* (6), 2551–2651.

[20] Wang, D.; Zou, L.; Jin, Q.; Hou, J.; Ge, G.; Yang, L. Human Carboxylesterases: A Comprehensive Review. *Acta Pharm. Sin. B* **2018**, *8* (5), 699–712.

[21] Amorín-Ferré, L.; Busqué, F.; Bourdelande, J. L.; Ruiz-Molina, D.; Hernando, J.; Novio, F. Encapsulation and Release Mechanisms in Coordination Polymer Nanoparticles. *Chem. Eur. J.* **2013**, *19* (51), 17508–17516

[22] Forbes, M. S. (2012). Chapter 5 - Cell Structure. In *Cell Physiology Source Book*, Elsevier, **2012**, *67–83.*

[23] Aggarwal, P.; Hall, J. B.; McLeland, C. B.; Dobrovolskaia, M. A.; McNeil, S. E. Nanoparticle Interaction with Plasma Proteins as It Relates to Particle Biodistribution, Biocompatibility and Therapeutic Efficacy. *Adv. Drug Deliv. Rev.* **2009**, *61* (6), 428–437.

[24] Albanese, A.; Chan, W. C. W. Effect of Gold Nanoparticle Aggregation on Cell Uptake and Toxicity. *ACS Nano* **2011**, *5* (7), 5478–5489.

[25] Aggarwal, P.; Hall, J. B.; McLeland, C. B.; Dobrovolskaia, M. A.; McNeil, S. E. Nanoparticle Interaction with Plasma Proteins as It Relates to Particle Biodistribution, Biocompatibility and Therapeutic Efficacy. *Adv. Drug Deliv. Rev.* **2009**, *61* (6), 428–437.

[26] Moore, T. L.; Rodriguez-Lorenzo, L.; Hirsch, V.; Balog, S.; Urban, D.; Jud, C.; Rothen-Rutishauser, B.; Lattuada, M.; Petri-Fink, A. Nanoparticle Colloidal Stability in Cell Culture Media and Impact on Cellular Interactions. *Chem. Soc. Rev.* **2015**, *44* (17), 6287–6305.

[27] Chiu, D. T.; Duesberg, P. H. The Toxicity of Azidothymidine (AZT) on Human and Animal Cells in Culture at Concentrations Used for Antiviral Therapy. *Genetica* **1995**, *95* (1–3), 103–109.

[28] Oguariri, R. M.; Dais, L.; Adelsberger, J. W.; Ruperts, A.; Stevens, R.; Yang, J.; Huang, D.; Lempicki, R. A.; Zhou, M.; Baseler, M. W.; et al. Interleukin-2 Inhibits HIV-1 Replication in Some Human T Cell Lymphotrophic Virus-1-Infected Cell Lines via the Induction and Incorporation of APOBEC3G into the Virion. *J. Biol. Chem.* **2013**, *288* (24), 17812–17822.

[29] Bedoya, L. M.; Beltrán, M.; Obregón-Calderón, P.; García-Pérez, J.; de la Torre, H. E.; González, N.; Pérez-Olmeda, M.; Auñón, D.; Capa, L.; Gómez-Acebo, E.; et al. Hydroxytyrosol: A New Class of Microbicide Displaying Broad Anti-HIV-1 Activity. *AIDS* **2016**, *30* (18), 2767–2776.

[30] Tsiang, M.; Jones, G. S.; Goldsmith, J.; Mulato, A.; Hansen, D.; Kan, E.; Tsai, L.; Bam, R. A.; Stepan, G.; Stray, K. M.; et al. Antiviral Activity of Bictegravir (GS-9883), a Novel Potent HIV-1 Integrase Strand Transfer Inhibitor with an Improved Resistance Profile. *Antimicrob. Agents Chemother.* **2016**, *60* (12), 7086–7097.

[31] Mainardes, R. M.; Gremiao, M. P. D.; Brunetti, I. L.; Fonseca, L. M. da; Khalil, N. M. Zidovudine-Loaded PLA and PLA–PEG Blend Nanoparticles: Influence of Polymer Type on Phagocytic Uptake by Polymorphonuclear Cells. *J. Pharm. Sci.* **2009**, *98* (1), 257–267.

[32] Mandal, S.; Zhou, Y.; Shibata, A.; Destache, C. J. Confocal Fluorescence Microscopy: An Ultra-Sensitive Tool Used to Evaluate Intracellular Antiretroviral Nano-Drug Delivery in HeLa Cells. *AIP Adv.* **2015**, *5* (8), 1–9.

[33] Le Roy, C.; Wrana, J. L. Clathrin- and Non-Clathrin-Mediated Endocytic Regulation of Cell Signalling. *Nat. Rev. Mol. Cell Biol.* **2005**, *6* (2), 112–126.

[34] Vonarbourg, A.; Passirani, C.; Saulnier, P.; Simard, P.; Leroux, J. C.; Benoit, J. P. Evaluation of Pegylated Lipid Nanocapsules versus Complement System Activation and Macrophage Uptake. *J. Biomed. Mater. Res., Part A* **2006**, *78*, 620–628.

[35] Beduneau, A.; Ma, Z.; Grotepas, C. B.; Kabanov, A.; Rabinow, B. E.; Gong, N.; Mosley, R. L.; Dou, H.; Boska, M. D.; Gendelman, H. E. Facilitated Monocyte-Macrophage Uptake and Tissue Distribution of Superparmagnetic Iron-Oxide Nanoparticles. *PLoS One* **2009**, *4*, e4343.

[36] Nowacek, A. S.; Miller, R. L.; McMillan, J.; Kanmogne, G.; Kannmogne, M.; Mosley, R. L.; Ma, Z.; Graham, S.; Chaubal, M.; Werling, J.; et al. NanoART Synthesis, Characterization, Uptake, Release and Toxicology for Human Monocyte-Macrophage Drug Delivery. *Nanomedicine* **2009**, *4*, 903–917.

[37] Zimmerman, T. P.; Mahony, W. B.; Prus, K. L. 3'-Azido-3'deoxythymidine: An Unusual Nucleoside Analogue That Permeates the Membrane of Human Erythrocytes and Lymphocytes by Nonfacilitated Diffusion. *J. Biol. Chem.* **1987**, *262* (12), 5748–5754.

[38] Errasti-Murugarren, E.; Pastor-Anglada, M. Drug Transporter Pharmacogenetics in Nucleoside-Based Therapies. *Pharmacogenomics* **2010**, *11* (6), 809–841.

[39] Sillman, B.; Bade, A. N.; Dash, P. K.; Bhargavan, B.; Kocher, T.; Mathews, S.; Su, H.; Kanmogne, G. D.; Poluektova, L. Y.; Gorantla, S.; et al. Creation of a Long-Acting Nanoformulated Dolutegravir. *Nat. Commun.* **2018**, *9* (1), 443.

[40] Zhou, T.; Su, H.; Dash, P.; Lin, Z.; Dyavar Shetty, B. L.; Kocher, T.; Szlachetka, A.; Lamberty, B.; Fox, H. S.; Poluektova, L.; et al. Creation of a Nanoformulated Cabotegravir Prodrug with Improved Antiretroviral Profiles. *Biomaterials* **2018**, *151*, 53–65.

[41] Adachi, A.; Gendelman, H. E.; Koenig, S.; Folks, T.; Willey, R.; Rabson, A.; Martin, M. A. Production of Acquired Immunodeficiency Syndrome-Associated Retrovirus in Human and Nonhuman Cells Transfected with an Infectious Molecular Clone. *J. Virol.* **1986**, *59* (2), 284–291.

[42] Larder, B. A.; Kemp, S. D.; Purifoy, D. J. Infectious Potential of Human Immunodeficiency Virus Type 1 Reverse Transcriptase Mutants with Altered Inhibitor Sensitivity. *Proc. Natl. Acad. Sci.* **1989**, *86* (13), 4803–4807.

[43] Larder, B. A.; Chesebro, B.; Richman, D. D. Susceptibilities of Zidovudine-Susceptible and -Resistant Human Immunodeficiency Virus Isolates to Antiviral Agents Determined by Using a Quantitative Plaque Reduction Assay. *Antimicrob. Agents Chemother.* **1990**, *34* (3), 436–441.

Chapter 4

Synthesis of NCPs using a combination of antiretroviral drugs

This chapter will expand the methodology of NCPs synthesis presented in chapter 3 by introducing nanoparticles formulated with a combination of antiretroviral drugs. In particular, the clinically-relevant combination composed by raltegravir (RAL) and emtricitabine (FTC) will be used to structure NCPs. In an analogous way to AZT functionalization with a catechol moiety, the synthetic pathway of raltegravir and emtricitabine conjugates (**catRAL** and **catFTC**, respectively) will be presented. Then, NCPs will be prepared using these conjugates following the methodology learned with **catAZT-NCPs** and characterized accordingly. As a step forward, new NCPs will be synthesized combining both conjugates (**catRAL-catFTC-NCPs**) and their properties will be compared to both the free antiviral drugs and their corresponding mono-antiviral NCPs. Additionally, the functionalization of other antiretroviral drugs, lamivudine (3TC) and tenofovir (TFV), with catechol moieties will be explored for its posterior use in the synthesis of ARV-NCPs.

4.1 Development of synthetic methodologies for the obtention of catFTC and catRAL

The proposed synthetic pathway to obtain target molecules **catRAL** and **catFTC** (scheme 4.1) was similar to that used for **catAZT** and started with the silyl-protected catechol intermediate **4**, whose synthesis has been described in chapter 3 in 3 steps and 55% overall yield. From that point, both antiretroviral drugs, FTC and RAL, would be introduced through an esterification reaction to obtain **catFTC** and **catRAL**, respectively.

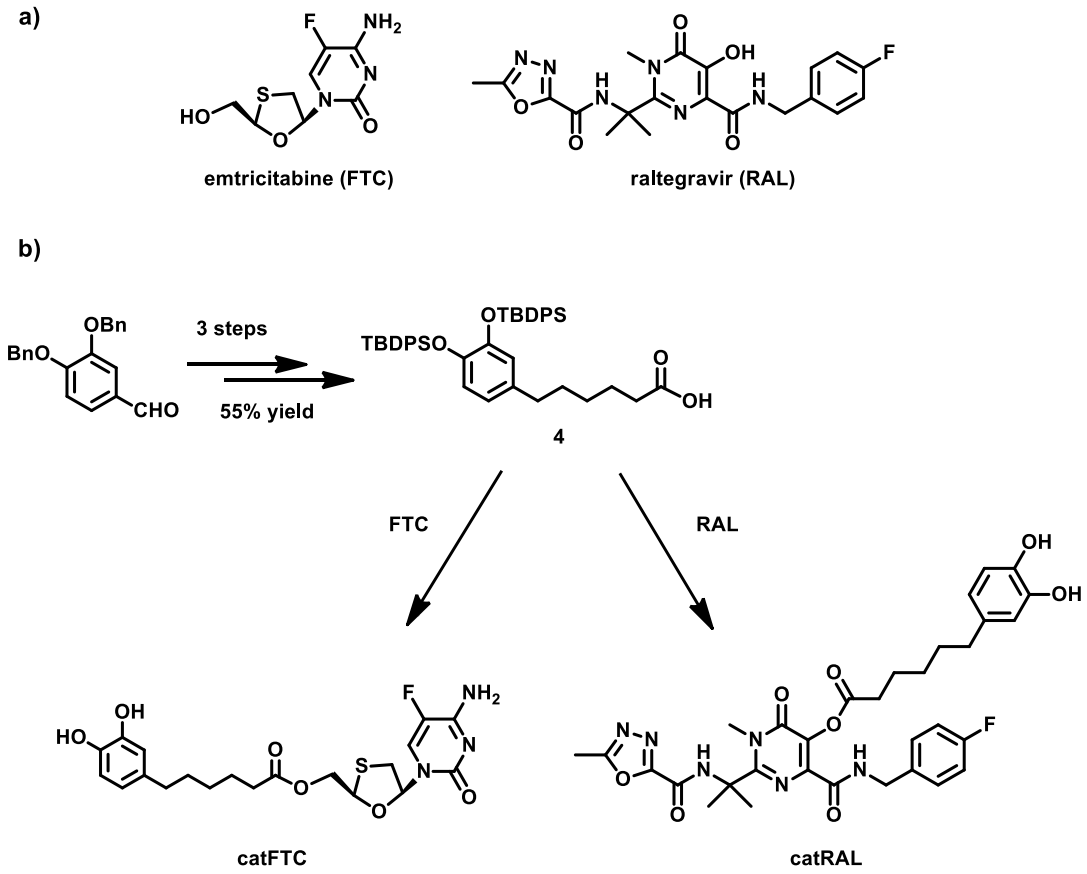

Scheme 4.1. a) Chemical structures of emtricitabine (FTC) and raltegravir (RAL). b) Synthetic route for the obtention of target molecules **catFTC** and **catRAL**.

4.1.1 Synthesis of catFTC

4.1.1.1 Synthesis of ((2*R*,5*S*)-5-(4-amino-5-fluoro-2-oxopyrimidin-1(2*H*)-yl)-1,3-oxathiolan-2-yl)methyl 6-(3,4-bis((tert-butyldiphenylsilyl)oxy)phenyl)hexanoate, 17

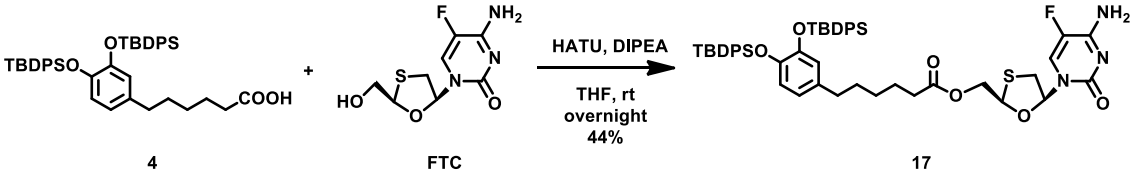

Coupling of FTC to **4** appeared to be straightforward, as coupling methodologies for the formation of **catAZT** or **catTHY** used in the previous chapter were expected to be applied successfully to it. Formation of **17** presented, however, a series of synthetic challenges. In a first screening, the optimized conditions for AZT coupling, HATU and DIPEA, were used to perform this transformation. A new compound, less polar than FTC, was identified in the reaction crude by TLC analysis. After a purification step by flash column chromatography, this new compound was identified as **17** in 44% yield by the presence of characteristic catechol (δ 6.10 – 6.30 ppm) and FTC peaks in its ^{1}H NMR spectrum. As mentioned in the previous chapter, ^{1}H-^{13}C HMBC experiments were useful for determining the position of the created ester bond in these types of conjugates. As expected for **17**, a cross-coupling between proton H-5' of FTC and carbon C-1'' was observed in the corresponding spectrum (figure 4.1). Additionally, when comparing both chemical shifts of H-5' in FTC and **17** ^{1}H NMR spectra, a displacement to lower fields was observed, indicating a change in the chemical environment of H-5' in agreement with the formation of the ester bond through this position.

However, when the reaction was repeated under the same experimental conditions, a new compound, apart from **17**, was observed in the reaction crude by TLC analysis. After its purification, ^{1}H NMR spectra revealed the presence of FTC and **4** signals, but no shift of the peaks attributed to H-5' was observed. Moreover, changes in chemical shift in the proton located within the nitrogenated base (H-6) suggested the anchoring of **4** through the amino group as opposed to the hydroxyl group, that is, molecule **18** (figure 4.2 a).

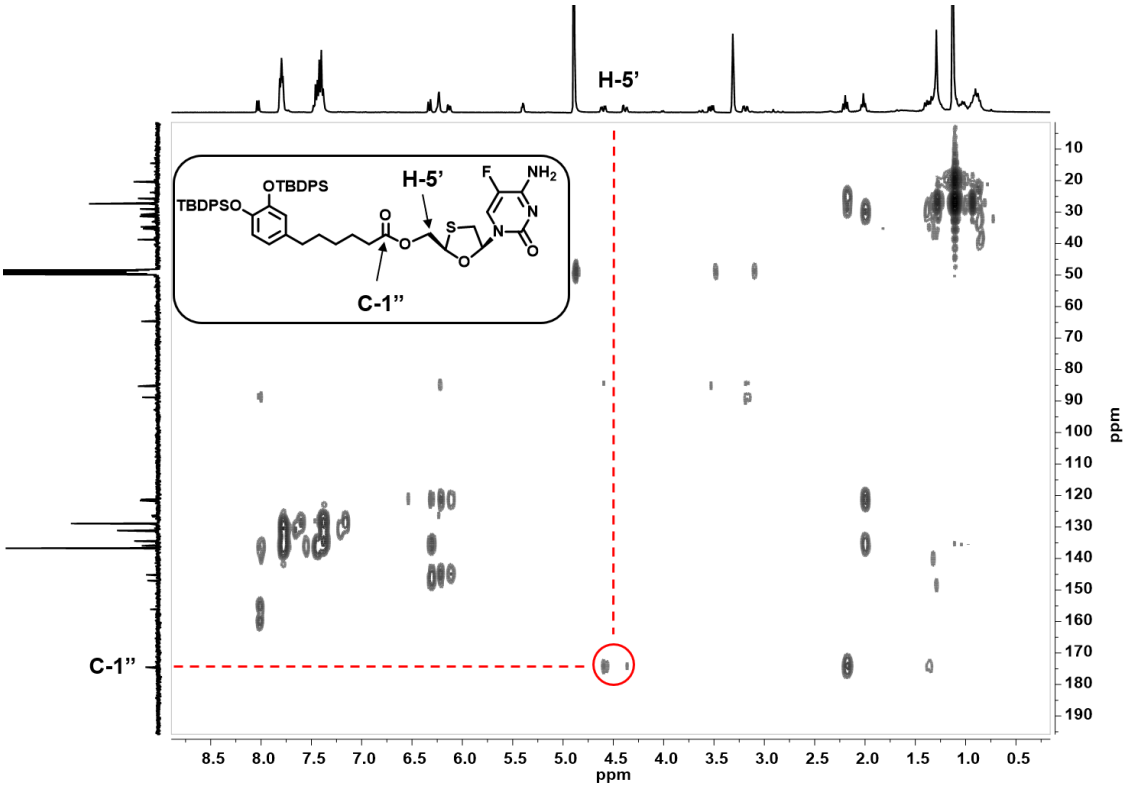

Figure 4.1. ^{1}H-^{13}C HMBC spectrum of **17** indicating the coupling between H-5' and C-1'.

HMBC experiments were also in agreement with structure **18**, since no cross-peak was observed between H-5' and C-1''. The lack of reproducibility became more evident since other attempts to carry out the reaction delivered mixtures of **17** and **18** in different proportions. In some cases, a compound less polar than both **17** or **18** was obtained and later identified as compound **19**, composed by an FTC core bearing two **4** moieties. Thus, a change in the experimental conditions was needed in order to obtain reproducible results and target compound **17** without the presence of other side products.

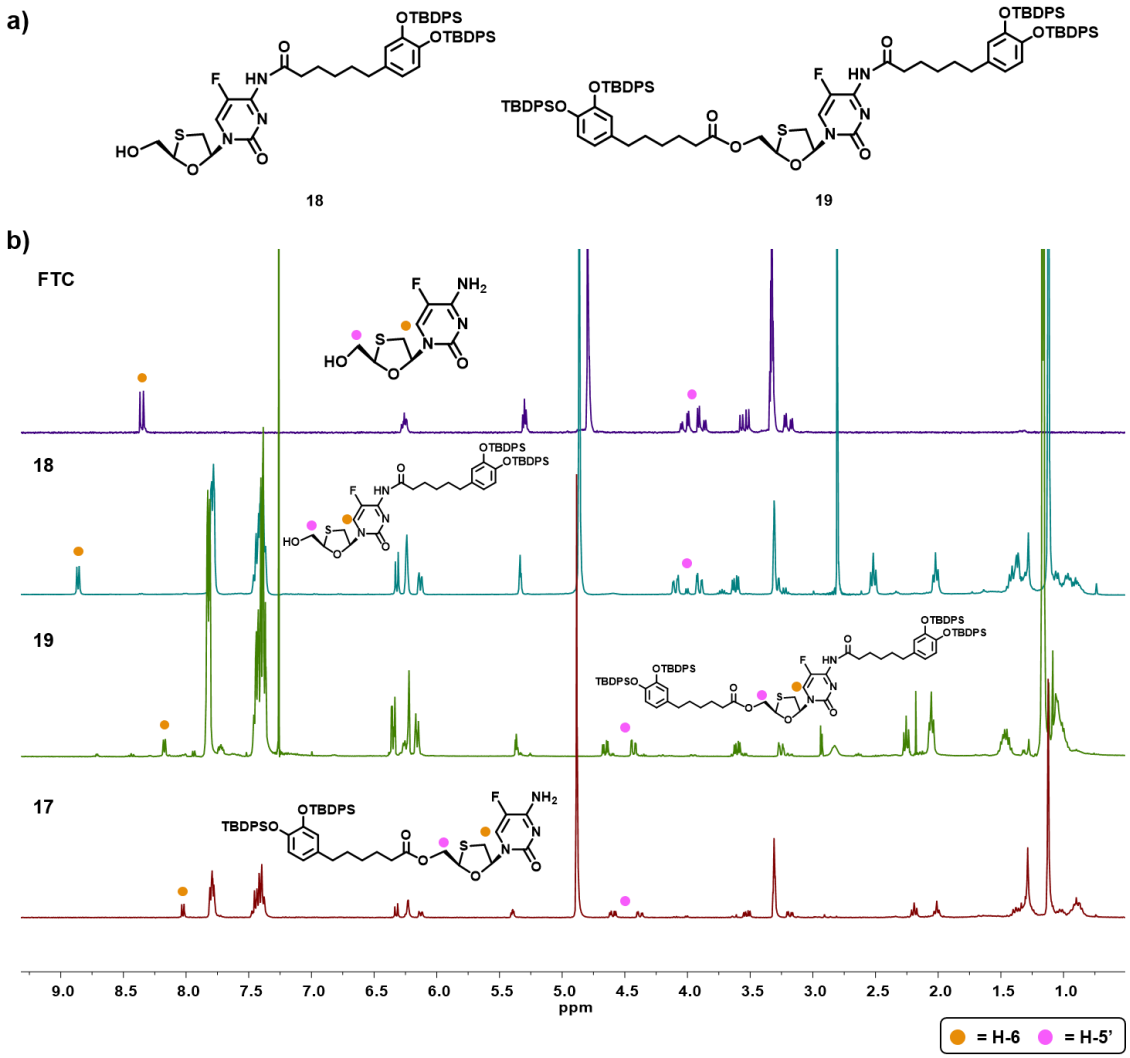

Figure 4.2. a) Chemical structures of side products found during the attempts of conjugation of FTC to **4**. b) ^{1}H NMR spectra of (top to bottom) FTC, **18**, **19** and **17**, recorded in CD_3OD, except **19** in $CDCl_3$. Signals corresponding to H-5' and H-6 are highlighted in each spectrum. The shift of the H-5' signal to lower fields indicate the formation of the ester bond through the hydroxyl group, while H-6 proton signal experiences a variation when the attachment is performed through the free amine group.

Therefore, a screening of different coupling agents, base and solvents was performed, summarized in table 4.1. First, the effect of variations in base equivalents was tested (table 4.1, entries 1-4). Ranging from 0 to 4 equivalents of DIPEA, the same mixture between ester **17** and amide **18** appeared, except for 0 equivalents, where no conversion was detected. Then, a Mitsunobu methodology using DBAD and PPh_3 was tested, but no conversion was observed by TLC analysis (table 4.1, entry 6). Following that, other coupling agents were examined, including PyBOP, CDI and DCC (table 4.1, entries 7-9). TLC and ^{1}H NMR analysis allowed the easy identification of products formed within reaction crudes. The presence of **19** was easily identified due to its high retention factor (R_f) in TLC and compounds **17** and **18**, which exhibited

similar Rf in TLC analysis, were identified by ^{1}H NMR due to the differences in chemical shift in their proton H-5' signals.

Table 4.1. Screening of different coupling agents for the synthesis of **17**. (*) indicates the use of a Mitsunobu methodology.

Entry	Coupling Agent	Base	Solvent	Temperature, reaction time	Product
1	HATU	DIPEA, 4 eq	THF	rt, overnight	**17/18**
2	HATU	-	THF	rt, overnight	-
3	HATU	DIPEA, 1.1 eq	THF	rt, overnight	**17/18**
4	HATU	DIPEA, 2.2 eq	THF	rt, overnight	**17/18**
5	HATU	DIPEA, 4 eq	THF/DMF (2:1)	rt, overnight	**17/18**
**6*	DBAD, PPh_3	-	THF	rt, overnight	**-**
7	PyBOP	DIPEA, 4 eq	THF (5% DMF)	rt, overnight	**18/19**
8	CDI	DIPEA, 4 eq	THF (5% DMF)	rt, overnight	**-**
9	DCC	DMAP, 0.3 eq	CH_2Cl_2	rt, overnight	**19**
10	EDCI	DMAP, 2 eq	DMF	rt, overnight	**17**

Finally, a bibliographic search revealed a chemoselective coupling of lamivudine (3TC), which is analogous to FTC, with 11-(acethylthio)undecanoic acid to afford the ester **20** as the only reaction product using EDCI and DMAP as base in DMF solution (scheme 4.2).[1]

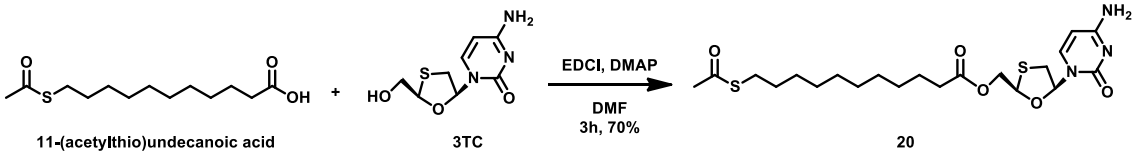

Scheme 4.2. Chemoselective coupling between lamivudine (3TC) and 11-(acetylthio)undecanoic acid to provide the ester product found in literature (ref 1).

Considering this data, the same conditions were applied to FTC and **4** (table 4.1, entry 10). Thus, after 3 h of reaction, an aliquot was extracted from the reaction mixture and analyzed by TLC. A new compound, less polar than FTC, and with the same R_f than the previously-obtained sample of **17** appeared. The reaction was then monitored by TLC at different time intervals and, in the end, it was left overnight to allow a full conversion. After no presence of FTC was detected by TLC, DMF was removed using aqueous washes, the crude was purified by column chromatography to afford a white solid identified as **17** in 97% yield (scheme 4.3). Repetition of the coupling by triplicate gave reproducible results ensuring the robustness of this methodology.

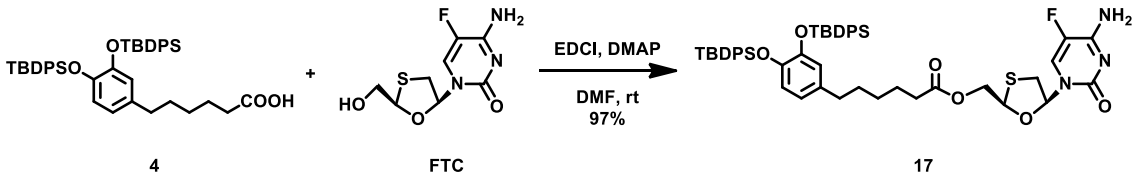

Scheme 4.3. Chemoselective coupling of **4** and FTC through its hydroxyl moiety using the experimental conditions described in reference 1.

4.1.1.2 Synthesis of ((2*R*,5*S*)-5-(4-amino-5-fluoro-2-oxopyrimidin-1(2*H*)-yl)-1,3-oxathiolan-2-yl)methyl 6-(3,4-dihydroxyphenyl)hexanoate, catFTC

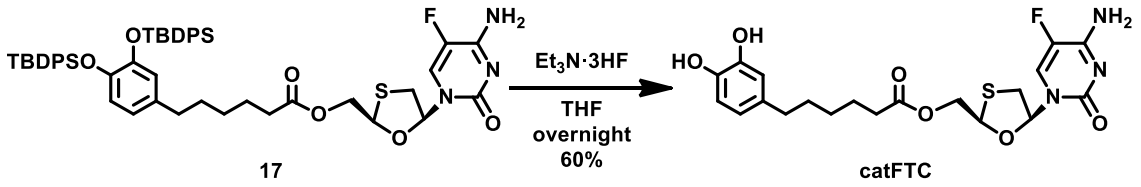

Final deprotection of **17** to afford target molecule **catFTC** was performed following the successful methodology previously used for **catAZT** and **catTHY**.[2] Thus, after addition of $Et_3N{\cdot}3HF$ to a solution of **17**, TLC analyses revealed the presence of a new, polar compound. After purification with flash column chromatography, this compound was identified as target molecule **catFTC** in 60% yield. Overall, **catFTC** was obtained through a 5-step synthetic sequence with 32% yield.

4.1.2 Synthesis of catRAL

4.1.2.1 Synthesis of 4-((4-fluorobenzyl)carbamoyl)-1-methyl-2-(2-(5-methyl-1,3,4-oxadiazole-2-carboxamido)propan-2-yl)-6-oxo-1,6-dihydropyrimidin-5-yl 6-(3,4-bis((tert-butyldiphenylsilyl)oxy)phenyl)hexanoate, 23

Concerning the functionalization of raltegravir through its –OH group, a previous bibliographic search showed a recent work in which cabotegravir, a molecule structurally similar to raltegravir, was functionalized in this position.[3] Specifically, in this work myristic acid (1-tetradecanoic acid) moiety was incorporated to the free hydroxyl group of cabotegravir in 85% yield via acyl chloride using myristoyl chloride, **21**, and DIPEA as base in DMF (scheme 4.4).

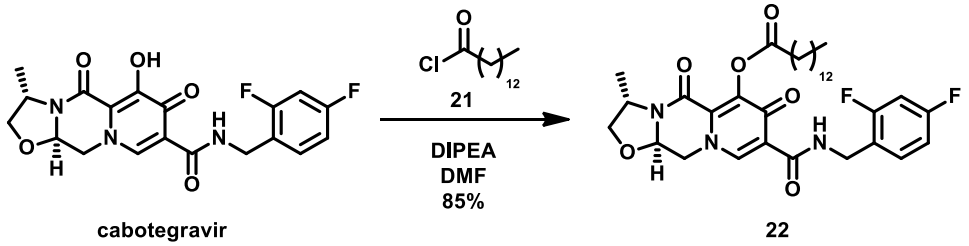

Scheme 4.4. Functionalization of the hydroxyl group of cabotegravir with myristic acid via acyl chloride.

Thus, taking into account these precedents, the synthetic strategy for the coupling of RAL and intermediate **4** was envisioned as follows (scheme 4.5). Fist, the acyl chloride derived from **4** was generated by the addition of oxalyl chloride to a solution of 4 in dichloromethane. After 3.5 h at room temperature, TLC analysis revealed the entire consumption of **4**. Then, the solvent was removed, and the crude was redissolved in DMF. Immediately and without further purification, raltegravir and DIPEA were added to the acyl chloride crude. After a few hours, a new compound, less polar than raltegravir was observed by TLC analysis. The reaction crude was left to evolve overnight to achieve the total consumption of raltegravir, and then purified by flash column chromatography. The ^{1}H NMR spectrum of the crude displayed characteristic signals for raltegravir and catechol moiety **4**. High resolution mass spectrometry (HRMS), ^{13}C NMR and bidimensional NMR experiments allowed the final identification of the new compound as conjugate **23**, obtained in 92% yield.

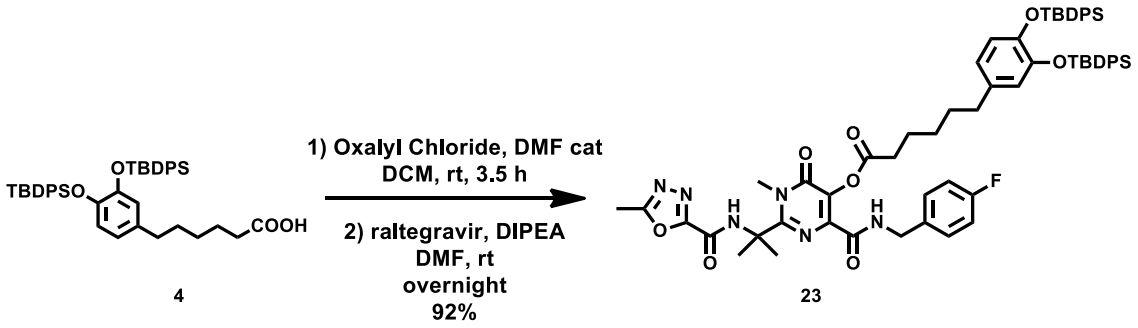

Scheme 4.5. Coupling of RAL and intermediate **4** via oxalyl chloride formation.

4.1.2.2 Synthesis of 4-((4-fluorobenzyl)carbamoyl)-1-methyl-2-(2-(5-methyl-1,3,4-oxadiazole-2-carboxamido)propan-2-yl)-6-oxo-1,6-dihydropyrimidin-5-yl 6-(3,4-dihydroxyphenyl)hexanoate, catRAL

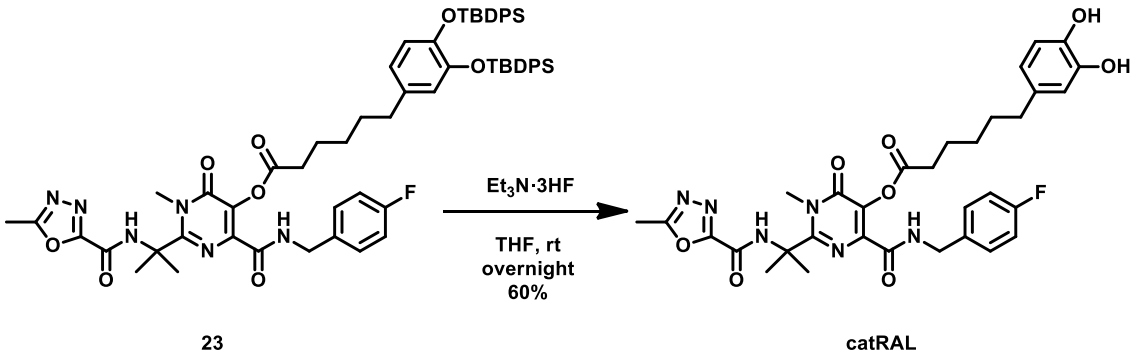

Removal of the silyl protecting groups TBDPS was performed following the same stablished methodology used in our research group.[2] Thus, simple addition of triethylamine trihydrofluoride to a solution of **23** allowed the disappearance of the characteristic TBDPS peaks (δ 7.80, 7.40 and 1.12 ppm) in the ^{1}H NMR spectrum and afforded target compound **catRAL** in

60% yield after a purification step using flash column chromatography. In summary, **catRAL** was obtained through five synthetic steps with a 30% overall yield.

4.2 Synthesis of NCPs using a combination of catRAL and catFTC

4.2.1 Synthesis of catRAL-NCPs and catFTC-NCPs

In this section, the synthesis of two different families of NCPs using **catRAL** (**catRAL-NCPs**) or **catFTC** (**catFTC-NCPs**) following the optimized procedure described for **catAZT-NCPs** will be described. Then, once both systems are characterized and fully understood, NCPs using a mixture of **catRAL** and **catFTC** (**catRAL-catFTC-NCPs**) will be prepared and compared with the previously prepared ARV-NCPs (section 4.2.2). First, the synthesis of nanoparticles made by the self-assembly of either **catRAL** or **catFTC** with the bridging ligand 1,4-bis((1*H*-imidazol-1-yl)methyl)benzene (**bix**) and Fe ions was attempted (scheme 4.6).

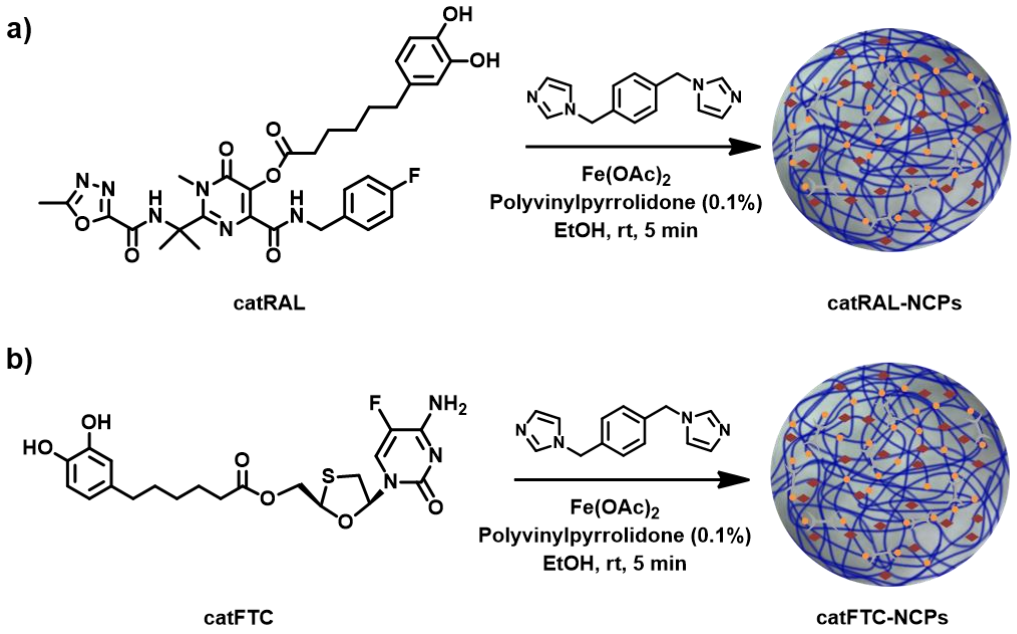

Scheme 4.6. Experimental conditions for the synthesis of a) **catRAL-NCPs** and b) **catFTC-NCPs**.

For this, the reactions were performed using the optimized experimental parameters applied for the synthesis of **catAZT-NCPs**, including the presence of 0.1% of polyvinylpyrrolidone (PVP) to control particle size. In this way, iron acetate (II) was added to a mixture of **bix** and the catechol-based ligand (**catRAL** or **catFTC**) inducing immediately the appearance of a dark-purple precipitate, which was collected by centrifugation, washed with ethanol and dried over vacuum.

SEM images revealed the formation of spherical particles for both ligands, with an average diameter of 104 ± 22 nm for **catRAL-NCPs** and 169 ± 29 nm for **catFTC-NCPs** (figure 4.3).

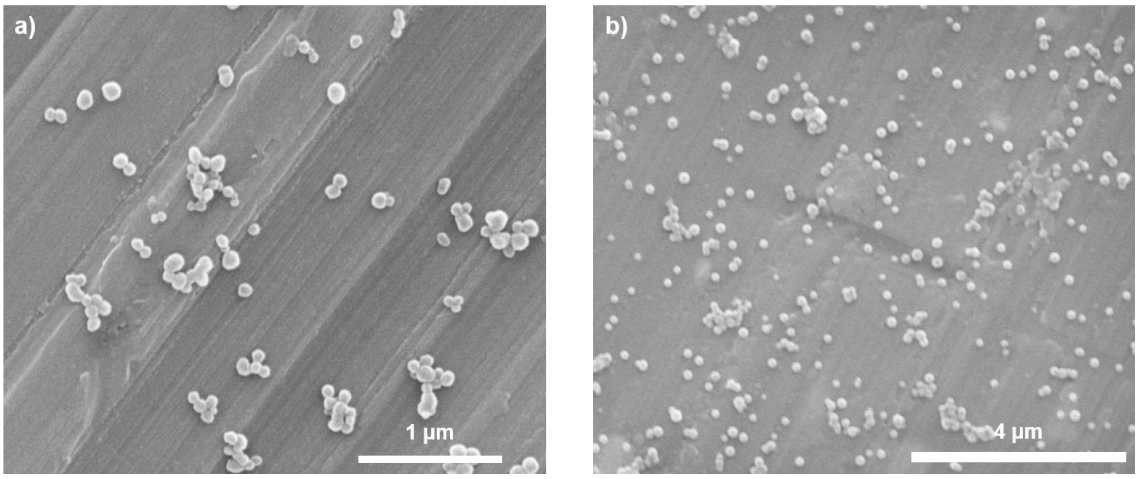

Figure 4.3. Representative SEM images of a) **catRAL-NCPs** and b) **catFTC-NCPs**.

Interestingly, DLS measurements in dispersion were in agreement with SEM micrographs, displaying a hydrodynamic diameter of 213 ± 3 nm in ethanol and 273 ± 34 nm in PBS/BSA 0.5 mM buffer for **catRAL-NCPs** and 166 ± 1 nm in ethanol and 179 ± 1 nm in PBS/BSA 0.5 mM buffer for **catFTC-NCPs** (figure 4.4). Additionally, FTIR spectra showed bands attributed to **bix** in both **catRAL-NCPs** (1509, 1258 and 1107 cm^{-1}) and **catFTC-NCPs** (1505, 1256 and 1114 cm^{-1}) as well as characteristic carbonyl absorption attributed to **catRAL** (1764, 1675 cm^{-1}) or **catFTC** ligands (1735, 1676 cm^{-1}).

In order to determine an average chemical formula for the polymeric structure of both **catRAL-NCPs** and **catFTC-NCPs**, different characterization techniques were used. The resulting data was then analyzed and finally an empirical formula in agreement with the aforementioned techniques was proposed. First, ^{1}H NMR was used to determine the ratio between NCPs ligands in each system, that is, **catRAL**/**bix** or **catFTC**/**bix** ratio. As before, NCPs were disassembled in an acidic media. Thus, the disaggregation of **catRAL-NCPs** and **catFTC-NCPs** was achieved in a methanolic solution of hydrochloric acid. Using deuterated hydrochloric acid and methanol, the ^{1}H NMR spectra of these solutions was recorded, as well as the corresponding spectra of **catRAL**, **catFTC**, RAL, FTC and **bix** (figure 4.5). The spectra of both NCPs revealed the presence of the corresponding catechol conjugates (**catRAL** or **catFTC**), **bix** and acetate ions from the iron acetate (II) salt used in NCPs synthesis. Then, the **catRAL**/**bix** and **catFTC**/**bix** ratio for **catRAL-NCPs** and **catFTC-NCPs**, respectively, was measured by peak integration of their characteristic signals shown in figure 4.5, averaging 3.20 in **catRAL-NCPs** and 1.58 in **catFTC-NCPs**. In both

cases, the ratio between ligands was observed to be reproducible in three independent batches of NCPs.

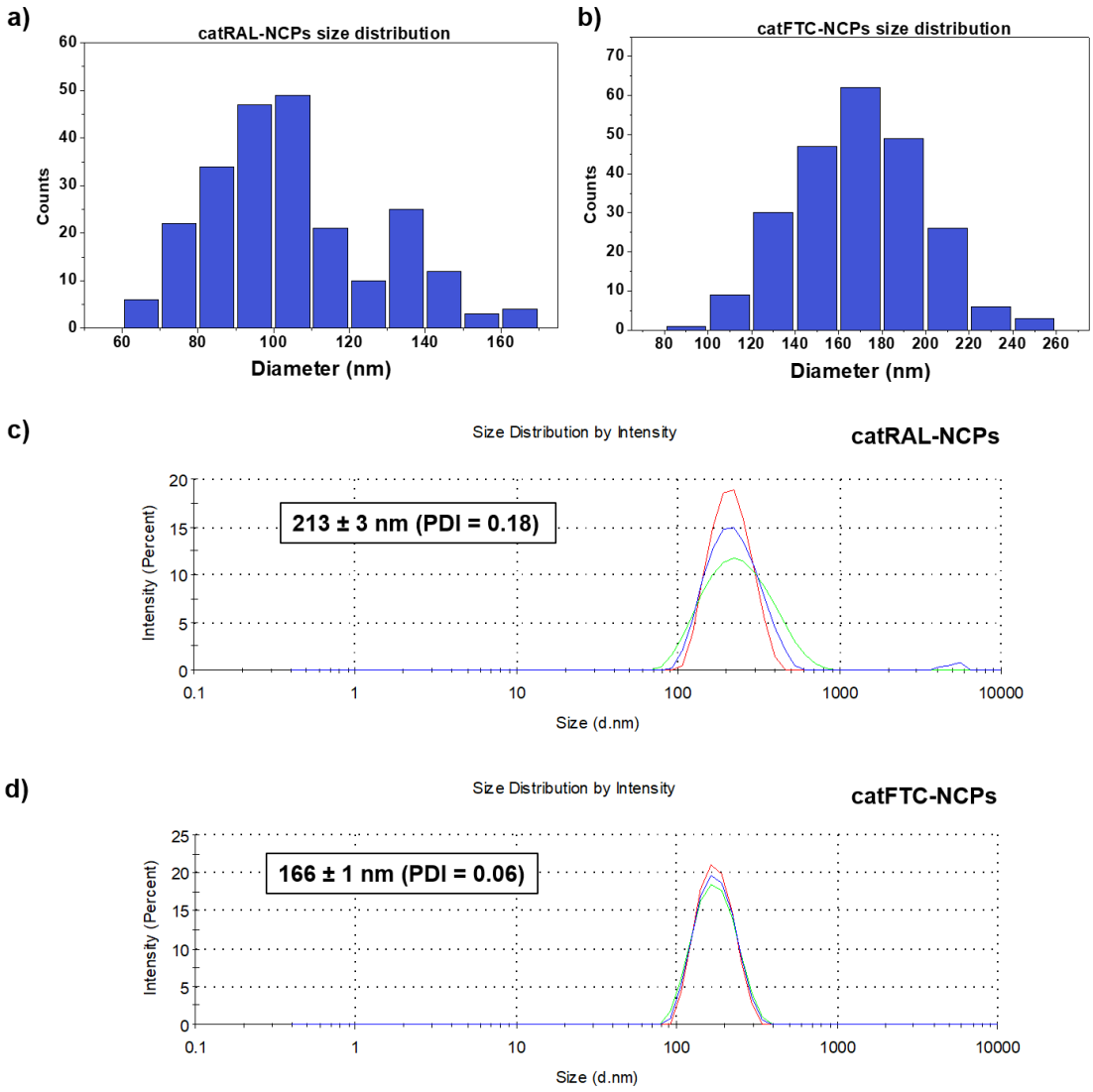

Figure 4.4. Particle size histogram extracted from SEM micrographs of a) **catRAL-NCPs** (233 particles, mean size 104 ± 22 nm) and b) **catFTC-NCPs** (233 particles, mean size 169 ± 29 nm). DLS measurements of c) **catRAL-NCPs** and d) **catFTC-NCPs** particle size in ethanol dispersion.

Elemental analysis was also used for stablishing an empirical formula for both **catRAL-NCPs** and **catFTC-NCPs**. First of all, consistent CHNS % values in three independent batches of each type of particle indicated the high robustness of our NCPs synthesis methodology. Then, a chemical formula for both polymers was fitted by the iterative adjustment of ligand stoichiometry using a software developed in our research group. This software determined the optimal empirical formula that simultaneously minimized the error with experimental CHNS % values while in agreement with the ligand ratios determined by ^{1}H NMR. Thus, the empirical formula $FeC_{28.5}H_{32.6}F_{0.8}N_{5.6}O_{8.2}$, adjusted as $Fe(catRAL)_{0.8}(bix)_{0.2}(AcO)_{0.2}(H_2O)_{1.6}$ was obtained for

catRAL-NCPs, whereas the empirical formula $FeC_{29.9}H_{35.6}F_{0.9}N_{5.0}O_{10.3}S_{0.9}$, adjusted as $Fe(catFTC)_{0.9}(bix)_{0.6}(AcO)_{2.0}(H_2O)_{1.0}$ was obtained for **catFTC-NCPs**. Despite the high reproducibility in the NCPs synthetic process, the empirical formula of both **catRAL-NCPs** and **catFTC-NCPs** was deviated from the theoretical stoichiometry, namely an Fe ion coordinated to two catechol moieties and one **bix** bridging ligand, in a similar way to **catAZT-NCPs** and **catTHY-NCPs**.

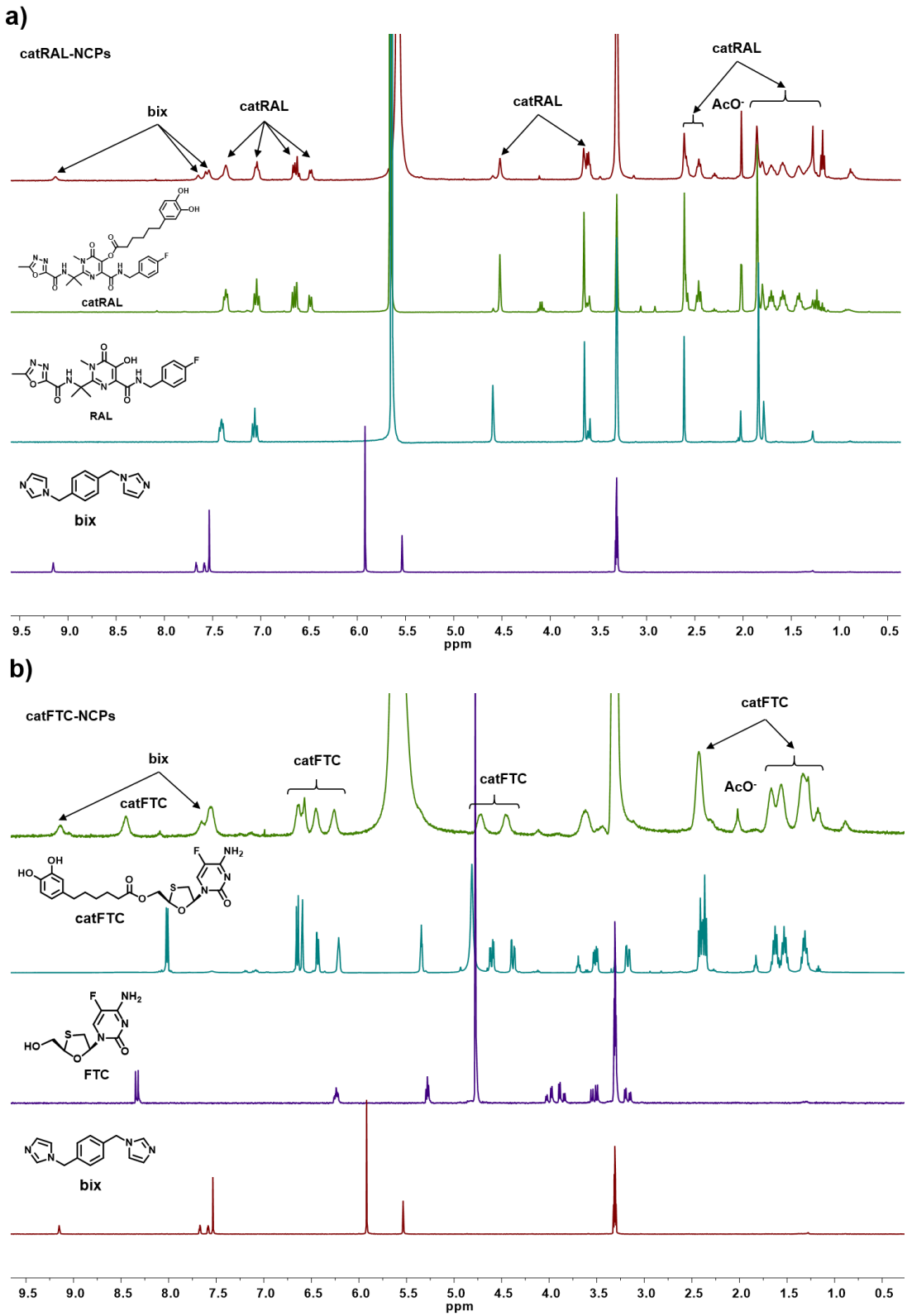

Figure 4.5. a) ^{1}H NMR spectra of (top to bottom) disassembled **catRAL-NCPs**, **catRAL**, RAL and **bix**. Peaks corresponding to **catRAL**, **bix** and acetate are observed in the ^{1}H NMR spectrum of **catRAL-NCPs**. b) ^{1}H NMR spectra of (top to bottom) disassembled **catFTC-NCPs**, **catFTC**, FTC and **bix**. Peaks corresponding to **catFTC**, **bix** and acetate are observed in the ^{1}H NMR spectrum of **catFTC-NCPs**. All spectra were recorded in a DCl/CD_3OD acidic solution (50 µL DCl/mL CD_3OD).

4.2.1.1 Quantification of drug release in catRAL-NCPs and catFTC-NCPs

As before, the release of antiretroviral drugs was expected to involve a two-step process, with a first stage of gradual NCPs degradation in aqueous media followed by the cleavage of the active ester bond through esterases (scheme 4.7).

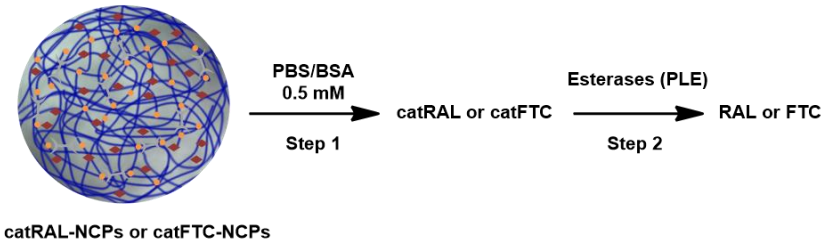

Scheme 4.7. Scheme of the different release steps for either **catRAL-NCPs** or **catFTC-NCPs**, including particle degradation (step 1) followed by enzymatic cleavage (step 2) of the ester bond.

Previous to the determination of the drug release kinetics of the NCPs, the enzymatic hydrolysis of **catRAL** and **catFTC** was studied independently. Both catechol-ARV conjugates were incubated at 37 °C in a simulated physiological media composed by a 0.5 mM solution of bovine serum albumin (BSA) in a phosphate buffer (PBS) at pH 7.4 in the presence or absence of the model esterase PLE (pig liver esterase) at a concentration comparable to that found inside the body (180 U/L).[4] Aliquots were then taken at different periods of time, from 5 min to 72 hours approximately, filtered through a 10 kDa membrane to remove BSA and PLE and stored in the freezer until injected into the HPLC instrument. At this point, the aliquots coming from **catRAL** and **catFTC** incubation were analyzed independently, that is, two different HPLC methods were developed to separate and quantify **catRAL** from RAL and **catFTC** from FTC.

For the quantification, in each case, standards containing both analytes, i.e. **catRAL**/RAL and **catFTC**/FTC, were prepared and injected into the reversed-phase HPLC system. pH of the mobile phase was set acidic using phosphoric acid due to the acidic nature of catechols, otherwise acid-base equilibria would cause problems of peak resolution and shape distortion, especially peak tailing.[5] Initially, an isocratic approach, that is, maintaining the same mobile phase composition during the entire analysis was attempted for simplification purposes. Although the separation of the peaks of both analytes was eventually accomplished using this approach, the difference in polarity between the analytes caused a large analysis runtime. To reduce the runtime, which was especially important here due to the large number of samples analyzed, a mixture of isocratic and gradient elution was used.[6] Detector wavelength was set at 214 nm as a control and at 280 nm due to the high absorptivity of the chemical species in that region. After the

modification of these parameters in a systematic approach, acceptable resolution between the different analytes in a reasonable runtime was obtained for both **catRAL**/RAL and **catFTC**/FTC standards (figures 4.6 a and b). Then, with these optimized methods, calibration curves using standards at concentrations ranging from 1 to 1150 µM for **catRAL**/RAL and 1 to 1800 µM for **catFTC**/FTC, approximately, were successfully prepared using the corresponding peak area for each analyte ($R^2 \geq 0.99$) (figures 4.6 c and d).

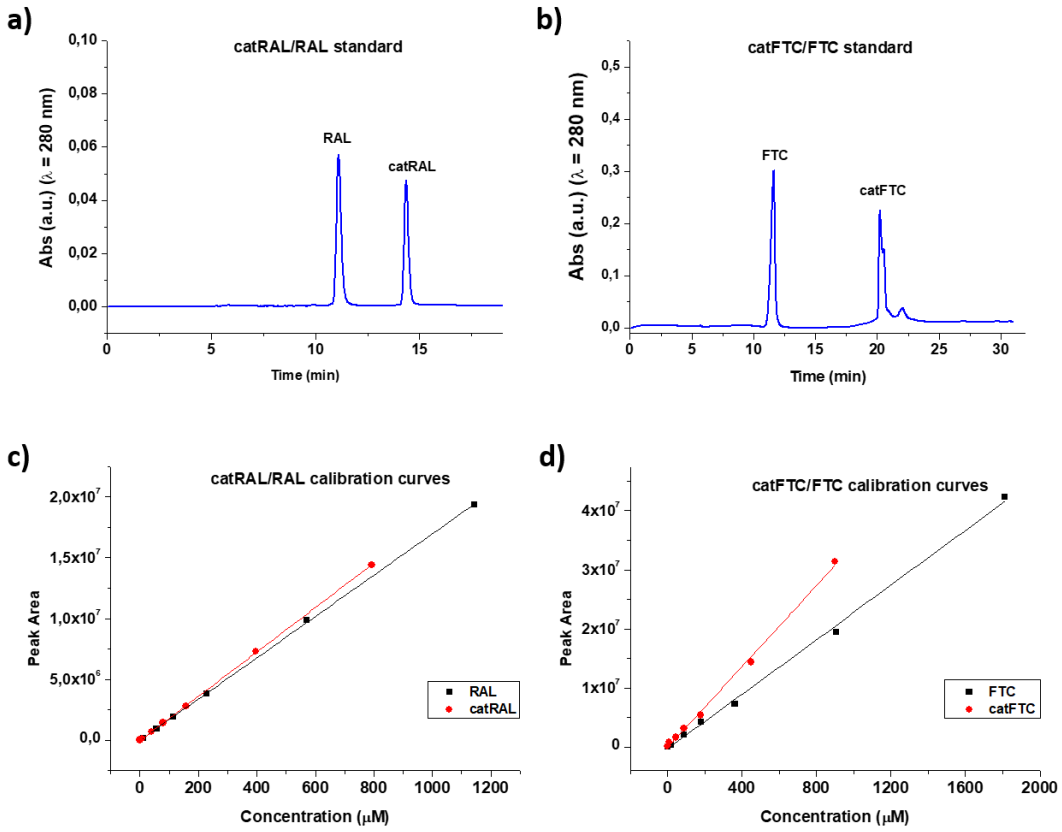

Figure 4.6. Representative chromatograms of a) **catRAL**/RAL (at 40 and 57 µM, respectively) and b) **catFTC**/FTC (at 180 and 362 µM, respectively) standards. Calibration curves for c) **catRAL** and RAL and d) **catFTC** and FTC (n = 7, $R^2 \geq 0.99$).

Next, the **catRAL**/**catFTC** incubation aliquots were analyzed following the corresponding optimized HPLC methods. Figures 4.7 a and b show the expected process for both catechol-ARV conjugates, consisting in a PLE-mediated cleavage of their ester bond. Figures 4.7 c and d show representative chromatograms obtained for both enzymatic processes. Employing the HPLC methods and the calibration curves developed previously, we were able to quantify the chemical species of interest in each sample. The amount of RAL and FTC released at different time intervals, in the presence or absence of esterases can be observed in figure 4.7 e and f. In this case, the data is presented as the relative amount of antiretroviral drug released versus time. This percentage of released drug was calculated as follows: for each point, a concentration of

RAL or FTC was determined by interpolation with their corresponding calibration curve, and it was divided by the concentration at the end of the hydrolysis, measured by triplicate in additional aliquots acidified with HCl.

Concerning **catRAL**, no significant variation in the reaction rate was observed independently of the presence or absence of esterases (~80% in 24 h). This could be attributed to the fact that pig liver esterase, the model esterase used, is classified in the EC 3.1.1.1 enzyme group, which includes carboxylesterases for the hydrolysis of aliphatic alcohols and therefore **catRAL** would not be a suitable substrate for it, requiring a EC 3.1.1.2 arylesterase instead.[7] The effects of esterases, on the other hand, were clearly visible in the case of **catFTC**. In the absence of PLE, hydrolysis of **catFTC** was observed to be slow, with approximately 50% of FTC released after 65 hours. When PLE was added under the same experimental conditions, a fast release of the antiretroviral drug was observed, with nearly 100% completed in 1 hour.

The next step consisted in the determination of RAL and FTC release in **catRAL-NCPs** and **catFTC-NCPs**, respectively (figure 4.8 a). In both cases, the release was performed under the same experimental conditions previously explained for **catRAL** and **catFTC**, i.e., NCPs were incubated under simulated physiological conditions at 37 °C in PBS/BSA 0.5 mM at pH 7.4 in the presence or absence of esterases at 180 U/L. Aliquots were taken at different time intervals, ranging from 5 min to 72 hours approximately, filtered through a 10 kDa membrane to remove BSA, PLE and non-degraded NCPs and stored in the freezer until analyzed by HPLC. The optimized HPLC methods for the analysis of **catRAL**/RAL and **catFTC**/FTC were used to unequivocally quantify each chemical species. Representative chromatograms of these aliquots can be observed in figures 4.8 b and c. Moreover, figures 4.8 d and show the graphical representation of the ratio of antiretroviral drug released versus time in **catRAL-NCPs** and **catFTC-NCPs**, respectively, in the presence or absence of esterases. To calculate each percentage value, the concentration determined by interpolation with their corresponding calibration curve was divided by the value corresponding to the 100% release. This value was calculated, for each experiment, by triplicate in aliquots treated with HCl in methanol. Under these conditions, as mentioned in the section 4.2.1, NCPs disassemble into their components, releasing in this case the remaining **catRAL** and **catFTC**, which are then transformed into RAL and FTC respectively. As the amount of NCPs in each incubation experiment had been perfectly weighted, the samples that represented the 100% release allowed, additionally, the quantification of drug loading of **catRAL-NCPs** and **catFTC-NCPs**. Thus, an average of 10 wt% of RAL was found in **catRAL-NCPs**, whereas FTC in **catFTC-NCPs** averaged a 27 wt%.

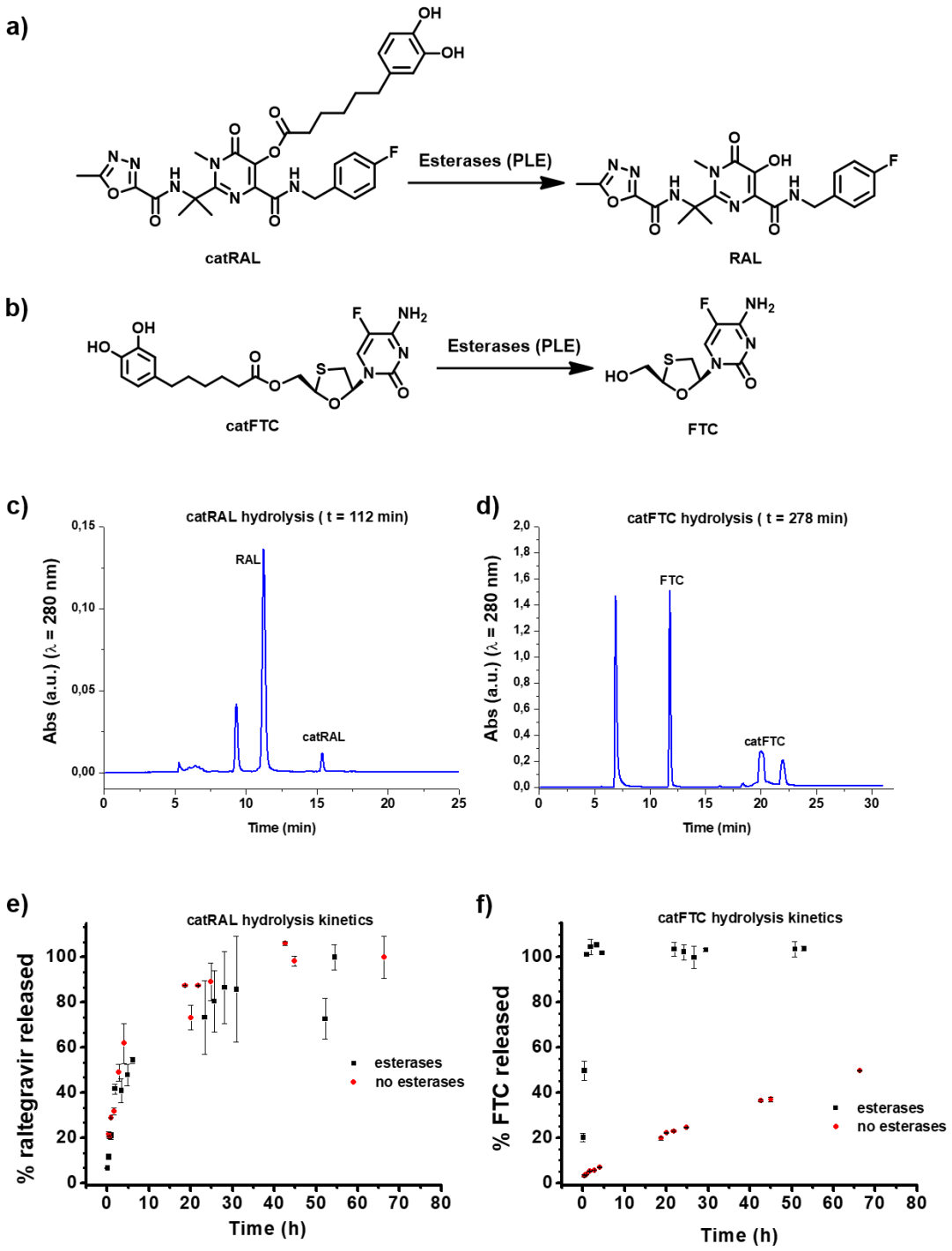

Figure 4.7. Scheme of the enzymatic cleavage of a) **catRAL** and b) **catFTC** by PLE. Representative chromatograms of c) **catRAL** (t = 112 min) and d) **catFTC** incubation aliquots (t = 278 min) at 37 °C in the presence of esterases (PLE, 180 U/L). Non-marked peaks are attributed to either solvent or degradation by-products of **catRAL** and **catFTC**. Hydrolysis kinetics of e) **catRAL** and f) **catFTC** in the presence (esterases) or absence (no esterases) of pig liver esterases (PLE, 180 U/L) at pH 7.4. Experiments were performed by duplicate in PBS/BSA 0.5 mM buffer at 37 °C.

The results for the NCPs and their comparison to the free ligands can be found in table 4.2. Regarding **catRAL-NCPs**, the data showed a slow release independently of the presence of esterases, in agreement with the behavior of the free ligand **catRAL**. However, effects of its

nanostructuration can be observed, as NCPs protects **catRAL** from hydrolysis, lowering its reaction rate and offering a more sustained release (78% in 24 h for the free ligand versus 39% in 24 h for NCPs). This effect was also observed for **catFTC-NCPs**. In absence of esterases, the presence of FTC was low (20% at 72 h), whereas with the addition of PLE, 86% of FTC was relased after 72 hours, with a half-life of ~3 hours. Thus, the protective effect of nanostructuring the ligand into NCPs was clearly observed as a 70-fold increase in the complete release time when compared with the free ligand **catFTC**.

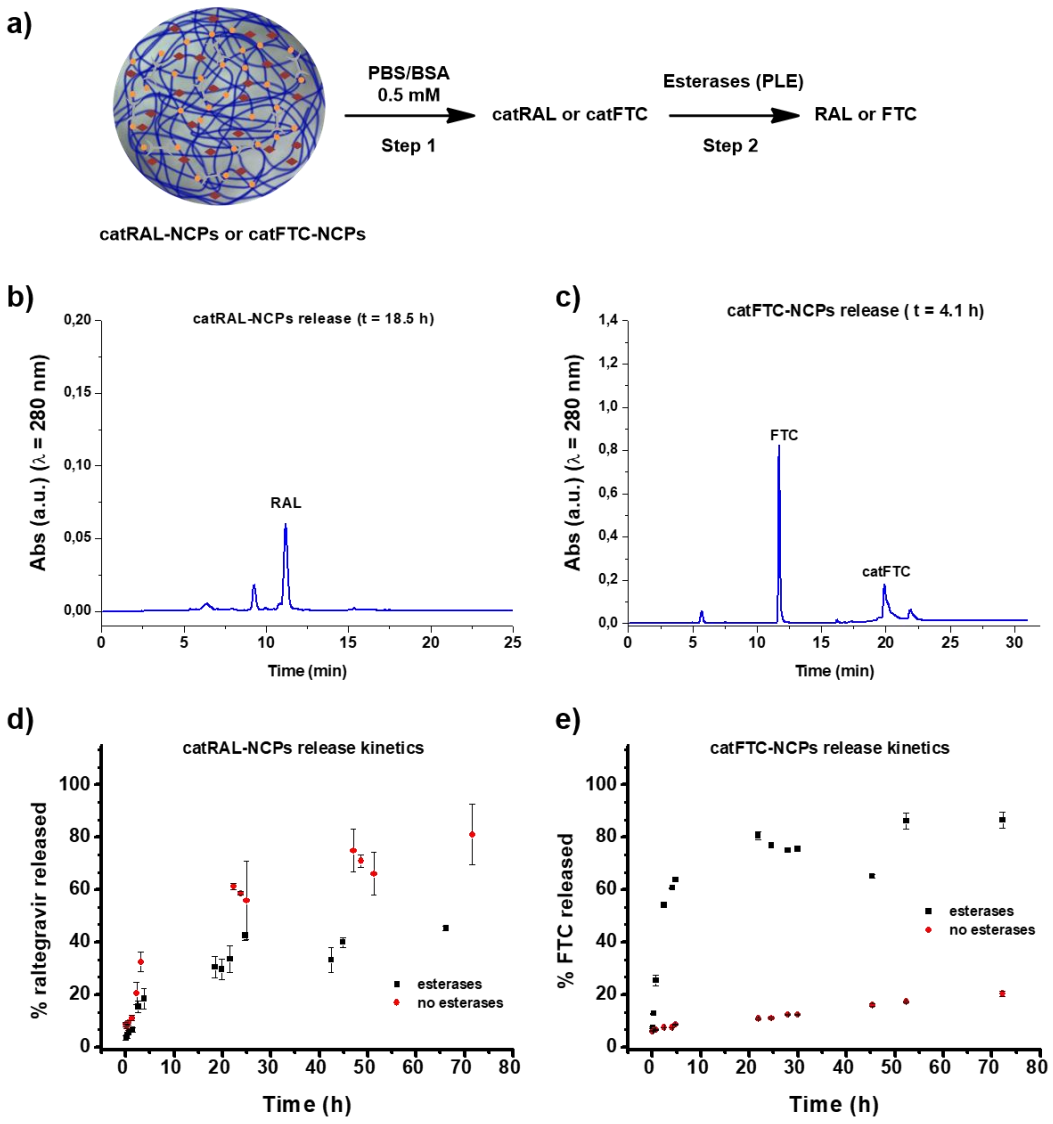

Figure 4.8. a) Schematic representation of the different release steps for either **catRAL-NCPs** or **catFTC-NCPs**, including particle degradation (step 1) followed by enzymatic cleavage (step 2) of the ester bond. b) and c) Representative chromatograms of **catRAL-NCPs** (t = 18.5 h) and **catFTC-NCPs** (t = 4.1 h) incubation aliquots at 37 °C in the presence of esterases. Non-marked peaks are attributed to either solvent or degradation by-products of **catRAL** and **catFTC**. d) and e) **catRAL** and **catFTC** release kinetics from the corresponding NCPs in the presence (esterases) or absence (no esterases) of pig liver esterase (PLE, 180 U/L). All experiments were performed by duplicate in PBS/BSA 0.5 mM pH 7.4 buffer at 37 °C.

Table 4.2. Summary of the amount of drug released at 24 and 72 h in **catRAL**, **catRAL-NCPs**, **catFTC** and **catFTC-NCPs** release experiments. (*) indicates the complete release within the first hour.

	% drug released at 24 h		**% drug released at 72 h**	
	PLE	*no PLE*	*PLE*	*no PLE*
catRAL	78	87	100	100
catRAL-NCPs	39	55	50	80
catFTC	100*	25	100*	50
catFTC-NCPs	77	11	86	20

4.2.2 Synthesis of NCPs combining catRAL and catFTC

Once the behavior of **catRAL-NCPs** and **catFTC-NCPs** was described, the next step was to incorporate both antiretroviral drugs inside the same NCP structure, namely **catRAL-catFTC-NCPs**. The objective was to emulate commercial ARV combinations, so that both drugs are guaranteed to be released simultaneously under the same mechanisms.

In particular, the ratio between ARV drugs corresponded to a raltegravir/lamivudine 1:1 molar ratio. Thus, an equimolar mixture of both **catRAL-NCPs** and **catFTC-NCPs** was used to form **catRAL-catFTC-NCPs**. The self-assembly of both catechol derivatives with the bridging ligand **bix** and Fe ions, was carried out following the same optimized procedure than for the previous NCPs. Consequently, iron acetate (II) dissolved in ethanol was added to an ethanolic mixture of **bix**, **catRAL** and **catFTC**, instantaneously inducing the appearance of a dark-purple precipitate, collected by centrifugation, washed with ethanol to remove unreacted ligands and dried over vacuum. As before, the reaction mixtures contained a 0.1% of polyvinylpyrrolidone to prevent aggregation and control particle size during the synthetic process. A representative illustration of the reaction is shown in scheme 4.8. SEM micrographs of the dark-purple precipitate obtained revealed the formation of spherical particles. Like in the previous NCPs synthesized, DLS measurements were in agreement with SEM micrographs, displaying in ethanol a hydrodynamic diameter of 232 ± 1 nm and 220 ± 1 nm in PBS/BSA 0.5 mM buffer. Additionally, FTIR spectra showed bands attributed to **bix** in both **catRAL-NCPs** (1509, 1258 and 1107 cm^{-1})and **catFTC-NCPs** (1508, 1257 and 1108 cm^{-1}) as well as characteristic carbonyl bands attributed to **catRAL** and **catFTC** (1737, 16775 cm^{-1}).

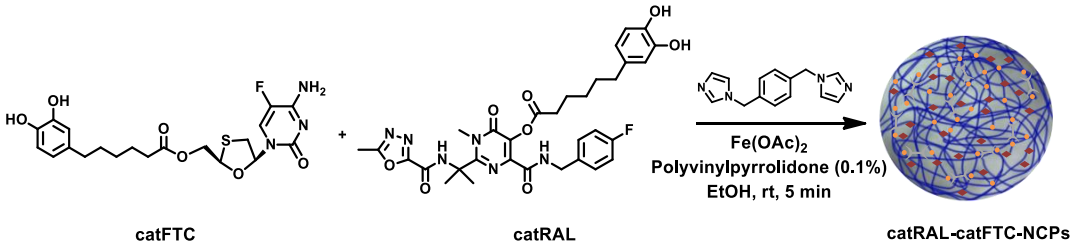

Scheme 4.8. Scheme of the synthesis of NCPs combining the antiretroviral drugs raltegravir and emtricitabine (**catRAL-catFTC-NCPs**).

The chemical composition of **catRAL-catFTC-NCPs** was studied in a similar way to that explained for **catRAL-NCPs and catFTC-NCPs** (section 4.2.1). First, ^{1}H NMR of disassembled **catRAL-catFTC-NCPs** was recorded in a methanolic solution of deuterated hydrochloric acid. The spectra revealed the presence of **catRAL**, **catFTC**, **bix** and acetate ions coming from the acetate salt used in the synthetic process as a source of iron ions (figure 4.9). Using the characteristic peaks for each chemical species marked in figure 4.9, the **catRAL**/**catFTC** ratio was determined and equal to 1.1, whereas the ratio between both catechol ligands and **bix**, i.e., (**catRAL**+**catFTC**)/**bix** ratio was found to average 3.7. In both cases, the aforementioned ratios were consistent among three independent batches of **catRAL-catFTC-NCPs**.

Elemental analysis data of **catRAL-catFTC-NCPs** was also consistent with the previous observation, as CHNS % values were maintained among three independent NCPs batches. Then, as before, a chemical formula for the NCPs was fitted by the iterative adjustment of its ligand stoichiometry. This adjustment calculated the empirical formula that simultaneously minimized the error with CHNS % experimental values while in agreement with the ligand ratios determined by ^{1}H NMR. However, similarly to the other families of NCPs described during this dissertation, despite the high degree of reproducibility in NCPs synthesis, the resulting empirical formula did not adjust to the theoretical 2:1 catechol-iron ratio. Accordingly, the formula $FeC_{36.8}H_{41.8}F_{1.2}N_{6.6}O_{11.3}S_{0.6}$ was acquired for **catRAL-catFTC-NCPs**, which translated into $Fe(catFTC)_{0.5}(bix)_{0.3}(catRAL)_{0.6}(AcO)_{1.0}(H_2O)_{1.2}$.

It is worth mentioning that, although an equimolar combination of catechols had been used in the synthesis of the particles, the resulting ratio **catRAL**/**catFTC** was found to be 1.1. Nevertheless, this ratio stands for an excellent result as it did not represent a considerable deviation from the original 1:1 ratio. Moreover, previous tests consisting in introducing different ligands in a specific proportion in NCPs, like the experiments described in Chapter 3, section 3.2, using **catAZT** and caffeic acid mixtures or other ones described previously in our research group had revealed the difficulties of controlling

ligand proportions in these materials. In this case, the rationale behind this fact could be attributed to similarities in steric hindrance and metal affinity between both ligands.

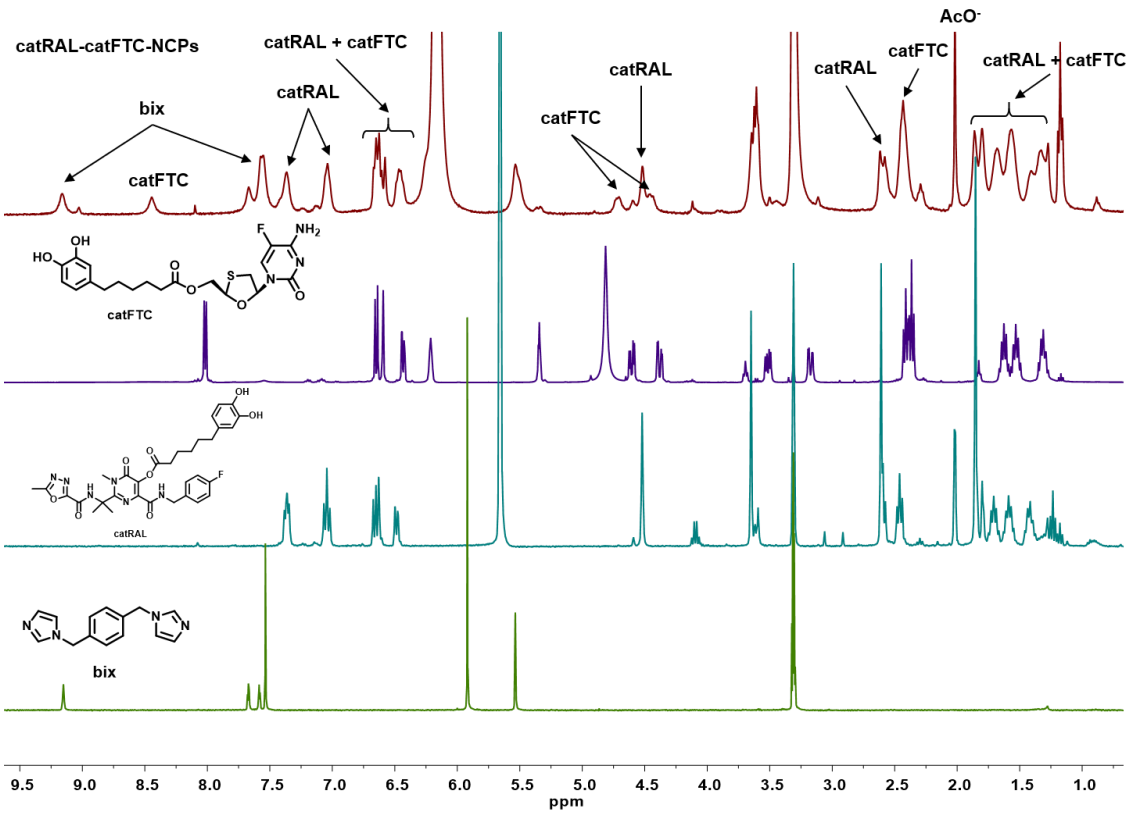

Figure 4.9. ^{1}H NMR spectra of (top to bottom) disassembled **catRAL-catFTC-NCPs**, **catFTC**, **catRAL** and **bix.** Peaks corresponding to **catRAL**, **catFTC**, **bix** and acetate are observed in the ^{1}H NMR spectrum of **catRAL-catFTC-NCPs**. All spectra were recorded in a DCl/CD_3OD acidic solution (50 µL DCl/mL CD_3OD).

4.2.2.1 Quantification of drug release in catRAL-catFTC-NCPs

The release of both antiretroviral drugs structuring **catRAL-catFTC-NCPs**, RAL and FTC, was monitored by HPLC-UV following similar procedures than for the free ligands catRAL and catFTC and the NCPs catRAL-NCPs and catFTC-NCPs.

Prior to this study, however, a further optimization in the HPLC methodology was necessary to quantify simultaneously the four potential chemical species released: RAL, **catRAL**, FTC and **catFTC**, along with other degradation by-products. In section 4.2.1.1, we described the preparation of HPLC methodologies to analyze **catRAL**/RAL and **catFTC**/FTC separately. Thus, samples containing the four species were injected into the HPLC system using both methods, but peak separation was not achieved in any case. Of the parameters described in section 4.2.1.1, the pH of the mobile phase was maintained and equal to acidic. Mobile phase composition and elution mode, isocratic and gradient, were systematically modified in this case to achieve the separation of the four species. FTC was initially separated easily from **catFTC**, RAL

and **catRAL** due to its high difference in polarity: FTC is poorly retained in the non-polar stationary phase of the HPLC column, whereas the other compounds are more retained under the same conditions. The separation of the three remaining compounds was more difficult due to their similarity in polarity. Acceptable resolution between their peaks, along with reasonable analysis runtime, was eventually achieved in a systematic approach way using a set of three different gradients alternated with isocratic periods (figure 4.10 a). Then, using this optimized parameters, a series of standards containing **catRAL**, RAL, **catFTC** and FTC were prepared at concentrations ranging from 1 to 1715 µM and analyzed to obtain the corresponding calibration curve for each analyte (figure 4.10 b).

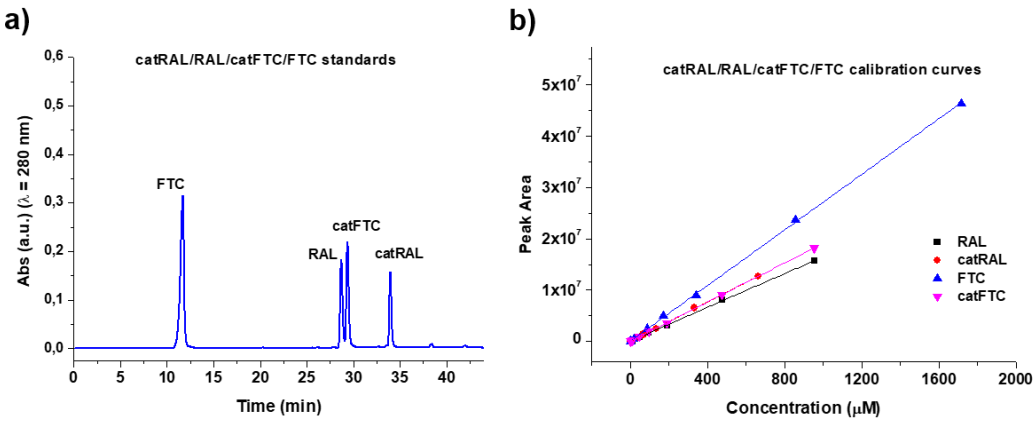

Figure 4.10. a) Representative chromatogram of **catRAL**/RAL/**catFTC**/FTC standards (at 133, 191, 191 and 343 µM, respectively. b) Calibration curves for **catRAL**, RAL, **catFTC** and FTC (n = 7, $R^2 \geq 0.999$).

The next step consisted of the evaluation of the two-step process of drug release in **catRAL-catFTC-NCPs** (figure 4.11 a). The nanoparticles were incubated at 37 °C in a simulated physiological media composed by a 0.5 mM solution of bovine serum albumin (BSA) in a phosphate buffer (PBS) at pH 7.4 in the presence or absence of the model esterase PLE (pig liver esterase) at a concentration comparable to that found inside the body (180 U/L). Aliquots were taken at different time intervals, ranging from 5 min to 140 hours approximately, filtered through a 10 kDa membrane to remove BSA, PLE and non-degraded NCPs and stored in the freezer until analyzed. The aforementioned optimized HPLC method was used to quantify RAL and FTC in these aliquots. A representative chromatogram can be found in figure 4.11 d. Figures 4.11 b and c display the relative amount of antiretroviral drug released versus time in **catRAL-catFTC-NCPs**. To calculate each value, the concentration determined by interpolation with their corresponding calibration curve was divided by the value corresponding to the 100% release. This value was calculated, for each experiment, by triplicate in aliquots treated with HCl in methanol. Under these conditions, as mentioned in the section 4.2.1, NCPs disassemble into

their components, releasing in this case the remaining **catRAL** and **catFTC**, which are then transformed into RAL and FTC respectively. Like in **catRAL-NCPs** and **catFTC-NCPs** release analysis, the samples representing the 100% release allowed the quantification of the % of drug inside the NCPs. Thus, **catRAL-catFTC-NCPs** presented and average of 13 wt% in RAL and 15 wt% in FTC. Finally, figure 4.11 e shows a representation of the RAL/FTC molar ratio at each time interval in the incubation with esterases (figure 4.11 b).

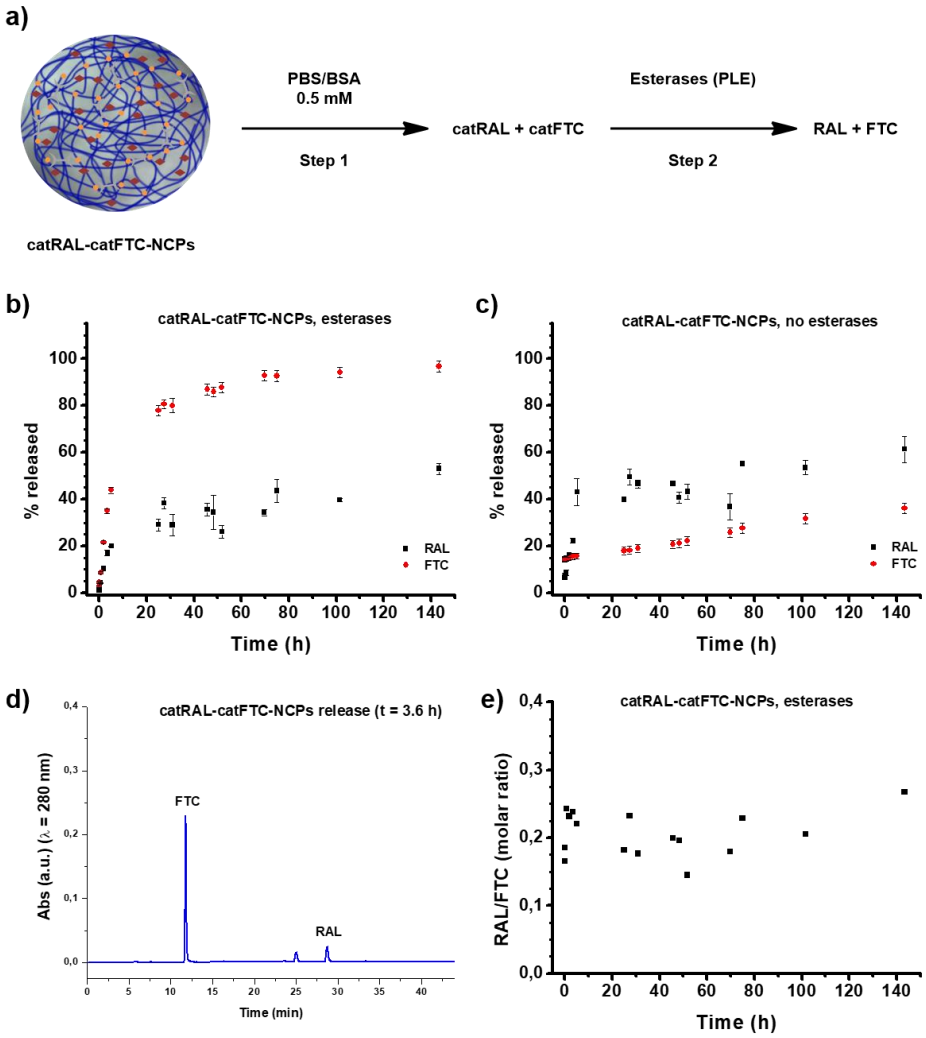

Figure 4.11 a) Scheme of the different release steps for **catRAL-catFTC-NCPs**, including particle degradation (step 1) followed by enzymatic cleavage (step 2) of the ester bond. b) and c) **catRAL-catFTC-NCPs** release kinetics in the presence (esterases) or absence (no esterases) of pig liver esterase (PLE, 180 U/L). All experiments were performed by duplicate in PBS/BSA 0.5 mM pH 7.4 buffer at 37 °C. d) Representative chromatogram of **catRAL-catFTC-NCPs** (t = 3.6 h) incubation aliquots at 37 °C in the presence of esterases. Non-marked peak is attributed to degradation by-products. e) Representation of the RAL/FTC molar ratio through the incubation of **catRAL-catFTC-NCPs** in the presence of esterases.

The antiretroviral drug release profile obtained for **catRAL-catFTC-NCPs** in the presence of esterases did not significantly differ from the data acquired for the NCPs containing a single antiretroviral drug, **catRAL-NCPs** and **catFTC-NCPs** (figure 4.12). Thus, both ARV drugs

experienced a slow release, being FTC released faster (~80% in 24 h) than RAL (~35% in 24 h) , but in any case, slower than the free ligands (100% in 1 h for **catFTC** and ~80% in 24 h for **catRAL**). In the absence of esterases, RAL experienced a slightly slower release compared to **catRAL-NCPs** at 24 h (~40% vs ~55%, respectively), whereas FTC release was slightly increased (~18% vs ~12%, respectively).

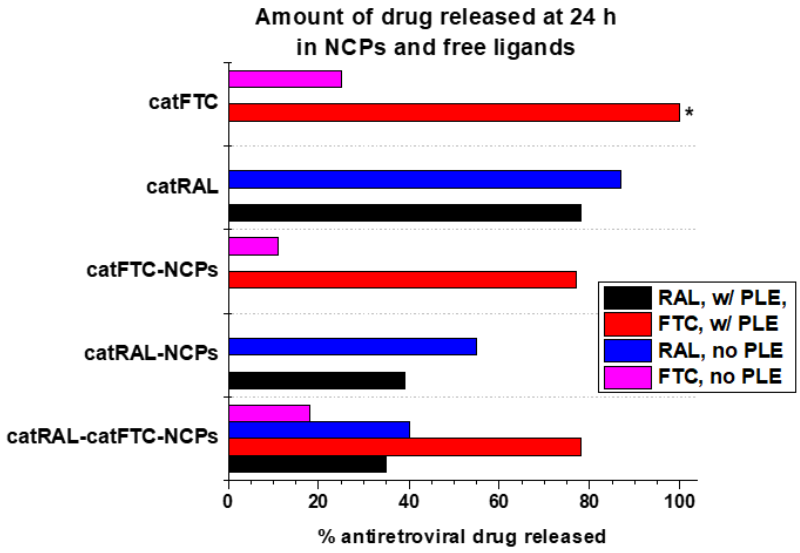

Figure 4.12. Comparison between % of drug released at 24 h in **catFTC**, **catRAL**, **catRAL-NCPs**, **catFTC-NCPs** and **catRAL-catFTC-NCPs** in the presence and absence of esterases (PLE). (*****) indicates the complete release within the first hour.

Lastly, although the composition of **catRAL-catFTC-NCPs** contained an equimolar amount of both RAL and FTC, the differences in their release profiles could suggest that, effectively, both drugs would not be delivered in a 1:1 molar ratio. In fact, the RAL/FTC molar ratio was calculated for each point in the incubation of **catRAL-catFTC-NCPs** in the presence of esterases (figure 4.12, b). Interestingly, the ratio between both drugs was rather constant but oscillated between 0.15 and 0.26, far from the desired value of 1. In order to achieve the desired RAL/FTC ratio, in the following section the formation and release profile of **catRAL-catFTC-NCPs** with different ARV drug proportions will be described.

4.2.2.2 Adjustment of RAL/FTC ratio in catRAL-catFTC-NCPs drug release

Taking into account the drug release data displayed in section 4.2.2.1 for **catRAL-catFTC-NCPs**, we hypothesized that a fine-tuning of the **catRAL/catFTC** ratio during the NCPs synthetic process could be achieved so that both RAL and FTC would be released in an equimolar ratio. Specifically, we hypothesized that modification of **catRAL/catFTC** ratio in NCPs would not affect the relative

release of each individual drug, that is, the % drug released vs time graph would remain unaltered (figures 4.11 b and c).

To calculate the required **catRAL/catFTC** ratio, we considered data from figures 4.11 b and e. From these graphs, we extracted that molar concentration of **catRAL** could be increased by a factor around 4 and 5 to achieve, as we needed to increase at this point **catRAL/catFTC** ratio from 0.20-0.25 to 1 approximately. The NCPs synthesis was repeated using the same conditions and experimental methodology than the ones explained in section 4.2.2, except for the **catRAL/catFTC** proportion, which was set to 5:1. For this new nanoparticle batch, from here on named **catRAL-catFTC-NCPs (5:1)**, ^{1}H NMR spectra of the disassembled material in acidic methanol were recorded. Interestingly, the spectra showed that the ratio between ligands, calculated by the integration of the corresponding peaks as explained in figure 4.9 was maintained in a high degree and equal to 4.6, approximately, along three independent batches of **catRAL-catFTC-NCPs (5:1)**.

Next, the drug release in **catRAL-catFTC-NCPs (5:1)** was determined in the same way that the procedure described in section 4.2.2.1 for **catRAL-catFTC-NCPs**. Thus, NCPs were incubated in simulated physiological conditions (PBS/BSA 0.5 mM buffer at pH 7.4 in the presence or absence of PLE (pig liver esterase) at a concentration of 180 U/L. Aliquots were taken at different time intervals, ranging from 5 min to 140 hours approximately, filtered through a 10 kDa membrane to remove BSA, PLE and non-degraded NCPs and stored in the freezer until analyzed. The HPLC methodology optimized in section 4.2.2.1 was also used to quantify RAL and FTC from the release aliquots, as well from aliquots treated with HCl with the purpose of setting the 100% release (figure 4.14). Like in the previous NCPs samples, the aliquots representing the 100% release allowed the quantification of the % of drug inside the NCPs. Thus, **catRAL-catFTC-NCPs (5:1)** presented and average of 24 wt% in RAL and 8 wt% in FTC. The data extracted from HPLC measurements is displayed as % of drug released, molar concentration or RAL/FTC ratio vs time.

As we had hypothesized, the relative release of both drugs, i.e., the liberation process (figures 4.14 a and b), did not experience significant variations with respect **catRAL-catFTC-NCPs**, being the release of FTC faster than the gradual release of RAL, especially in the presence of esterases. However, when this data was represented as absolute concentration vs time (figures 4.14 c and d), we observed that, in fact, the slower release of RAL was compensated by the large amount of it present in the NCPs structure, causing both antiretroviral drugs to be released in a ratio close to 1 in the presence of esterases, as we had predicted previously. Indeed, when RAL/FTC ratio vs time was represented (figure 4.14 e), values oscillating between 0.7 and 1.1 were found

after a stabilization time of approximately 20 hours. In the absence of esterases (figures 4.14 d and f), the different behavior of **catRAL** and **catFTC** towards esterases found along this thesis caused a steady increase of the RAL/FTC ratio.

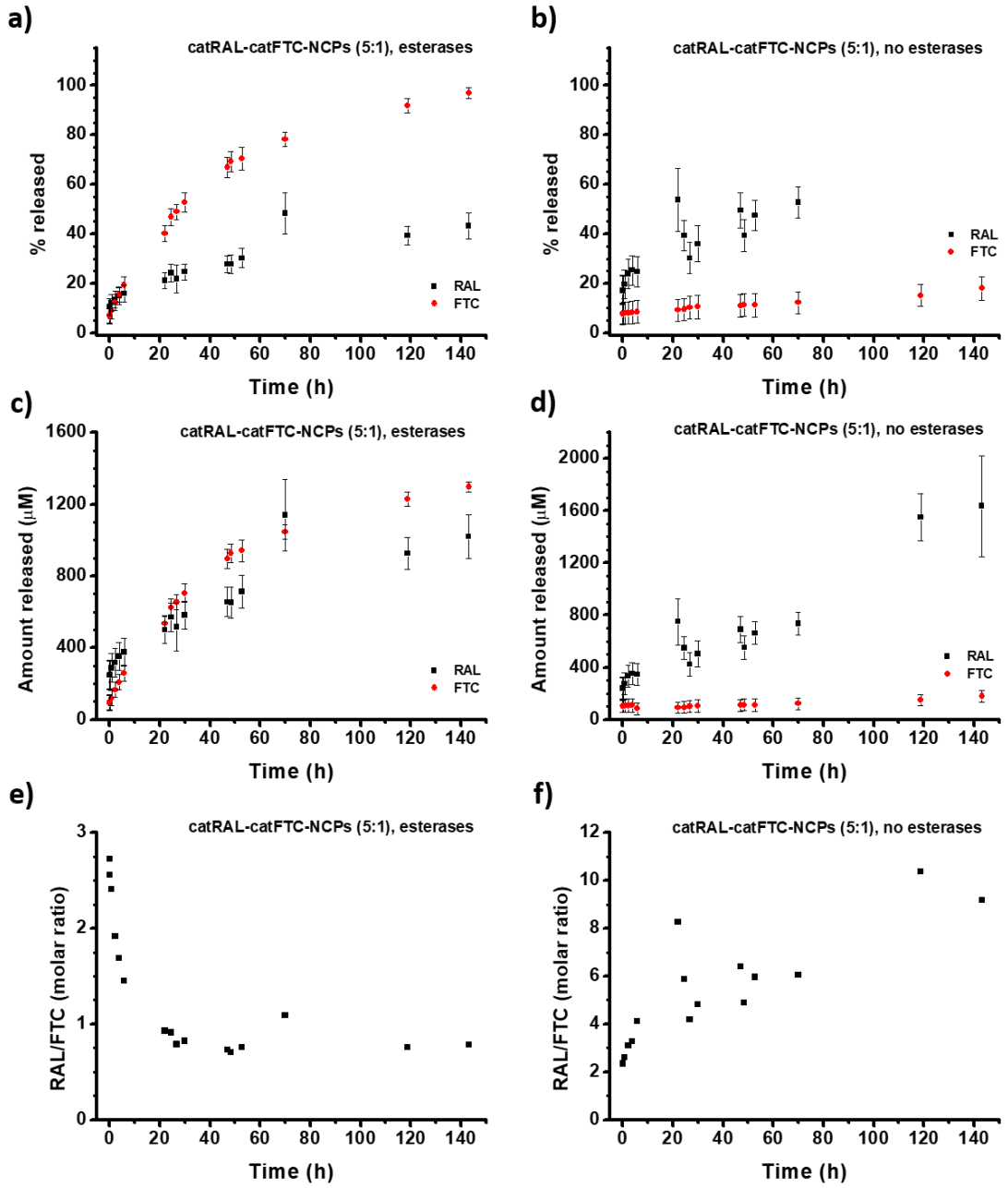

Figure 4.14. catRAL-catFTC-NCPs (5:1) drug release profile in the presence (a, c and e) and in absence of esterases (b, d and f) (PLE, 180 U/L). All experiments were performed by duplicate in PBS/BSA 0.5 mM pH 7.4 buffer at 37 °C. Data is displayed as % of drug released (a, b); in absolute RAL and FTC concentration (c, d) and as the RAL/FTC molar ratio at each time interval (e, f).

4.3 Development of synthetic methodologies for the obtention of cat3TC and catTFV

In this section, methodologies for the functionalization of lamivudine (3TC) and raltegravir (RAL) with catechol moieties will be explored (scheme 4.9 a). The synthesis of **cat3TC** will be attempted following the approach described for **catFTC**, as both ARV drugs only differ in the presence or absence of a fluorine atom and therefore their reactivity is expected to be similar (scheme 4.9 b). Thus, 3TC would be attached to intermediate **4**, obtained in three synthetic steps in 55% yield, using the coupling conditions for **catFTC**. A final deprotection step would remove the silyl ether protecting groups (TBDPS) and afford **cat3TC**.

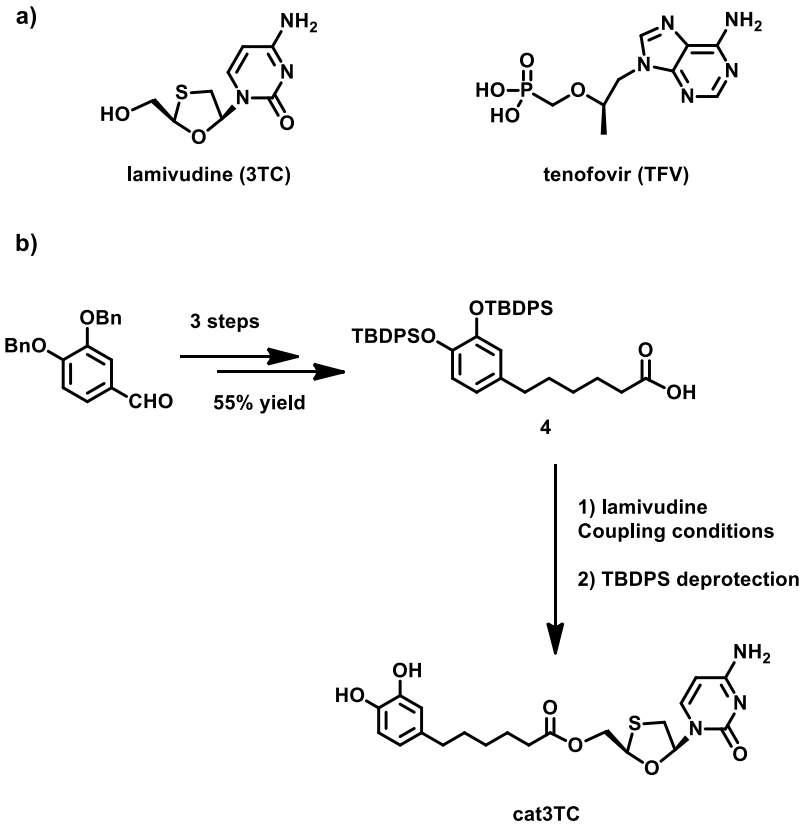

Scheme 4.9. a) Chemical structures of lamivudine (3TC) and tenofovir (TFV). b) Synthetic approach for the obtention of **cat3TC**.

A more challenging question remained in the synthesis of **catTFV**. The starting point for the planification of the synthetic approach fell on the patent from Gilead for the manufacturing of tenofovir disoproxil.[8] During this approach, disoproxil side chains are attached to the tenofovir core by means of an alkylative esterification using chloromethyl isopropyl carbonate (scheme

4.10) in 35% yield. This low yield reported in the patent and the fact that, for this step, the highest yield reported so far is 62%,[9] emphasizes the inherent complexity of the reaction.

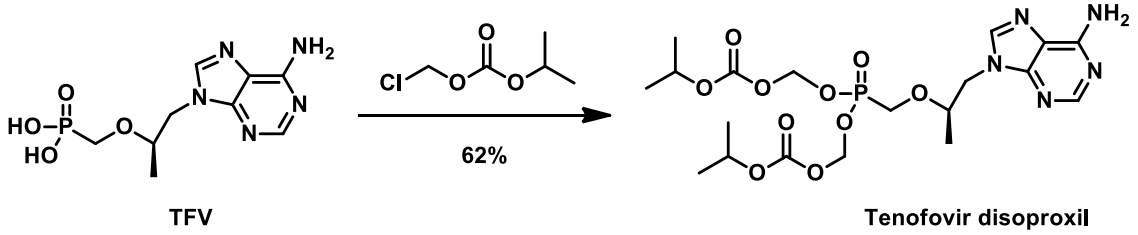

Scheme 4.10. Scheme of the alkylative esterification step in tenofovir disoproxil manufacturing route, extracted from reference 9.

Thus, a synthetic sequence using a suitable chloromethyl carbonate was proposed to attach a catechol-containing molecule to tenofovir to finally form **catTFV** (scheme 4.11). Starting from intermediate **4**, a reduction of its carboxylic moiety to alcohol would be performed to afford compound **24**. This alcohol would allow the formation of chloromethyl carbonate **26** by the reaction between **24** and commercially-available chloromethyl chloroformate, **25**. Then, tenofovir (TFV) would be attached to **26** following similar experimental conditions to those described for tenofovir disoproxil in reference 9.

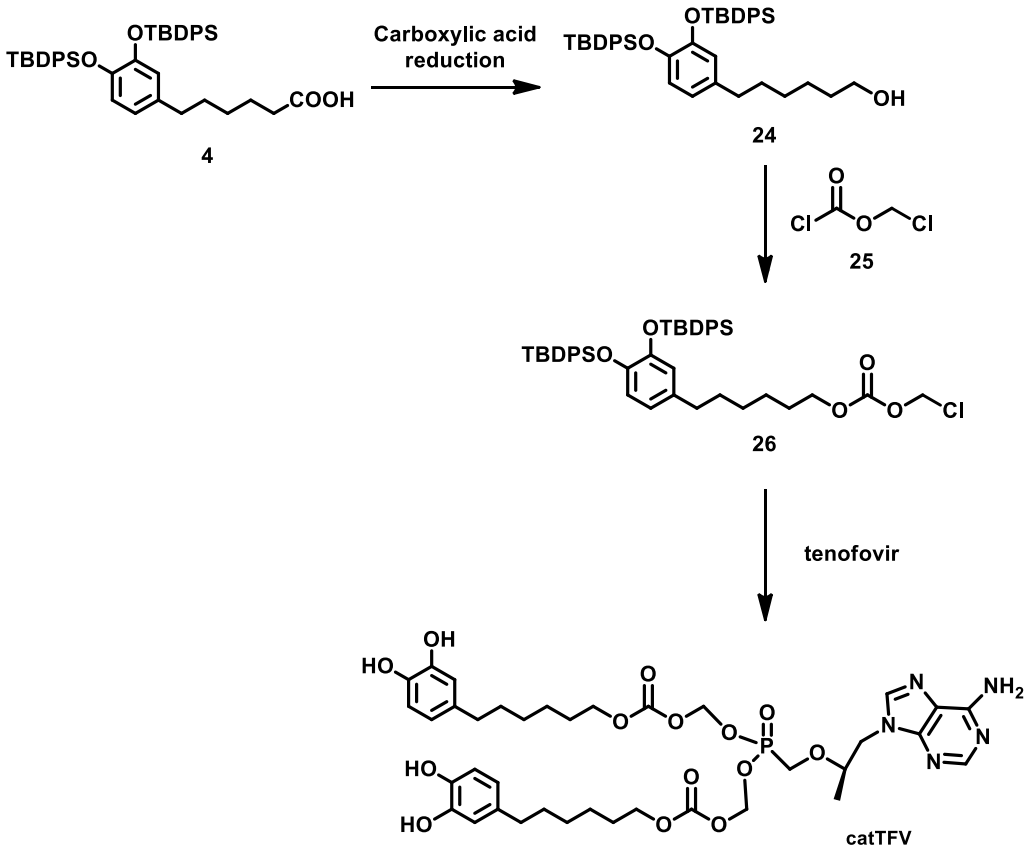

Scheme 4.11. Synthetic approach for **catTFV** from intermediate **4**.

4.3.1 Synthesis of cat3TC

In order to expand the scope of ARV-NCPs and using the knowledge acquired during **catFTC** synthesis, the conjugation of lamivudine (3TC) to **4** (**cat3TC**) was proposed at this point (scheme 4.6). Therefore, the optimized conditions for esterification were directly applied and, similarly to the previous case, a chemoselective coupling (as confirmed by 2D NMR experiments) took place through the free hydroxyl group, allowing the isolation of **27** in 76% yield. Moreover, removal of the silyl protecting groups was more problematic than it appeared. When the reaction was performed under the previous methodology based on the addition of triethylamine trihydrofluoride, TLC controls showed the appearance of a new, polar compound within the reaction mixture. After the purification by column chromatography following similar conditions to those used for **catFTC**, however, extremely low yields were observed (<1%). As no starting material was recovered either, some attempts of improving the reaction yield were performed by modifying chromatographic parameters (stationary and mobile phase composition) or attempting to precipitate **cat3TC** as its hydrochloride salt. In the end, the best yield obtained, 12%, was achieved with phase-reversed flash column chromatography, that is, using C18-coated silica as stationary phase and water/methanol as eluent. These low yields obtained in the synthesis of **cat3TC** did not encourage its use for ARV-NCPs synthesis.

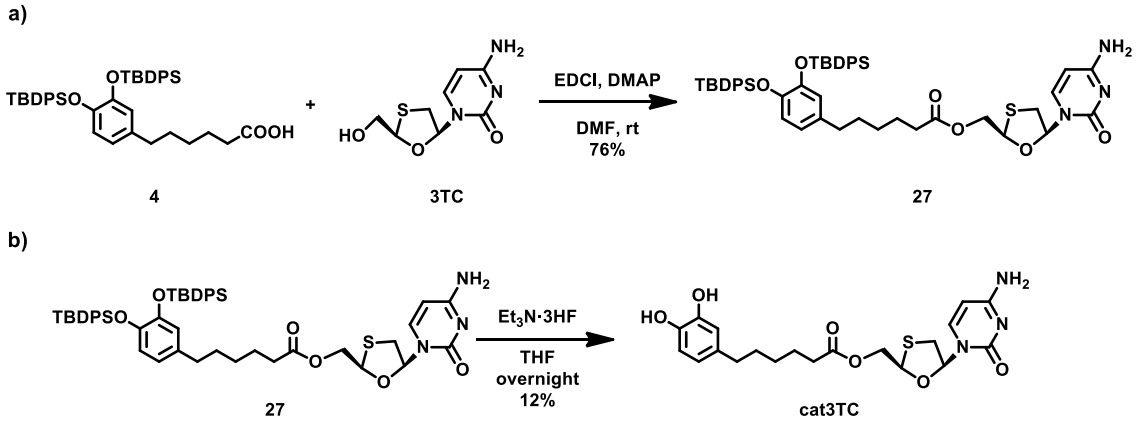

Scheme 4.12. a) Synthesis of **27** using the same optimized methodology applied in **17** synthesis. b) Removal of TBDPS protecting groups of **27** to yield **cat3TC**.

4.3.2 Attempts to prepare catTFV

As explained before, the route for **catTFV** synthesis would involve a key step of phosphonate formation through an alkylative esterification between commercial tenofovir and a suitable alcohol. Due to the inherent complexity of the transformation and the need of controlling a series of experimental parameters,[9] this esterification was proposed to be performed first using a cheap, easily-available alcohol, 2-phenylethanol, as a model (scheme 4.13). In this way,

limitations arising from the low availability of intermediate **4** and its time-consuming synthesis could be avoided during a first screening of the reaction.

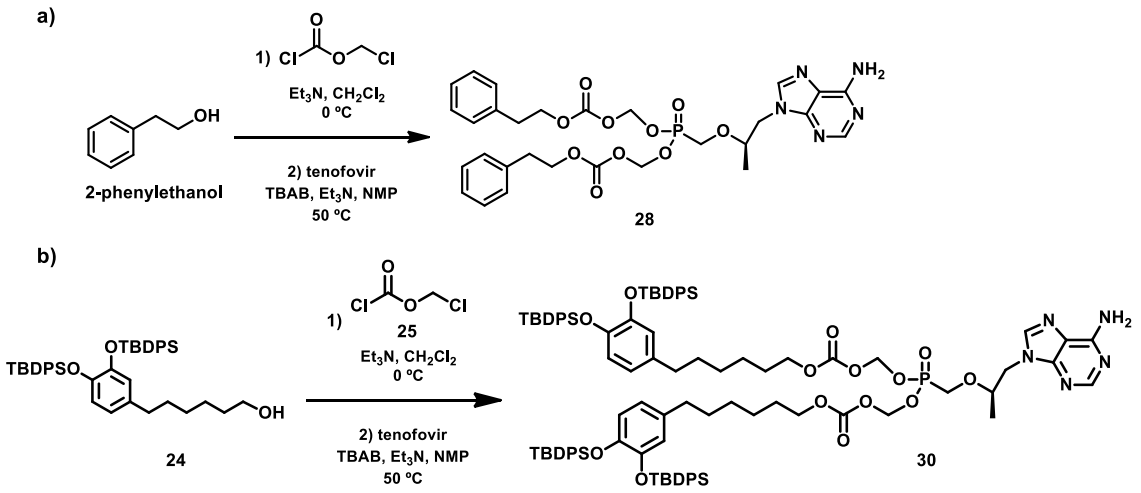

Scheme 4.13. a) Model esterification between 2-phenylethanol and tenofovir via chloromethyl carbonate to explore the feasibility of b) coupling of alcohol **24** to tenofovir.

Synthesis of **28** comprises three stages: i) reaction of 2-phenylethanol with chloromethyl chloroformate to form the corresponding chloromethyl carbonate; ii) its coupling reaction to tenofovir and; iii) isolation and purification of phosphonate **28**. The first step includes a straightforward transformation, that is, esterification using an acyl chloride. However, due to the several parameters that limit the remaining stages, the rationale behind the formation of tenofovir disoproxil will be explained in the next paragraph and later applied to **28** synthesis.[9]

Thus, during this alkylative esterification, the reaction is typically performed in a polar, aprotic solvent due to the low solubility of tenofovir and its salts. The best solvent reported is *N*-methyl-2-pyrrolidone (NMP), although subsequent work-up is difficulted by its high boiling point (202 °C). A non-nucleophilic amine base (triethylamine is preferred) allows the dissolution of the initial suspension of tenofovir in NMP followed by the precipitation of its mono- and bis-triethylammonium salts. Subsequent solubilization of the esterification products (monoester and diester) drives the reaction forward. The conversion rate of monoester to diester, however, is slower than the initial formation of monoester and causes the reverse reaction (hydrolysis) to become competitive as the reaction time increases. Additionally, the use of phase-transfer agents, like tetrabutylammonium bromide (TBAB), increases reaction conversion and rate as it increases the solubility of triethylammonium tenofovir salts. The key impurities in this transformation are summarized in scheme 4.14, which include monoester **31** along with *N*-hydroxymethylated products **32** and **34** and isopropylcarbamates **33** and **35**. Regarding reagent concentration, a compromise between high (favors the formation of such impurities) and low

(complicates the posterior work-up due to an increase in NMP volume) must be taken. Presence of water is identified as the major source of impurities, with **32** and **34** comprising up to 25% of the product mixture when water content is not controlled. Mainly, two approaches for reducing water levels are applied, frequently in combination. The first one involves drying hygroscopic tenofovir at 70-90 °C under reduced pressure, whereas the second strategy relies on azeotropic distillation of tenofovir suspended in NMP using cyclohexane or toluene. During the work-up, product degradation is enhanced in aqueous basic solutions, therefore the direct addition of water in the presence of excess triethylamine is discouraged. Instead, cyclohexane washes remove excess triethylamine and a significant amount of NMP. Following this step, partition of the residue between ethyl acetate and water provides an organic solution of tenofovir disoproxil. Tenofovir disoproxil can be then isolated by precipitation as a fumarate salt.

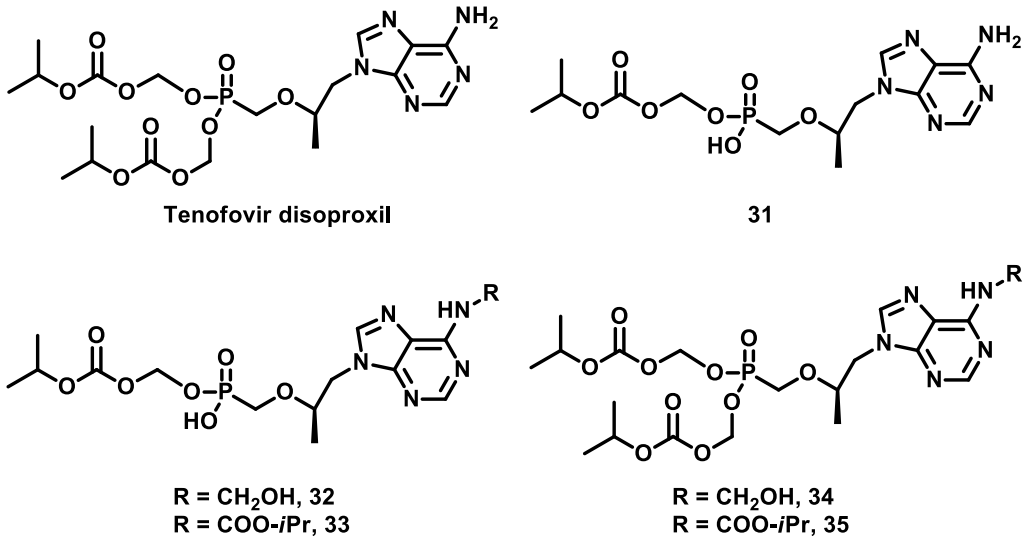

Scheme 4.14. Chemical structure of tenofovir disoproxil and the main impurities formed within the esterification step.

Thus, **28** was prepared following the previous procedure (figure 4.15 a). Simple addition of chloromethyl chloroformate to a basic solution of 2-phenylethanol afforded chloromethyl carbonate **36**, as observed by the entire consumption of the starting material by TLC and the appearance in ^{1}H NMR of a new singlet at δ 5.7 ppm corresponding to chloromethyl protons (COO-C**H**$_2$-Cl) (figure 4.15 b). **36** was used immediately without further purification. For the next step, commercial tenofovir was dried overnight at the oven at 80 °C and later using azeotropic distillation at reduced pressure with cyclohexane. For that, an experimental setup using a distilling trap was prepared so that cyclohexane could be removed and added from the system without introducing air and therefore humidity. To this dried suspension of tenofovir in NMP, **36** was added along with triethylamine and tetrabutylammonium bromide (TBAB) and stirred at

50 °C for 17 h. Although temperatures of 65-70 °C are reported for this step in the patent of tenofovir, the presence of TBAB allows a decrease to 50-60 °C, maximizing conversion and product stability.[9] The reaction work-up was performed in the way described before, that is, avoiding basic pH with the use of cyclohexane washes. The ^{1}H NMR spectrum of the resulting wax included peaks attributed to tenofovir and 2-phenylethanol. Finally, **28** was isolated as a fumarate salt in 43% yield for the combined reactions by the simple addition of fumaric acid to the purified product.

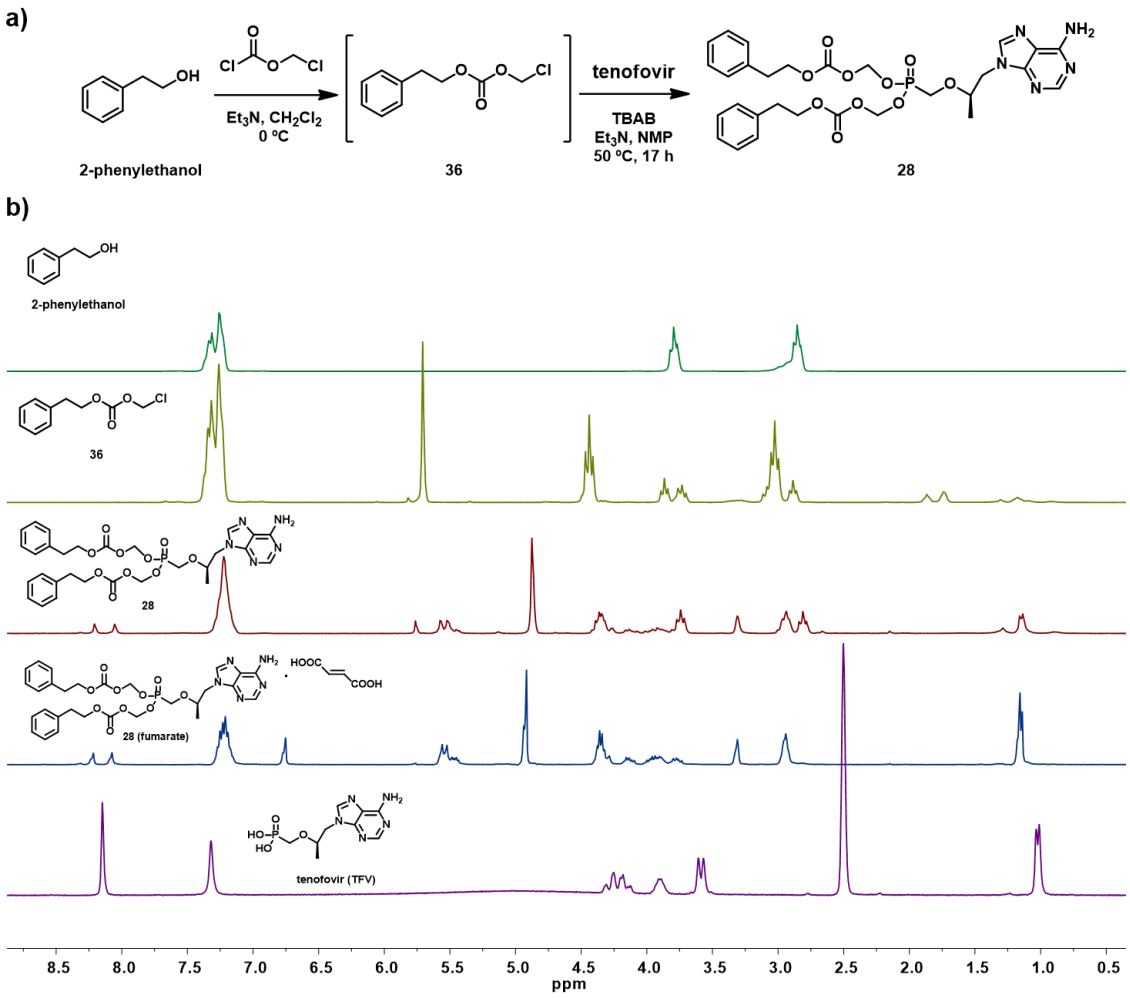

Figure 4.15. a) Preparation of **28** via chloromethyl carbonate **36**. b) ^{1}H NMR spectra of (top to bottom) 2-phenylethanol, **36**, **28**, fumarate salt of **28** and tenofovir. All spectra were recorded in CD_3OD, except tenofovir in $(CD_3)_2SO$

The next step now was to accomplish this transformation using the alcohol of interest **24**), which was easily prepared from **4** by a reduction with borane in 75% yield (scheme 4.15 a).

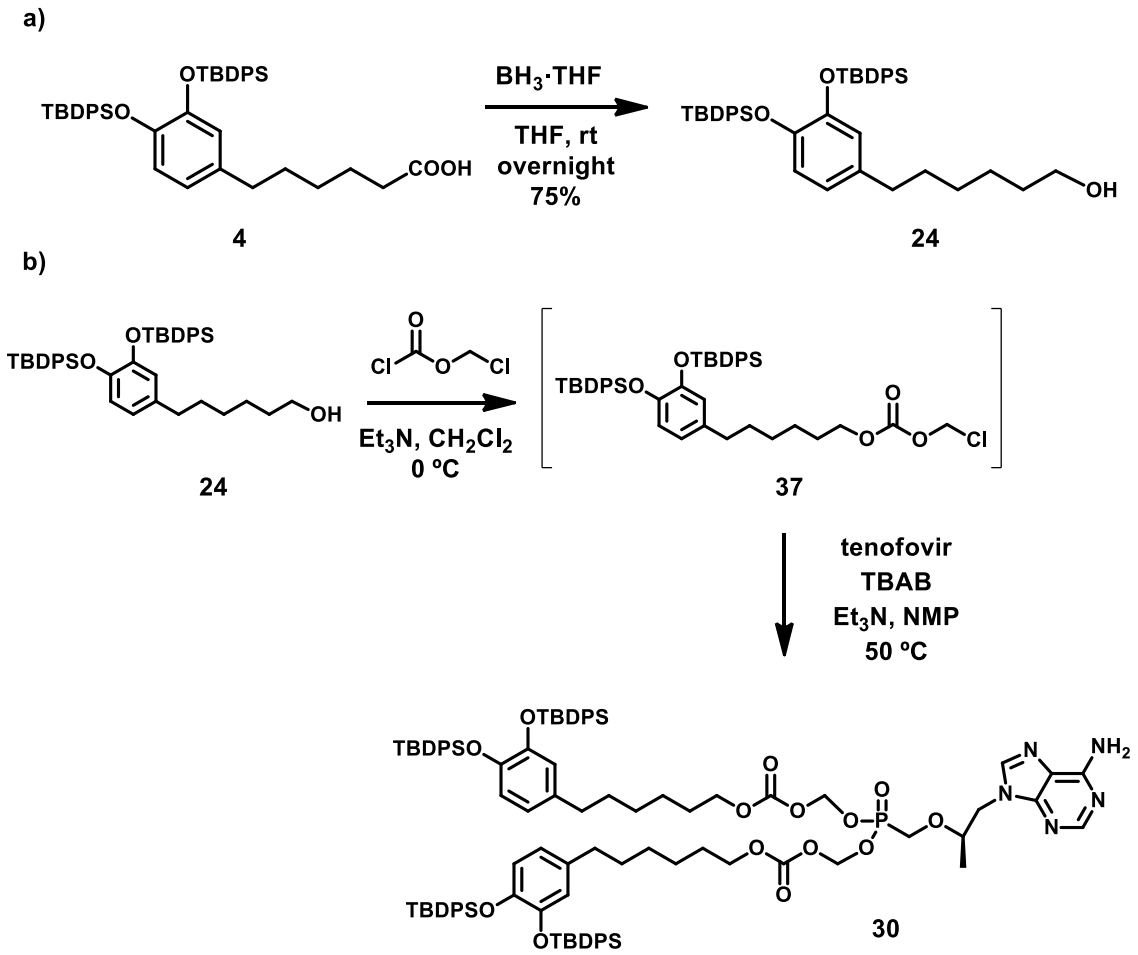

Scheme 4.15. a) Reduction of carboxylic acid **4** to alcohol **24** using borane. b) Synthesis of **30** via the chloromethyl carbonate **37**.

In the same way that in the model reaction, chloromethyl carbonate **37** was successfully prepared by the addition of chloromethyl chloroformate to a basic solution of alcohol **24**, as determined by TLC and ^{1}H NMR. Then, the same procedure for drying of tenofovir explained before (overnight drying at 80 °C and azeotropic distillation over cyclohexane) was used. Compound **37**, TBAB and Et_3N were added to the suspension of dry tenofovir and stirred at 50 °C. Aliquots at different time intervals (4, 17, 24 h) were taken and a workup consisting in cyclohexane washes and liquid-liquid extraction in ethyl acetate was performed for all aliquots. Although the reaction was carried out by triplicate, ^{1}H NMR spectra of the different aliquots and independently of the reaction time only showed peaks attributed to the starting material, protected catechol **37**.

At this point, the inherent complexity of the transformation and other challenges arising from this particular system, namely the large molecular weight of **24** which, coupled to the 2:1 stoichiometry, required the use of large amounts of it with respect to tenofovir (13 mg of **24** /

mg tenofovir) and the limited amount of starting material available due to its time-consuming synthetic process; caused the renounce of this route to obtain **catFTV**.

4.4 Summary and conclusions

In this Chapter, additional conjugates between catechol and antiretroviral drugs were designed, synthesized and used in the formation of nanoscale coordination polymers (NCPs). Specifically, synthetic methodologies for the preparation of catechol conjugates of emtricitabine (FTC) and raltegravir (RAL), **catFTC** and **catRAL** respectively, were developed. Both target compounds were successfully synthesized through a 5-step sequence with an overall yield of 32% for **catFTC** and 30% for **catRAL**. Then, iron-based NCPs were prepared using both conjugates separately to afford **catFTC-NCPs** and **catRAL-NCPs**, exhibiting an average size of 169 ± 29 nm and 104 ± 22 nm respectively. After their physicochemical characterization, HPLC methodologies were developed to compare the drug release profile of **catFTC-NCPs** and **catRAL-NCPs** with their corresponding free ligand **catFTC** or **catRAL** in simulated physiological conditions in the presence or absence of esterases. According to the data obtained, nanostructuration protected **catFTC** and **catRAL** from hydrolysis, allowing a more sustained release over longer periods of time.

The next step was the formation of NCPs containing both ligands, **catFTC** and **catRAL**, in a 1:1 molar ratio. Thus, **catRAL-catFTC-NCPs** were prepared using the optimized methodology for NCPs synthesis. Their physicochemical characterization revealed to presence of both **catFTC** and **catRAL** in a molar ratio of 1.1 (catRAL/catFTC). Then, to study their drug release profile in vitro, HPLC methodologies were refined to allow the simultaneous quantification of **catFTC**, **catRAL** and their hydrolysis products. Although the data obtained from the release experiments showed relative liberation of both drugs, RAL and FTC, similar to **catRAL-NCPs** and **catFTC-NCPs**, their different behavior towards esterases effectively reduced the ratio of the delivered mixture from the expected 1.1 to approximately 0.2 (RAL/FTC molar ratio). To increase this ratio during the release process, NCPs containing **catRAL** and **catFTC** in a 5:1 ratio were prepared (**catRAL-catFTC-NCPs (5:1)**). In these new particles, the ratio between RAL and FTC during the release process was observed to oscillate between 0.7 and 1.1 (RAL/FTC).

Lastly, the functionalization of additional ARV drugs with catechol was explored. Specifically, lamivudine (3TC) was successfully attached to catechol moieties, **cat3TC**, through a 5-step synthetic route with an overall yield of 5%. These low yields, especially at the purification in the final deprotection step, discouraged its use in NCPs synthesis. Moreover, the synthesis of tenofovir (TFV) attached to catechol moieties, **catTFV**, was attempted. The key step in this

transformation, the formation of a phosphonate presented several experimental challenges and thus it was attempted first in commercially-available compounds as a model. Although eventually the desired product in the model reaction was obtained, attempts to reproduce this result using catechol-containing compounds did not afford target molecule **catTFV**.

4.5 Experimental section

Characterization Methods. 250 MHz ^{1}H NMR spectra were recorded on a Bruker DPX 250 MHz spectrometer; 360 MHz ^{1}H NMR, ^{1}H-^{1}H COSY, ^{1}H-^{13}C HSQC, ^{1}H-^{13}C HMBC, DEPT135 and 100 MHz ^{13}C NMR were recorder on a Bruker DPX 360 MHz spectrometer; 400 MHz ^{1}H NMR, ^{1}H-^{1}H COSY, ^{1}H-^{13}C HSQC, ^{1}H-^{13}C HMBC, DEPT135 and 100 MHz ^{13}C NMR spectra were recorded on a Bruker DPX 400 MHz spectrometer. Chemical shifts (δ) are given in ppm, using the residual non-deuterated solvent as internal reference. Signal multiplicities are described using the following abbreviations: singlet (s), doublet (d), triplet (t), quartet (q), quintet (quint), doublet of doublets (dd), doublet of triplets (dt), doublet of doublet of doublets (ddd), multiplet (m) and *J* to indicate the coupling constant (Hz). High-resolution mass spectra were obtained by direct injection of the sample with electrospray techniques in a Bruker microTOF-Q instrument. SEM images were performed on a scanning electron microscope (FEI Quanta 650 FEG) at acceleration voltages of 5–20 kV. The samples were prepared by drop casting of the corresponding dispersion on aluminum tape followed by evaporation of the solvent under room conditions. Before analysis, the samples were metalized with a thin layer of platinum by using a sputter coater (Emitech K550). IR spectra were recorded by using a Tensor 27 (Bruker) spectrophotometer equipped with a single-reflection diamond window ATR accessory (MKII Golden Gate, Specac). Size distribution and surface charge of the nanoparticles were measured by DLS, using a ZetasizerNano 3600 instrument (Malvern Instruments, UK), the size range limit of which is 0.6 nm to 6 mm. Note: the diameter measured by DLS is the hydrodynamic diameter. The samples were comprised of aqueous dispersions of the nanoparticles in distilled water or in buffer. All samples were diluted to obtain an adequate nanoparticle concentration.

Synthesis of ((2*R*,5*S*)-5-(4-amino-5-fluoro-2-oxopyrimidin-1(2*H*)-yl)-1,3-oxathiolan-2-yl)methyl 6-(3,4-bis((*tert*-butyldiphenylsilyl)oxy)phenyl)hexanoate, 17

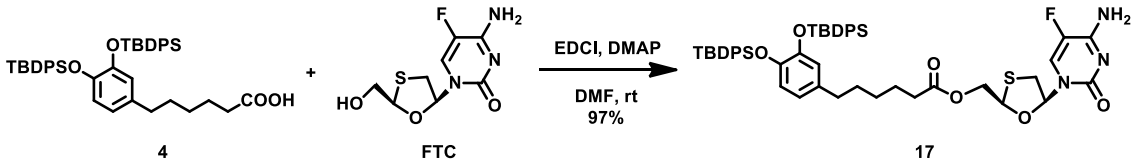

N-(3-Dimethylaminopropyl)-*N*'-ethylcarbodiimide hydrochloride (1.78 g, 9.22 mmol) was added dropwise to a stirred ice-cooled solution of **4**, (3.88 g, 5.53 mmol), emtricitabine (FTC) (1.14 g, 4.61 mmol) and 4-dimethylaminopyridine (DMAP) (1.13 g, 9.22 mmol) in dry DMF (80 mL). The

mixture was allowed to warm to rt and stirred overnight. After TLC analysis (CH_2Cl_2/CH_3OH 90:10) showed the entire consumption of emtricitabine, the mixture was diluted with EtOAc (80 mL) and washed with water/brine 1:1 (4x130 mL). The combined aqueous phases were extracted with EtOAc (50 mL) and the resulting organic phases were dried over anhydrous Na_2SO_4 and concentrated under vacuum. The resulting brownish wax was purified by flash column chromatography (CH_2Cl_2/CH_3OH, 98:2 → 95:5) to afford a white solid identified as **17** (4.15 g, 4.46 mmol, 97% yield). **HRMS (EI)** calcd for $([C_{52}H_{60}FN_3O_6SSi_2]+H)^+$ 930.3804, found 930.3796.

^{1}H NMR (360 MHz, CD_3OD) δ 8.03 (d, $^3J_{6,F}$ = 6.8 Hz, 1H, H-6), 7.86 – 7.73 (m, 8H, Ph (TBDPS)), 7.52 – 7.32 (m, 12H, Ph (TBDPS)), 6.32 (d, $^3J_{5''',6'''}$ = 8.2 Hz, 1H, H-5'''), 6.27 – 6.20 (m, 2H, H-1' + H-2'''), 6.13 (dd, $^3J_{6''',5'''}$ = 8.2 Hz, $^4J_{6''',2'''}$ = 2.1 Hz, 1H, H-6'''), 5.40 (dd, $^3J_{4',5'}$ = 4.5 Hz, $^3J_{4',5'}$ = 3.1 Hz, 1H, H-4'), 4.60 (dd, $^2J_{gem}$ = 12.5 Hz, $^3J_{5',4'}$ = 4.5 Hz, 1H, H-5'), 4.38 (dd, $^2J_{gem}$ = 12.4 Hz, $^3J_{5',4'}$ = 3.1 Hz, 1H, H-5'), 3.53 (dd, $^2J_{gem}$ = 12.3 Hz, $^3J_{2',1'}$ = 5.4 Hz, 1H, H-2'), 3.18 (dd, J_{gem} = 12.3 Hz, $^3J_{2',1'}$ = 3.8 Hz, 1H, H-2'), 2.19 (t, $^3J_{2'',3''}$ = 7.5 Hz, 2H, H-2''), 2.01 (t, $^3J_{6'',5''}$ = 7.5 Hz, 2H, H-6''), 1.42 – 1.35 (m, 2H, H-3'' + H-4'' + H-5''), 1.12 (s, 9H, *t*-Bu (TBDPS)), 1.11 (s, 9H, *t*-Bu (TBDPS)) 1.06 – 0.98 (m, 2H, H-3'' + H-4'' + H-5''), 0.96 – 0.84 (m, 2H, H-3'' + H-4'' + H-5''). **^{13}C NMR** (91 MHz, CD_3OD) δ 174.49 (C-1''), 156.12 (C-6), 146.99 (C-5'''), 145.15 (C-4'''), 136.72 (Ph (TBDPS)), 135.95 (C-3), 134.42 (C-1'''), 131.10 (Ph (TBDPS)), 128.92 (Ph (TBDPS)), 126.51 (d, $^2J_{2,F}$ = 32.6 Hz, C-2), 121.77 (C-6'''), 121.57 (C-2'''), 121.20 (C-3'''), 88.82 (C-1'), 85.27 (C-4'), 64.69 (C-5'), 38.72 (C-2'), 35.28 (C-6''), 34.67 (C-2''), 31.34 (C-3''/C-4''/C-5''), 30.77 (C-3''/C-4''/C-5''), 27.29 (*t*-Bu (TBDPS)), 25.64 (C-3''/C-4''/C-5''), 20.31 (*t*-Bu (TBDPS)).

Synthesis of ((2*R*,5*S*)-5-(4-amino-5-fluoro-2-oxopyrimidin-1(2*H*)-yl)-1,3-oxathiolan-2-yl)methyl 6-(3,4-dihydroxyphenyl)hexanoate, catFTC

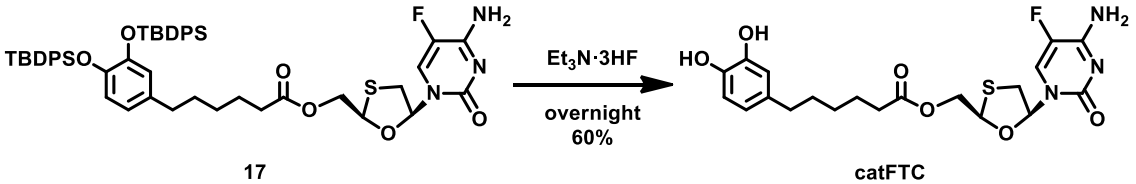

Triethylamine trihydrofluoride (4.5 mL, 27.0 mmol) was added to a stirred ice-cooled solution of **17**, (4.07 g, 4.37 mmol) in dry THF (60 mL). The mixture was allowed to warm to rt and stirred overnight. The reaction was quenched with 2 mL of brine, diluted with 60 mL diethyl ether, filtered and the solvent was evaporated under vacuum. The resulting crude was purified by column chromatography ($CHCl_3$/CH_3OH 95:5 → 90:10) to furnish **catFTC** as a white solid (0.76 g,

1.67 mmol, 60%). R_f (CH_2Cl_2/CH_3OH 90:10) = 0.30. **HRMS (EI)** calcd for $[C_{20}H_{24}FN_3O_6S]$+ 454.1448, found 454.1442. mp. 69 – 72 ˚C ($CHCl_3$/CH_3OH).

^{1}H NMR (400 MHz, CD_3OD) δ 8.02 (d, $^3J_{6,F}$ = 6.7 Hz, 1H, H-6), 6.65 (d, $^3J_{5''',6'''}$ = 8.0 Hz, 1H, H-5'''), 6.60 (d, $^4J_{2''',6'''}$ = 1.9 Hz, 1H, H-2'''), 6.43 (dd, $^3J_{6''',5'''}$ = 8.0 Hz, $^4J_{2''',6'''}$ = 1.9 Hz, 1H, H-6), 6.25 – 6.18 (m, 1H, H-1'), 5.34 (t, $^3J_{4',5'}$ = 3.3 Hz, 1H, H-4'), 4.60 (dd, J_{gem} = 12.5 Hz, $^3J_{5',4'}$ = 4.2 Hz, 1H, H-5'), 4.38 (dd, J_{gem} = 12.7 Hz, $^3J_{5',4'}$ = 2.9 Hz, 1H, H-5'), 3.51 (dd, J_{gem} = 12.3 Hz, $^3J_{2',1'}$ = 5.4 Hz, 1H, H-2'), 3.17 (dd, J_{gem} = 12.4 Hz, $^3J_{2',1'}$ = 3.4 Hz, 1H, H-2'), 2.41 (t, $^3J_{6'',5''}$ = 7.5 Hz, 2H, H-6''), 2.37 (t, $^3J_{2'',3''}$ = 7.4 Hz, 2H, H-2''), 1.63 (quint, $^3J_{3'',2''}$ = $^3J_{3'',4''}$ = 7.4 Hz, 2H, H-3''), 1.53 (quint, $^3J_{5'',4''}$ = $^3J_{5'',6''}$ = 7.6 Hz, 2H, H-5''), 1.31 (quint, $^3J_{4'',3''}$ = $^3J_{4'',5''}$ = 7.8 Hz, 2H, H-4''). **^{13}C NMR** (101 MHz, CD_3OD) δ 174.59 (C-1''), 159.58 (C-4), 155.89 (C-5), 145.84 (C-4'''), 143.91 (C-3'''), 136.78 (C-2), 135.32 (C-1'''), 126.46 (C-6), 120.60 (C-6'''), 116.50 (C-5'''), 116.20 (C-2'''), 88.63 (C-1'), 85.49 (C-4'), 64.40 (C-5'), 38.92 (C-2'), 35.92 (C-6''), 34.72 (C-2''), 32.20 (C-5''), 29.50 (C-4''), 25.76 (C-3'').

Synthesis of 4-((4-fluorobenzyl)carbamoyl)-1-methyl-2-(2-(5-methyl-1,3,4-oxadiazole-2-carboxamido)propan-2-yl)-6-oxo-1,6-dihydropyrimidin-5-yl 6-(3,4-bis((*tert*-butyldiphenylsilyl)oxy)phenyl)hexanoate, 23

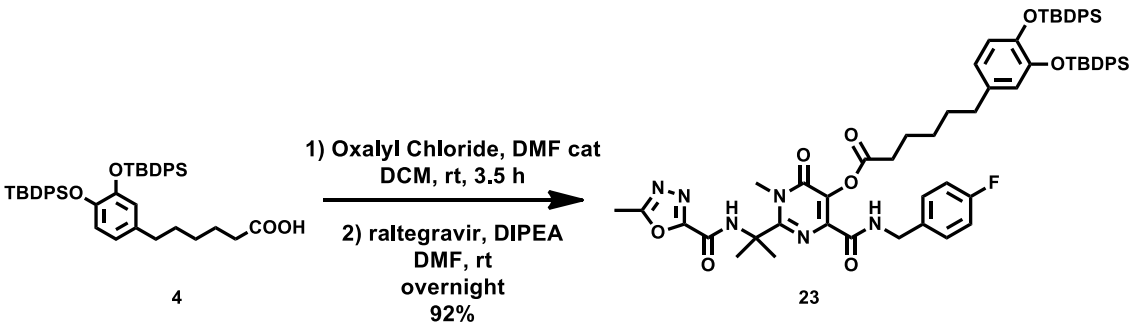

Carboxylic acid **4**, (1.04 g, 1.48 mmol) was dissolved in dry DCM (7 mL). Dry DMF (80 µL) was added, and then oxalyl chloride (250 µL, 2.97 mmol) was added dropwise. The mixture was stirred for 3.5 hours at rt. Then, the solvent was removed under vacuum and the crude was dissolved in dry DMF and added to a solution of raltegravir (0.60 g, 1.35 mmol) and DIPEA (1080 µL, 6.75 mmol) in dry DMF. The mixture was stirred overnight at rt. Then, the solvent was removed under vacuum and the crude was purified by column chromatography (EtOAc 100%) to furnish compound **23**, (1.39 g, 1.24 mmol, 92%) as a white solid. **R_f** (EtOAc) = 0.32. **HRMS (EI)** calcd for $([C_{64}H_{71}FN_6O_8Si_2]+H)^+$ 1127.4934, found 1127.4913.

^{1}H NMR (400 MHz, CD_3OD) δ 7.82 – 7.76 (m, 8H, TBDPS), 7.51 – 7.36 (m, 13H, TBDPS), 7.37 – 7.28 (m, 2H, H-3), 7.00 (t, $^3J_{2,3}$ = 8.8 Hz, 2H, H-2), 6.33 (d, $^3J_{5'',6''}$ = 8.2 Hz, 1H, H-5''), 6.25 (d, $^4J_{2'',6''}$

= 2.1 Hz, 1H, H-2''), 6.13 (dd, $^{3}J_{6'',5''}$ = 8.2 Hz, $^{4}J_{6'',2''}$ = 2.1 Hz, 1H. H-6''), 4.49 (s, 2H, H-5), 3.64 (s, 3H, H-14), 2.58 (s, 3H, H-24), 2.39 (t, $^{3}J_{2',3'}$ = 7.7 Hz, 2H, H-2'), 2.02 (t, $^{3}J_{6',5'}$ = 6.2 Hz, 2H, H-6'), 1.83 (s, 6H, H-16), 1.48 – 1.39 (m, 2H, H-3'), 1.13 (s, 9H, *t*Bu), 1.12 (s, 9H, *t*Bu), 1.07 – 0.93 (m, 4H, H-4'+H-5'). **^{13}C NMR** (101 MHz, CD_3OD) δ 172.35 (C-1'), 167.91 (C-21), 164.67 (C-7), 159.68 (C-10), 145.12 (C-3''), 142.31 (C-4'') 136.73 (TBDPS), 136.71 (TBDPS), 136.07 (C-1''), 135.70 (C-4), 134.46 (C-1), 131.20 (TBDPS), 131.05 (TBPDS), 130.42 (TBDPS), 130.34 (TBDPS), 129.05 (TBPDS), 128.98 (TBDPS), 128.86 (C-2 / C-3), 121.76 (C-2''), 121.60 (C-6''), 121.19 (C-5''), 116.32 (C-3 / C-2), 59.61 (C-15), 43.22 (C-5), 35.35 (C-6'), 34.39 (C-2'), 34.18 (C-14), 31.42 (C-4'), 28.98 (C-5'), 27.33 (C-16), 27.28 (TBDPS), 25.24 (C-3'), 20.33 (TBDPS), 10.82 (C-24).

Synthesis of 4-((4-fluorobenzyl)carbamoyl)-1-methyl-2-(2-(5-methyl-1,3,4-oxadiazole-2-carboxamido)propan-2-yl)-6-oxo-1,6-dihydropyrimidin-5-yl 6-(3,4-dihydroxyphenyl)hexanoate, catRAL

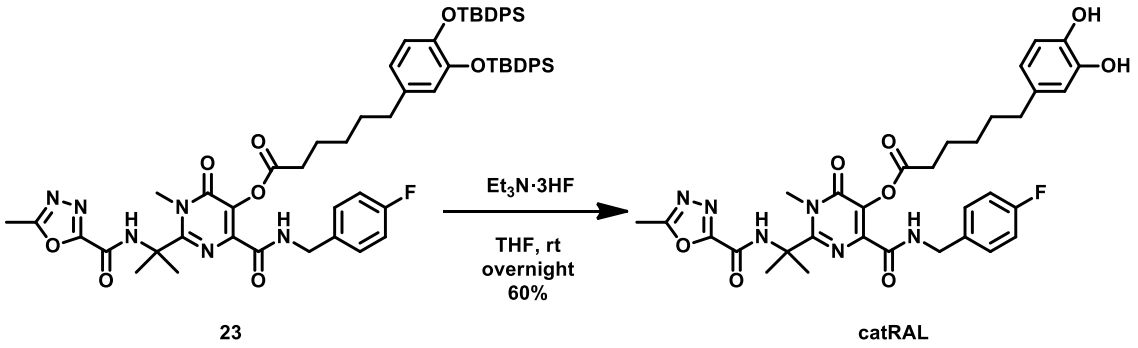

Triethylamine trihydrofluoride (1.0 mL, 3.72 mmol) was added to a stirred ice-cooled solution of compound **23**, (0.84 g, 0.74 mmol) in dry THF (40 mL). The mixture was allowed to warm to rt and stirred overnight. The reaction was quenched with 0.8 mL of brine, diluted with 20 mL diethyl ether, filtered and the solvent was evaporated under vacuum. The resulting crude was purified by column chromatography ($CHCl_3$/EtOAc 50:50 → EtOAc 100%) to furnish **catRAL** as a white solid (0.29 g, 0.45 mmol, 60%). R_f (EtOAc) = 0.18. **HRMS (EI)** calcd for $([C_{32}H_{35}FN_6O_8]+H)^+$ 651.2579, found 651.2575. mp. 84 – 87 ˚C ($CHCl_3$/EtOAc).

^{1}H NMR (400 MHz, CD_3OD) δ 7.37 – 7.33 (m, 2H, H-3), 7.09 – 6.99 (m, 2H, H-2), 6.65 (d, $^{3}J_{5'',6''}$ = 8.0 Hz, 1H, H-5''), 6.62 (d, $^{4}J_{2'',6''}$ = 2.1 Hz, 1H, H-2''), 6.49 (dd, $^{3}J_{6'',5''}$ = 8.0, $^{4}J_{6'',2''}$ = 2.1 Hz, 1H, H-6''), 4.51 (s, 2H, H-5), 3.64 (s, 3H, H-14), 2.61 (t, $^{3}J_{6',5'}$ = 7.4 Hz, 1H, H-6'), 2.58 (s, 3H, H-24), 2.47 (t, $^{3}J_{2',3'}$ = 7.6 Hz, 2H, H-2'), 1.83 (s, 6H, H-16), 1.72 (p, $^{3}J_{3',2'}$ = 6.8 Hz, $^{3}J_{3',4'}$ = 6.8 Hz, 2H, H-3'), 1.60 (quint, $^{3}J_{5',4'}$ = 7.3 Hz, $^{3}J_{5',6'}$ = 7.3 Hz, 2H, H-5'), 1.48 – 1.37 (m, 2H, H-4'). **^{13}C NMR** (101 MHz, CD_3OD) δ 172.41 (C-1'), 167.91 (C-21), 164.70 (C-7), 159.67 (C-10), 145.98 (C-3''), 144.06 (C-4''),

136.04 (C-4), 135.68 (C-1''), 135.53 (C-1), 130.44 (C-2/C-3), 120.65 (C-2''), 116.52 (C-6''), 116.20 (C-5''), 116.10 (C-3/C-2), 59.62 (C-15), 43.22 (C-5), 36.01 (C-6'), 34.47 (C-14), 34.18 (C-2'), 32.49 (C-4'), 29.56 (C-5'), 27.18 (C-16), 25.38 (C-3'), 10.86 (C-24).

Synthesis of catRAL-NCPs

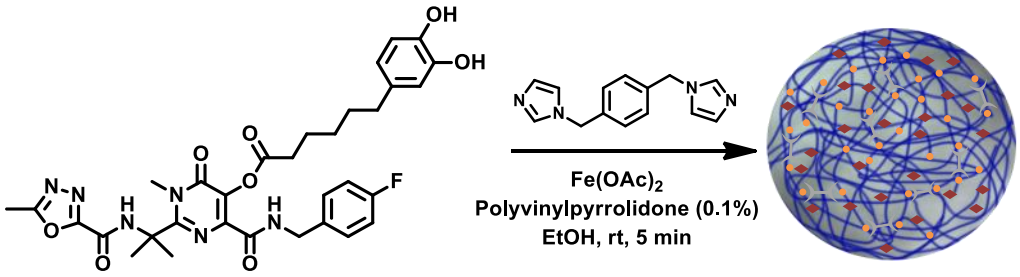

catRAL catRAL-NCPs

1,4-Bis(imidazole-1-ylmethyl)-benzene (**bix**) (27 mg, 0.11 mmol), **catRAL** (150 mg, 0.23 mmol) and polyvinylpyrrolidone (PVP) (average MW 40000) (70 mg) were dissolved in ethanol (62 mL). Under stirring (700 rpm), a solution of $Fe(CH_3COO)_2$ (20 mg, 0.11 mmol in 8 mL ethanol) was added dropwise. Instantaneously, a dark-purple precipitate appeared. After the reaction mixture was stirred at rt for 5 min, the precipitate was collected by centrifugation and then washed with ethanol four times. Finally, the solid was irradiated with a UV lamp for 15 min, and the nanoparticles stored as a solid. SEM images of the resulting material showed spherical nanoparticles with a size distribution of 104 ± 22 nm. Elemental analysis: found (%) C 52.36, H 5.02, N 11.36. Calculated empirical formula: $FeC_{28.5}H_{32.6}F_{0.8}N_{5.6}O_{8.2}$, adjusted as $Fe(catRAL)_{0.77}(bix)_{0.24}(AcO)_{0.24}(H_2O)_{1.56}$.

Synthesis of catFTC-NCPs

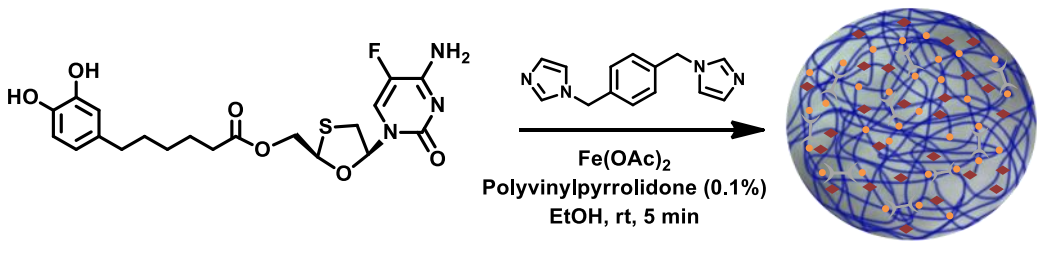

catFTC catFTC-NCPs

1,4-Bis(imidazole-1-ylmethyl)-benzene (bix) (13 mg, 0.05 mmol), **catFTC** (50.0 mg, 0.11 mmol) and polyvinylpyrrolidone (PVP) (average MW 40000) (33 mg) were dissolved in ethanol (30 mL). Under stirring (700 rpm), a solution of $Fe(CH_3COO)_2$ (10 mg, 0.05 mmol in 4 mL ethanol) was added dropwise. Instantaneously, a dark-purple precipitate appeared. After the reaction mixture was stirred at rt for 5 min, the precipitate was collected by centrifugation and then washed with ethanol four times. Finally, the solid was irradiated with a UV lamp for 15 min, and the nanoparticles stored as a solid. SEM images of the resulting material showed spherical nanoparticles with a size distribution of 169 ± 29 nm. Elemental analysis: found (%) C 49.11, H 4.91, N 9.24, S 4.67. Calculated empirical formula: $FeC_{29.9}H_{35.6}F_{0.9}N_{5.0}O_{10.3}S_{0.9}$, adjusted as $Fe(catFTC)_{0.90}(bix)_{0.57}(AcO)_{1.96}(H_2O)_{0.98}$.

Synthesis of catRAL-catFTC-NCPs

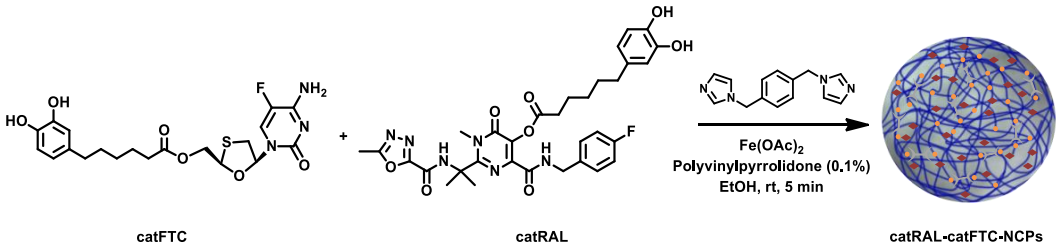

1,4-Bis(imidazole-1-ylmethyl)-benzene (**bix**) (26 mg, 0.11 mmol), **catRAL** (72 mg, 0.11 mmol), **catFTC** (50.0 mg, 0.11 mmol) and polyvinylpyrrolidone (PVP) (average MW 40000) (33 mg) were dissolved in ethanol (30 mL). Under stirring (700 rpm), a solution of $Fe(CH_3COO)_2$ (19 mg, 0.11 mmol in 4 mL ethanol) was added dropwise. Instantaneously, a dark-purple precipitate appeared. After the reaction mixture was stirred at rt for 5 min, the precipitate was collected by centrifugation and then washed with ethanol four times. Finally, the solid was irradiated with a UV lamp for 15 min, and the nanoparticles stored as a solid. SEM images of the resulting material showed spherical nanoparticles. Elemental analysis: found (%) C 51.87, H 4.96, N 10.78, S 2.09. Calculated empirical formula: $FeC_{36.8}H_{41.8}F_{1.2}N_{6.6}O_{11.3}S_{0.6}$, adjusted as $Fe(catFTC)_{0.55}(bix)_{0.31}(catRAL)_{0.61}(AcO)_{0.95}(H_2O)_{1.19}$

In vitro drug release studies in presence/absence of esterases

catRAL, **catFTC**, **catRAL-NCPs** or **catFTC-NCPs** (15 mg) were added to a PBS/BSA 0.5 mM buffer solution at pH 7.4 (25 mL) with and without pig liver esterases (PLE) (180 mU/mL). All samples were maintained at 37 °C under constant stirring. Aliquots (400 µL) were taken at different periods of time, the volume extracted was replaced with additional 400 µL of the PBS/BSA 0.5 mM solution and kept at -22 °C until their analysis. When the last aliquot was taken, three additional aliquots (380 µL) were extracted and treated with HCl 2 M in methanol (20 µL) to measure the remaining amount of non-released drug. Then, all the aliquots were filtered through a 10 kDa membrane (Amicon® Ultra 0.5 mL) (15 min x 14.6k RFC) before their injection in the HPLC system. All experiments were done by duplicate.

HPLC methods for release kinetics quantification

Chromatographic conditions for catRAL and catRAL-NCPs: Analyses were performed using a HPLC Waters 2695 separation module coupled to a Waters 2487 UV-Vis detector (suitable for dual detection). The column used was a Restek Ultra C18 (250 mm x 4.6 mm). Eluent A was a 0.1% (v/v) H_3PO_4 aqueous solution and eluent B was methanol (HPLC grade). Injection volume was 20 µL. Before the analysis, the RP column was pre-equilibrated using the starting conditions of the method (30 % A (v/v)) for 30 min. Initial flow rate was set at 0.4 mL/min. The analysis began with an isocratic elution for 5 min. Then, a gradual increase of B from 70% to 80% (v/v) was performed for 3 min and isocratic elution was maintained for 9 min. Finally, mobile phase composition was reset to the initial conditions (A:B) 30:70 (v/v) in 1 min and stayed for 7 min to equilibrate for the next injection. Column temperature was kept at 25˚C and the detection wavelengths were 214 and 280 nm. Calibration curves: A calibration curve using raltegravir (RAL) and 4-((4-fluorobenzyl)carbamoyl)-1-methyl-2-(2-(5-methyl-1,3,4-oxadiazole-2-carboxamido)propan-2-yl)-6-oxo-1,6-dihydropyrimidin-5-yl 6-(3,4-dihydroxyphenyl)hexanoate (catRAL) as external standards was prepared. Standards were prepared by duplicate, diluting a stock solution containing RAL and catRAL (0.51 mg/mL) dissolved in a water/methanol 30:70 mixture. In both cases, results were adjusted to linear regression models with $R^2 > 0.999$ between the ranges of 0.5-508 and 0.5-516 µg/mL for RAL and catRAL, respectively. $\mathbf{t_{R,RAL}}$ = 11.1 min; $\mathbf{t_{R,catRAL}}$ = 14.3 min.

Chromatographic conditions for catFTC and catFTC-NCPs: Analyses were performed using a HPLC Waters 2695 separation module coupled to a Waters 2487 UV-Vis detector

(suitable for dual detection). The column used was a Restek Ultra C18 (250 mm x 4.6 mm). Eluent A was a 0.1% (v/v) H_3PO_4 aqueous solution and eluent B was methanol (HPLC grade). Injection volume was 20 µL. Before the analysis, the RP column was pre-equilibrated using the starting conditions of the method (80 % A (v/v)) for 30 min. Initial flow rate was set at 0.4 mL/min. The analysis began with an isocratic elution for 2 min. Then, a gradual increase of B from 20% to 40% (v/v) was performed for 3 min. Additional increases of B from 40% to 60% (v/v) in 5 min and from 60% to 90% (v/v) in 2 min were done. Then, an isocratic elution was maintained for 11 min. Finally, mobile phase composition was reset to the initial conditions (A:B) 80:20 (v/v) in 1 min and stayed for 7 min to equilibrate for the next injection. Column temperature was kept at 25˚C and the detection wavelengths were 214 and 280 nm. Calibration curves: A calibration curve using emtricitabine (FTC) and ((2*R*,5*S*)-5-(4-amino-5-fluoro-2-oxopyrimidin-1(2*H*)-yl)-1,3-oxathiolan-2-yl)methyl 6-(3,4-dihydroxyphenyl)hexanoate (catFTC) as external standards was prepared. Standards were prepared by duplicate, diluting a stock solution containing FTC and catFTC (1 mg/mL) dissolved in methanol and diluted with distilled water to a final water/methanol ratio of 80:20. In both cases, results were adjusted to linear regression models with $R^2 > 0.99$ between the ranges of 0.4-448 and 0.4-408 µg/mL for FTC and catFTC, respectively. $\mathbf{t_{R,FTC}}$ = 11.6 min; $\mathbf{t_{R,catFTC}}$ = 20.2 min.

Chromatographic conditions for catRAL-catFTC-NCPs: Analyses were performed using a HPLC Waters 2695 separation module coupled to a Waters 2487 UV-Vis detector (suitable for dual detection). The column used was a Restek Ultra C18 (250 mm x 4.6 mm). Eluent A was a 0.1% (v/v) H_3PO_4 aqueous solution and eluent B was methanol (HPLC grade). Injection volume was 20 µL. Before the analysis, the RP column was pre-equilibrated using the starting conditions of the method (80 % A (v/v)) for 30 min. Initial flow rate was set at 0.4 mL/min. The analysis began with an isocratic elution for 2 min. Then, a gradual increase of B from 20% to 40% (v/v) was performed for 3 min. An additional increase of B from 40% to 60% (v/v) in 5 min was done. Then, an isocratic elution was maintained for 6 min. A third gradient from 60% to 80% (v/v) was performed for 13 min, an isocratic elution was then maintained for 7 min. Finally, mobile phase composition was reset to the initial conditions (A:B) 80:20 (v/v) in 1 min and stayed for 7 min to equilibrate for the next injection. Column temperature was kept at 25˚C and the detection wavelengths were 214 and 280 nm. Calibration curves: A calibration curve using raltegravir (RAL), 4-((4-fluorobenzyl)carbamoyl)-1-methyl-2-(2-(5-methyl-1,3,4-oxadiazole-2-carboxamido)propan-2-yl)-6-oxo-1,6-dihydropyrimidin-5-yl 6-(3,4-

dihydroxyphenyl)hexanoate (catRAL), emtricitabine (FTC) and ((2*R*,5*S*)-5-(4-amino-5-fluoro-2-oxopyrimidin-1(2*H*)-yl)-1,3-oxathiolan-2-yl)methyl 6-(3,4-dihydroxyphenyl)hexanoate (catFTC) as external standards was prepared. Standards were prepared by duplicate, diluting a stock solution containing RAL, catRAL, FTC and catFTC (1 mg/mL) dissolved in methanol and diluted with distilled water to a final water/methanol ratio of 80:20. In both cases, results were adjusted to linear regression models with $R^2 > 0.999$ between the ranges of 0.4-424, 0,4-432, 0.4-424 and 0.4-432 µg/mL for RAL, catRAL, FTC and catFTC, respectively. $\mathbf{t_{R,RAL}}$ = 28.7 min; $\mathbf{t_{R,catRAL}}$ = 34.0 min; $\mathbf{t_{R,FTC}}$ = 11.7 min; $\mathbf{t_{R,catFTC}}$ = 29.4 min.

Synthesis of ((2*R*,5*S*)-5-(4-amino-2-oxopyrimidin-1(2*H*)-yl)-1,3-oxathiolan-2-yl)methyl 6-(3,4-bis((tert-butyldiphenylsilyl)oxy)phenyl)hexanoate, 27

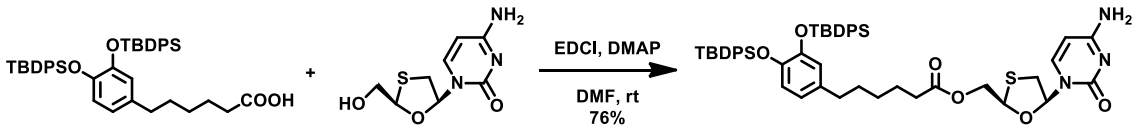

4 3TC 27

N-(3-Dimethylaminopropyl)-*N*'-ethylcarbodiimide hydrochloride (0.33 g, 1.74 mmol) was added dropwise to a stirred ice-cooled solution of **4**, (0.73 g, 1.05 mmol), lamivudine (3TC) (0.20 g, 0.87 mmol) and 4-dimethylaminopyridine (DMAP) (0.21 g, 1.74 mmol) in dry DMF (30 mL). The mixture was allowed to warm to rt and stirred overnight. After TLC analysis (CH_2Cl_2/CH_3OH 90:10) showed the entire consumption of lamivudine, the mixture was diluted with EtOAc (30 mL) and washed with water/brine 1:1 (4x50 mL). The combined aqueous phases were extracted with EtOAc (20 mL) and the resulting organic phases were dried over anhydrous Na_2SO_4 and concentrated under vacuum. The resulting brownish wax was purified by flash column chromatography (CH_2Cl_2/CH_3OH, 98:2 → 95:5) to afford a white solid identified as **27** (0.61 g, 0.66 mmol, 76% yield). **HRMS (EI)** calcd for $([C_{52}H_{61}N_3O_6SSi_2]+H)^+$ 912.3898, found 912.3892.

^{1}H NMR (400 MHz, CD_3OD) δ 7.83 (d, $^3J_{6,5}$ = 7.6 Hz, 1H, H-6), 7.79 (m, 8H, Ph (TBDPS)), 7.55 – 7.26 (m, 12H, Ph (TBDPS)), 6.32 (d, $^3J_{5''',6'''}$ = 8.2 Hz, 1H, H-5'''), 6.29 (t, $^3J_{1',2'}$ = 5.1 Hz, 1H, H-1'), 6.23 (d, $^4J_{2''',6'''}$ = 2.1 Hz, 1H, H-2'''), 6.12 (dd, $^3J_{6''',5'''}$ = 8.2 Hz, $^4J_{6''',2'''}$ = 2.1 Hz, 1H, H-6'''), 5.87 (d, $^3J_{5,6}$ = 7.6 Hz, 1H, H-5), 5.38 (dd, $^3J_{4',5'}$ = 5.4 Hz, $^3J_{4',5'}$ = 3.4 Hz, 1H, H-4'), 4.53 (dd, $^2J_{gem}$ = 12.2 Hz, $^3J_{5',4'}$ = 5.4 Hz, 1H, H-5'), 4.34 (dd, $^2J_{gem}$ = 12.2 Hz, $^3J_{5',4'}$ = 3.4 Hz, 1H, H-5'), 3.49 (dd, $^2J_{gem}$ = 12.0 Hz, $^3J_{2',1'}$ = 5.4 Hz, 1H, H-2'), 3.11 (dd, $^2J_{gem}$ = 12.0 Hz, $^3J_{2',1'}$ = 4.7 Hz, 1H, H-2'), 2.15 (t, $^3J_{2'',3''}$ = 7.5 Hz, 2H, H-2''), 2.01 (t, $^3J_{6'',5''}$ = 7.2 Hz, 2H, H-6''), 1.36 (quint, $^3J_{3'',2''}$ = 7.5 Hz, $^3J_{3'',4''}$ = 7.5 Hz, 2H, H-3''), 1.12 (s, 9H, *t*-Bu (TBDPS)), 1.11 (s, 9H, *t*-Bu (TBDPS)), 1.07 – 0.98 (m, 2H, H-5''), 0.97 – 0.86 (m, 2H, H-4''). **^{13}C NMR** (101 MHz, CD_3OD) δ 174.23 (C-1''), 147.00 (C-4), 145.17 (C-2), 142.10 (C-

6), 136.72 (TBDPS), 134.47 (TBDPS), 134.40 (TBDPS), 131.12 (TBDPS), 131.06 (TBDPS), 128.94 (TBDPS), 128.88 (TBDPS), 128.87 (TBDPS), 121.76 (C-2'''), 121.59 (C-6'''), 121.21 (C-5'''), 95.90 (C-5), 88.93 (C-1'), 84.23 (C-4'), 65.40 (C-5'), 38.15 (C-2'), 35.28 (C-6''), 34.67 (C-2''), 31.34 (C-5''), 28.99 (C-4''), 27.28 (*t*-Bu), 27.24 (*t*-Bu), 25.64 (C-3'').

Synthesis of ((2*R*,5*S*)-5-(4-amino-2-oxopyrimidin-1(2*H*)-yl)-1,3-oxathiolan-2-yl)methyl 6-(3,4-dihydroxyphenyl)hexanoate, cat3TC

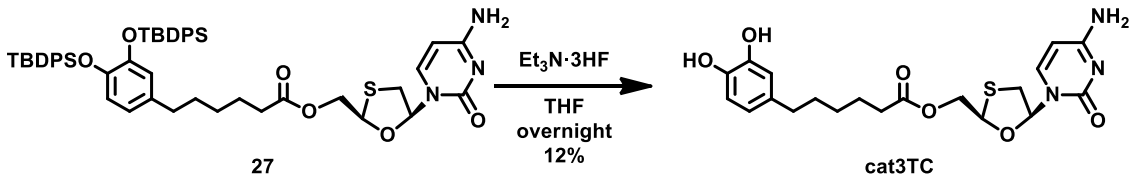

Triethylamine trihydrofluoride (1.4 mL, 8.63 mmol) was added to a stirred ice-cooled solution of **27** (1.31 g, 1.44 mmol) in dry THF (28 mL). The mixture was allowed to warm to rt and stirred overnight. The reaction was quenched with 0.6 mL of brine, diluted with 28 mL diethyl ether, filtered and the solvent was evaporated under vacuum. The resulting crude was purified by phase-reversed (C18) flash column chromatography (H_2O/CH_3OH 50:50 → 30:70 → 0:100) to furnish **cat3TC** as a yellowish solid (0.07 g, 0.18 mmol, 12%). R_f ($CHCl_3/CH_3OH$ 90:10) = 0.16. **HRMS (EI)** calcd for $[C_{20}H_{25}N_3O_6S]$+ 436.1542, found 436.1542.

^{1}H NMR (360 MHz, CD_3OD) δ 7.86 (d, $^3J_{6,5}$= 7.5 Hz, 1H, H-6), 6.64 (d, $^3J_{5''',6'''}$ = 8.0 Hz, 1H, H-5'''), 6.58 (d, $^4J_{2''',6'''}$ = 1.8 Hz, 1H, H-2'''), 6.45 (dd, $^3J_{6''',5'''}$ = 7.9 Hz, $^4J_{6''',2'''}$ = 1.9 Hz, 1H, H-6'''), 6.28 (t, $^3J_{1',2'}$ = 4.9 Hz, 1H, H-1'), 5.89 (d, $^3J_{5,6}$ = 7.6 Hz, 1H, H-5), 5.41 – 5.37 (dd, $^3J_{4',5'}$ = 5.1 Hz, $^3J_{4',5'}$ = 3.3 Hz, 1H, H-4'), 4.58 (dd, $^2J_{gem}$ = 12.3 Hz, $^3J_{5',4'}$ = 5.2 Hz, 1H, H-5'), 4.37 (dd, $^2J_{gem}$ = 12.3 Hz, $^3J_{5',4'}$ = 3.3 Hz, 1H, H-5'), 3.53 (dd, $^2J_{gem}$ = 12.1 Hz, $^3J_{2',1'}$ = 5.4 Hz, 1H, H-2', 3.14 (dd, $^2J_{gem}$ = 12.1 Hz, $^3J_{2',1'}$ = 4.6 Hz, 1H, H-2'), 2.44 (t, $^3J_{6'',5''}$ = 7.5 Hz, 2H, H-6''), 2.38 (t, $^3J_{2'',3''}$ = 7.2 Hz, 2H, H-2''), 1.65 (quint, $^3J_{3'',2''}$ = 7.6 Hz, $^3J_{3'',4''}$ = 7.6 Hz, 2H, H-3''), 1.56 (quint, $^3J_{5'',6''}$ = 7.6 Hz, $^3J_{5'',4''}$ = 7.6 Hz, 2H, H-5''), 1.40 – 1.31 (m, 4H, H-4'').

Synthesis of (*R*)-(((((1-(6-amino-9*H*-purin-9-yl)propan-2-yl)oxy)methyl)phosphoryl)bis(oxy))bis(methylene) diphenethyl dicarbonate, 28

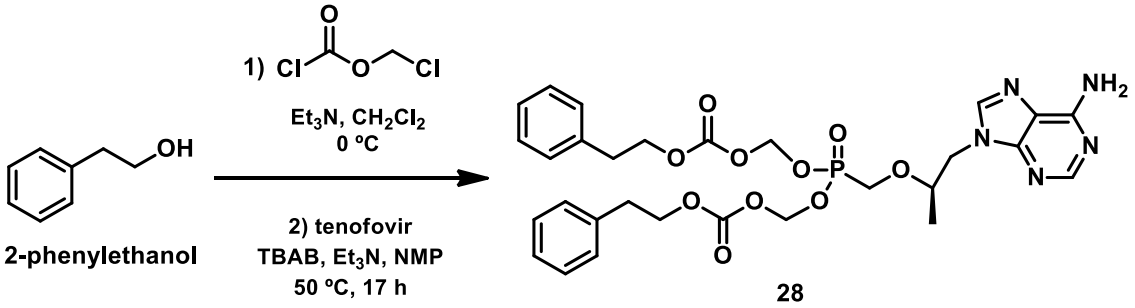

Chloromethyl chloroformate (0.3 mL, 3.34 mmol) was added to a stirred ice-cooled solution of 2-phenylethanol (0.4 mL, 3.34 mmol) and anhydrous triethylamine (0.7 mL, 5.01 mmol) in dry CH_2Cl_2 (19 mL). TLC analysis revealed the consumption of 2-phenyethanol in 3 hours. The solvent was removed under reduced pressure and the crude was used without further purification in the next synthetic step. Tenofovir monohydrate (0.26 g, 0.87 mmol) was previously dried at 80 °C overnight and suspended in dry *N*-methyl-2-pyrrolidone (NMP) (2 mL). To this suspension, 3 mL of cyclohexane were added and distilled at 40 °C and 70 mbar three times, removing distilled cyclohexane each at cycle. Then, tetra-n-butylammonium bromide (TBAB) (0.28 g, 0.87 mmol) dissolved in 1 mL of dry NMP and triethylamine (0.5 mL, 3.46 mmol) were added to the suspension of tenofovir and heated to 50 °C. After 17 h of stirring, the crude was washed with fresh cyclohexane (4x8 mL). Then, ethyl acetate (8 mL) and water (4 mL) were added to the NMP phase and the organic layer was collected. The organic phase was further washed with cold water (3x8 mL) and NaCl 10% (8 mL). The combined organic layers were dried over Na_2SO_4 and the solvent was removed under reduced pressure. To the resulting wax dissolved in isopropanol (3 mL), fumaric acid (0.07 g, 0.64 mmol) was added and stirred for 2 h at 50 °C. The mixture was submerged in an ice bath and stirred for an additional hour until a precipitate identified as the fumarate salt of **28** (0.24 g, 0.37 mmol, 43%) appeared.

^{1}H NMR (360 MHz, CD_3OD) δ 8.22 (s, 1H, H-4), 8.08 (s, 1H, H-9), 7.34 – 7.13 (m, 10H, Ph), 6.76 (s, 2H, fumarate), 5.65 – 5.38 (m, 4H, H-1''), 4.45 – 4.31 (m, 4H, H-1'''), 4.13 (dd, $^2J_{gem}$ = 14.7 Hz, $^3J_{1',2'}$ = 7.2 Hz, 1H, H-1'), 4.04 – 3.89 (m, 1H, H-2'), 3.85 – 3.72 (m, 2H, H-5'), 3-02 - 2.91 (m, 4H, H-2'''), 1.19 (s, 3H, H-3'). **^{13}C NMR** (91 MHz, CD_3OD) δ 168.23 (C=O), 156.82 (C-6), 154.98 (C-2), 153.00 (C-4), 143.87 (C-9), 138.67 (C-7), 135.25 (fumarate), 129.99 (Ph), 129.55 (Ph), 127.69 (Ph), 85.90 (C-1''), 70.45 (C-1'''), 64.74 (C-2'), 62.55 (C-5'), 49.71 (C-1'), 35.81 (C-2'''), 25.25 (C-3').

Synthesis of 6-(3,4-bis((*tert*-butyldiphenylsilyl)oxy)phenyl)hexan-1-ol, 24

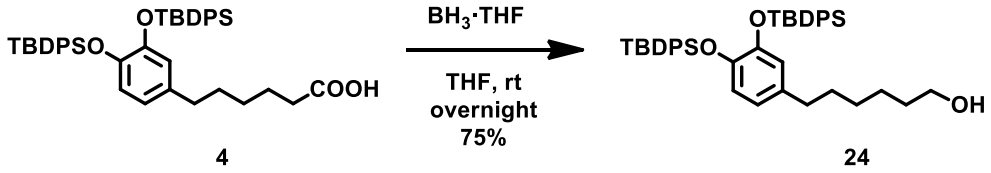

Borane tetrahydrofuran complex solution (1 M) in THF (2.6 mL, 2.57 mmol) was added to a solution of **4** (0.60 g, 0.86 mmol) in dry THF (5 mL) and stirred overnight at rt. After purification by flash column chromatography (hexane/CH_2Cl_2 20:80 → CH_2Cl_2 100%), the resulting colorless wax was identified as **24** (0.44 g, 0.64 mmol, 75%).

^{1}H NMR (250 MHz, CD_3Cl) δ 8.03 – 7.72 (m, 8H, Ph (TBDPS)), 7.49 -7.34 (m, 12H, Ph (TBDPS)), 6.41 (d, $^3J_{5',6'}$ = 8.0 Hz, 1H, H-5'), 6.28 (s, 1H, H-2'), 6.21 (d, $^3J_{6',5'}$ = 8.3 Hz, 1H, H-6'), 3.70 (t, $^3J_{1,2}$ = 6.7 Hz, 2H, H-1), 2.21 (t, $^3J_{6,5}$ = 7.7 Hz, 2H, H-6), 1.43 - 1.31 (m, 2H, H-2), 1.22 (s, 9H, TBDPS), 1.20 (s, 9H, TBDPS), 1.14 – 0.85 (m, 6H, H-3 + H-4 + H-5).

Attempts to synthesize (*R*)-(((((1-(6-amino-9*H*-purin-9-yl)propan-2-yl)oxy)methyl)phosphoryl)bis(oxy))bis(methylene) bis(6-(3,4-bis((*tert*-butyldiphenylsilyl)oxy)phenyl)hexyl) dicarbonate, 30

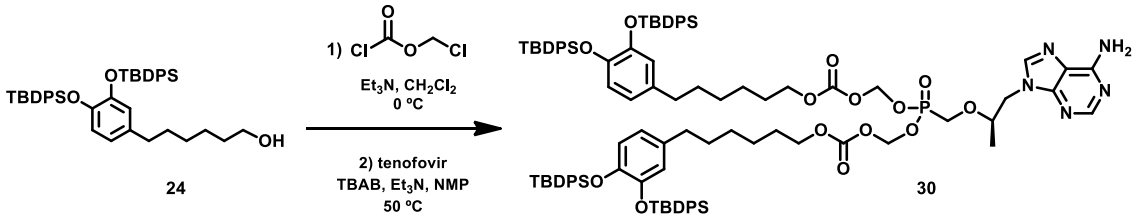

Chloromethyl chloroformate (0.06 mL, 0.64 mmol) was added to a stirred ice-cooled solution of **24** (0.44 g, 0.64 mmol) and anhydrous triethylamine (0.13 mL, 0.96 mmol) in dry CH_2Cl_2 (20 mL). TLC analysis revealed the consumption of **24** in 4 hours. The solvent was removed under reduced pressure and the crude was used without further purification in the next synthetic step. Tenofovir monohydrate (0.04 g, 0.13 mmol) was previously dried at 80 °C overnight and suspended in dry *N*-methyl-2-pyrrolidone (NMP) (2 mL). To this suspension, 3 mL of cyclohexane were added and distilled at 40 °C and 70 mbar three times, removing distilled cyclohexane each at cycle. Then, tetra-n-butylammonium bromide (TBAB) (0.04 g, 0.13 mmol) dissolved in 1 mL of dry NMP and triethylamine (0.07 mL, 0.52 mmol) were added to the suspension of tenofovir and heated to 50 °C. After 15.5 h of stirring, the crude was washed with fresh cyclohexane (4x6 mL). Then, ethyl acetate (4 mL) and water (3 mL) were added to the NMP phase and the organic layer

was collected. The combined organic layers were dried over Na_2SO_4 and the solvent was removed under reduced pressure.

4.6 References

[1] Chiodo, F.; Marradi, M.; Calvo, J.; Yuste, E.; Penadés, S. Glycosystems in Nanotechnology: Gold Glyconanoparticles as Carrier for Anti-HIV Prodrugs. *Beilstein J. Org. Chem.* **2014**, *10*, 1339–1346.

[2] Evangelio, E.; Hernando, J.; Imaz, I.; Bardají, G. G.; Alibés, R.; Busqué, F.; Ruiz-Molina, D. Catechol Derivatives as Fluorescent Chemosensors for Wide-Range PH Detection. *Chem. Eur. J.* **2008**, *14* (31), 9754–9763.

[2] Zhou, T.; Su, H.; Dash, P.; Lin, Z.; Dyavar Shetty, B. L.; Kocher, T.; Szlachetka, A.; Lamberty, B.; Fox, H. S.; Poluektova, L.; et al. Creation of a Nanoformulated Cabotegravir Prodrug with Improved Antiretroviral Profiles. *Biomaterials* **2018**, *151*, 53–65.

[3] Chiodo, F.; Marradi, M.; Calvo, J.; Yuste, E.; Penadés, S. Glycosystems in Nanotechnology: Gold Glyconanoparticles as Carrier for Anti-HIV Prodrugs. *Beilstein J. Org. Chem.* **2014**, *10*, 1339–1346.

[4] Wang, D.; Zou, L.; Jin, Q.; Hou, J.; Ge, G.; Yang, L. Human Carboxylesterases: A Comprehensive Review. *Acta Pharm. Sin. B* **2018**, *8* (5), 699–712.

[5] Neue, U. D.; Mndez, A.; Tran, K.; Diehl, D. M.; McBrien, M.; Kuss, H.-J.; Schmer, S. Fundamentals of Optimization: Sections 1.3–1.6. *HPLC Made to Measure: A Practical Handbook for Optimization*. **2006**, 71–147.

[6] Kromidas, S.; Neue, U. D.; Cheng, Y.-F.; Lu, Z. (n.d.). Fundamentals of Optimization: Sections 1.1 and 1.2. *HPLC Made to Measure: A Practical Handbook for Optimization*. **2006**, 1–70.

[7] Montella, I. R.; Schama, R.; Valle, D. The Classification of Esterases: An Important Gene Family Involved in Insecticide Resistance, a Review. *Mem. Inst. Oswaldo Cruz* **2012**, *107* (4), 437–449.

[8] Arimilli, M. N.; Cundy, K. C.; Dougherty, J. P.; Kim, C. U.; Oliyai, R.; Stella, V. J., Gilead Sciences, Inc. Antiviral phosphonomethyoxy nucleotide analogs having increased oral bioavailability. U.S. Patent 5,922,695, **1998**.

[9] Ripin, D. H. B.; Teager, D. S.; Fortunak, J.; Basha, S. M.; Bivins, N.; Boddy, C. N.; Byrn, S.; Catlin, K. K.; Houghton, S. R.; Jagadeesh, S. T.; et al. Process Improvements for the Manufacture of Tenofovir Disoproxil Fumarate at Commercial Scale. *Org. Process Res. Dev.* **2010**, *14* (5), 1194–1201.

Chapter 5

General conclusions

During the present thesis, the modification of antiretroviral drugs with catechol moieties has been applied in the synthesis of nanoscale coordination polymers (NCPs) with antiretroviral drug loading. To achieve this, several experimental techniques have been employed throughout the development of the thesis, including organic synthesis and characterization, preparation and characterization of coordination polymers and nanoparticles, development of chromatographic methodologies for the analysis of NCPs, their degradation products and quantification of cellular uptake and, lastly, biological evaluation of the NCPs, including cytotoxicity, cellular uptake and anti-HIV evaluation. The results are summarized next:

1. Catechol conjugates with zidovudine and thymidine, **catAZT** and **catTHY**, have been synthesized and fully characterized with a 32% and 19% overall yield respectively.
2. Iron-based NCPs using **catAZT** or **catTHY**, **catAZT-NCPs** or **catTHY-NCPs**, have been successfully prepared and characterized.
3. The determination of the drug release profile of **catAZT-NCPs** has shown the effects of NCPs formation, namely stabilization of the drug in physiological media as colloidal suspension and control over the release properties of the drug by pH and presence of enzymes. Additionally, biological evaluation of **catAZT-NCPs** has shown reduction in AZT toxicity and increase of cellular uptake while maintaining its anti-HIV properties.
4. Additional catechol conjugates using emtricitabine (FTC), **catFTC**, and raltegravir (RAL), **catRAL**, have been successfully prepared with a 32% and 30% overall yield and characterized accordingly. Then, particles containing a single drug, **catFTC-NCPs** and **catRAL-NCPs** have been prepared and their in vitro drug release profile has been determined. Although NCPs combining **catFTC** and **catRAL** in a 1:1 molar ratio have been prepared, **catRAL-catFTC-NCPs**, the analysis of their drug release profile has revealed a different ratio between drugs during the delivery process. To correct it, new NCPs combining catRAL and catFTC in a 5:1 ratio, **catRAL-catFTC-NCPs (5:1)**, have been prepared and their release has displayed RAL/FTC ratio values near 1.
5. Synthetic approaches for the functionalization of other antiretroviral drugs with catechol have been attempted. Conjugation of catechol to lamivudine (3TC), **cat3TC**, has been achieved, although the low yields obtained (5%) have discouraged their use in NCPs synthesis. Functionalization of tenofovir, **catTFV**, has been challenging, and, although the transformation has been performed succesfully using model compounds, the preparation of target molecule **catTFV** has not been achieved.

Annex

S1. Additional spectra

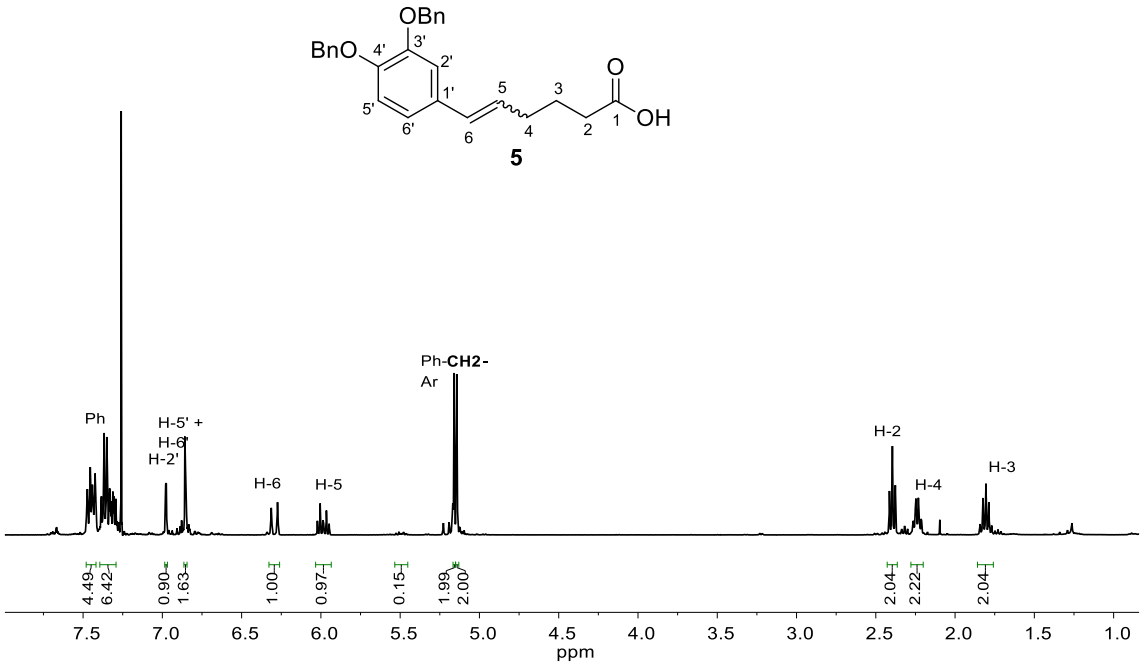

^{1}H NMR (400 MHz, $CDCl_3$)

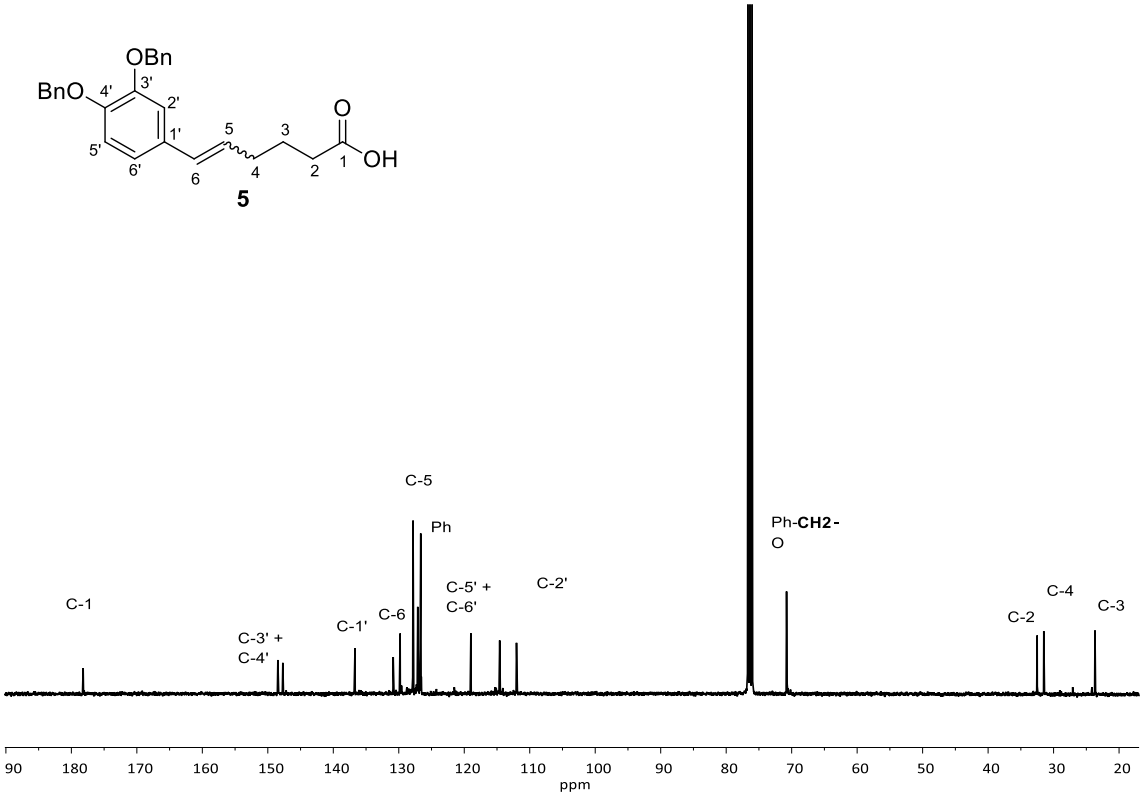

^{13}C NMR (100 MHz, $CDCl_3$)

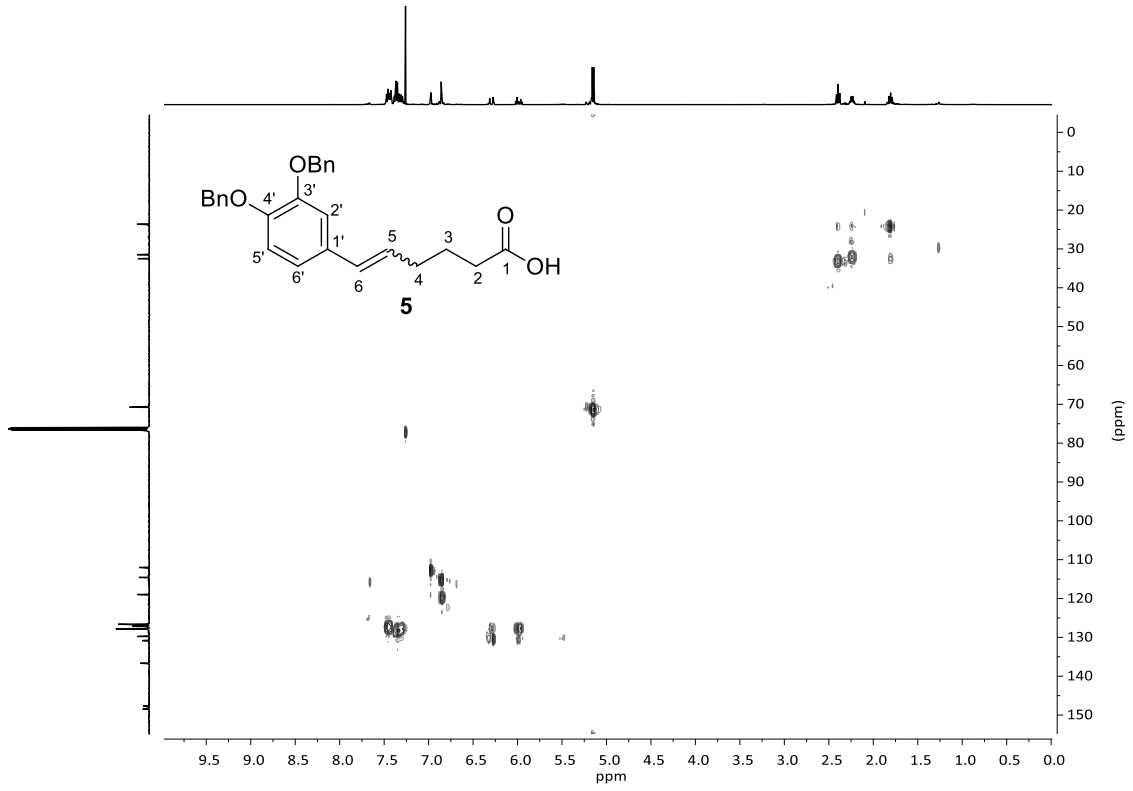

^{1}H – ^{13}C HSQC ($CDCl_3$)

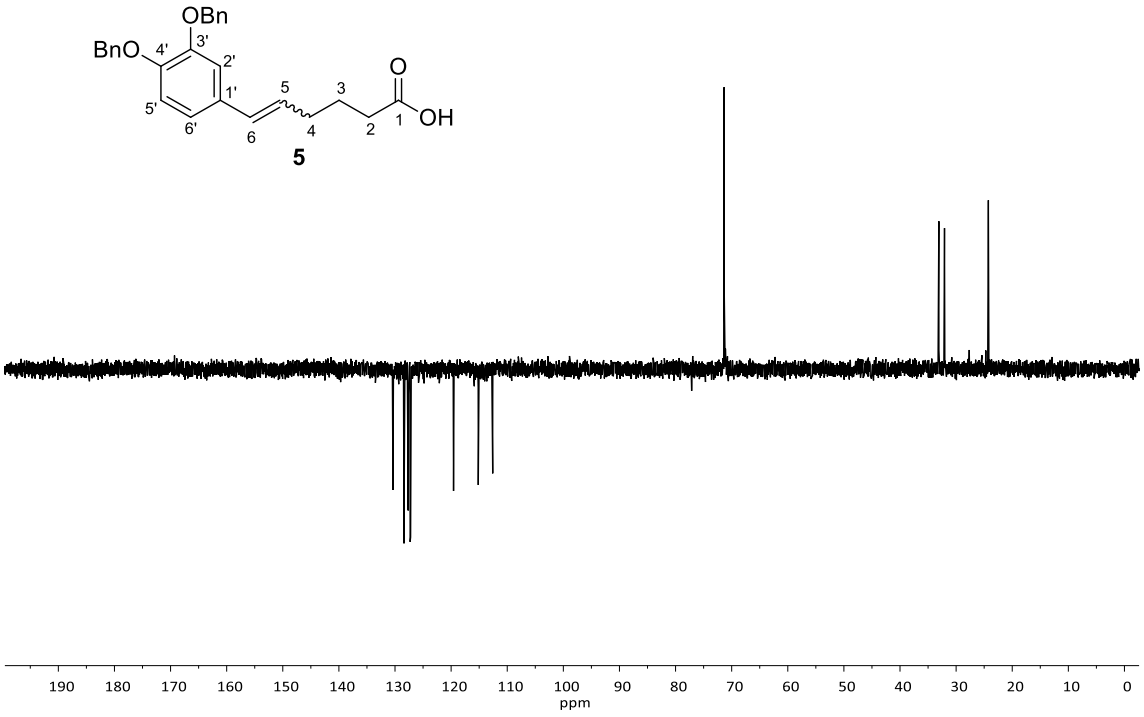

DEPT135 (100 MHz, $CDCl_3$)

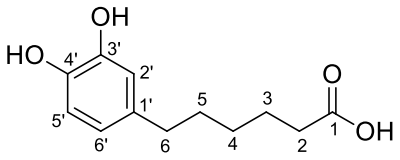

3

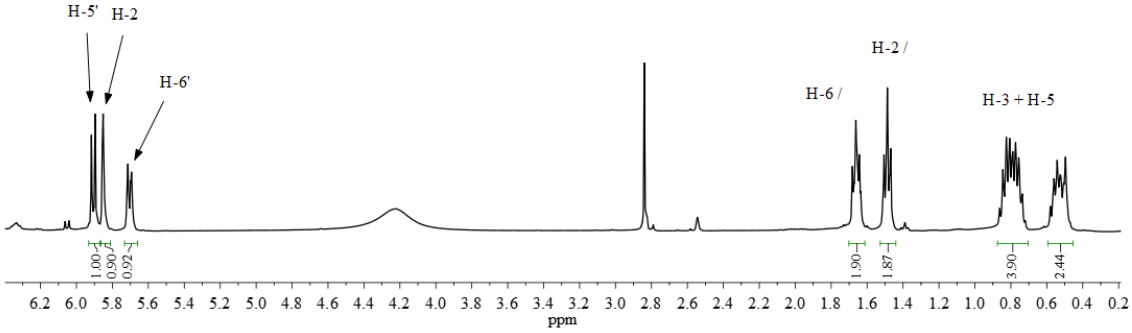

^{1}H NMR (400 MHz, acetone-d_6)

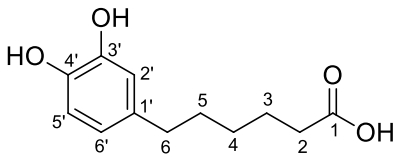

3

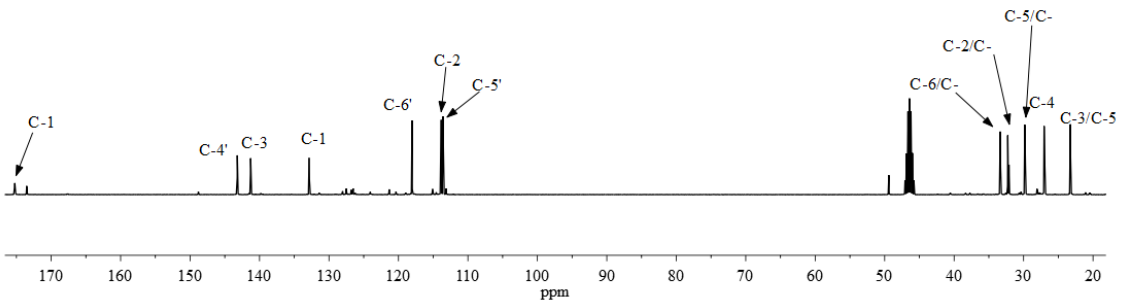

^{13}C NMR (100 MHz, acetone-d_6)

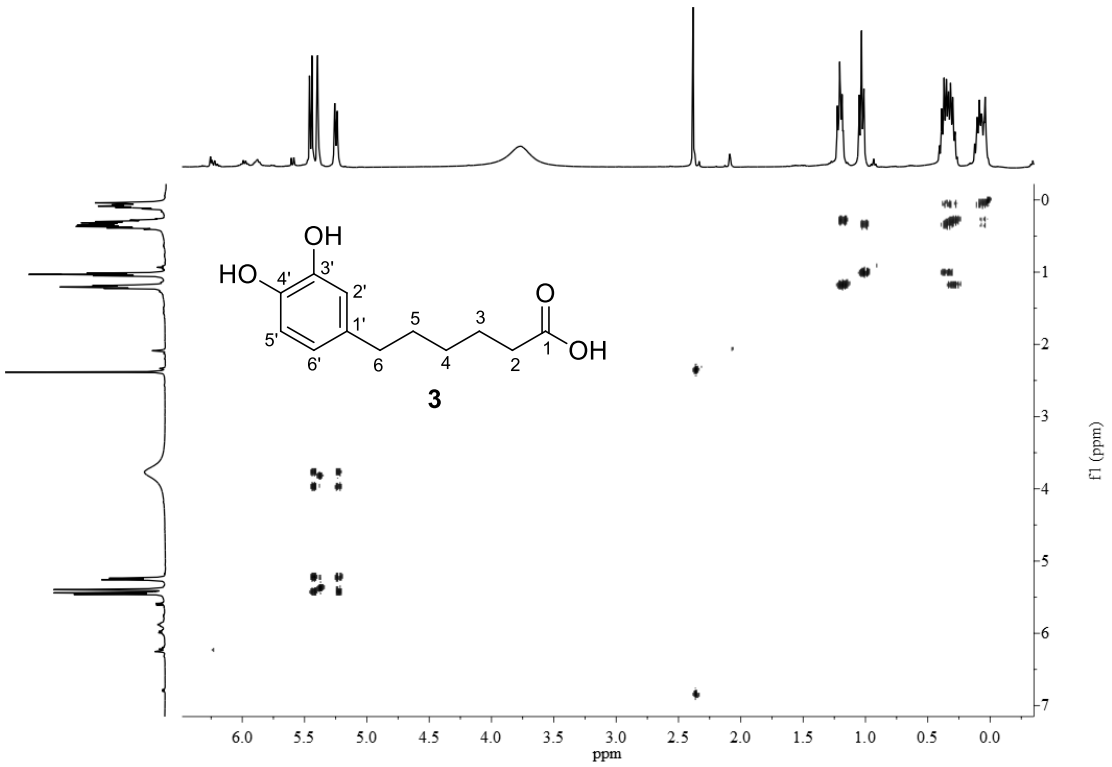

^{1}H – ^{1}H COSY (400 MHz, acetone-d_6)

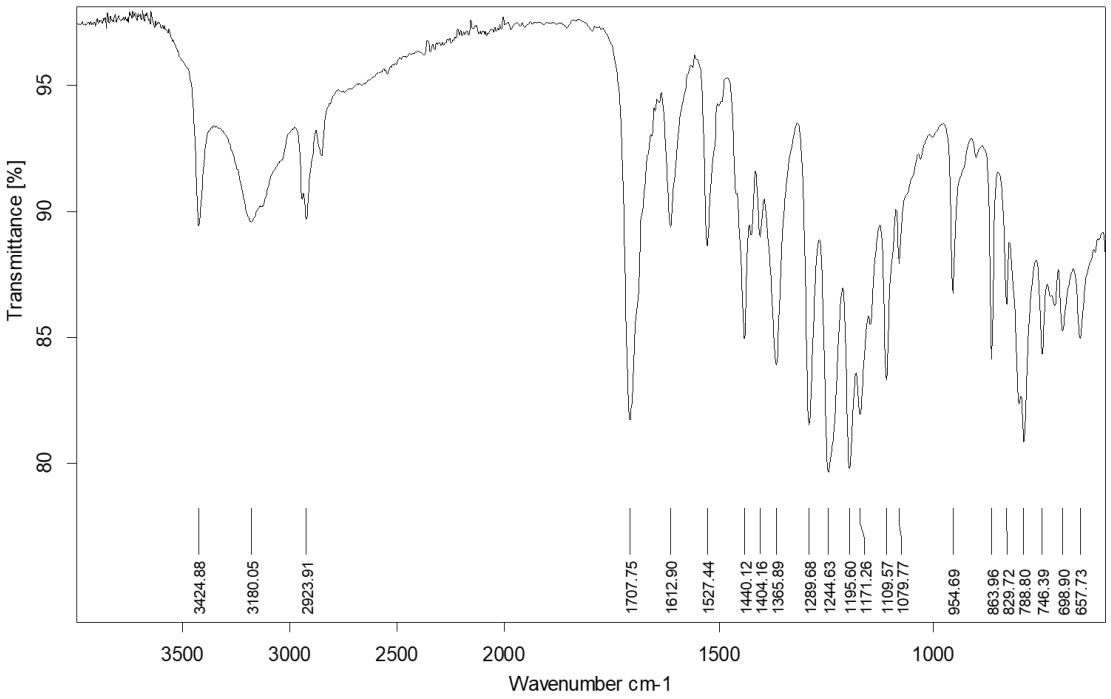

FTIR

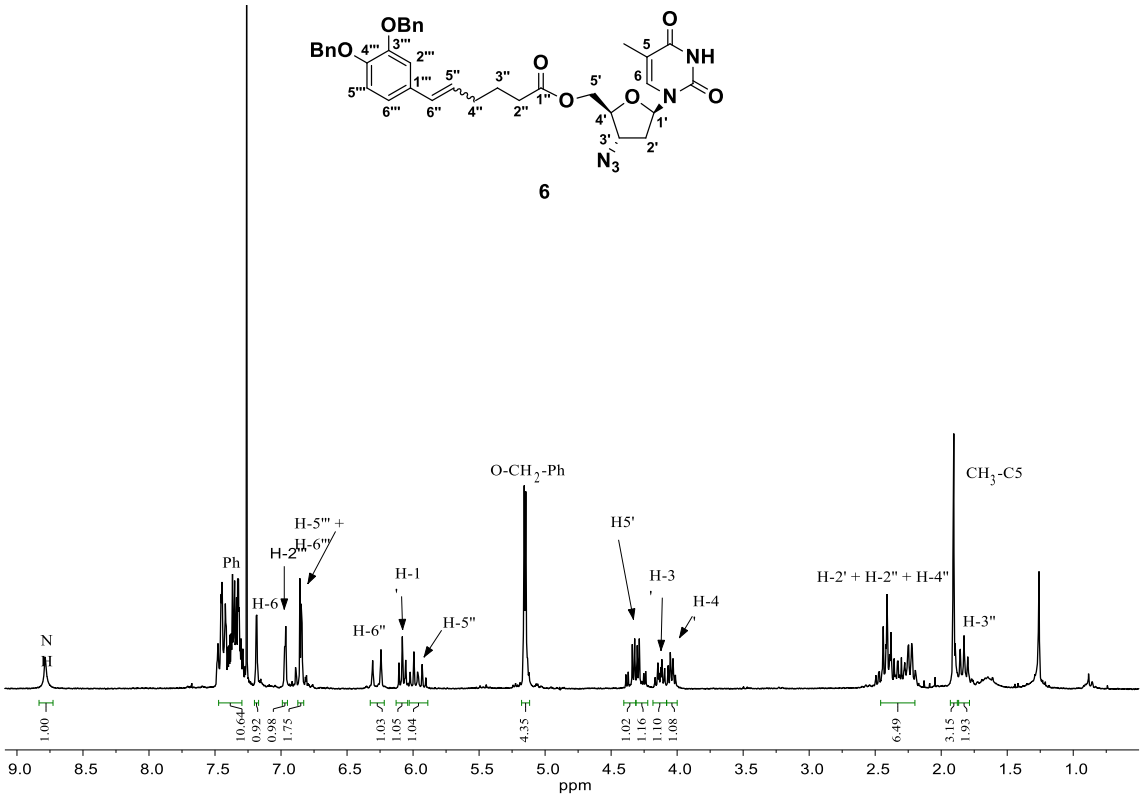

^{1}H NMR (250 MHz, $CDCl_3$)

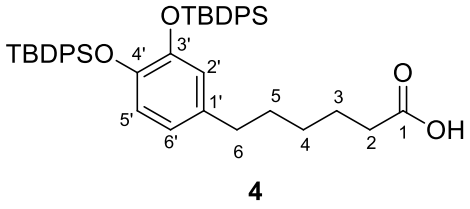

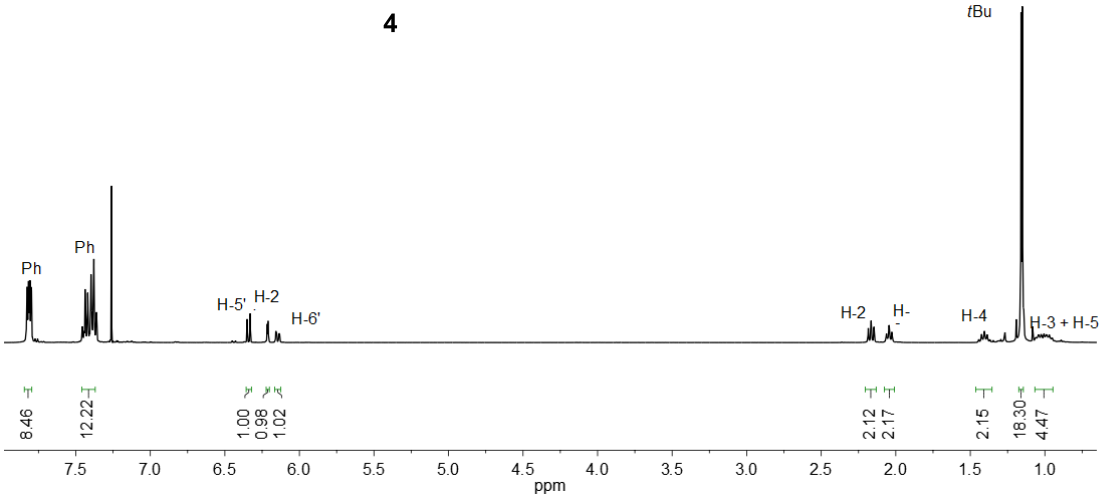

^{1}H NMR (400 MHz, $CDCl_3$)

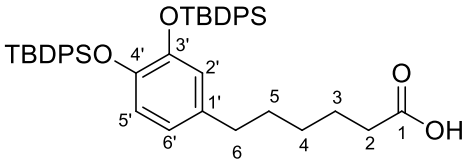

4

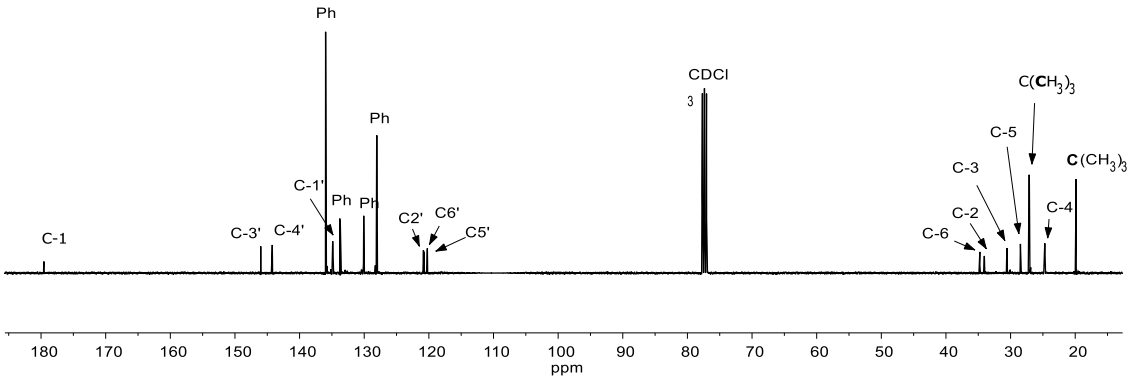

^{13}C NMR (100 MHz, $CDCl_3$)

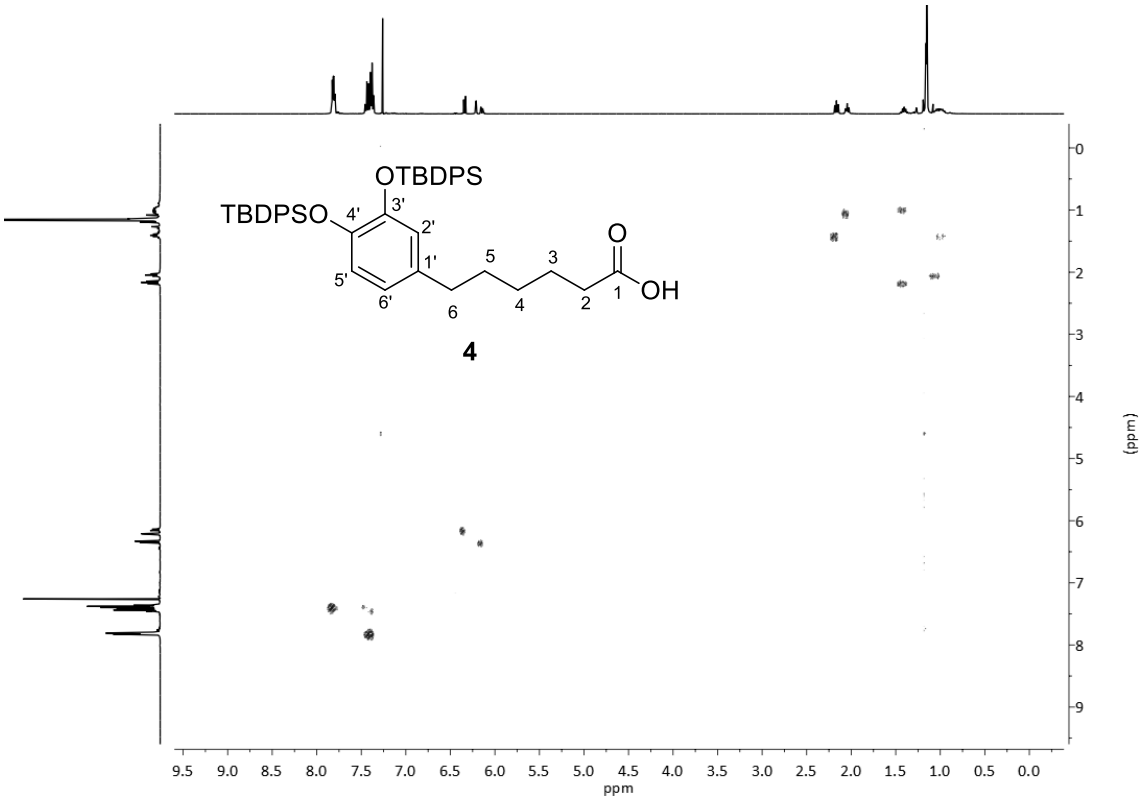

^{1}H – ^{1}H COSY (400 MHz, $CDCl_3$)

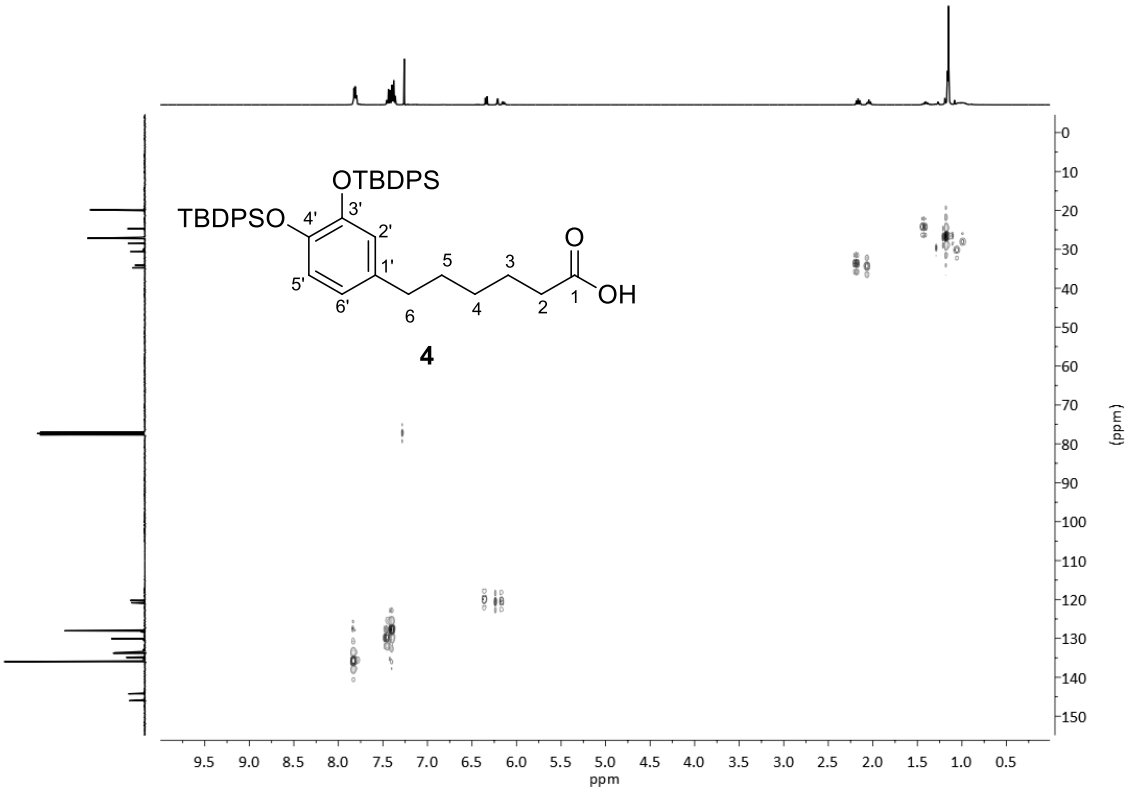

^{1}H – ^{13}C HSQC ($CDCl_3$)

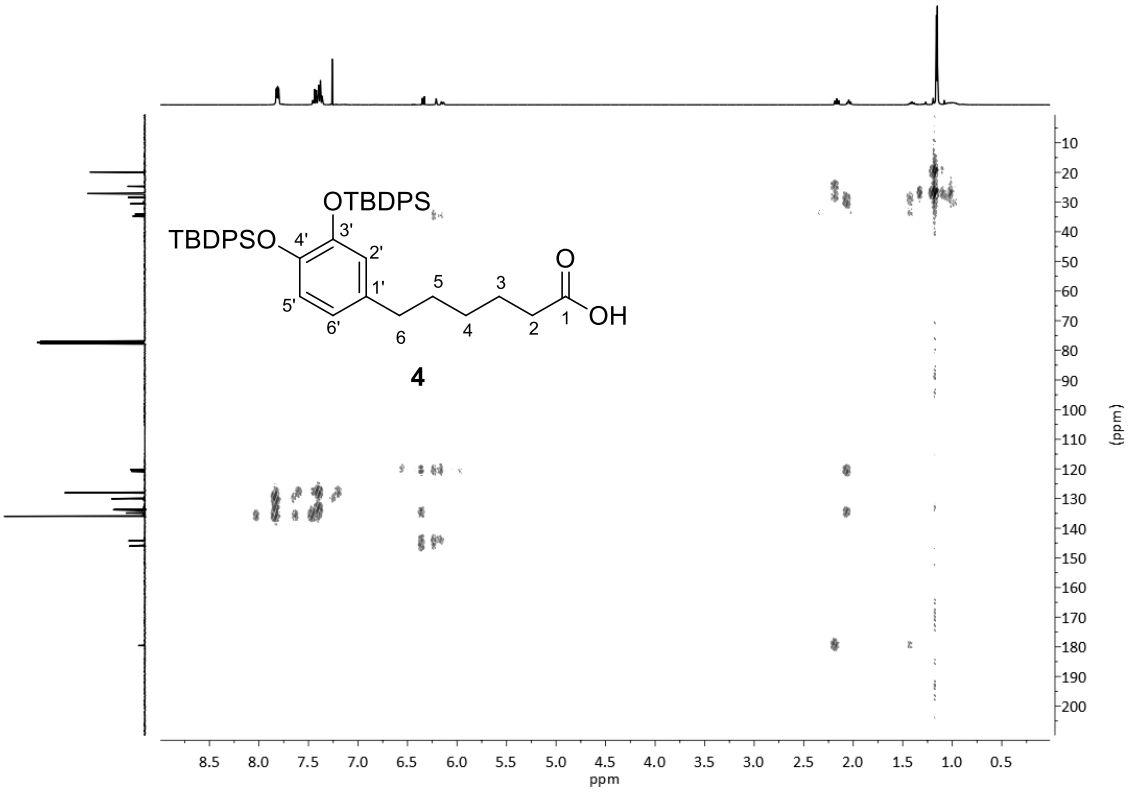

^{1}H – ^{13}C HMBC ($CDCl_3$)

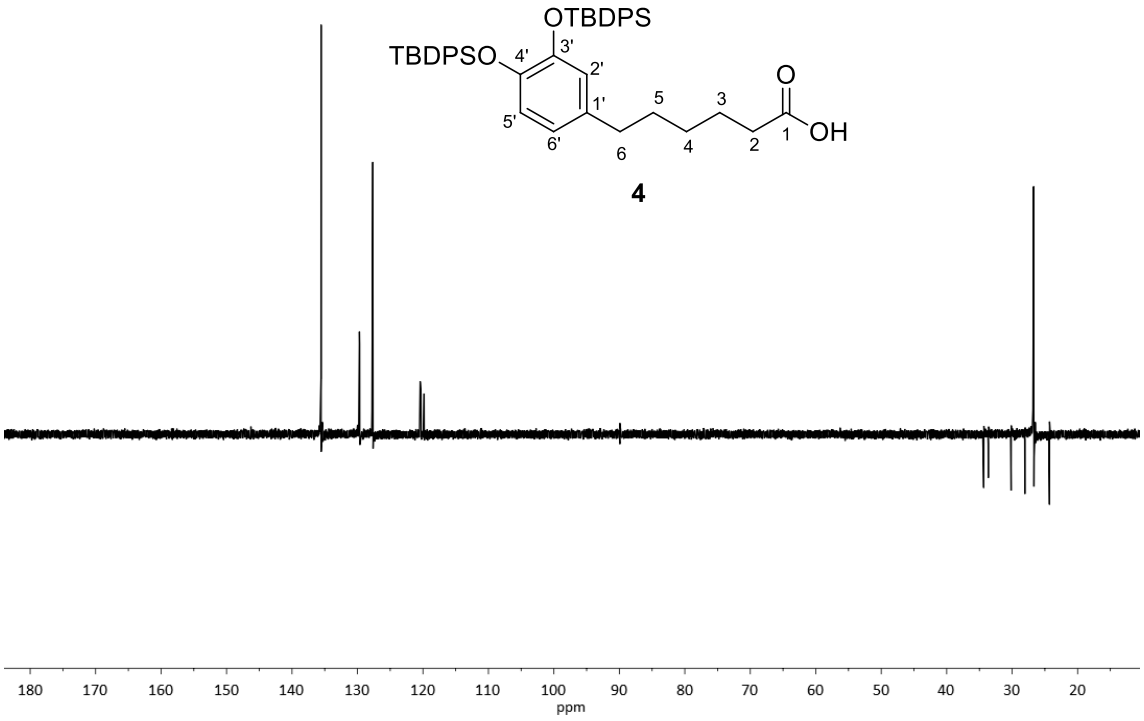

DEPT135 (100 MHz, $CDCl_3$)

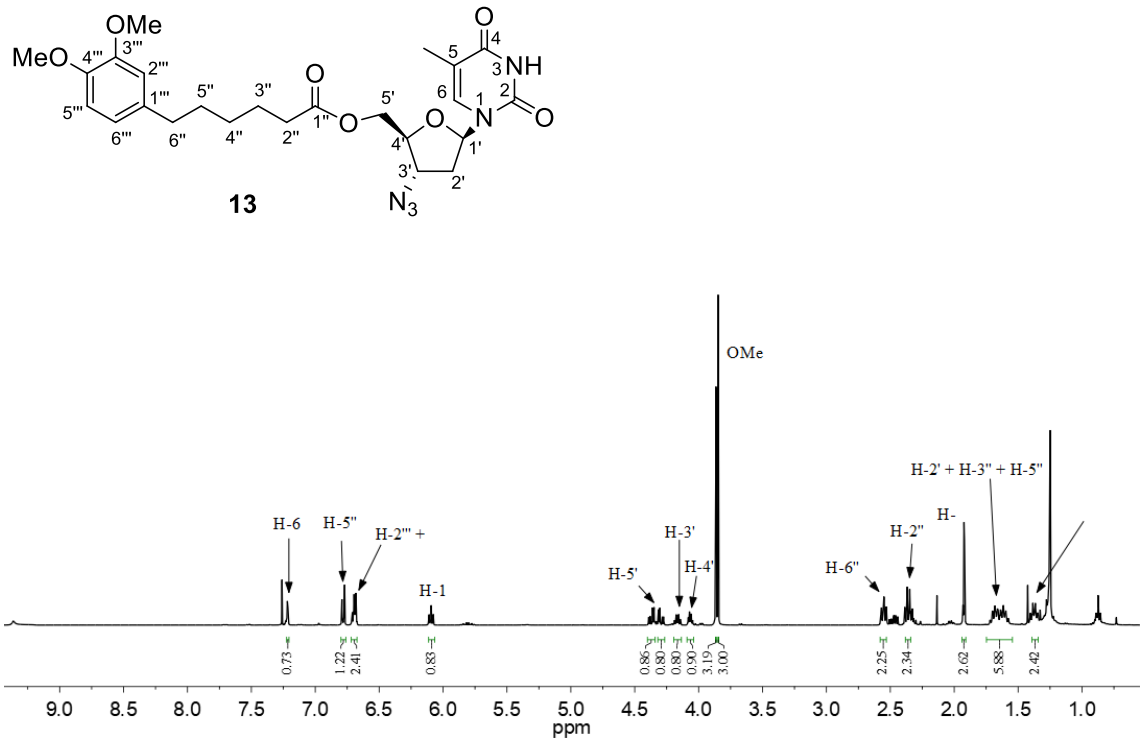

^{1}H NMR (400 MHz, $CDCl_3$)

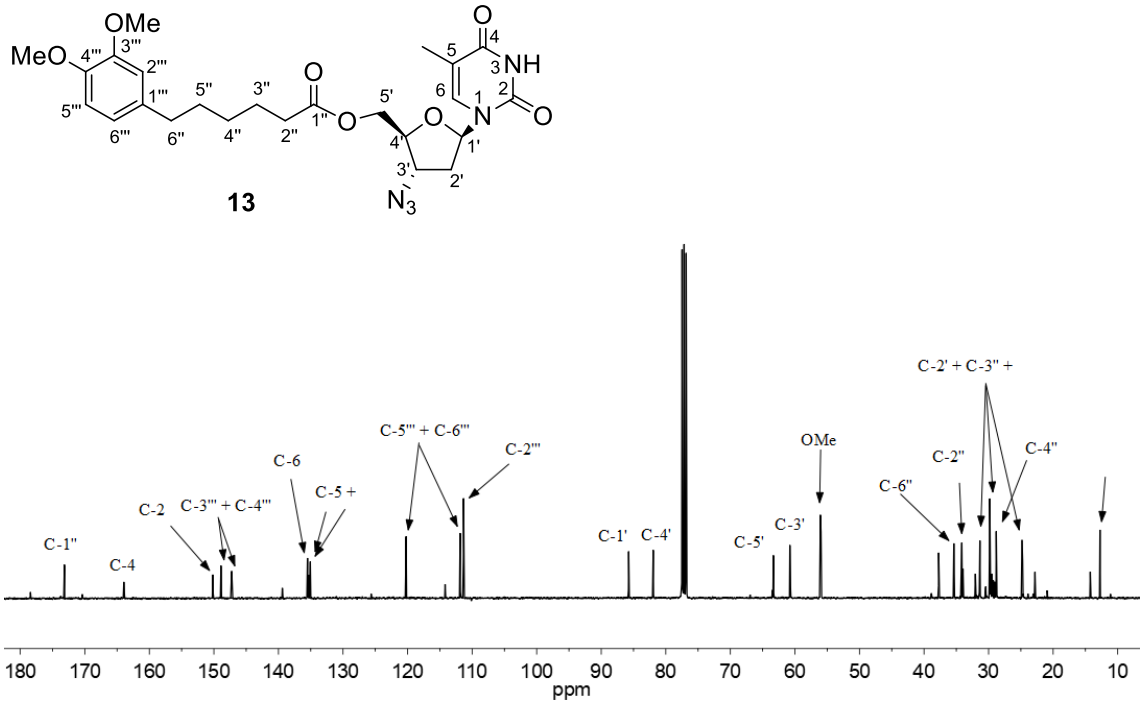

^{13}C NMR (100 MHz, $CDCl_3$)

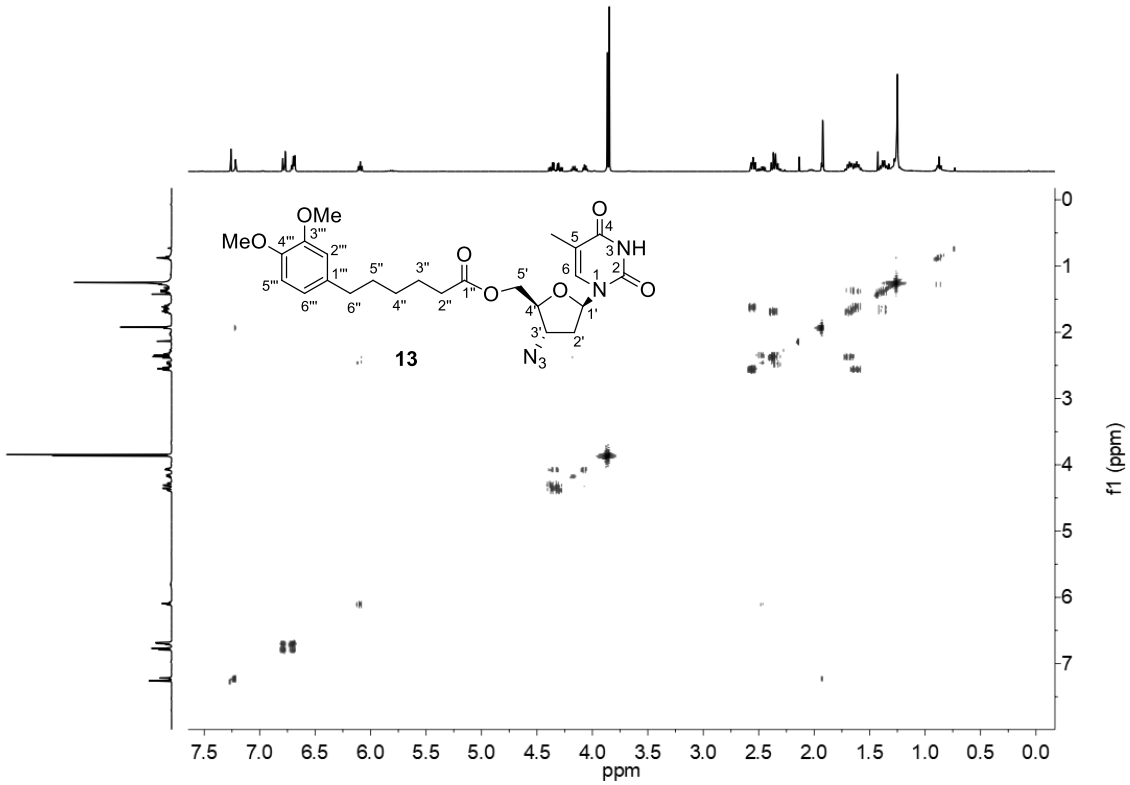

^{1}H – ^{1}H COSY (400 MHz, $CDCl_3$)

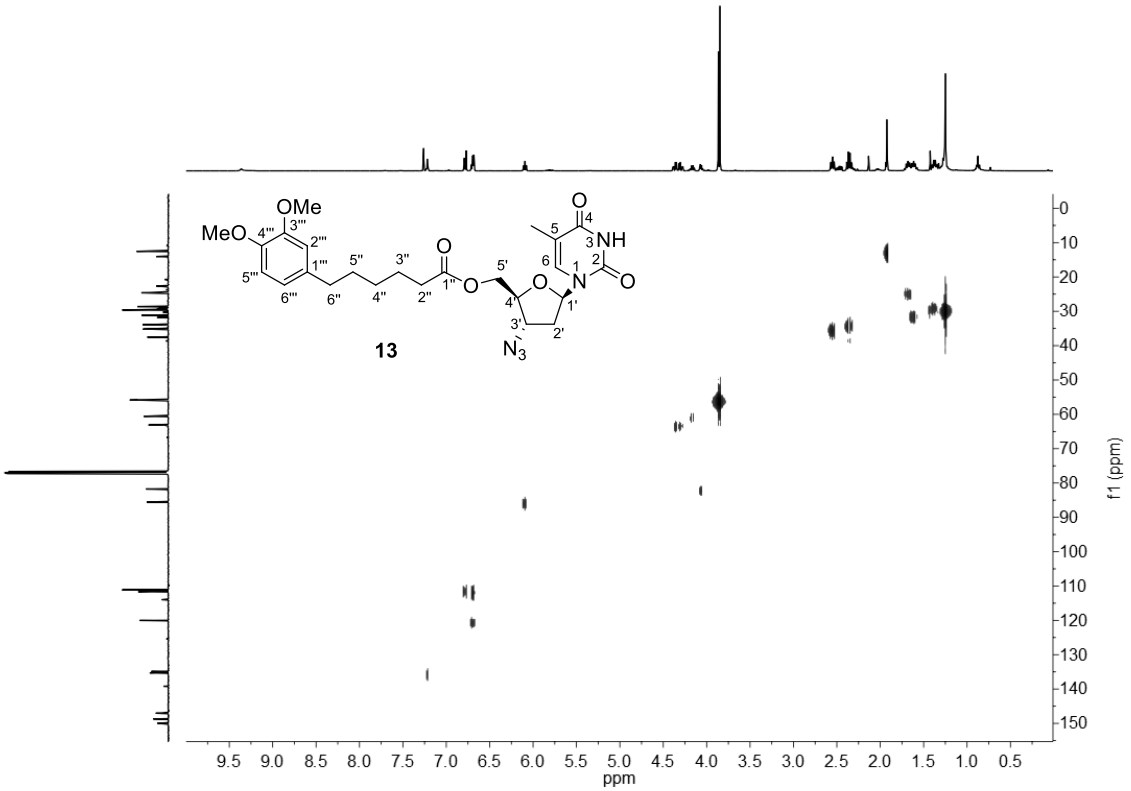

^{1}H – ^{13}C HSQC (400 MHz, $CDCl_3$)

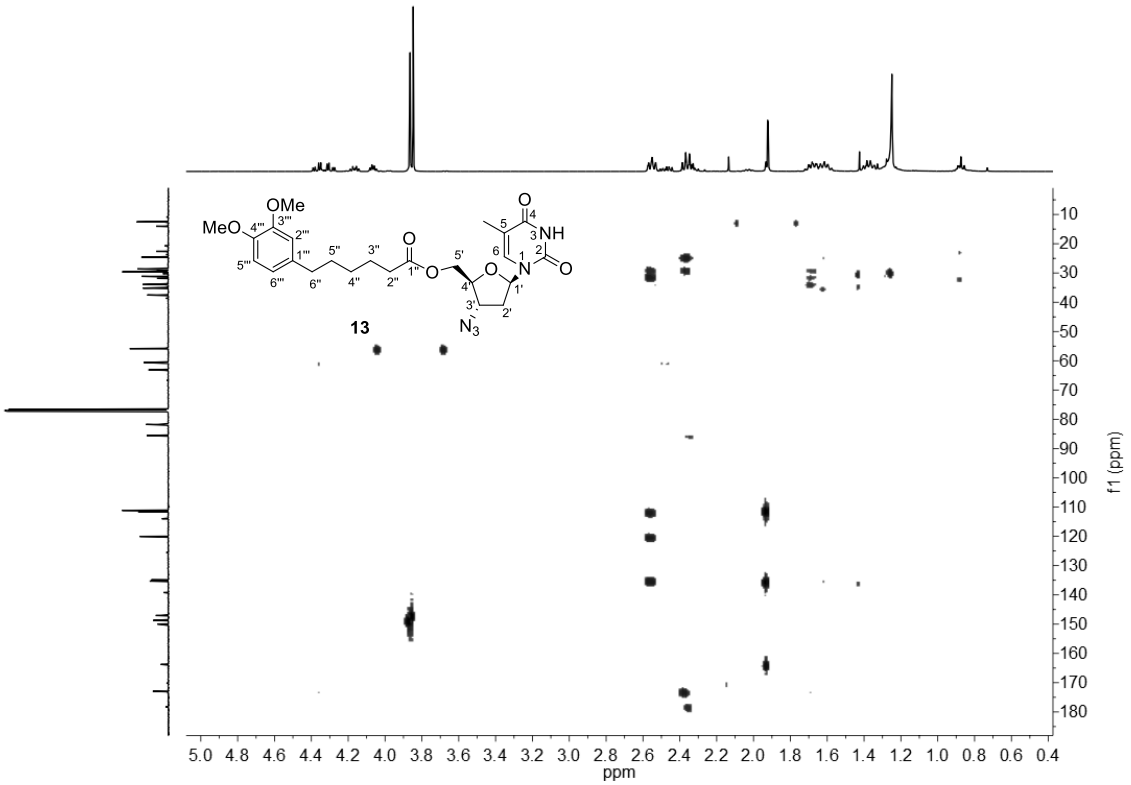

^{1}H – ^{13}C HMBC (400 MHz, $CDCl_3$)

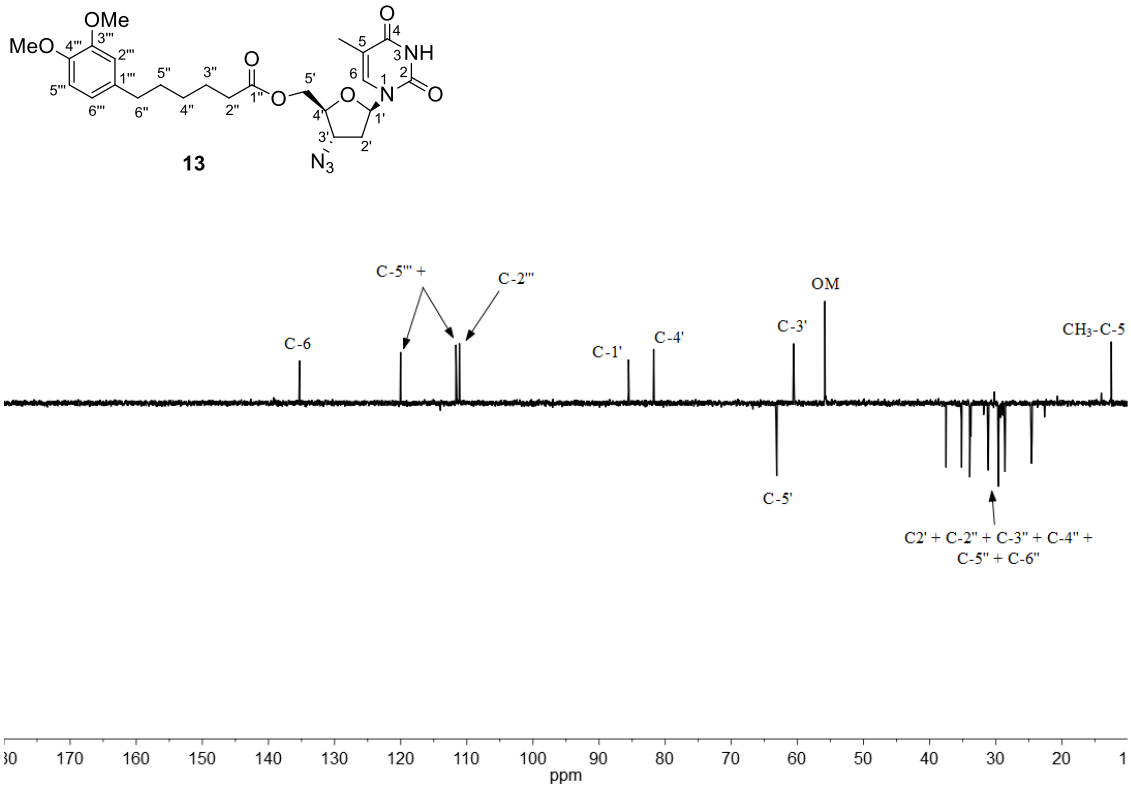

DEPT 135 (100 MHz, $CDCl_3$)

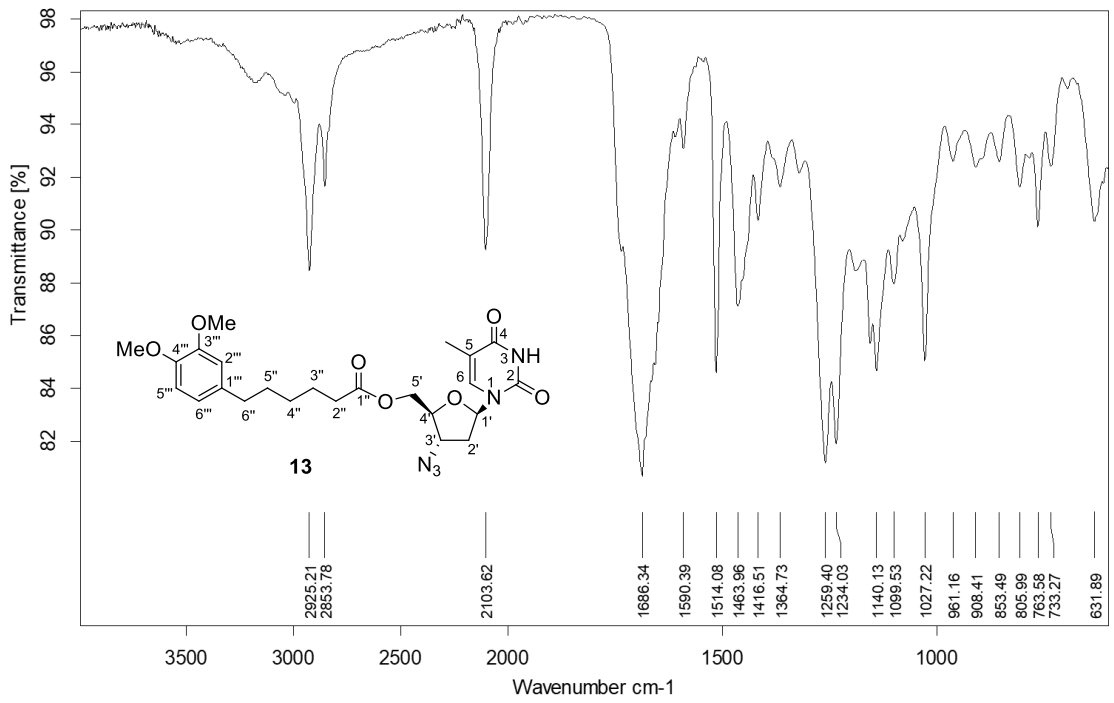

FTIR

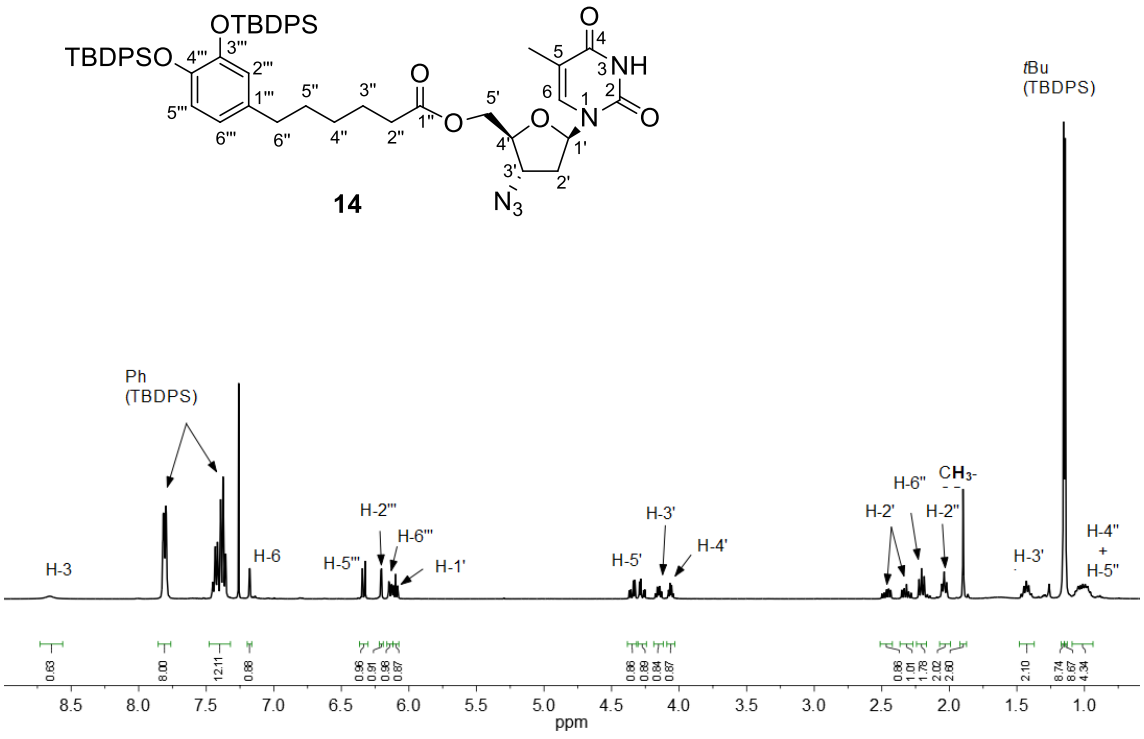

^{1}H NMR (400 MHz, $CDCl_3$)

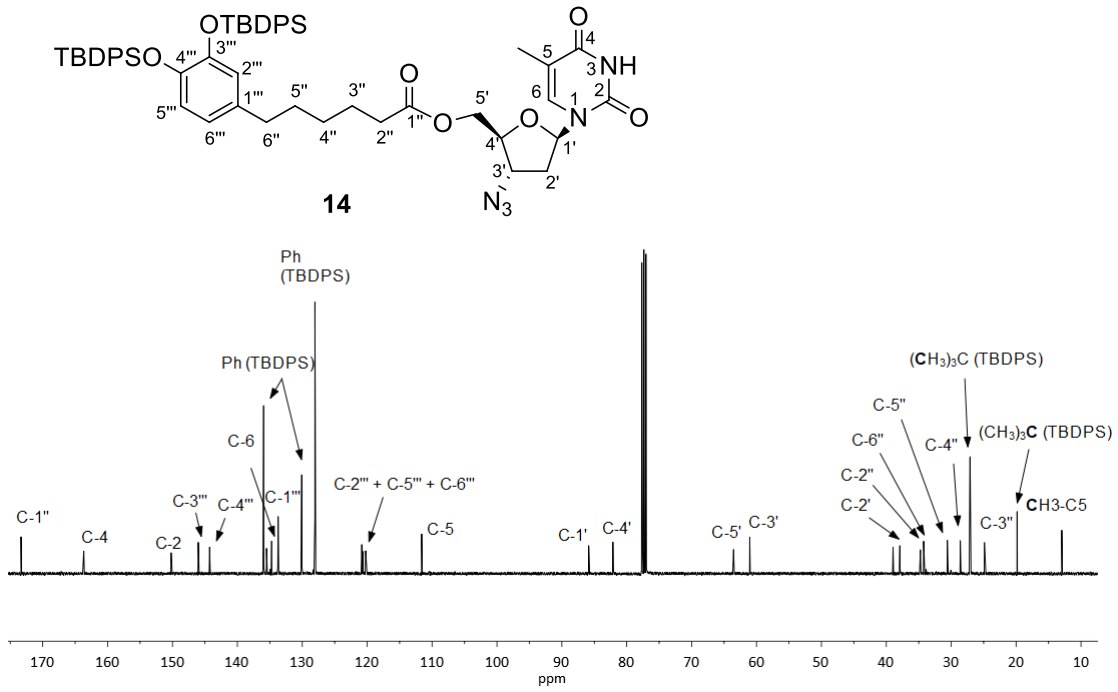

^{13}C NMR (100 MHz, $CDCl_3$)

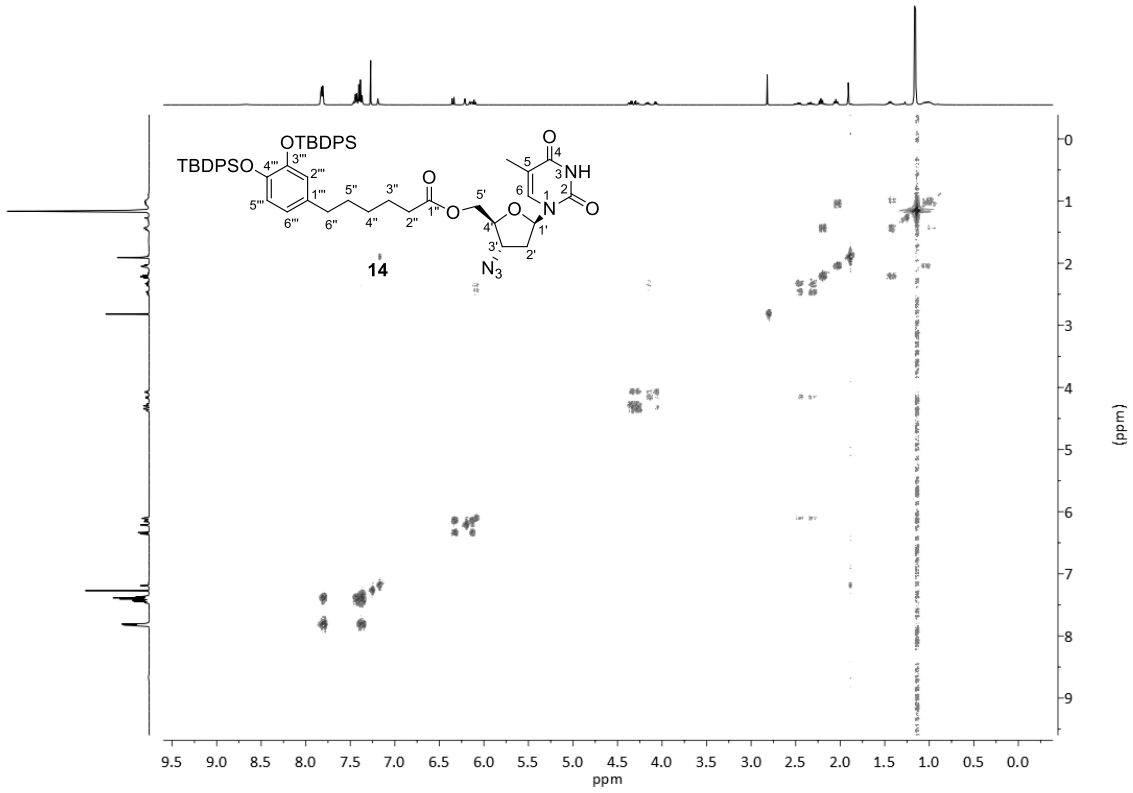

^{1}H – ^{1}H COSY (400 MHz, $CDCl_3$)

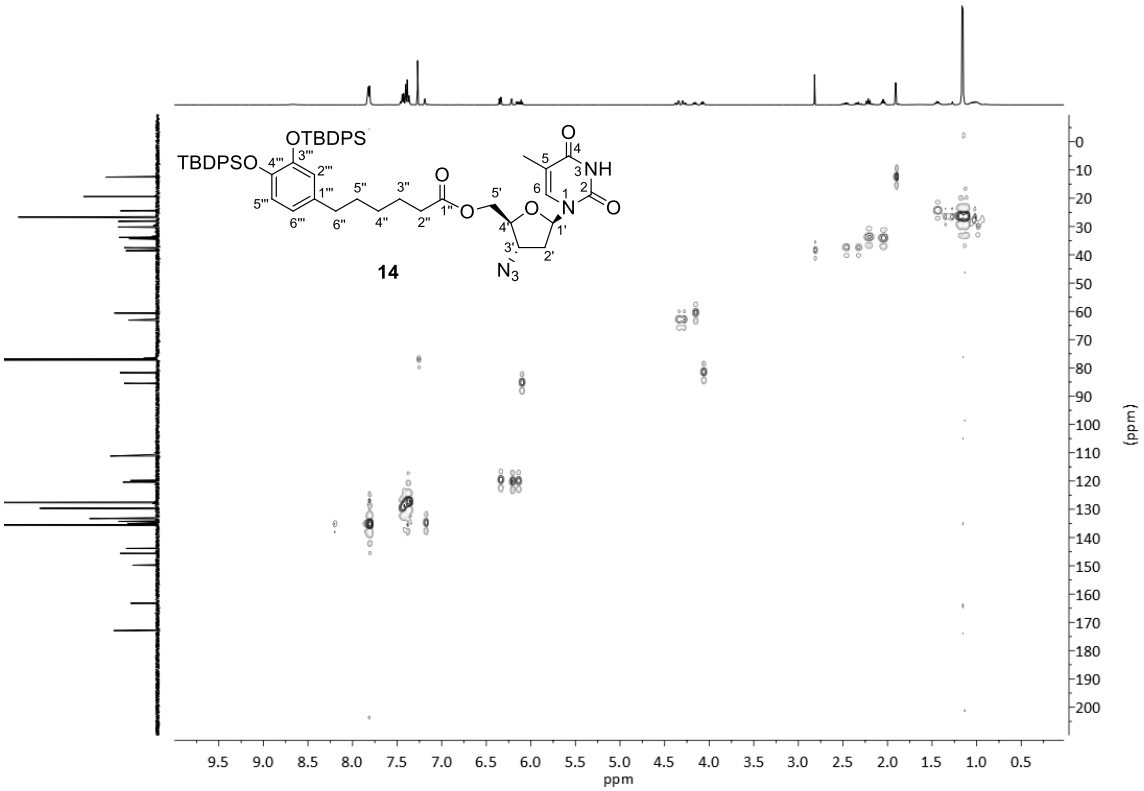

^{1}H – ^{13}C HSQC ($CDCl_3$)

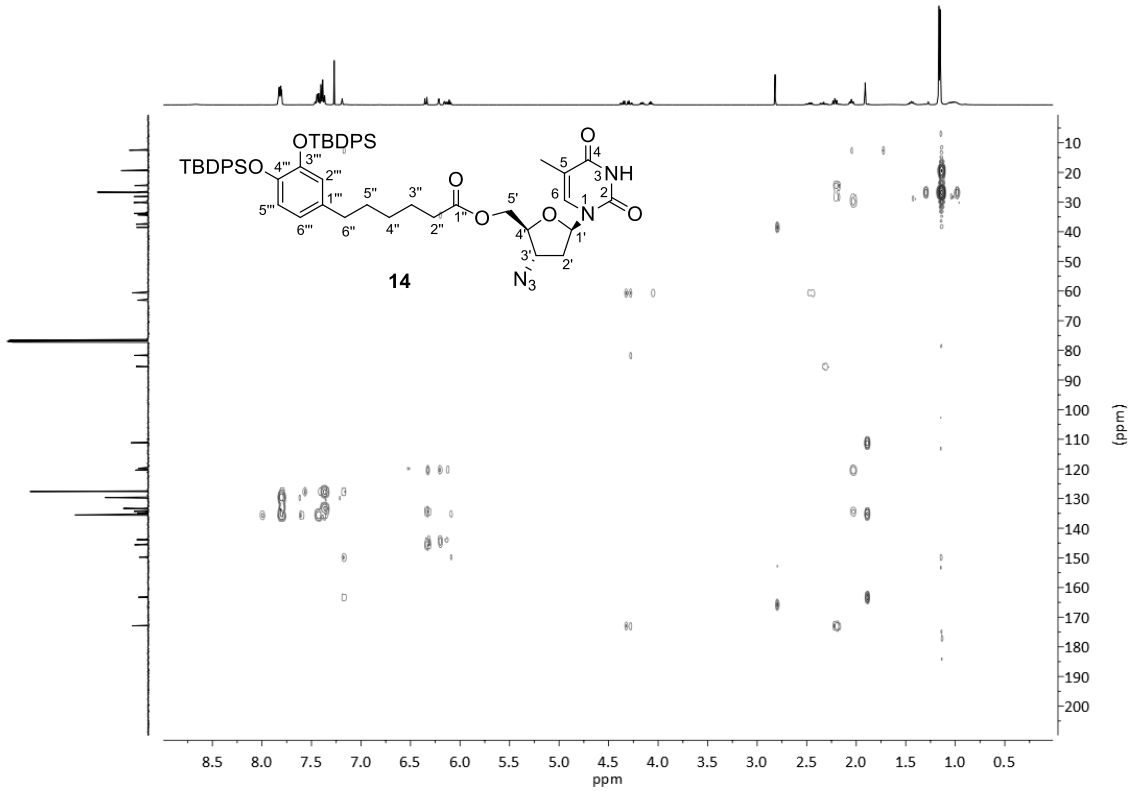

^{1}H – ^{13}C HMBC ($CDCl_3$)

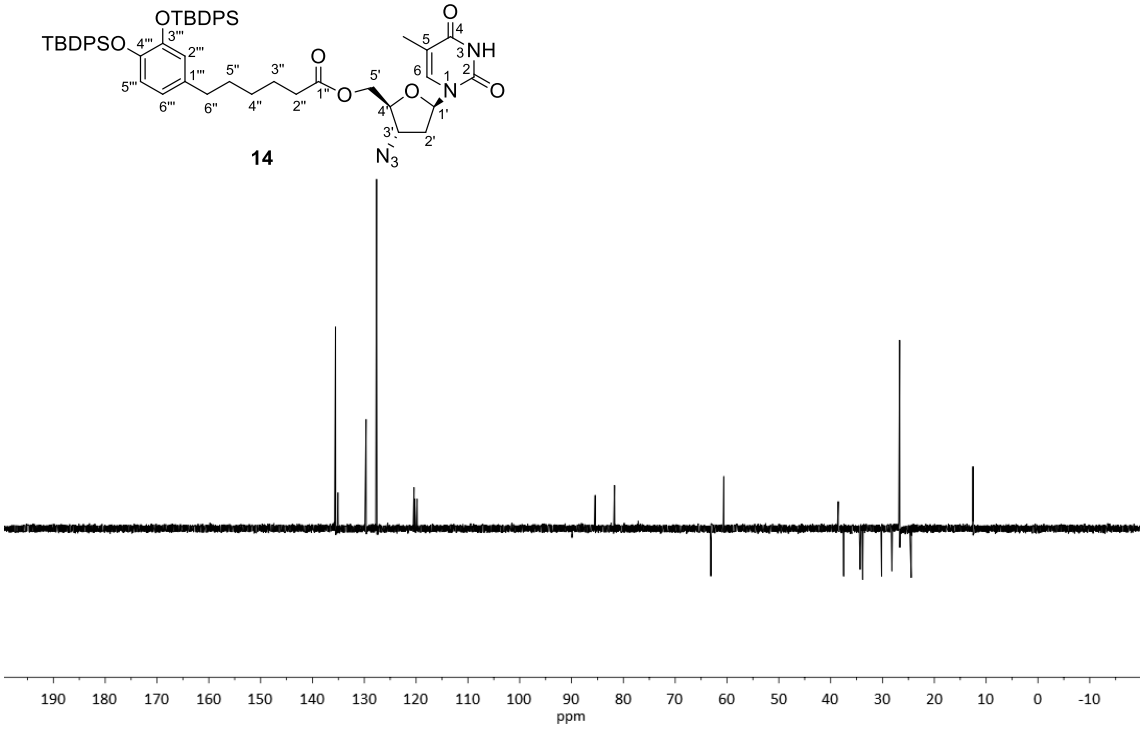

DEPT135 (100 MHz, $CDCl_3$)

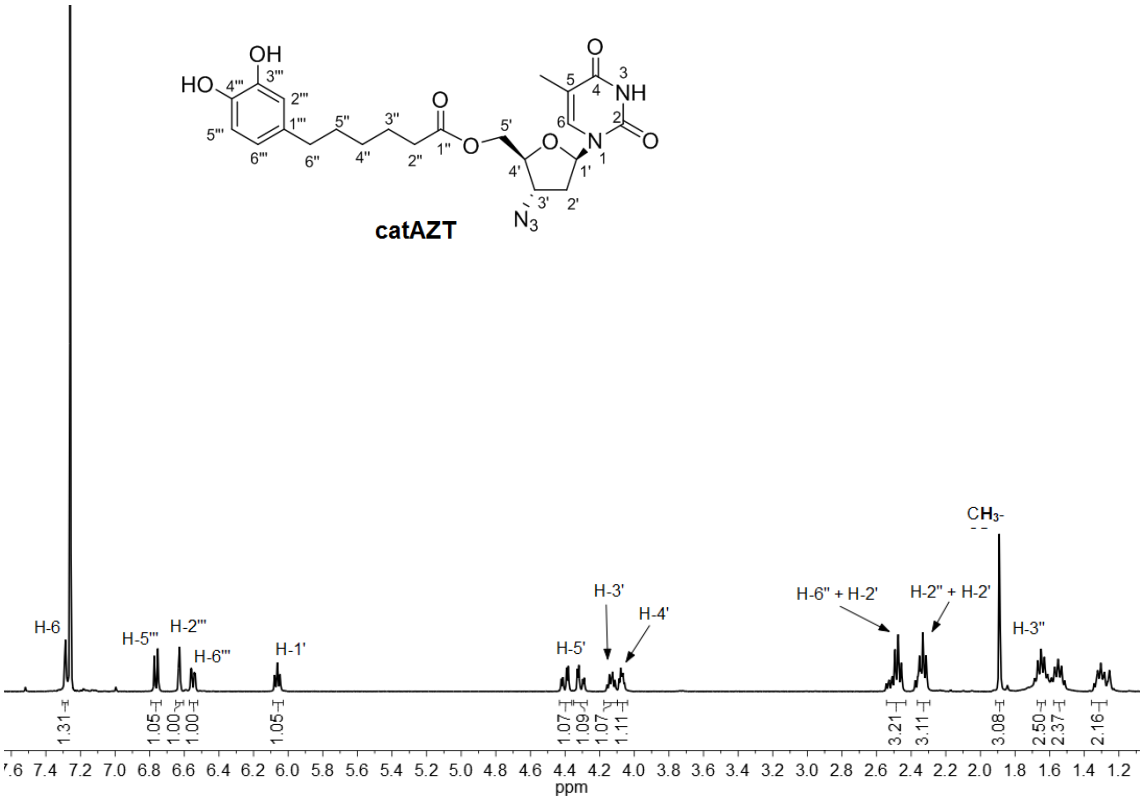

^{1}H NMR (400 MHz, $CDCl_3$)

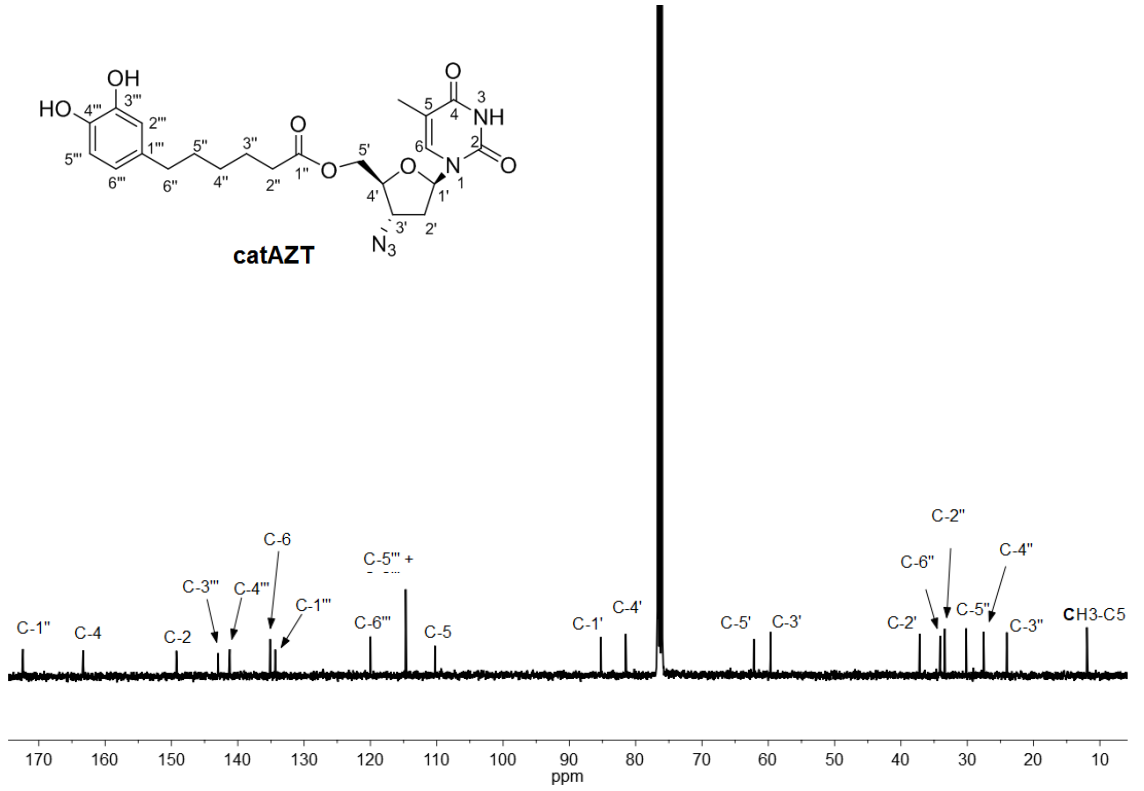

^{13}C NMR (100 MHz, $CDCl_3$)

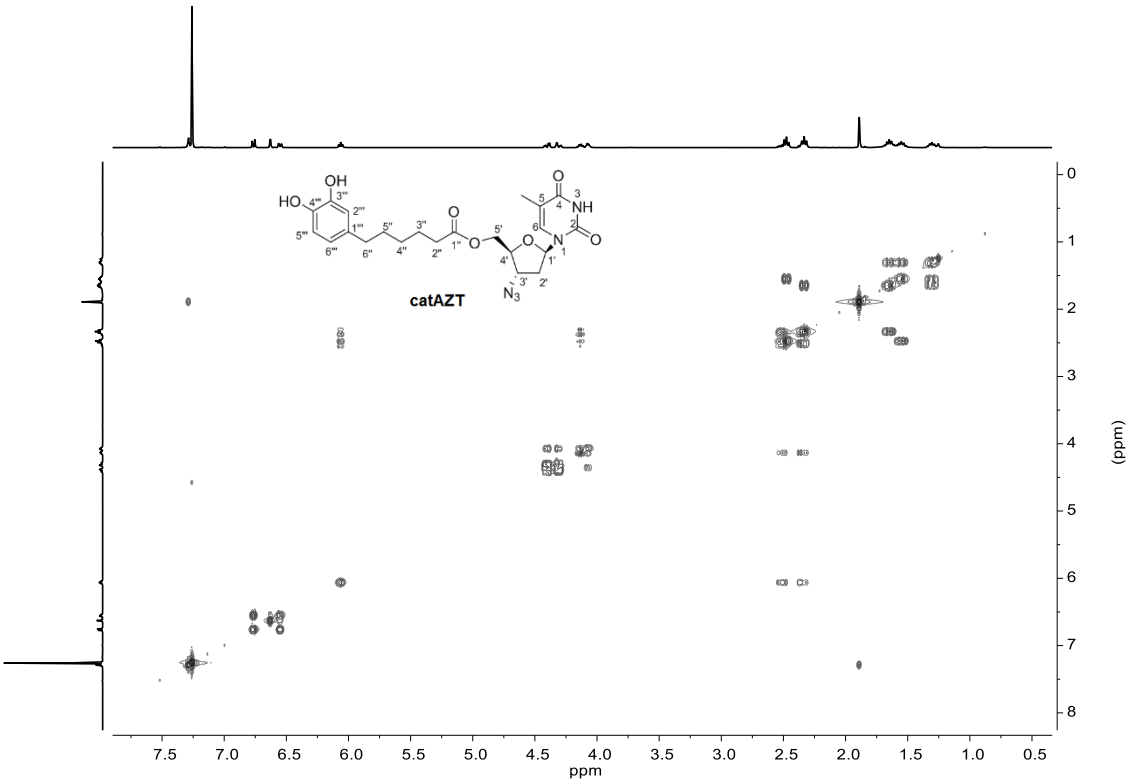

^{1}H – ^{1}H COSY (400 MHz, $CDCl_3$)

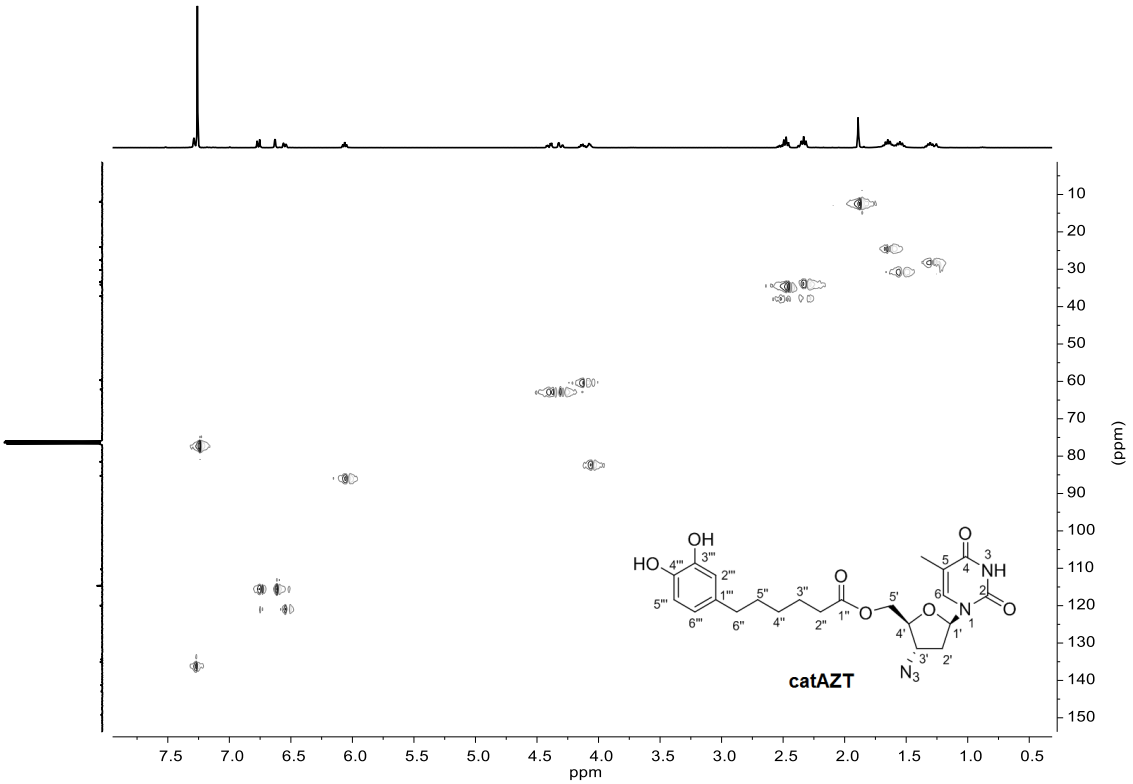

^{1}H – ^{13}C HSQC ($CDCl_3$)

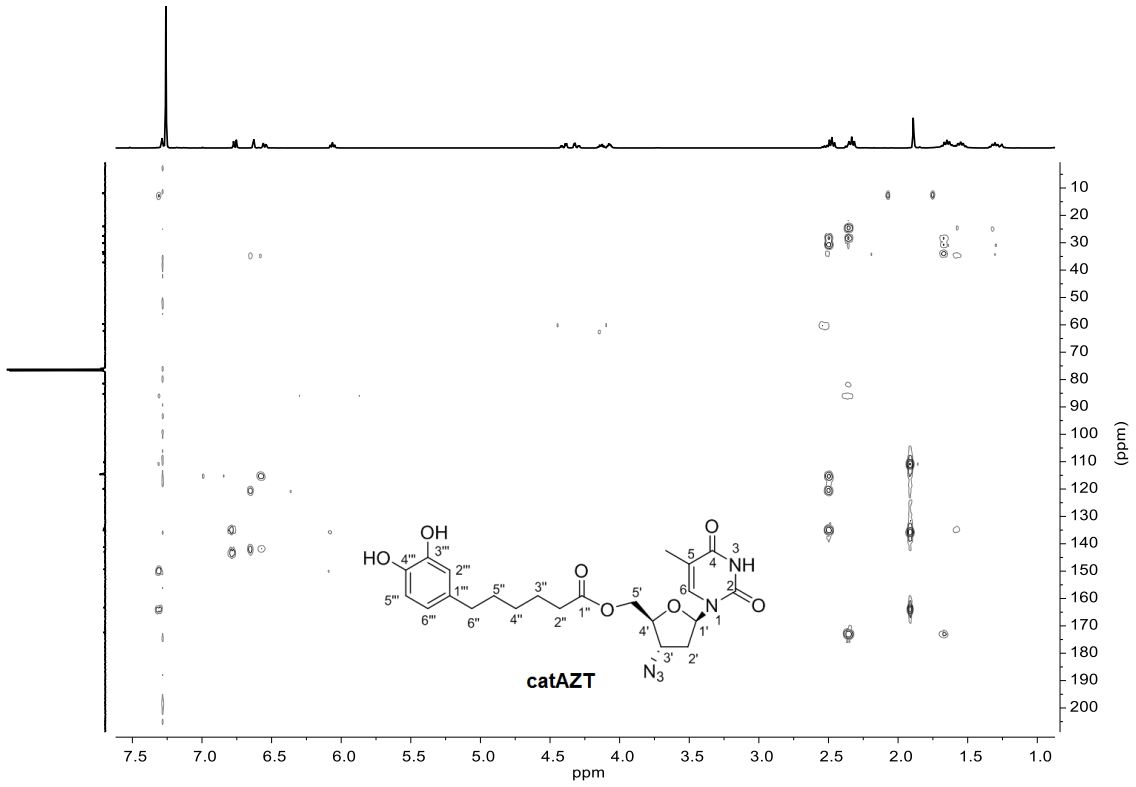

^{1}H – ^{13}C HMBC ($CDCl_3$)

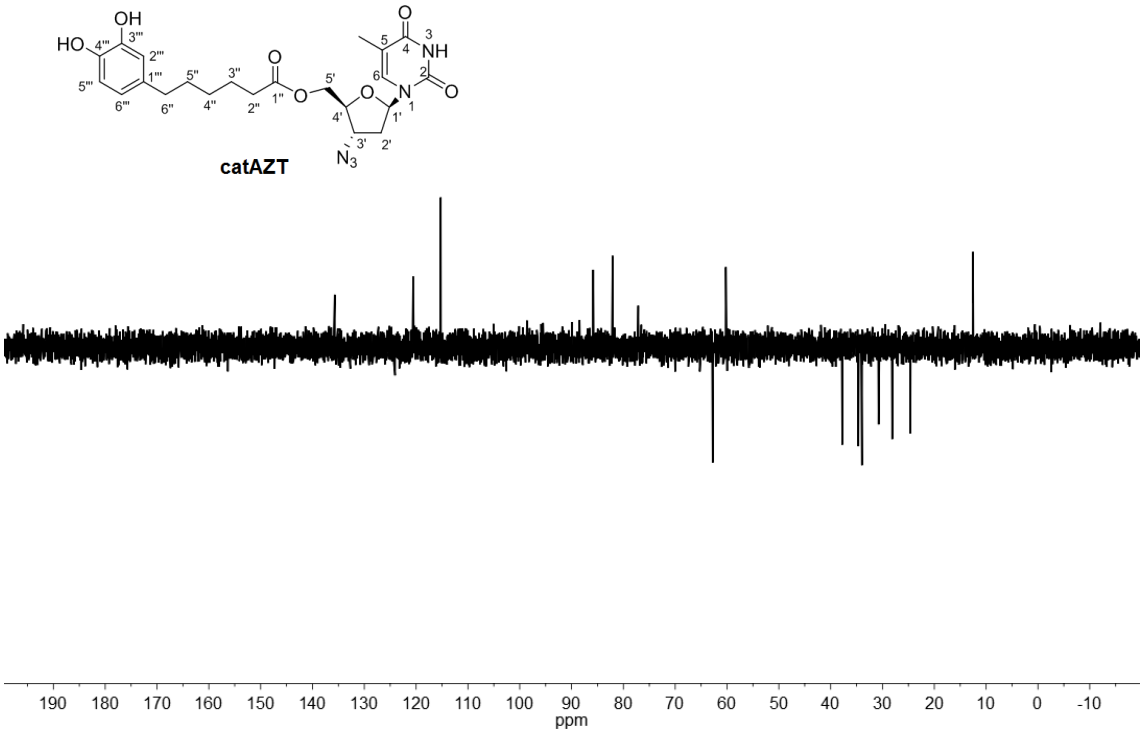

DEPT135 (100 MHz, $CDCl_3$)

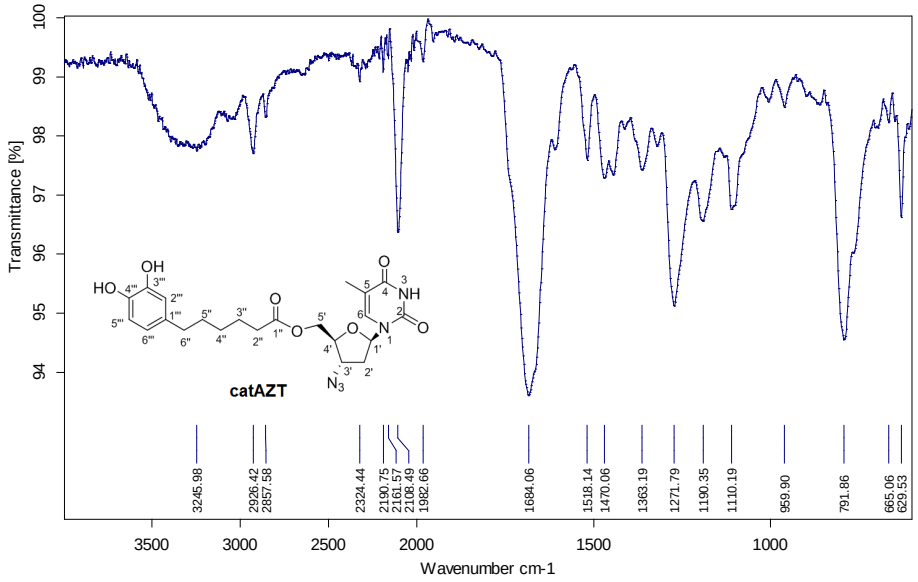

FTIR

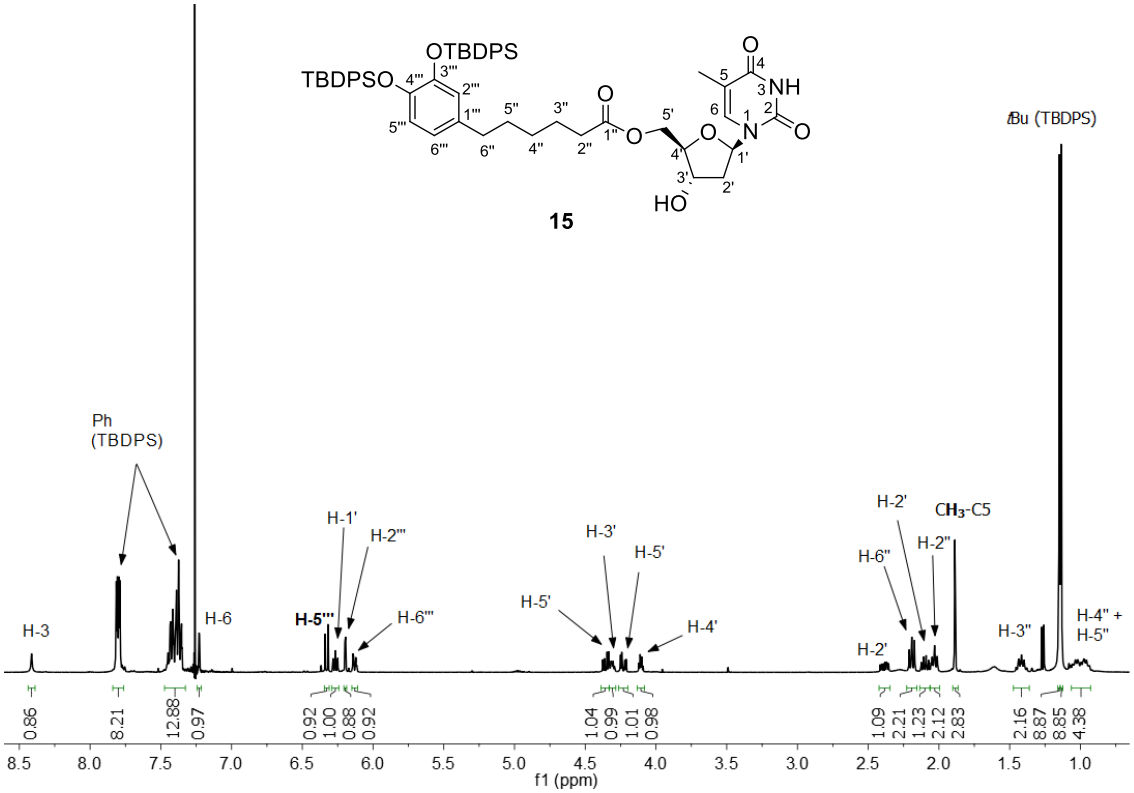

^{1}H NMR (400 MHz, $CDCl_3$)

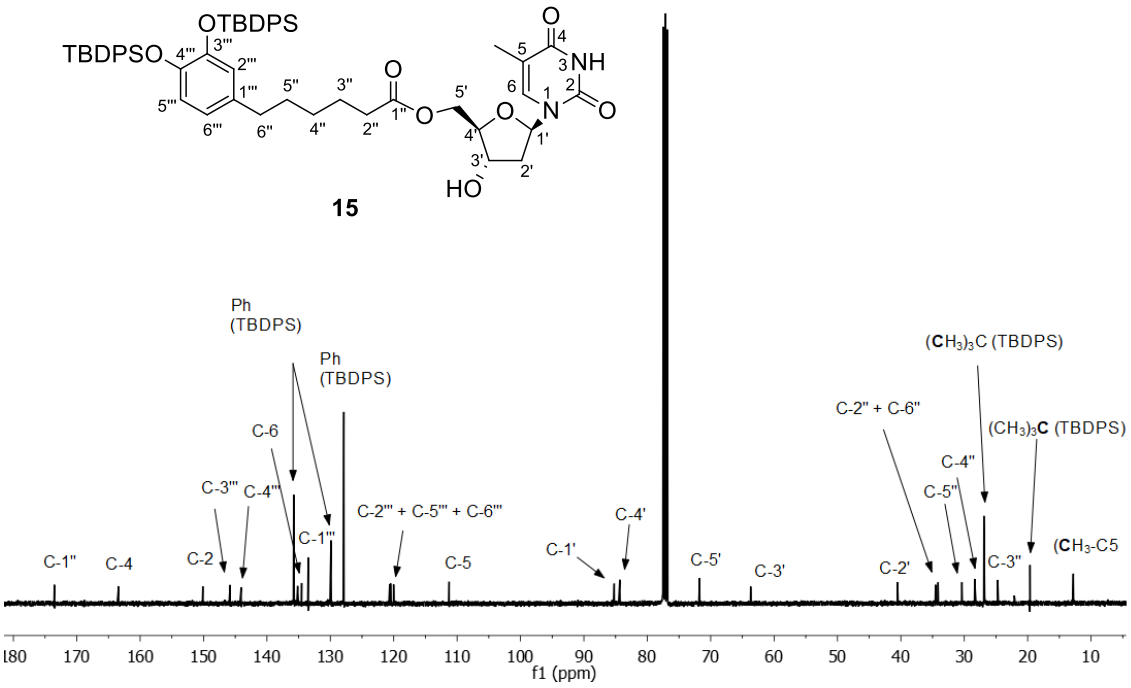

^{13}C NMR (100 MHz, $CDCl_3$)

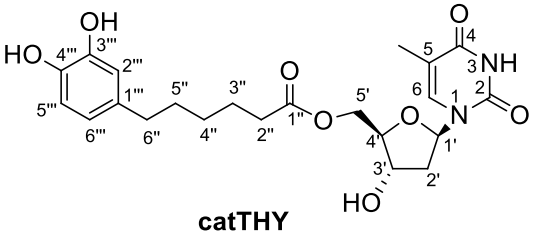

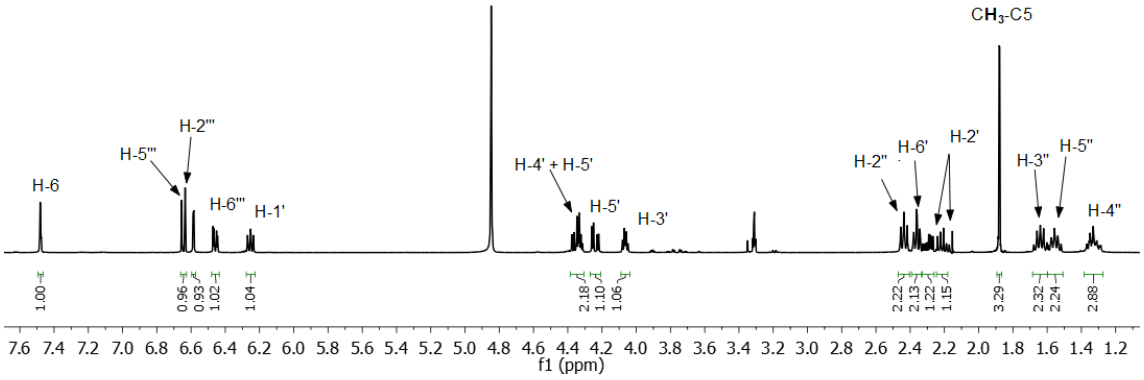

^{1}H NMR (400 MHz, CD_3OD)

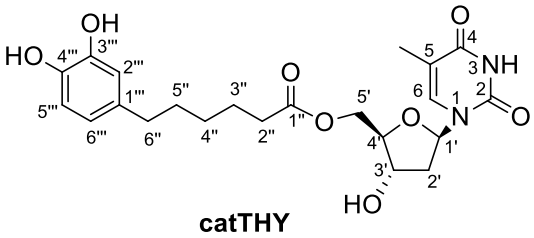

catTHY

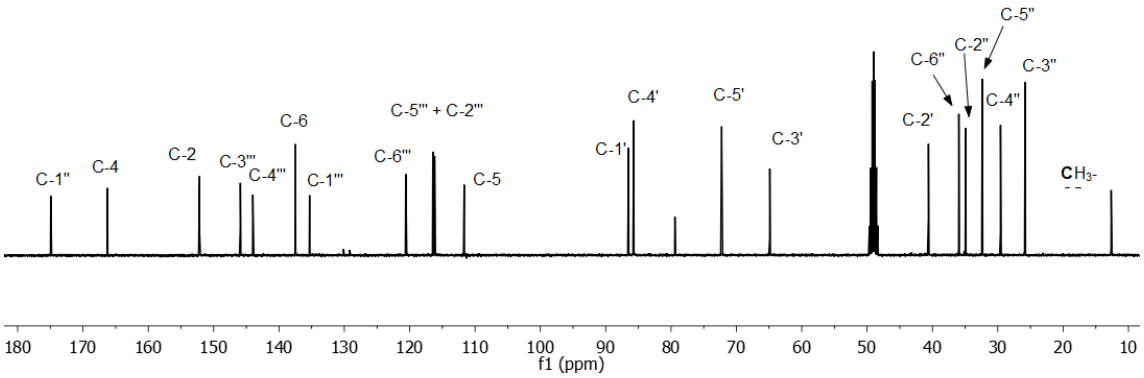

^{13}C NMR (100 MHz, CD_3OD)

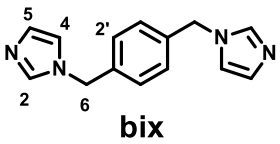

bix

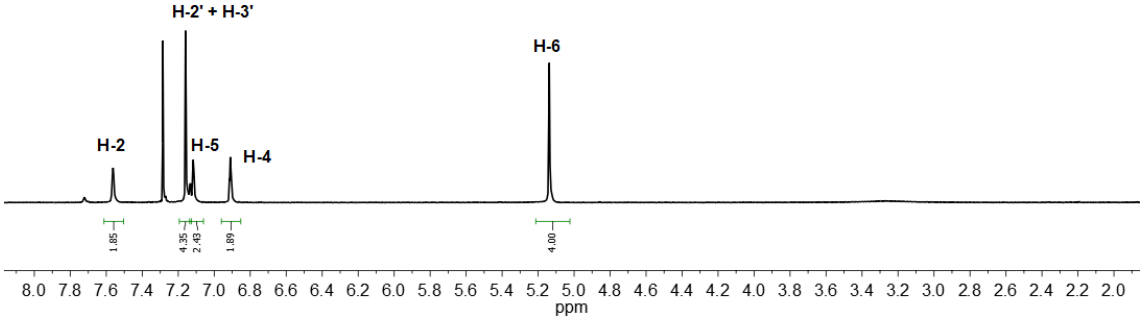

^{1}H NMR (360 MHz, $CDCl_3$)

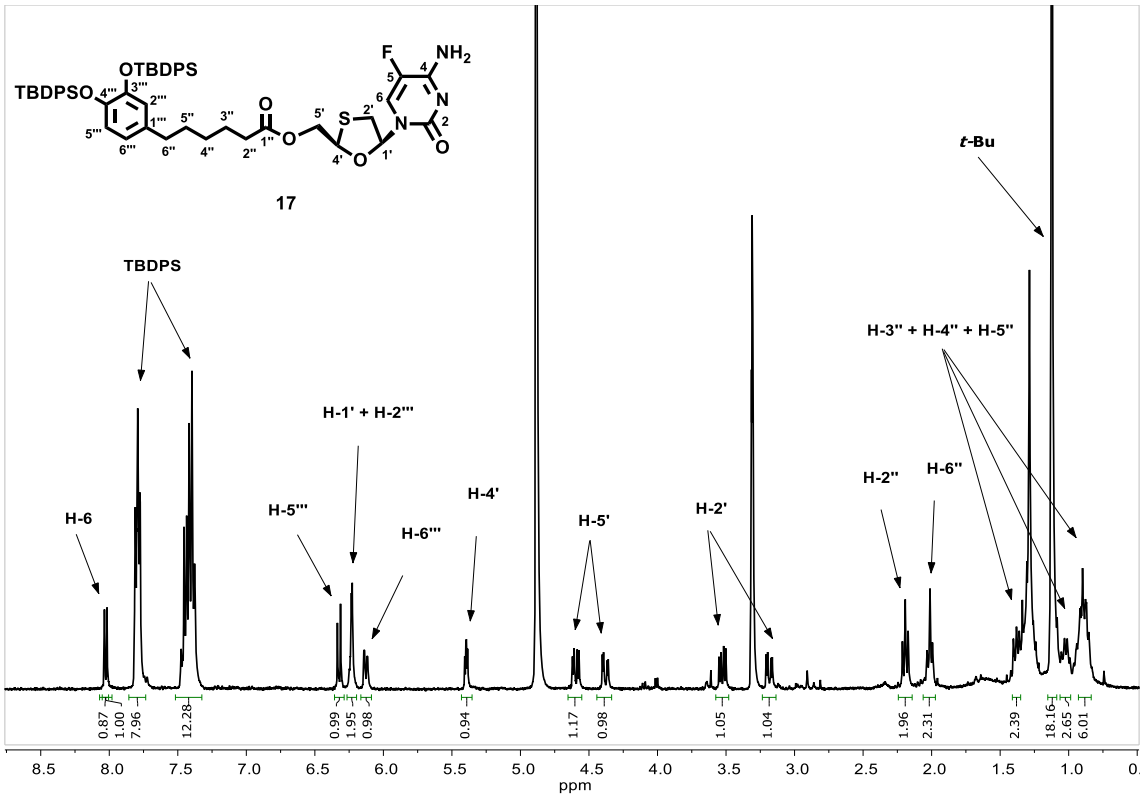

^{1}H NMR (360 MHz, CD_3OD)

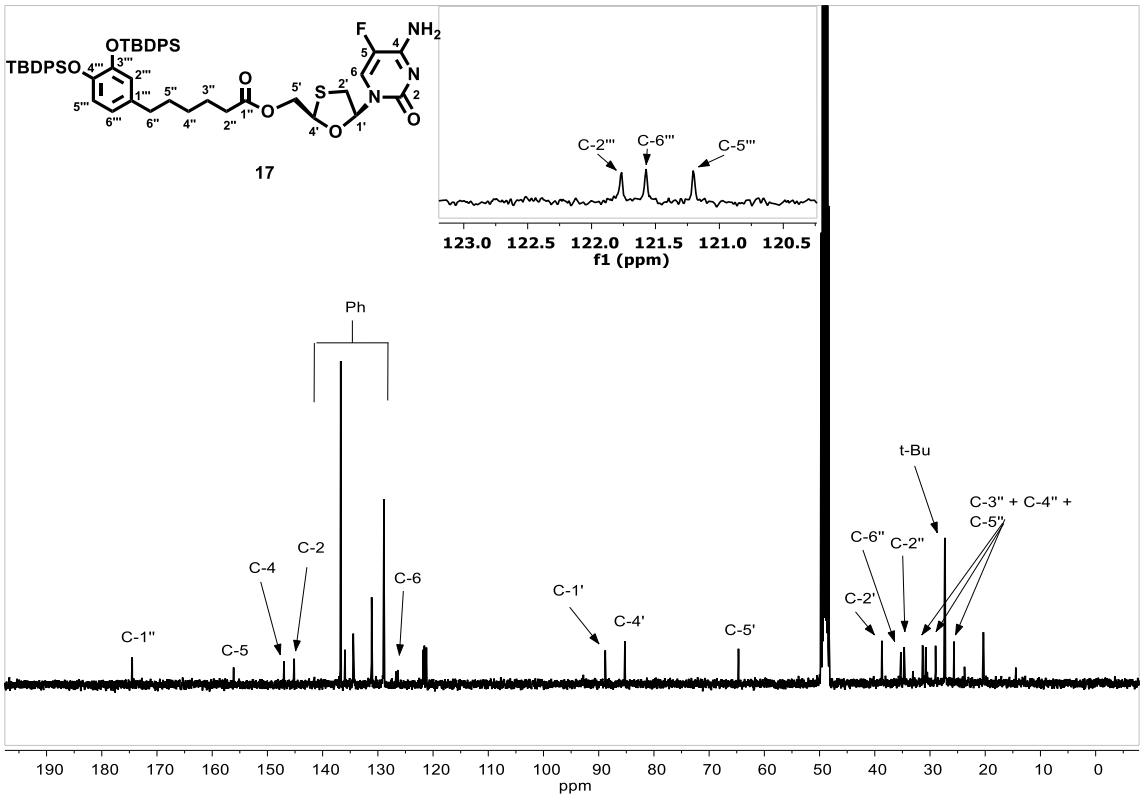

^{13}C NMR (90 MHz, CD_3OD)

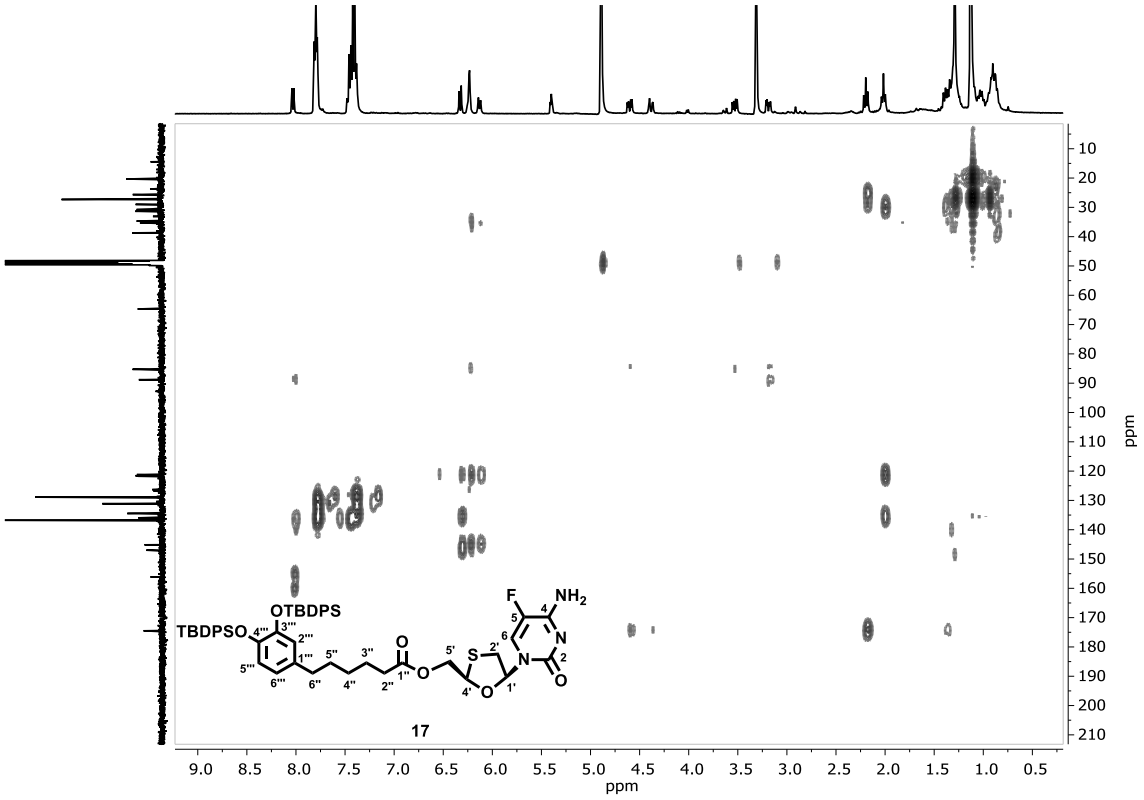

^{1}H-^{13}C HMBC (CD_3OD)

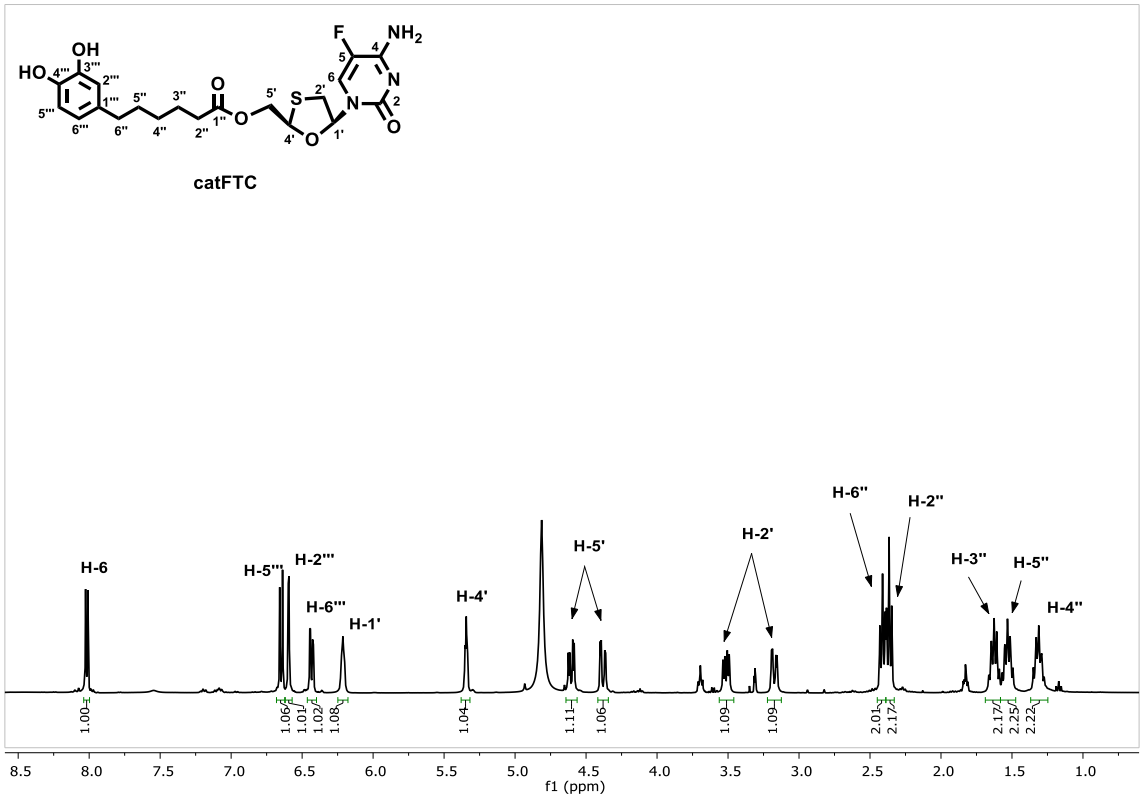

^{1}H NMR (400 MHz, CD_3OD)

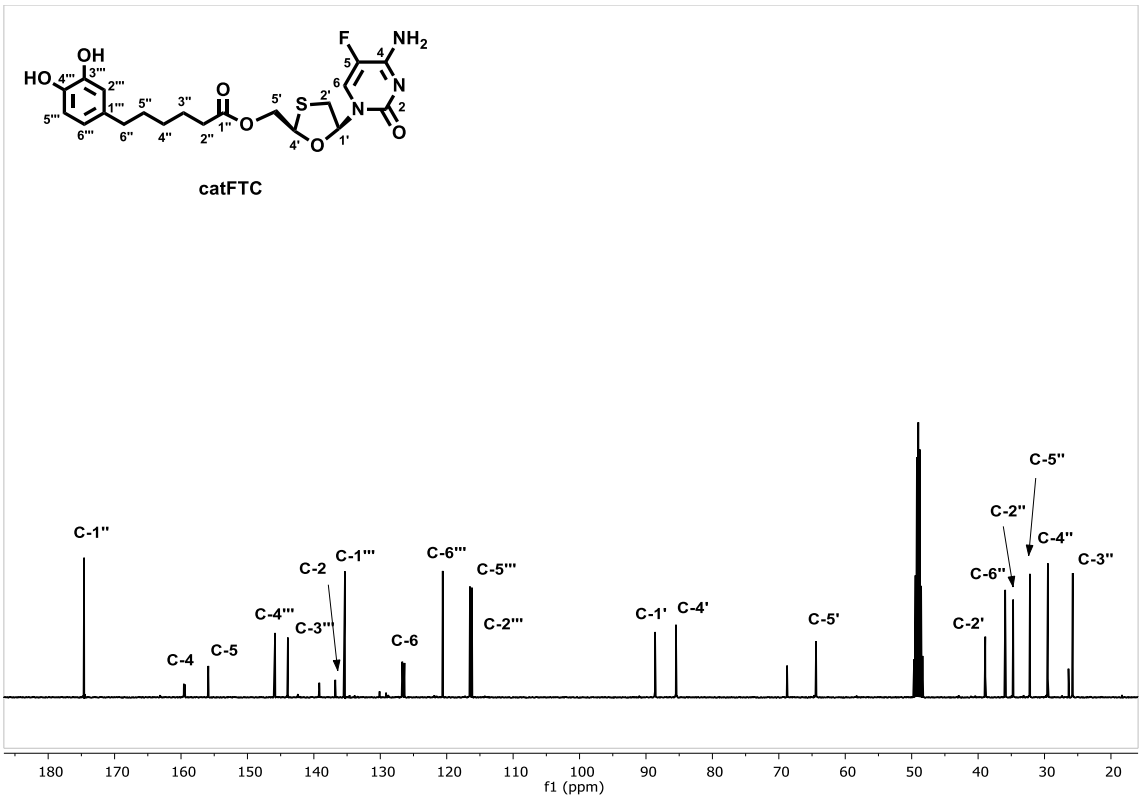

^{13}C NMR (100 MHz, CD_3OD)

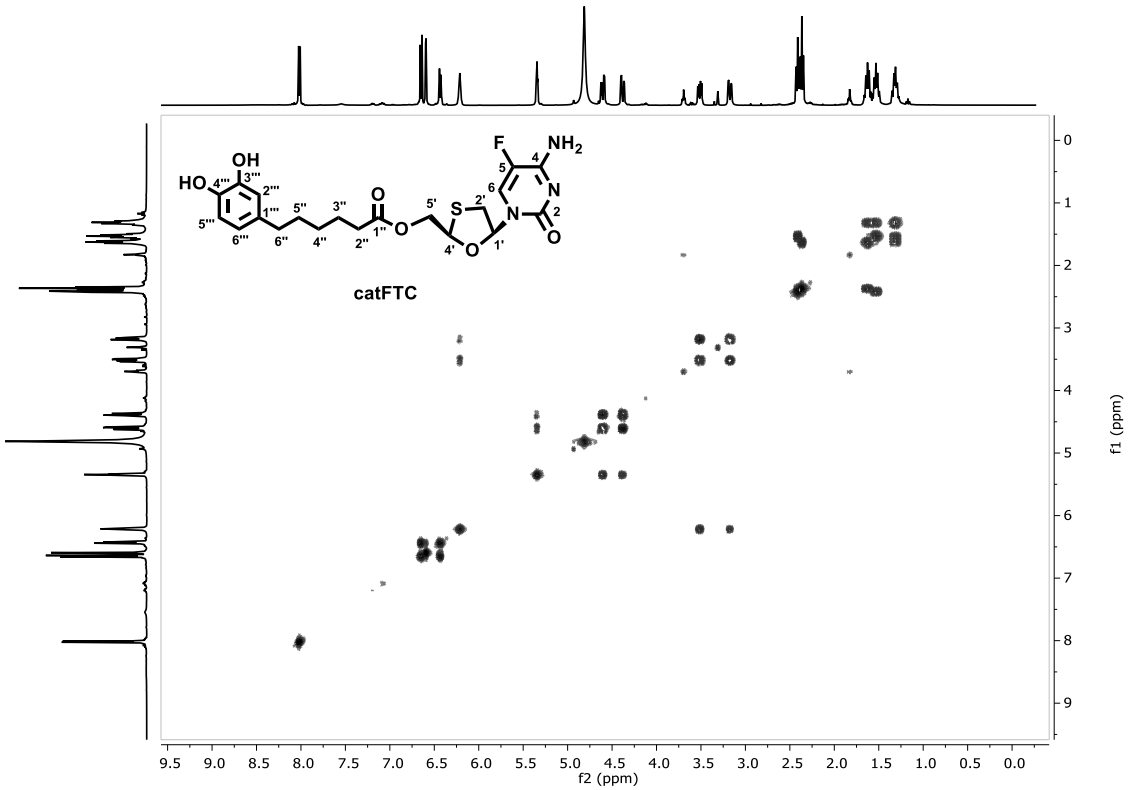

^{1}H-^{13}C HSQC (CD_3OD)

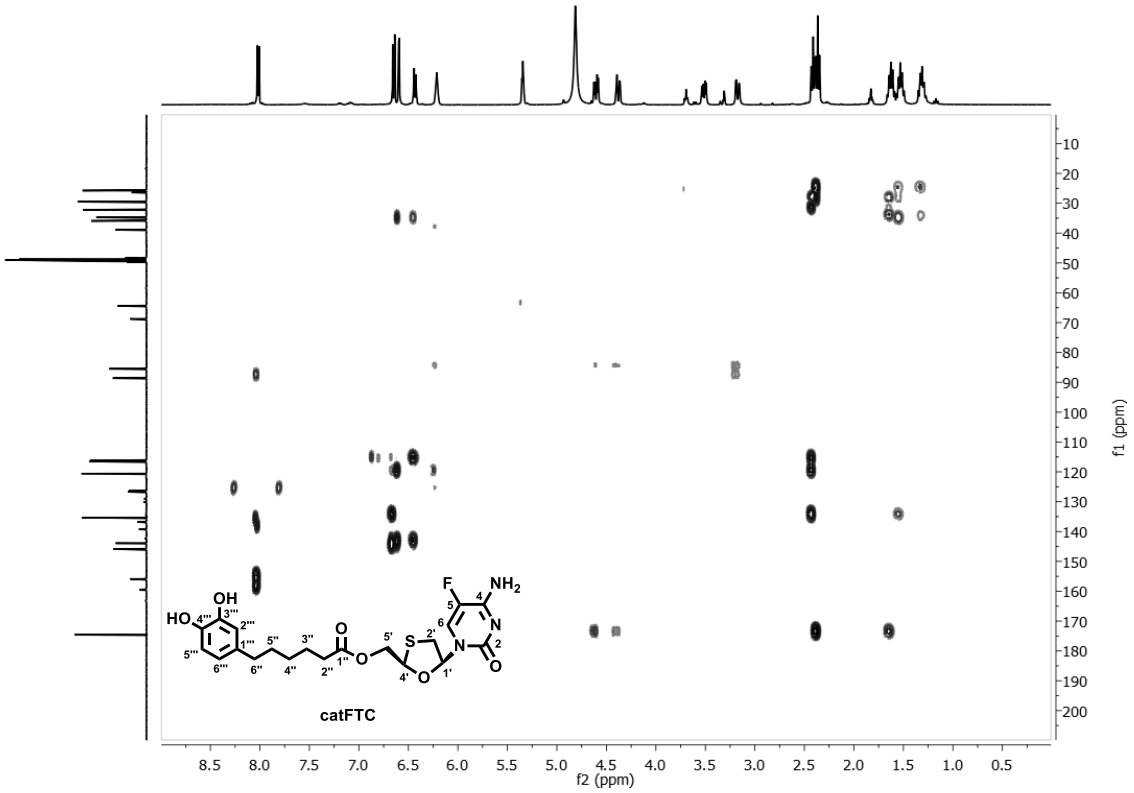

^{1}H-^{13}C HMBC (CD_3OD)

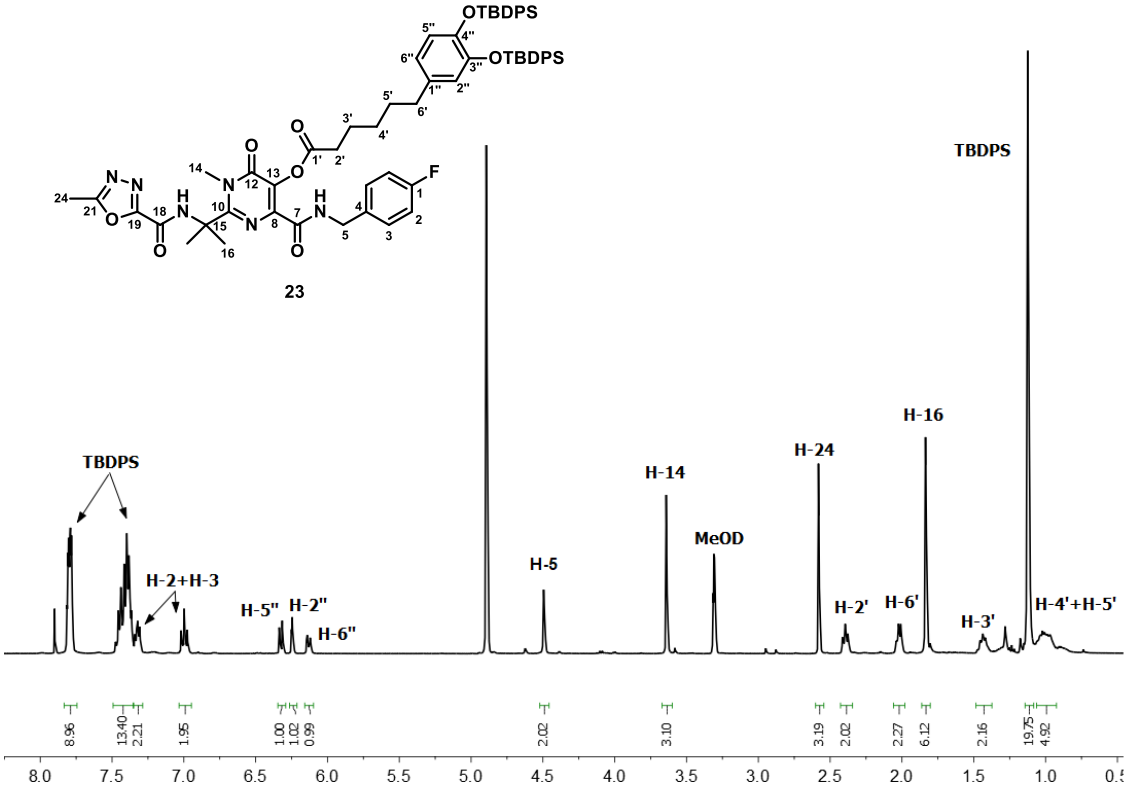

^{1}H NMR (400 MHz, CD_3OD)

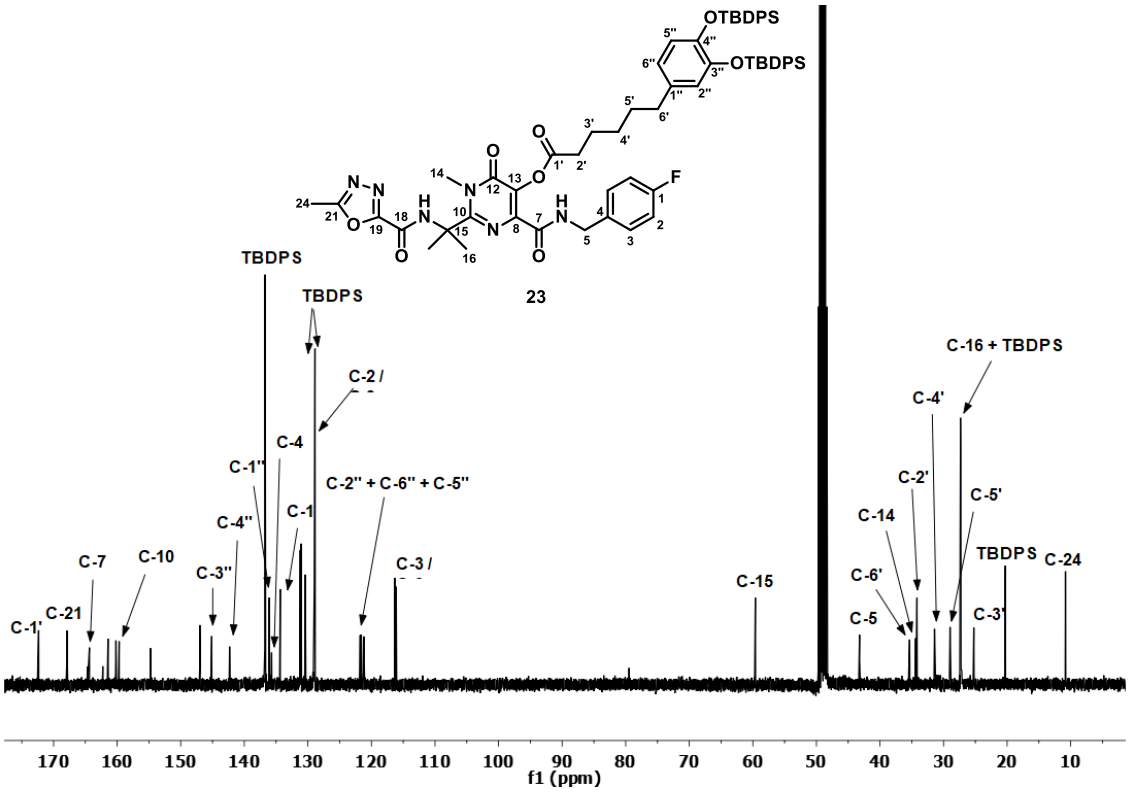

^{13}C NMR (100 MHz, CD_3OD)

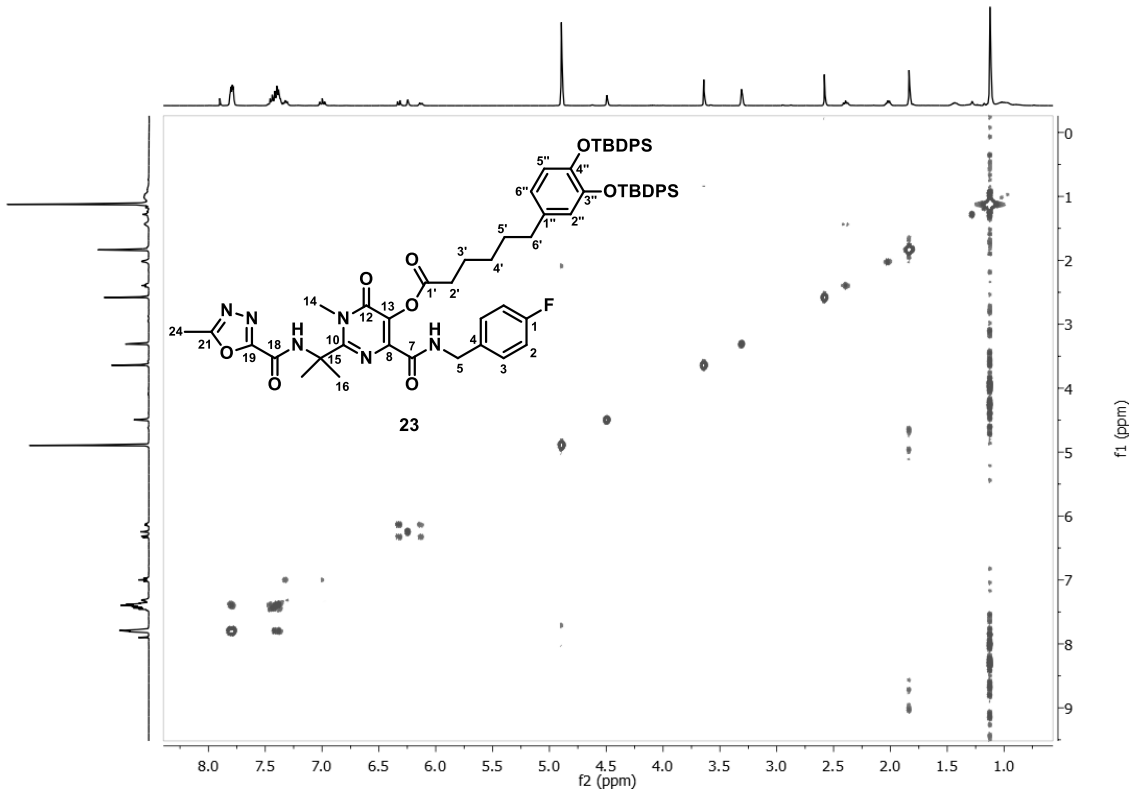

^{1}H – ^{1}H COSY (400 MHz, CD_3OD)

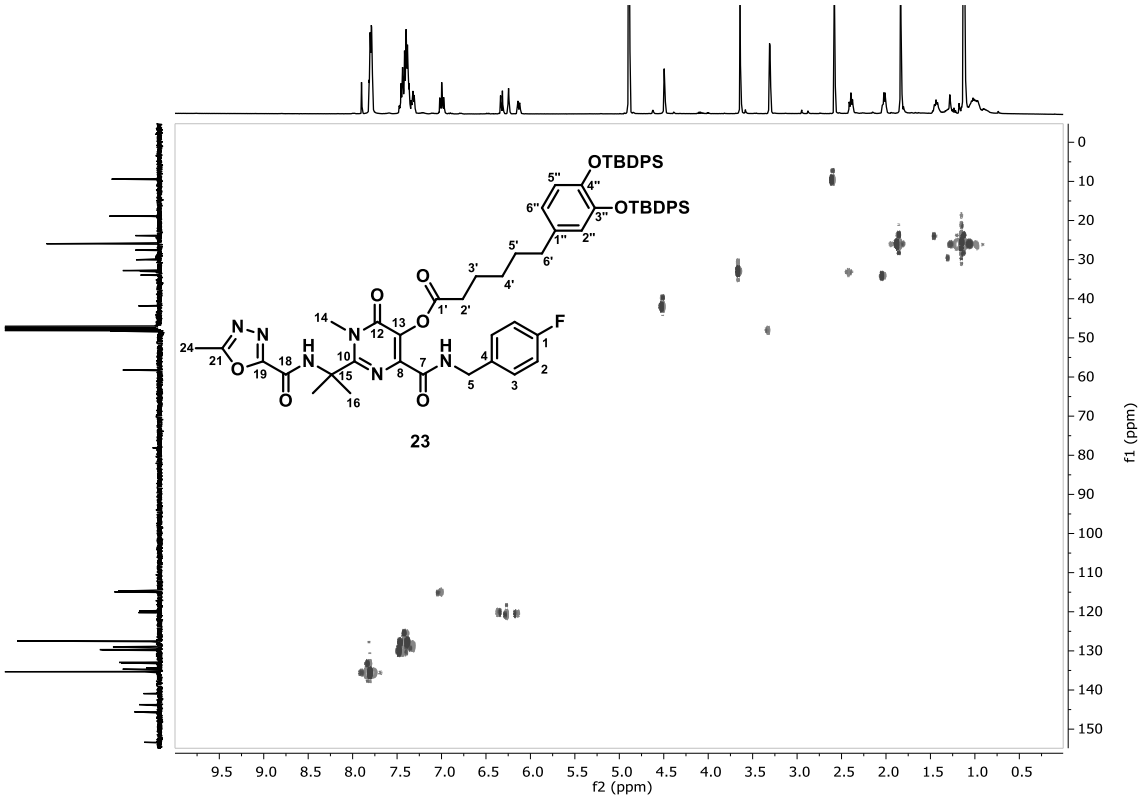

^{1}H – ^{13}C HSQC (400 MHz, CD_3OD)

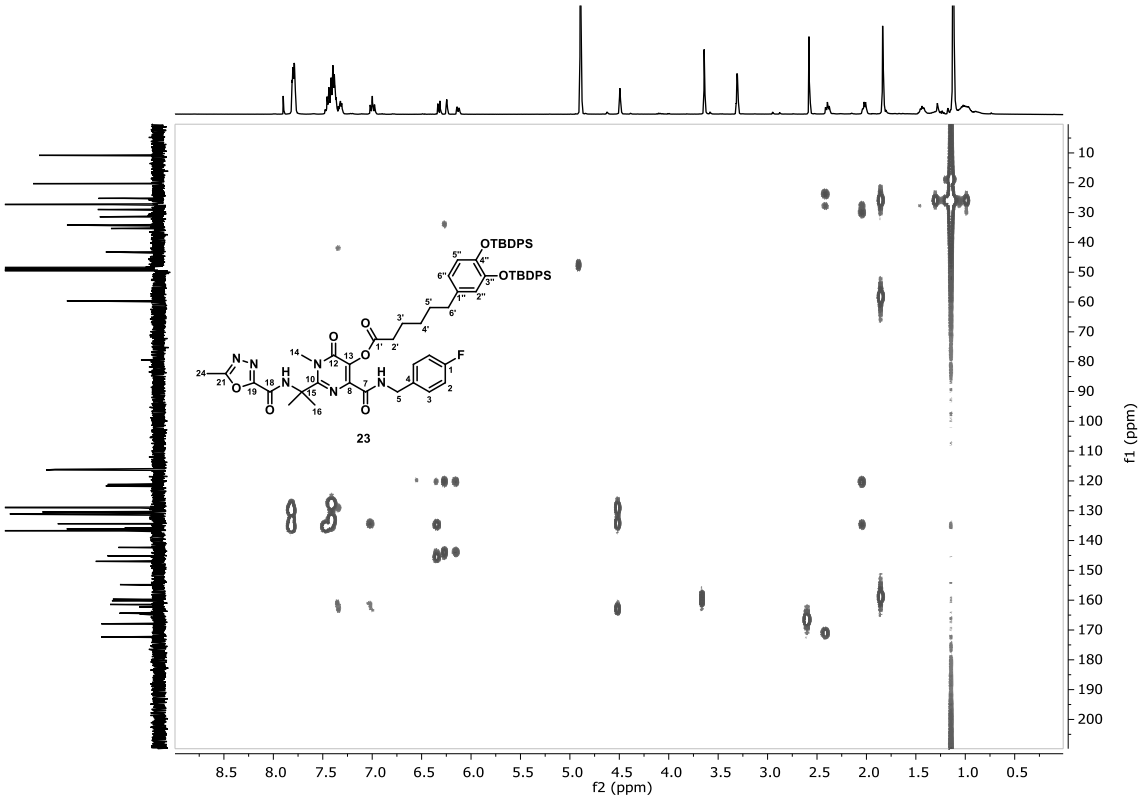

^{1}H – ^{13}C HMBC (400 MHz, CD_3OD)

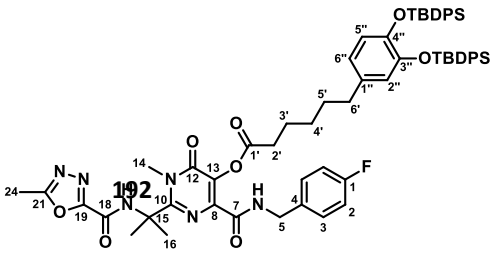

192

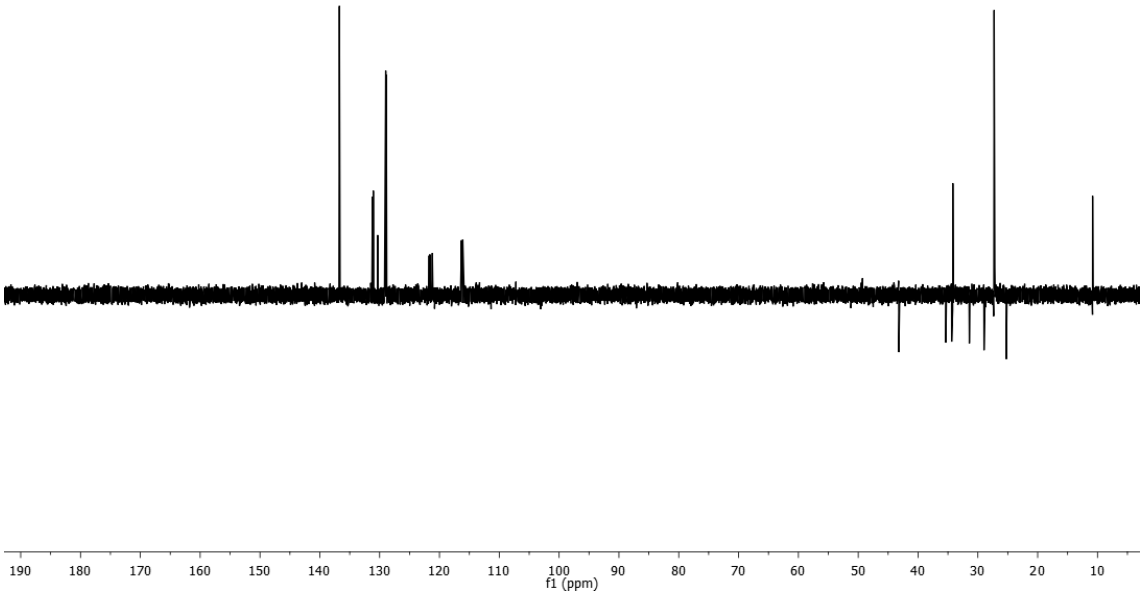

DEPT135 (100 MHz, CD_3OD)

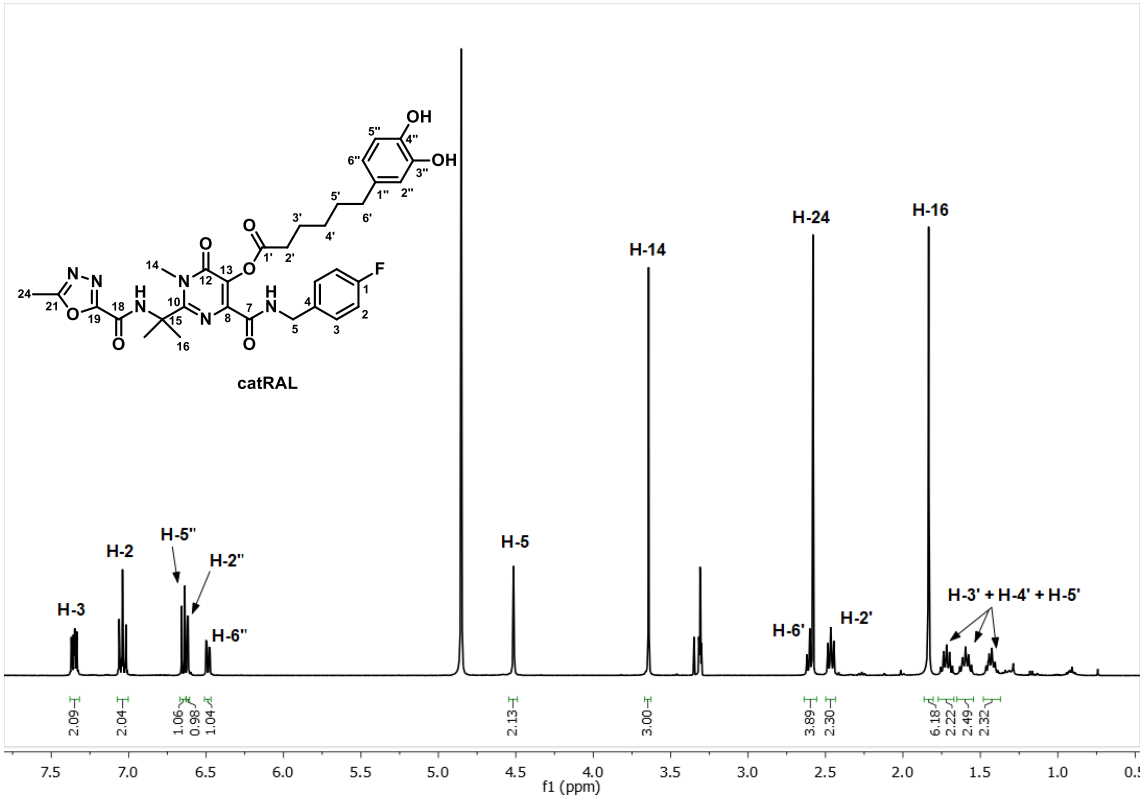

^{1}H NMR (400 MHz, CD_3OD)

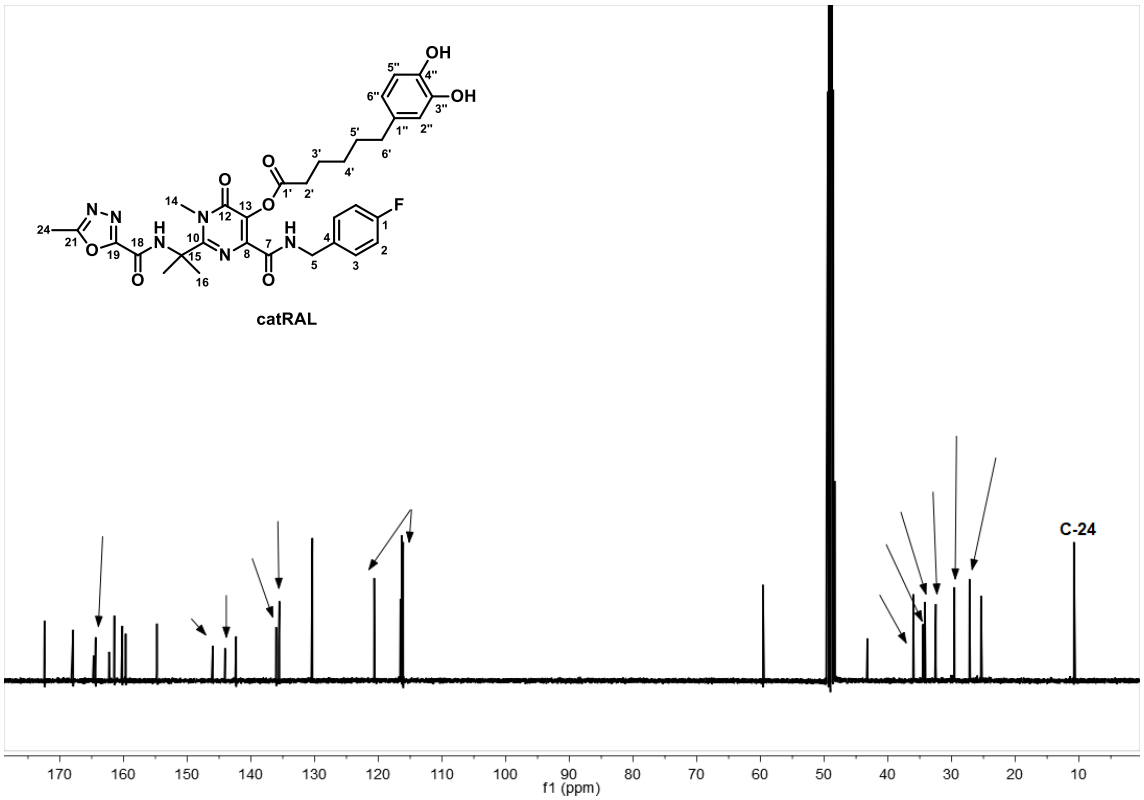

^{13}C NMR (100 MHz, CD_3OD)

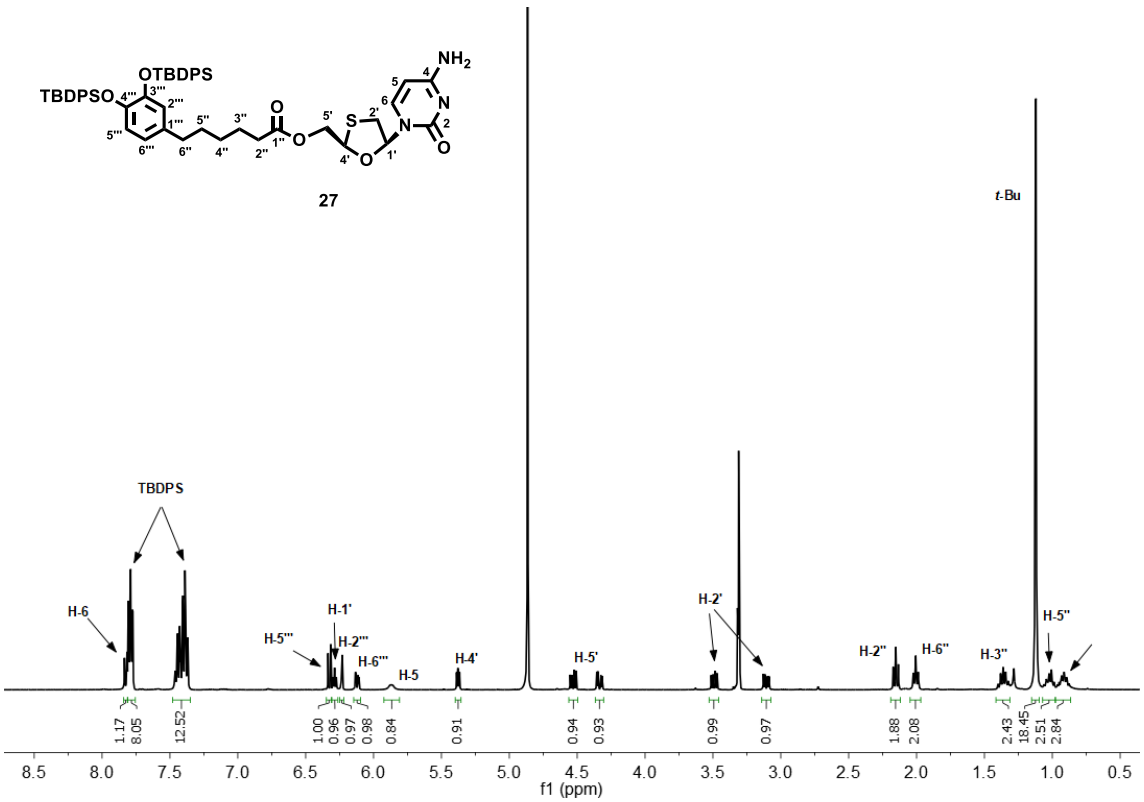

^{1}H NMR (400 MHz, CD_3OD)

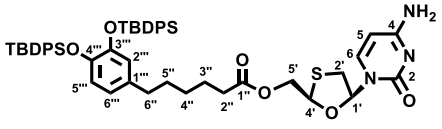

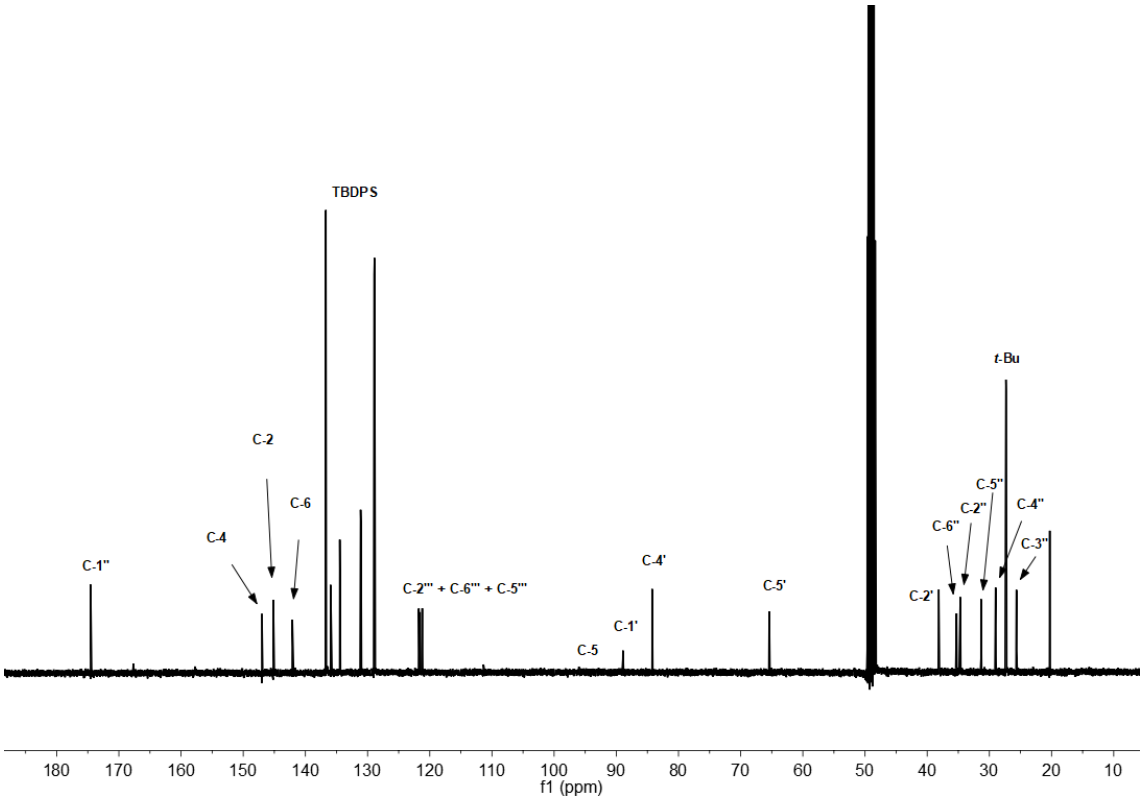

^{13}C NMR (100 MHz, CD_3OD)

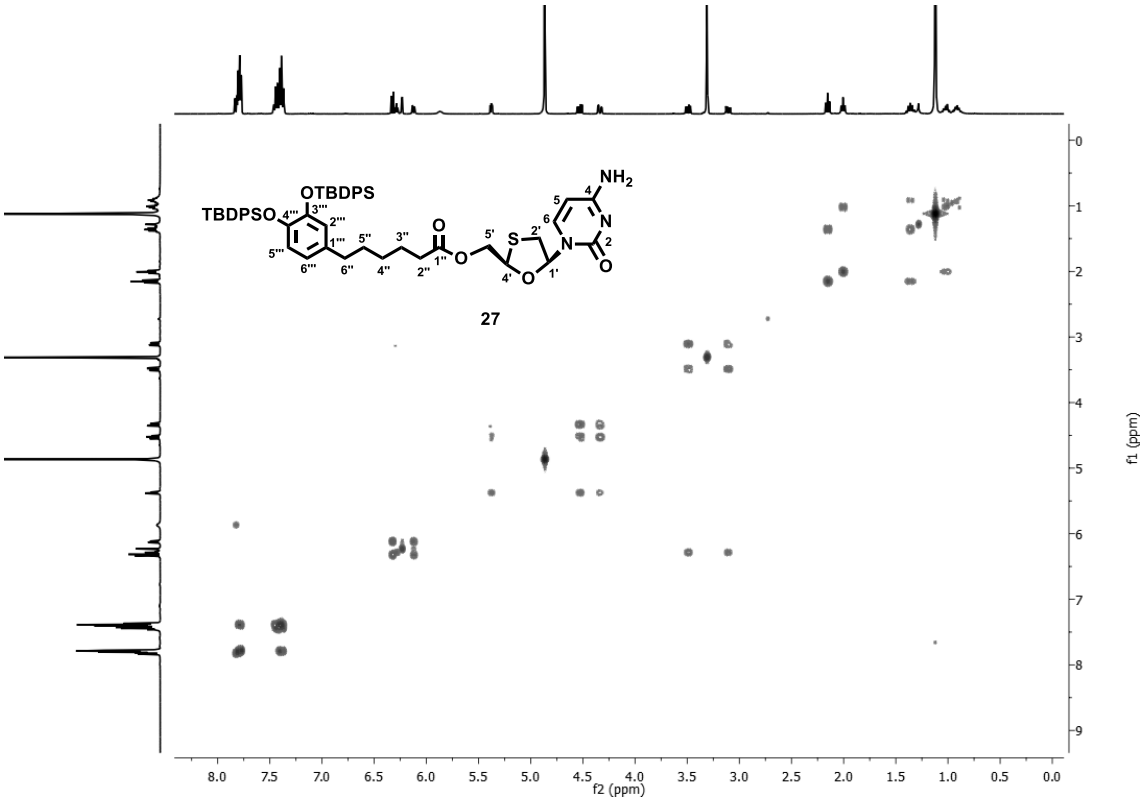

^{1}H-^{1}H COSY (CD_3OD)

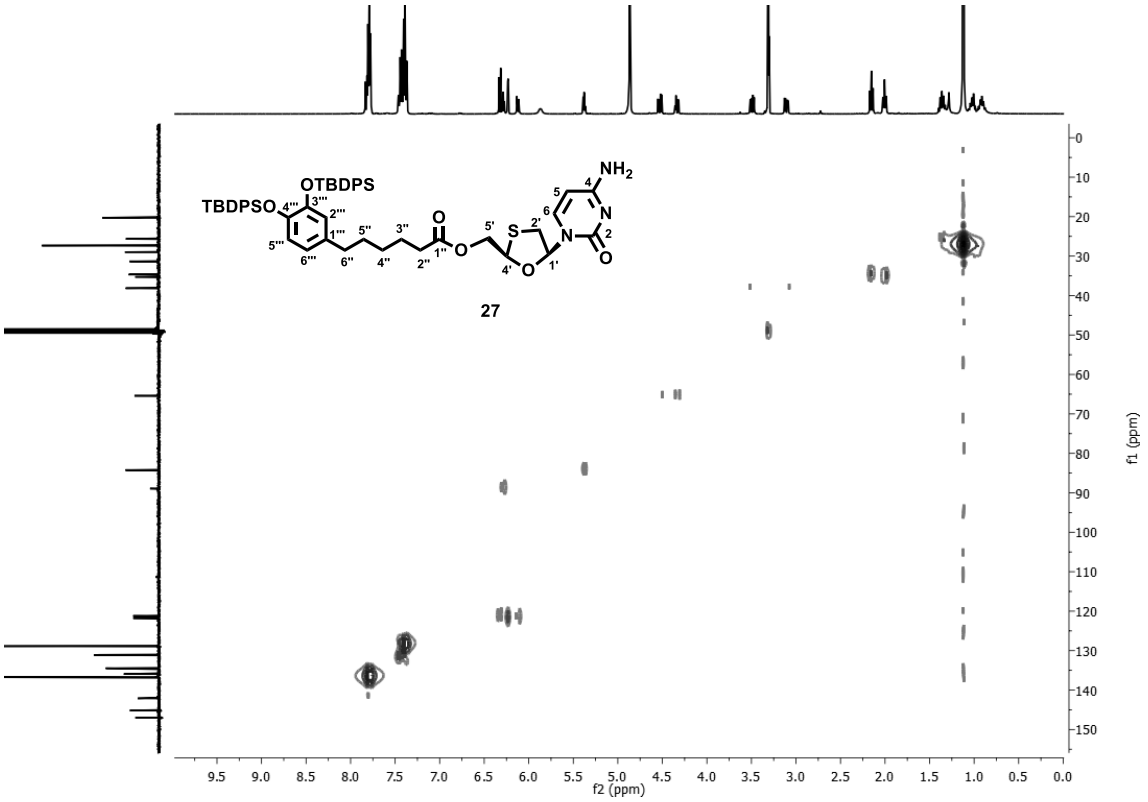

^{1}H-^{13}C HSQC (CD_3OD)

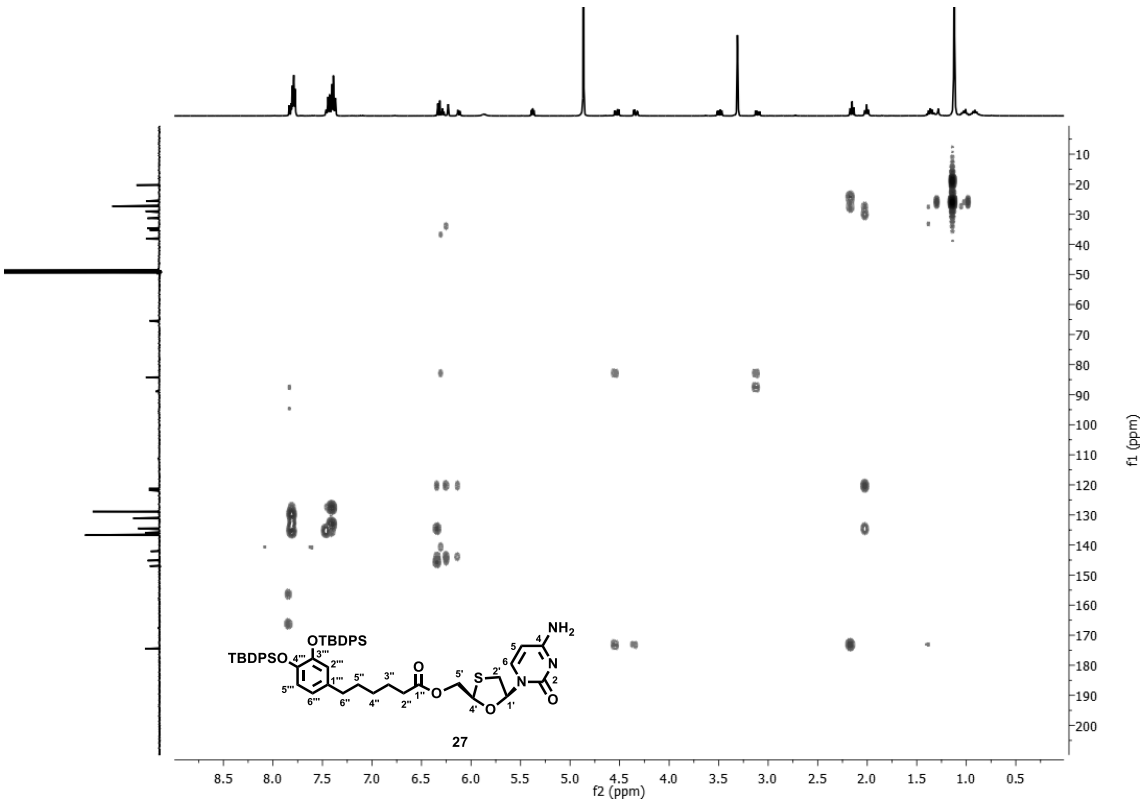

^{1}H-^{13}C HMBC (CD_3OD)

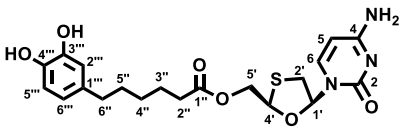

cat3TC

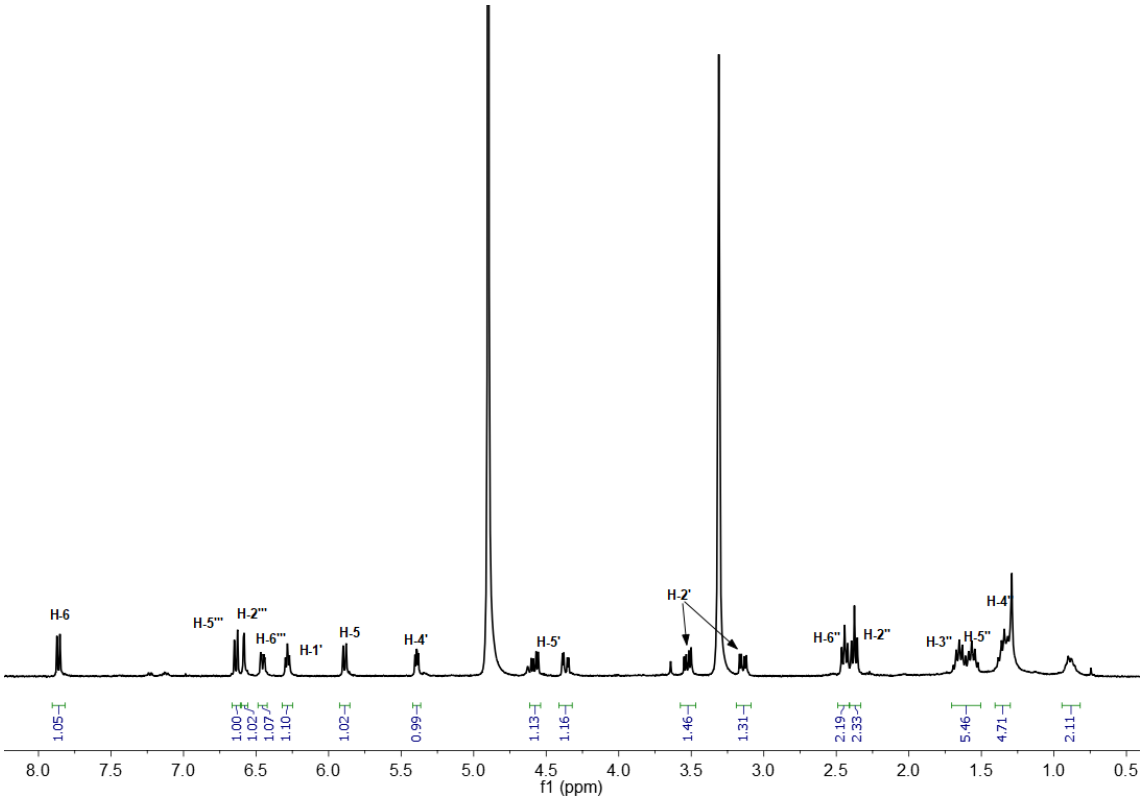

^{1}H NMR (360 MHz, CD_3OD)

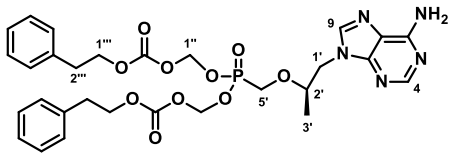

28

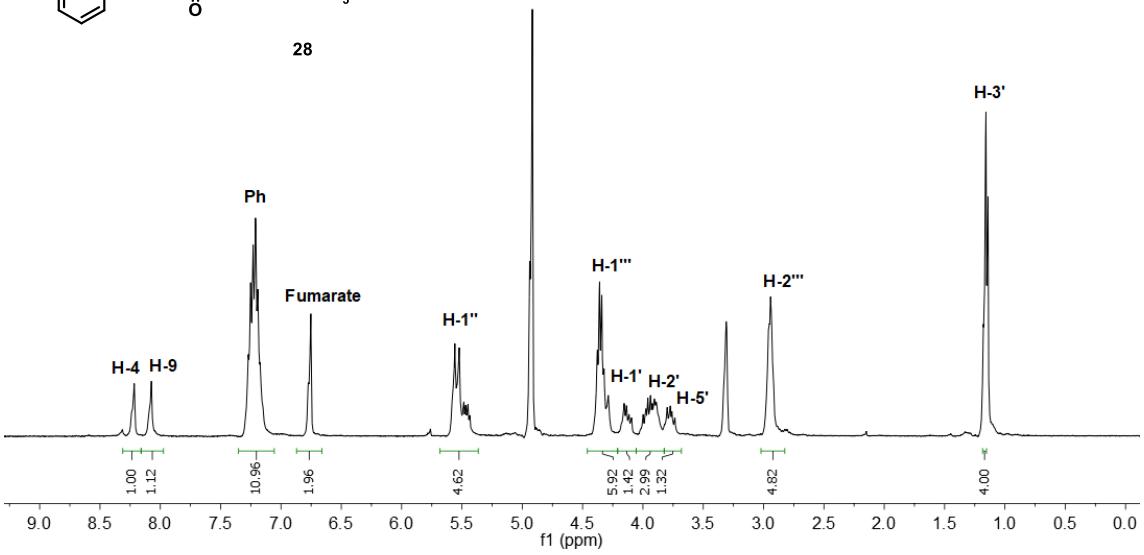

^{1}H NMR (360 MHz, CD_3OD)

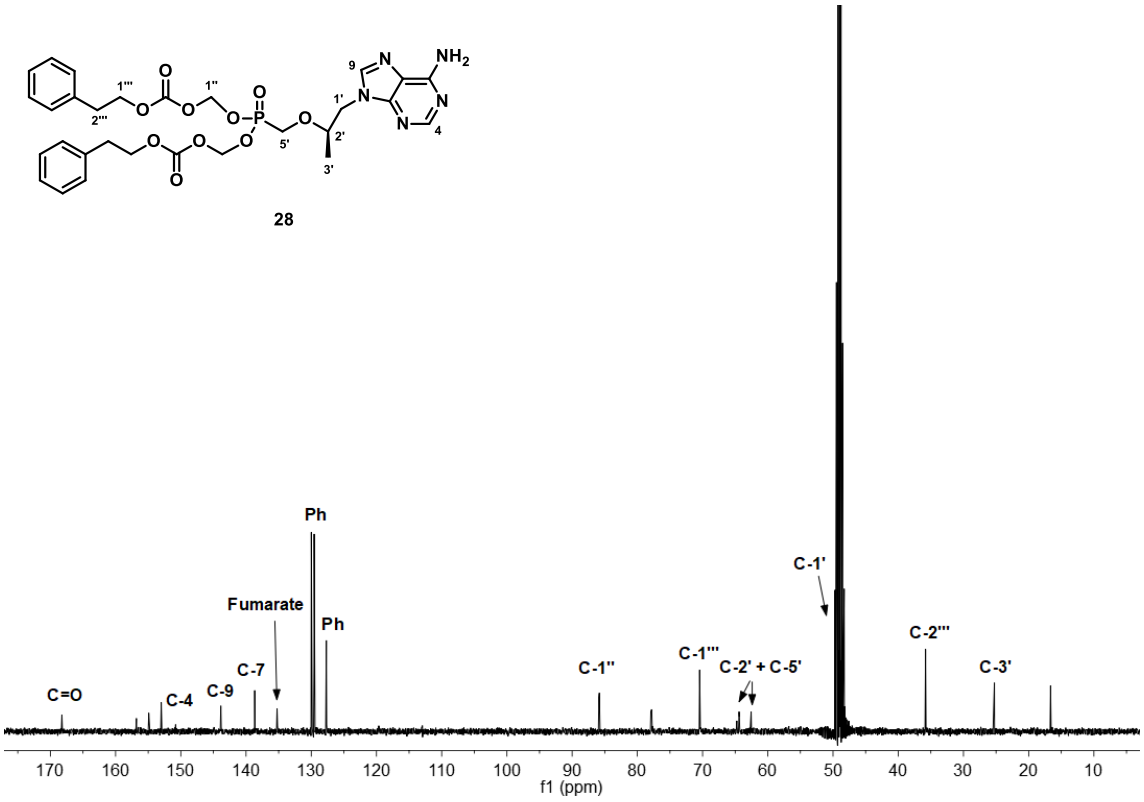

^{13}C NMR (90 MHz, CD_3OD)

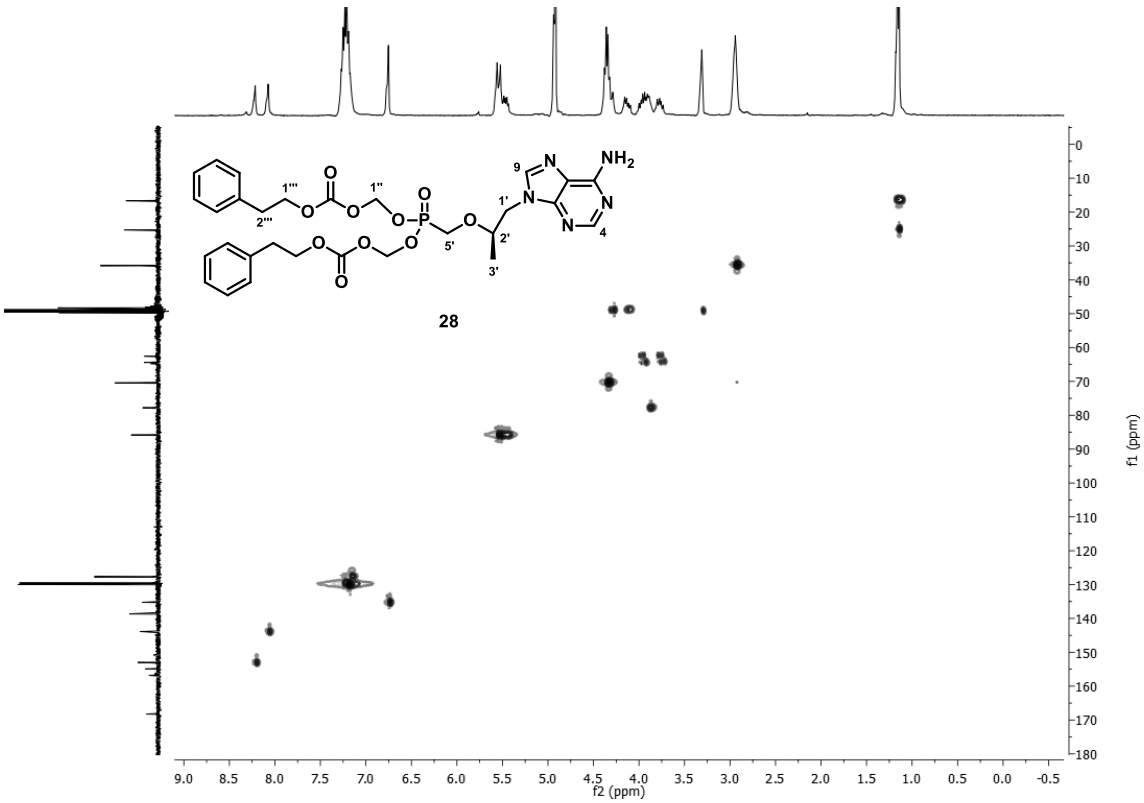

^{1}H-^{13}C HSQC (CD_3OD)

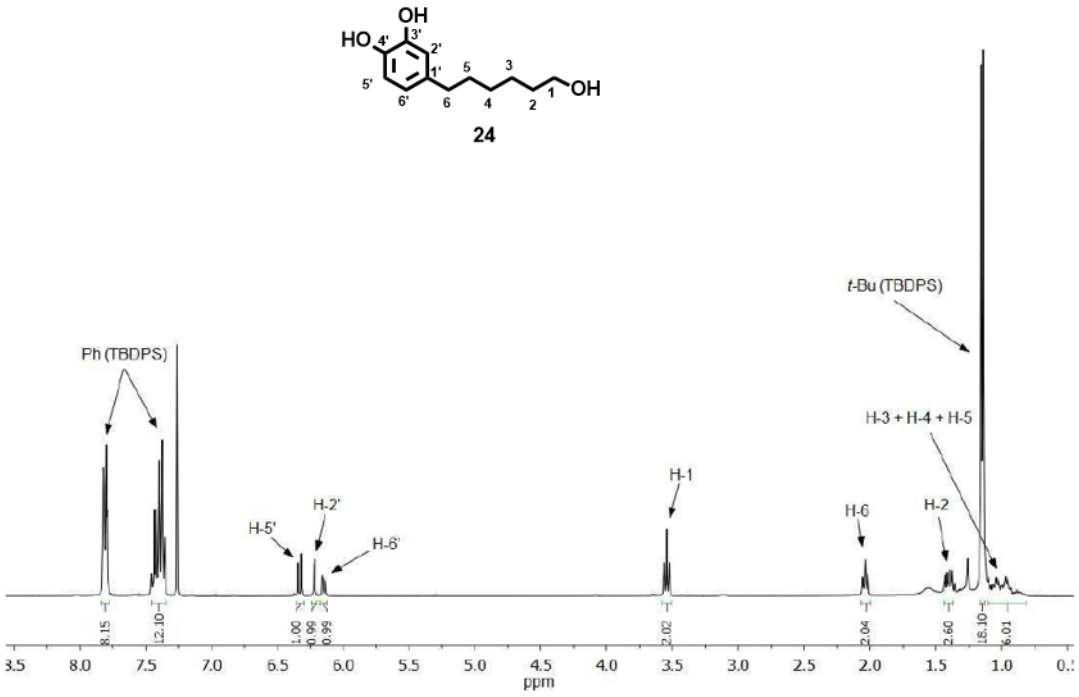

^{1}H NMR (250 MHz, $CDCl_3$)

S2. Characterization of catAZT-NCPs and catTHY-NCPs

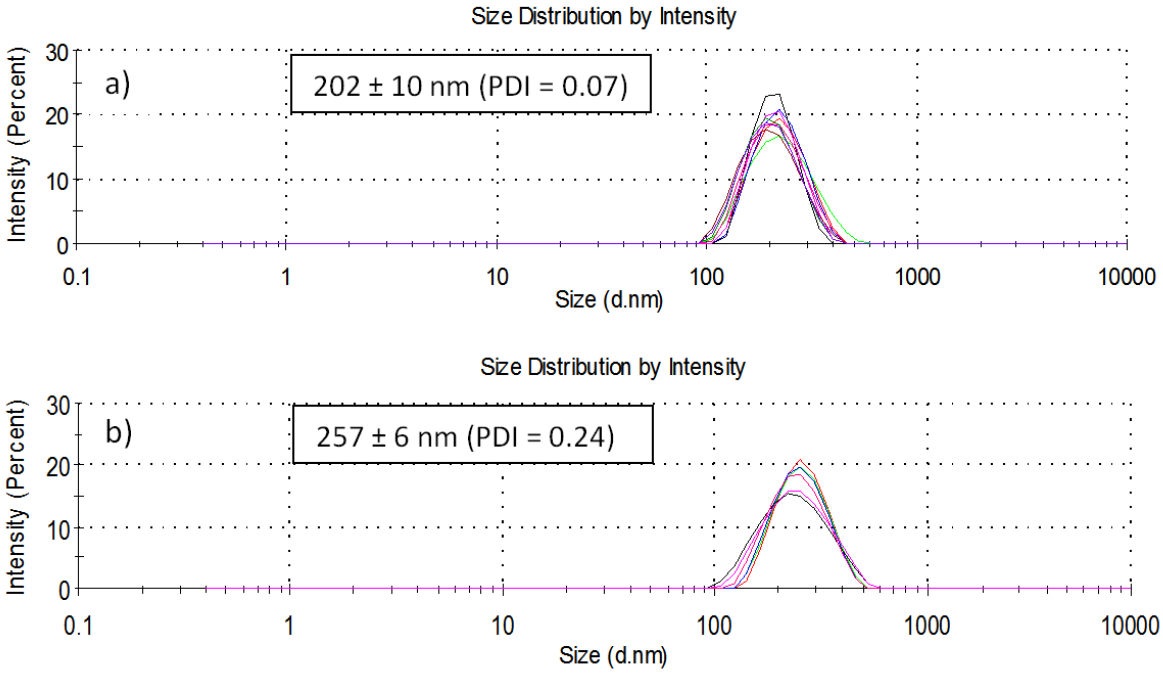

Figure S1. DLS measurements of **catAZT-NCPs** in a) ethanol, and b) PBS/BSA 0.5 mM.

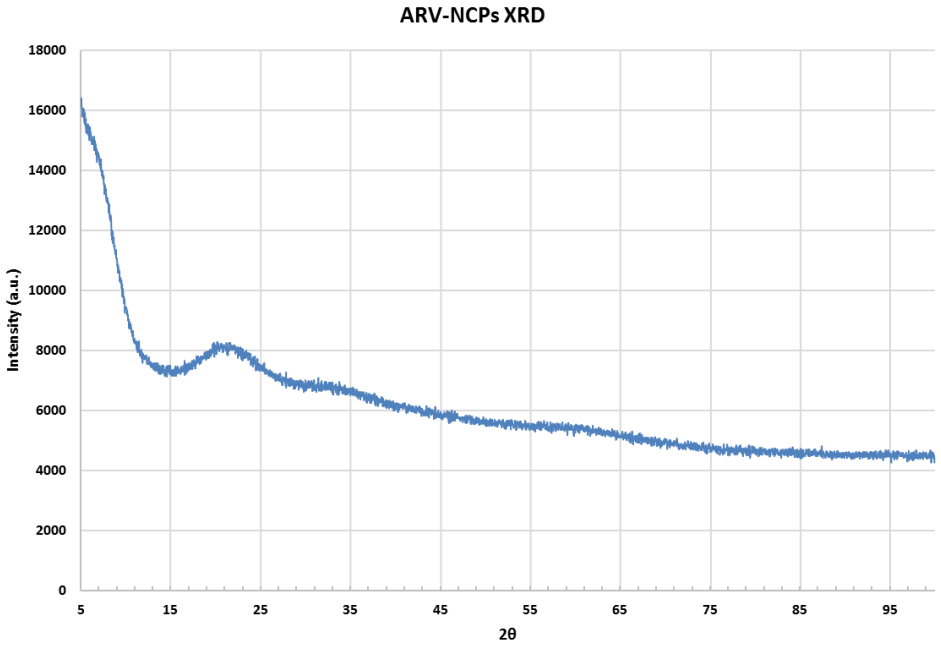

Figure S2. XRD pattern of **catAZT-NCPs**.

Table S1. Table of Elemental Analysis results for three different synthesis and comparison between the average results and the proposed chemical formula. The results indicate a good reproducibility of the synthetic method.

Batch	%C	%H	%N
1	51.93	5.08	13.83
2	51.96	5.00	13.77
3	51.29	5.03	13.72
Average	51.73	5.04	13.77
$[Fe(catAZT)_{1.51}(bix)_{0.62}(AcO)(H_2O)_{2.45}]$	51.76	5.38	13.79

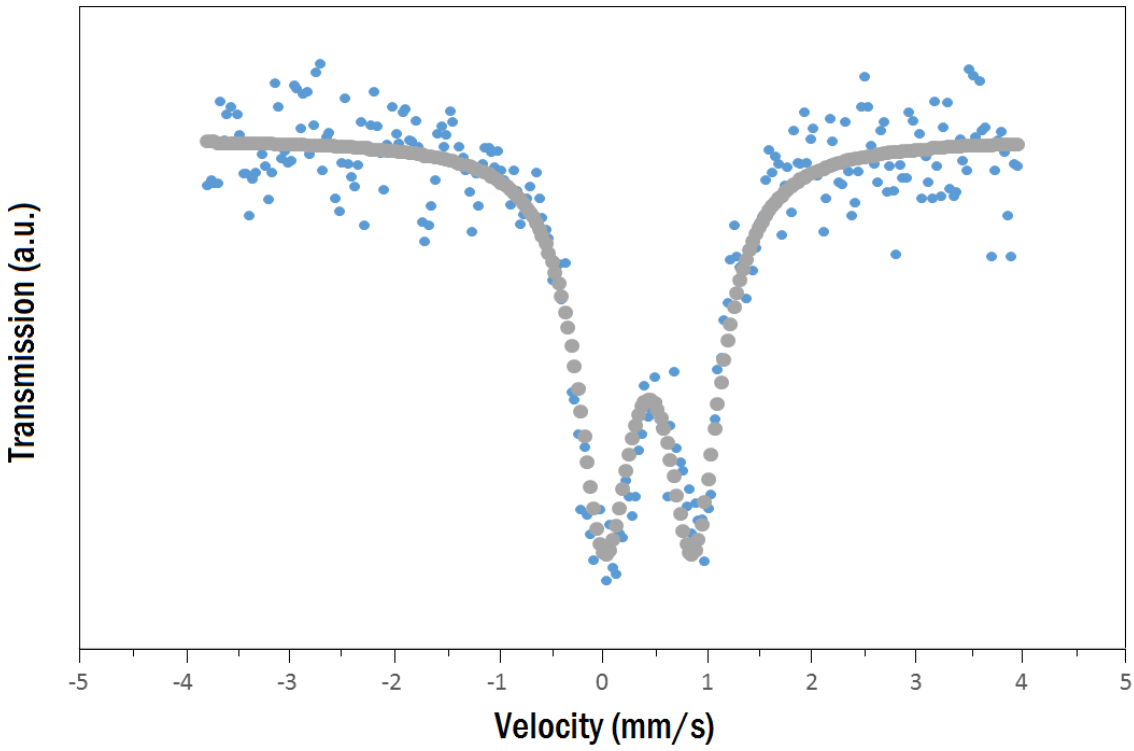

Figure S3. Mössbauer spectra for **catAZT-NCPs** at 293 K. Experimental data (small blue dots), and computer fitted spectrum (big grey dots) for high-spin Fe(III). Hyperfine parameters of the fitting of the Mössbauer spectra at 293 K showed the isomer shift relative to the metallic iron (δFe), quadrupolar splitting (ΔEq) and the full width at half maximum (Γ). The spectrum was fitted to a single doublet with a ΔEq= 0.85 ± 0.02 mm/s and Γ= 0.31 mm/s. The fitting was centered at an isomeric shift δ= 0.44±0.01 mm/s attributed to high-spin Fe(III) ions.

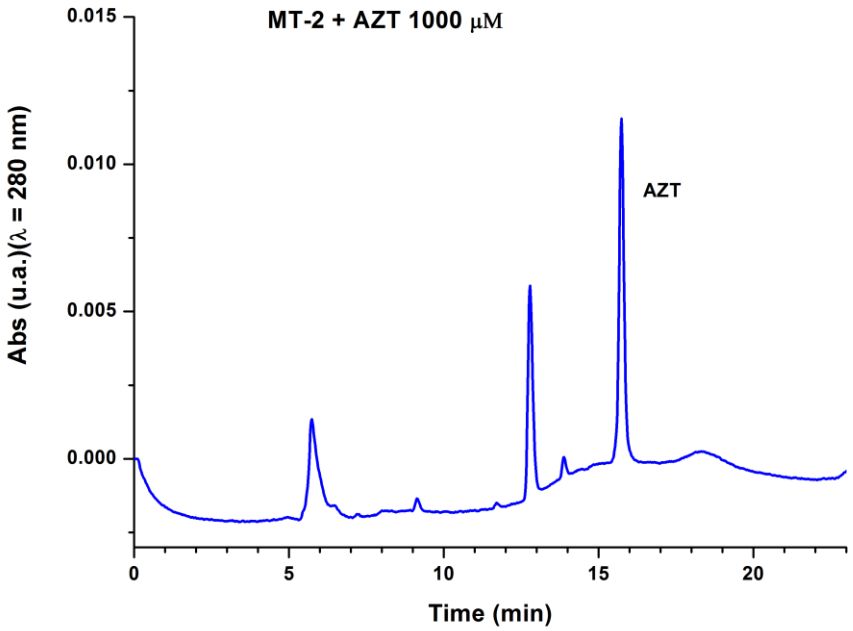

Figure S4. Chromatograms of MT-2 cell lysates incubated with AZT 1000 µM for 4 hours at 37 °C.

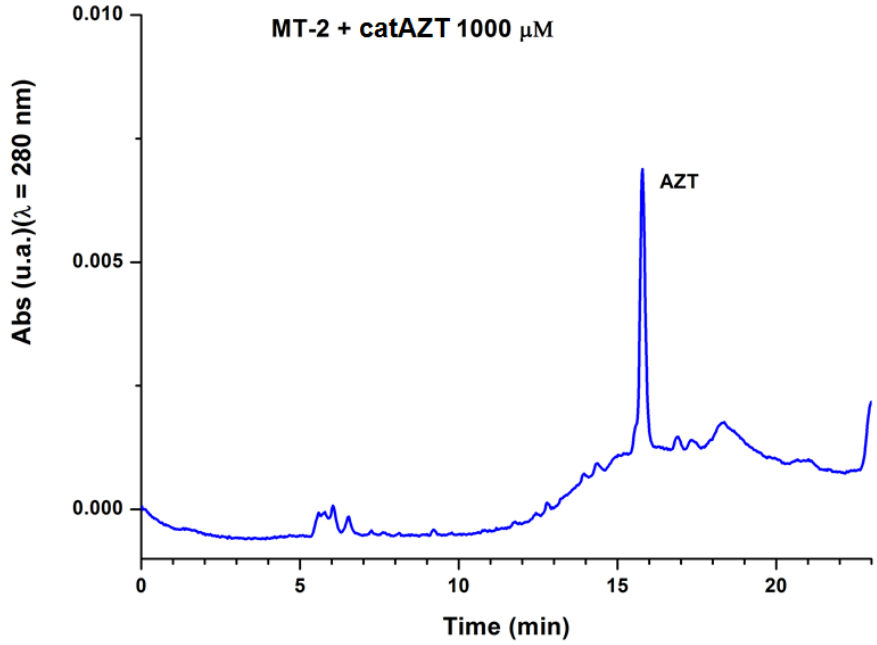

Figure S5. Chromatograms of MT-2 cell lysates incubated with **catAZT** 1000 µM for 4 hours at 37 °C.

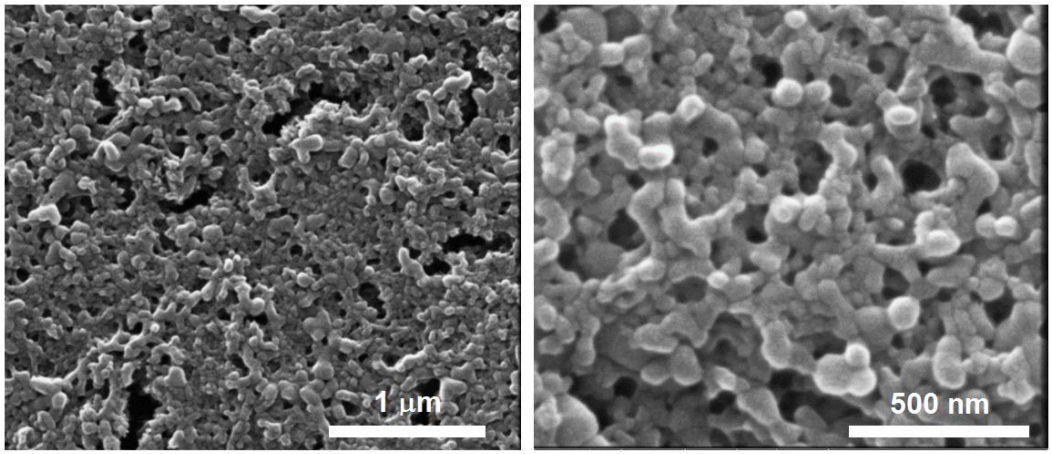

Figure S6. SEM images of **catTHY-NCPs** at different magnifications.

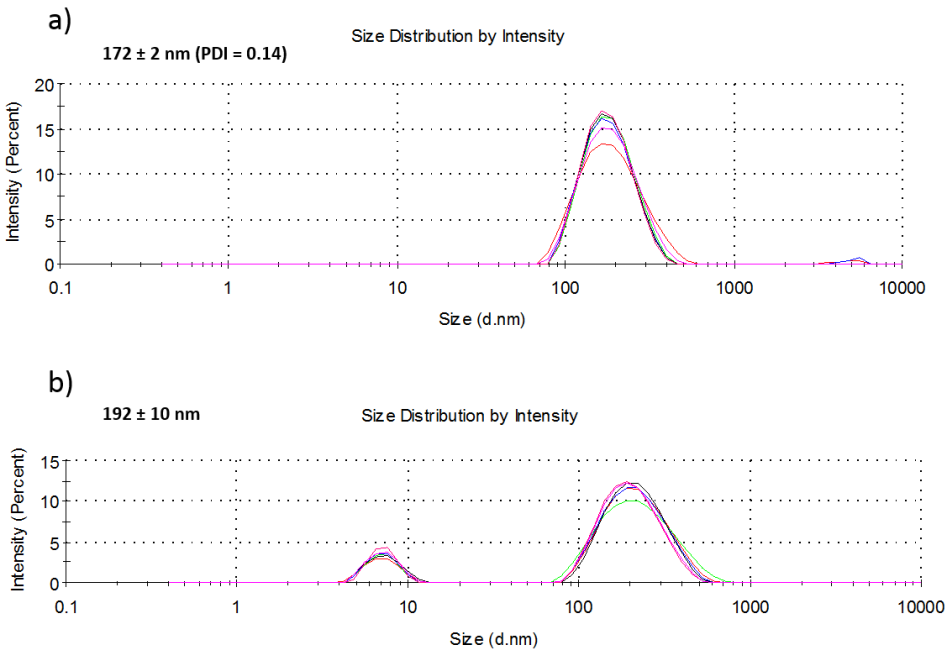

Figure S7. DLS measurements of **catTHY-NCPs** in a) ethanol and b) PBS/BSA 0.5 mM.

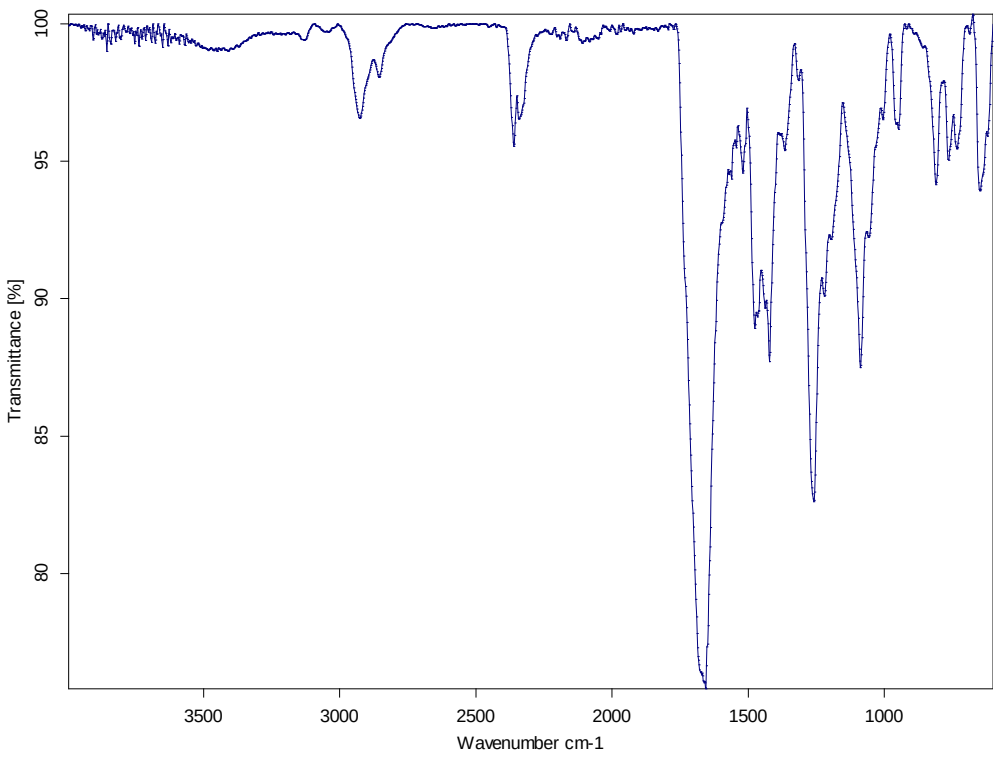

Figure S8. FT-IR spectrum of **catTHY-NCPs**.

Table S2. Table of elemental analysis results for three different batches of **catTHY-NCPs** and comparison between the average and the proposed formula. The results indicate a good reproducibility of the synthetic method.

Batch	%C	%H	%N
1	45.22	4.92	6.64
2	45.18	4.85	6.91
3	45.59	4.96	6.86
Average	45.33	4.91	6.80
$Fe(catTHY)_{2.18}bix(AcO)_{0.7}(H_2O)_{20.2}$	45.48	6.82	7.0

S3. Characterization of catFTC-NCPs, catRAL-NCPs and catRAL-catFTC-NCPs

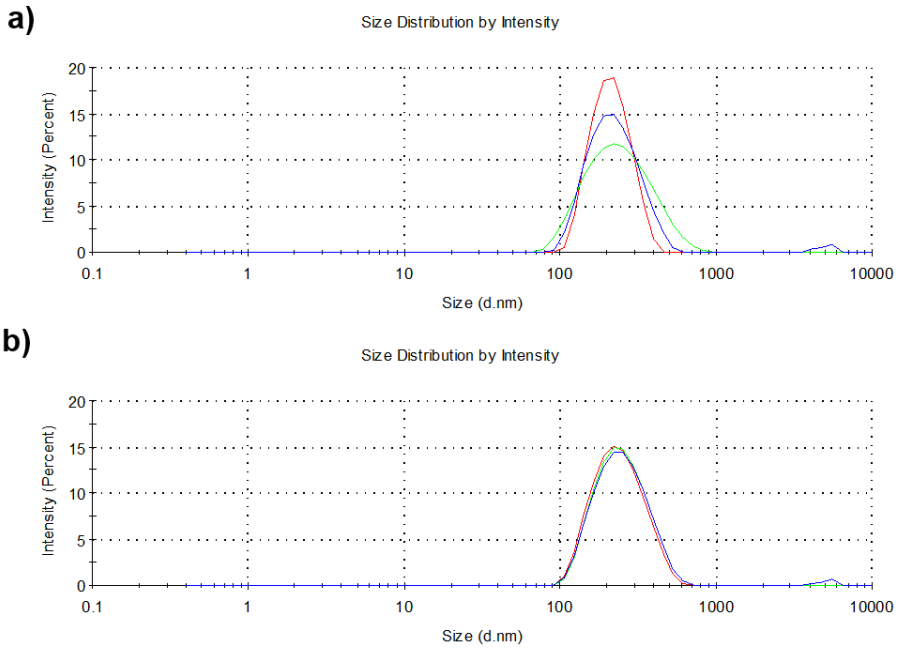

Figure S9. DLS measurements of **catRAL-NCPs** in a) ethanol (213 ± 3 nm), and b) PBS/BSA 0.5 mM (273 ± 34 nm).

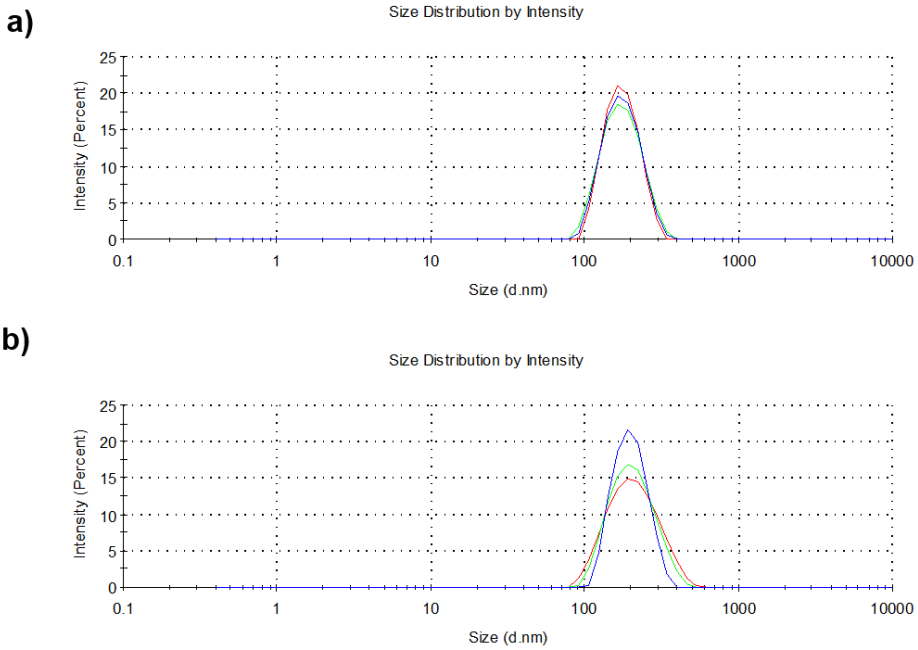

Figure S10. DLS measurements of **catFTC-NCPs** in a) ethanol (166 ± 1 nm), and b) PBS/BSA 0.5 mM (179 ± 1 nm).

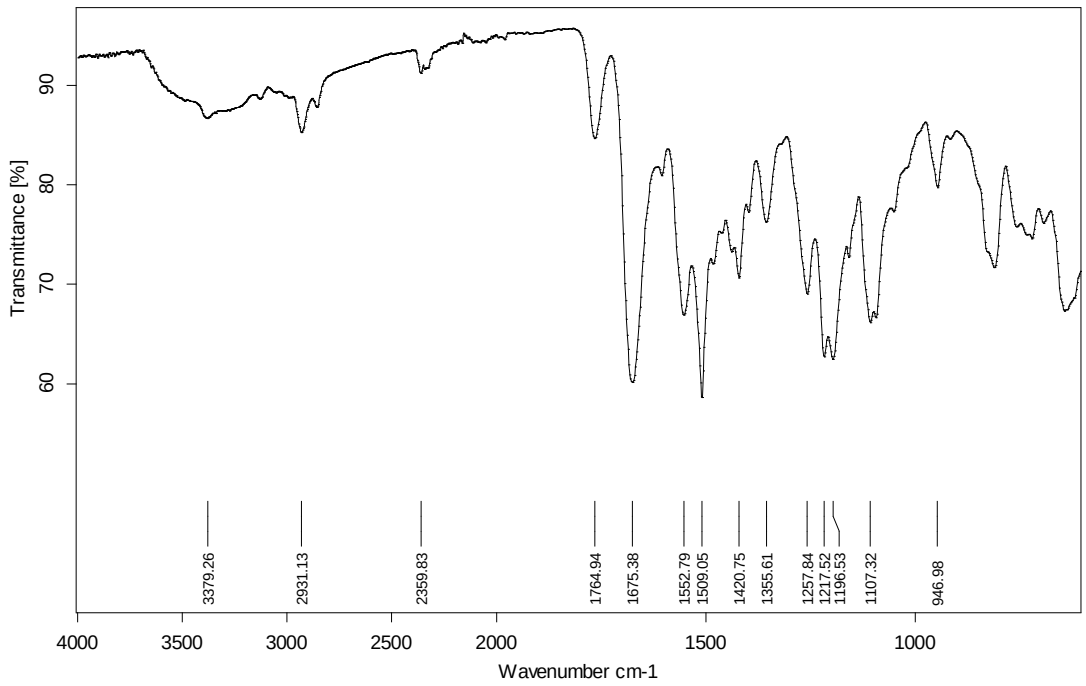

Figure S11. FTIR spectrum of **catRAL-NCPs**.

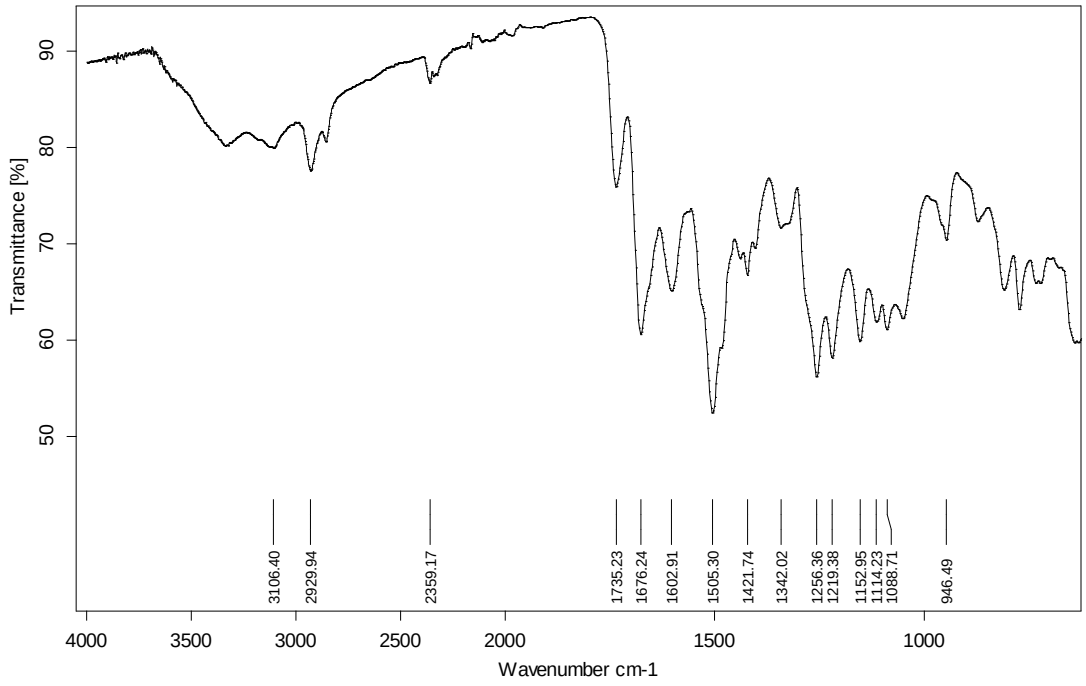

Figure S12. FTIR spectrum of **caFTC-NCPs**.

Table S3. Table of elemental analysis results for three different batches of **catRAL-NCPs** and comparison between the average and the proposed formula. The results indicate a good reproducibility of the synthetic method.

Batch	%C	%H	%N
1	53.64	5.25	11.74
2	52.86	5.05	11.44
3	50.59	4.75	10.89
Average	52.36	5.02	11.36
$Fe(catRAL)_{0.77}(bix)_{0.24}(AcO)_{0.24}(H_2O)_{1.56}$	52.23	5.02	11.36

Table S4. Table of elemental analysis results for three different batches of **catFTC-NCPs** and comparison between the average and the proposed formula. The results indicate a good reproducibility of the synthetic method.

Batch	%C	%H	%N	%S
1	48.64	4.78	9.22	4.31
2	49.14	4.98	9.27	4.80
3	49.56	4.96	9.23	4.89
Average	49.11	4.91	9.24	4.67
$Fe(catFTC)_{0.90}(bix)_{0.57}(AcO)_{1.96}(H_2O)_{0.98}$	49.11	4.91	9.54	3.95

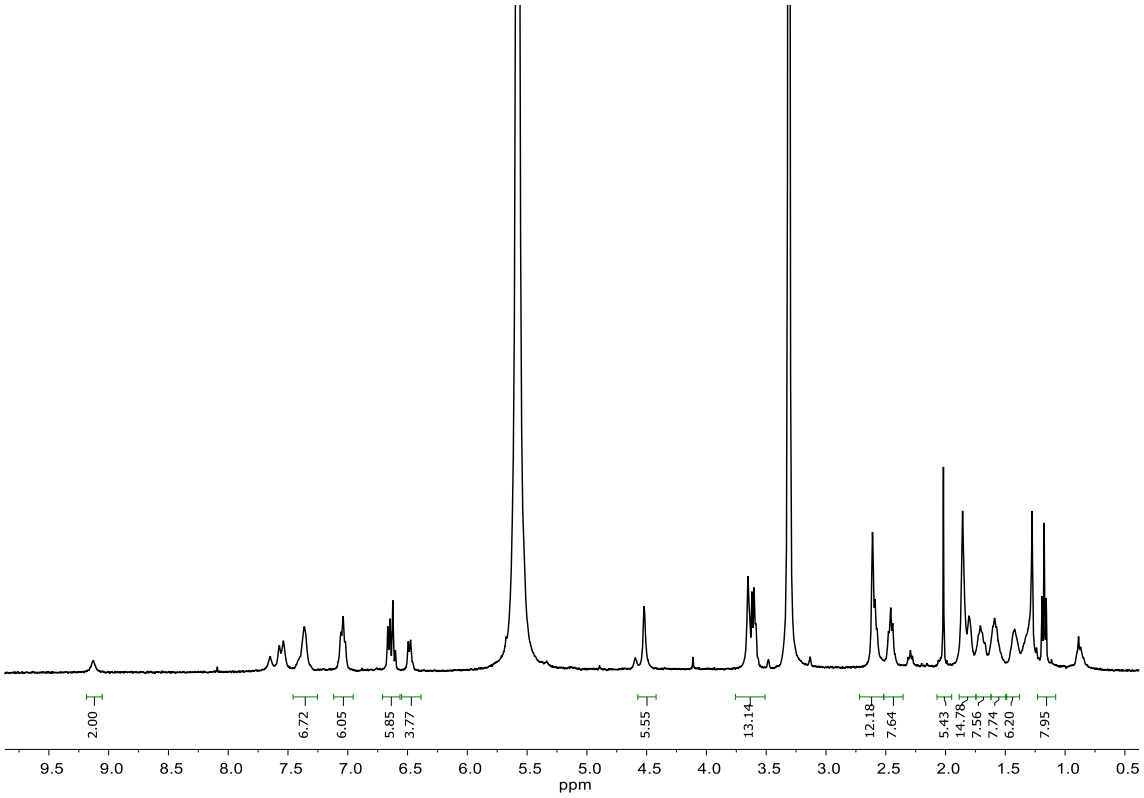

Figure S13. ^{1}H NMR spectrum of disassembled **catRAL-NCPs** in a DCl/CD_3OD solution (50 µL DCl/mL CD_3OD).

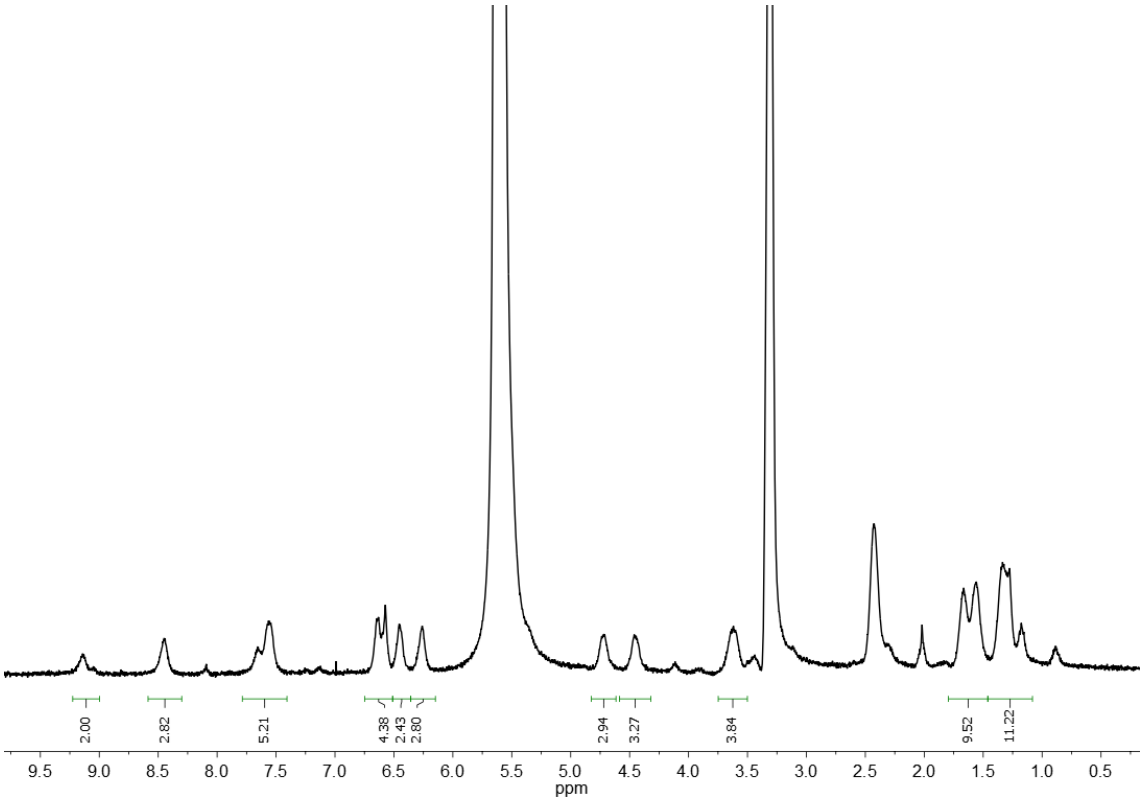

Figure S14. ^{1}H NMR spectrum of disassembled **catFTC-NCPs** in a DCl/CD_3OD solution (50 µL DCl/mL CD_3OD).

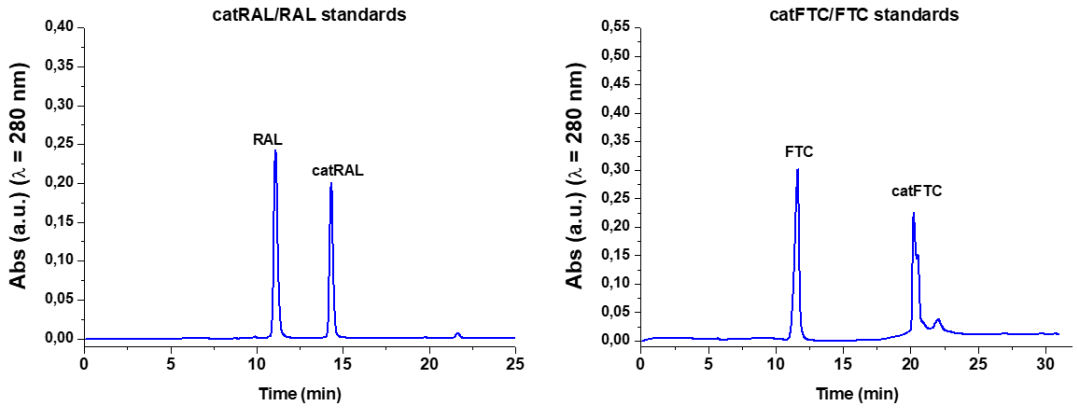

Figure S15. Representative HPLC chromatograms of (left) **catRAL**/RAL standards (102 and 103 µg/mL, respectively) and (right) **catFTC**/FTC standards (90 and 82 µg/mL). $t_{R,RAL}$ = 11.1 min; $t_{R,catRAL}$ = 14.3 min; $t_{R,FTC}$ = 11.6 min; $t_{R,catFTC}$ = 20.2 min.

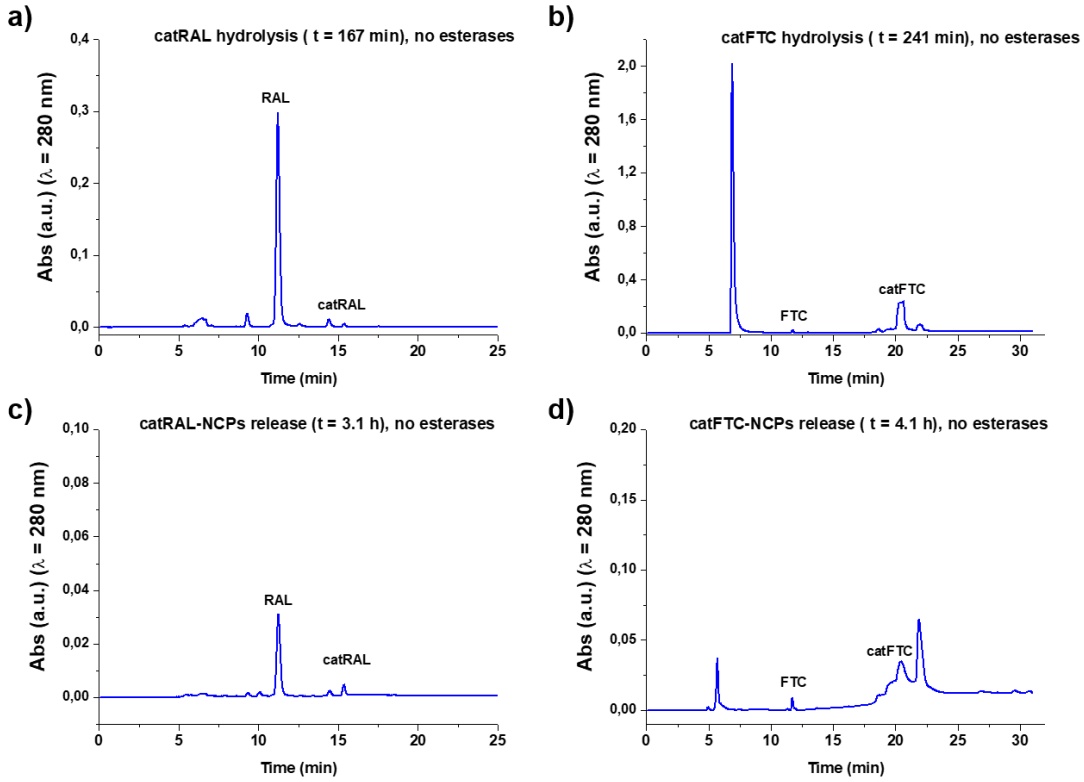

Figure S16. Representative HPLC chromatograms of a) **catRAL**, b) **catFTC**, c) **catRAL-NCPs** and d) **catFTC-NCPs** incubation at 37 °C in absence of esterases.

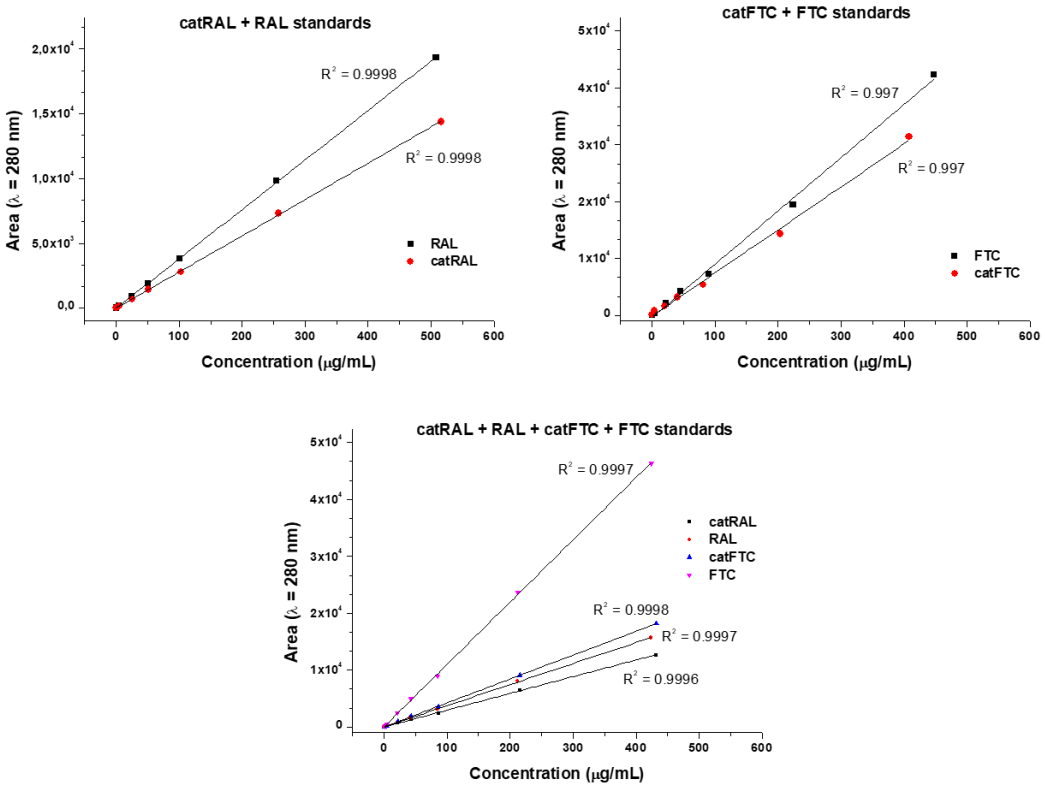

Figure S17. Calibration curves for **catRAL**, RAL, **catFTC** and FTC in the different HPLC methods used.

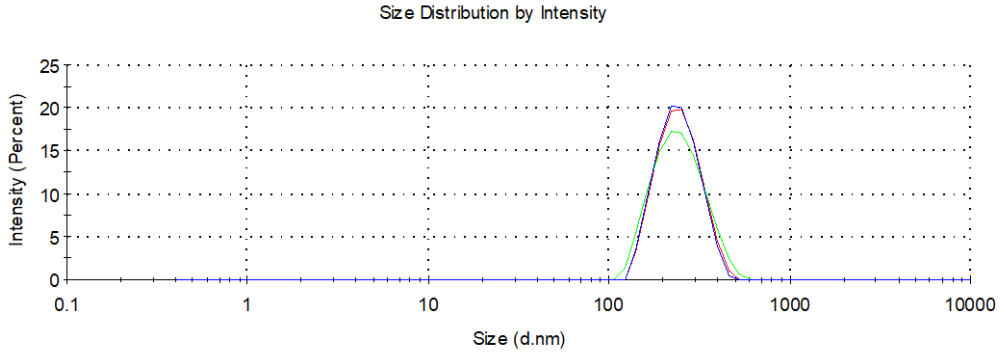

Figure S18. DLS measurements of **catRAL-catFTC-NCPs** in ethanol dispersion.

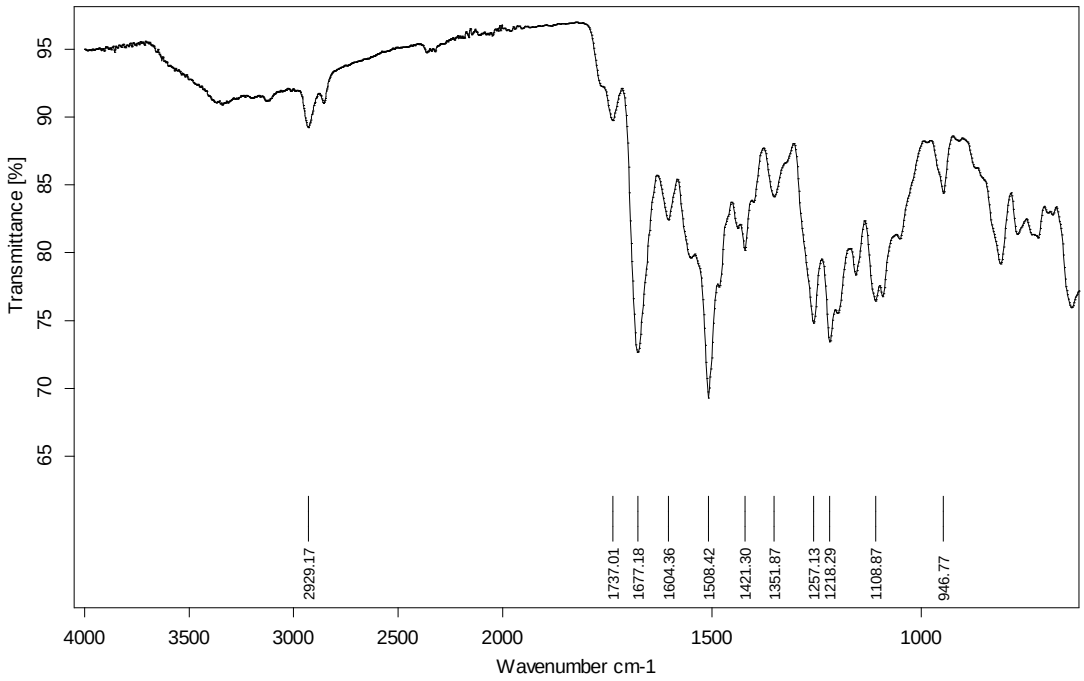

Figure S19. FTIR spectrum of **catRAL-catFTC-NCPs**.

Table S5. Table of elemental analysis results for three different batches of **catRAL-catFTC-NCPs** and comparison between the average and the proposed formula. The results indicate a good reproducibility of the synthetic method.

Batch	%C	%H	%N	%S
1	51.05	4.91	10.44	4.31
2	52.39	5.02	11.02	2.00
3	52.17	4.92	10.88	2.10
Average	51.87	4.95	10.78	2.09
$Fe(catFTC)_{0.55}(bix)_{0.31}(catRAL)_{0.61}(AcO)_{0.95}(H_2O)_{1.19}$	51.87	4.95	10.78	2.08

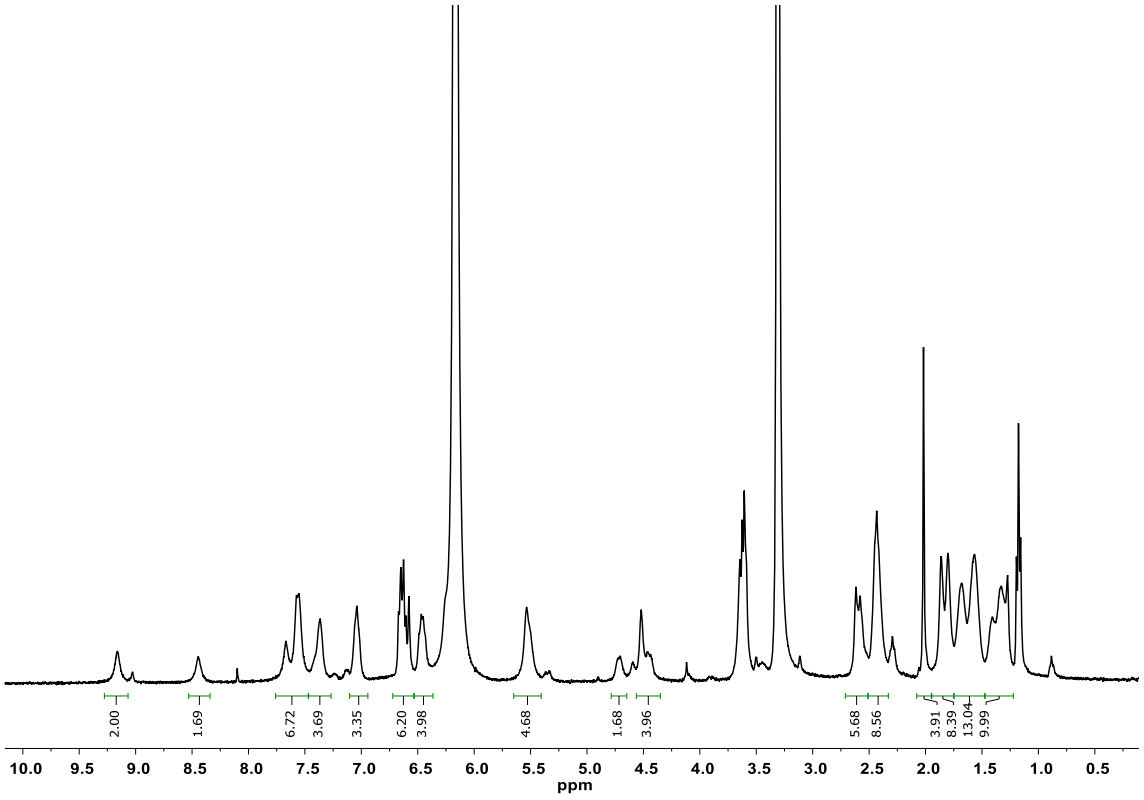

Figure S20. ^{1}H NMR spectrum of disassembled **catRAL-catFTC-NCPs** in a DCl/CD_3OD solution (50 µL DCl/mL CD_3OD).

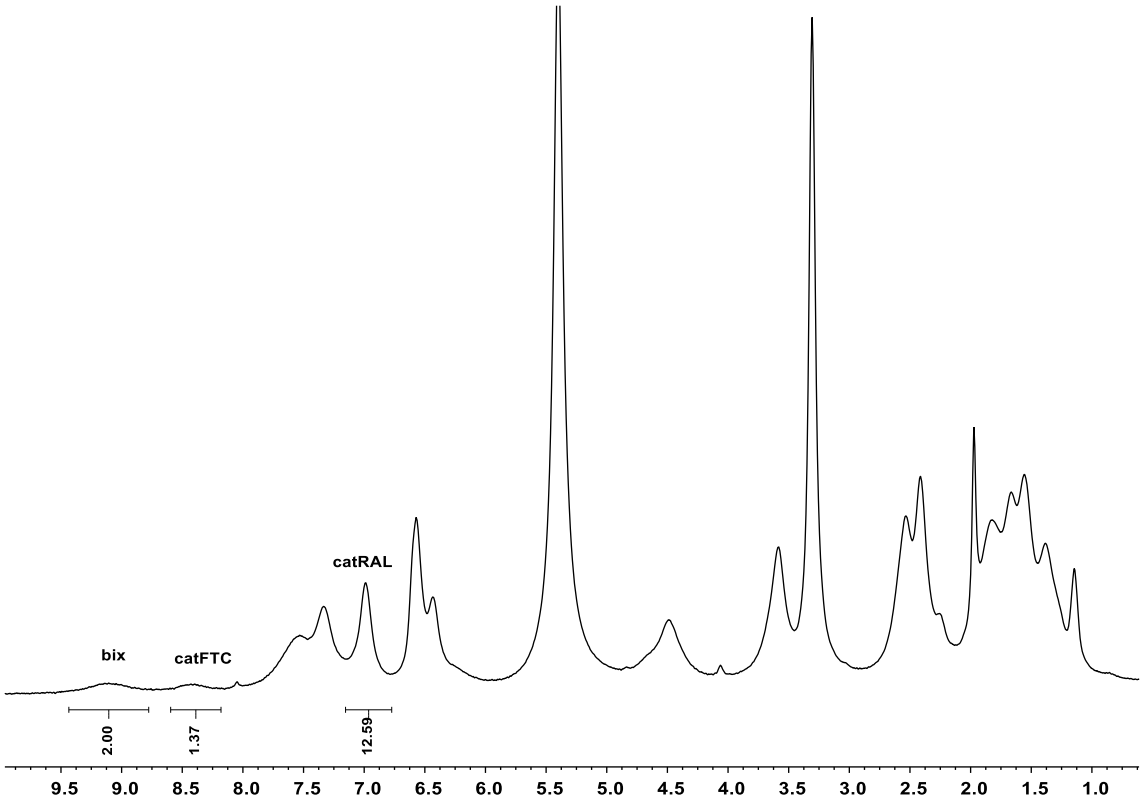

Figure S21. ^{1}H NMR spectra of disassembled **catRAL-catFTC-NCPs (5:1)** in a DCl/CD_3OD solution (50 µL DCl/mL CD_3OD).